Relief Visualization Toolbox in Python

ZRC SAZU and University of Ljubljana

Mar 18, 2024

CONTENTS

Relief Visualization Toolbox (RVT) was produced to help scientists visualize raster elevation model datasets. We have narrowed down the selection to include techniques that have proven to be effective for identification of small scale features. The default settings therefore assume working with high resolution digital elevation models derived from airborne laser scanning missions (lidar), however RVT methods can also be used for other purposes.

Sky-view factor, for example, can be efficiently used in numerous studies where digital elevation model visualizations and automatic feature extraction techniques are indispensable, e.g. in geography, archaeology, geomorphology, cartography, hydrology, glaciology, forestry and disaster management. It can even be used in engineering applications, such as predicting the availability of the GPS signal in urban areas.

CHAPTER

ONE

RVT VISUALIZATION METHODS

Methods currently implemented are:

- hillshading
- hillshading from multiple directions
- slope gradient
- simple local relief model
- multi-scale relief model
- sky illumination
- sky-view factor (as developed by our team)
- anisotropic sky-view factor
- positive and negative openness
- local dominance

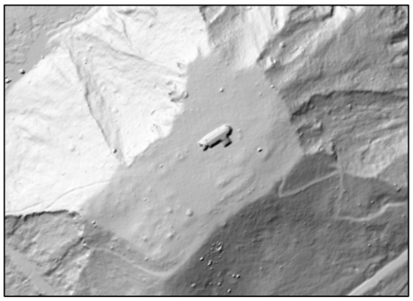

hillshading
azimuth: 315°
sun elevation: 35°

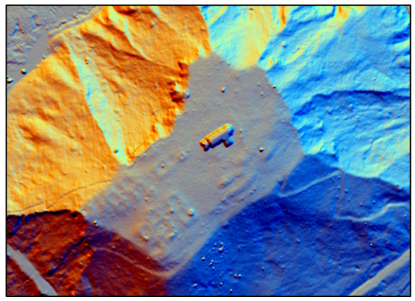

hillshadings in 3 directions
R: 315°
G: 15°
B: 75°

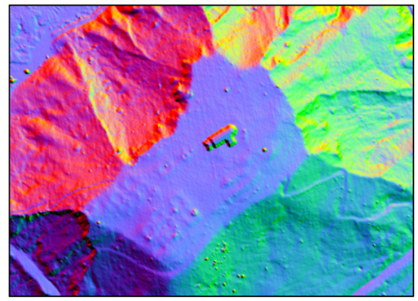

PCA of hillshadings
R: 1st component
G: 2nd component
B: 3rd component

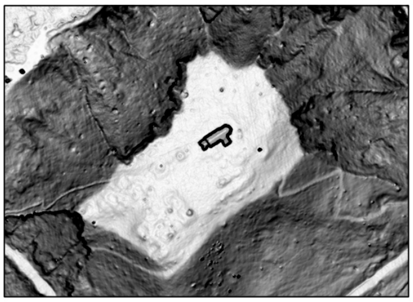

slope
0 50°

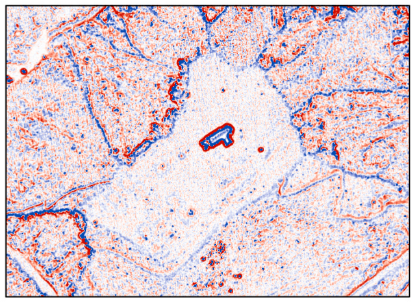

local relief model
radius: 10 m
-0.1 0.1

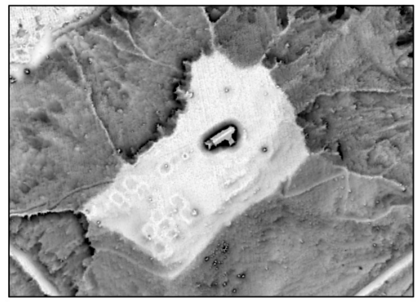

sky-view factor
number of directions: 32
search radius: 10 m
0.55 1

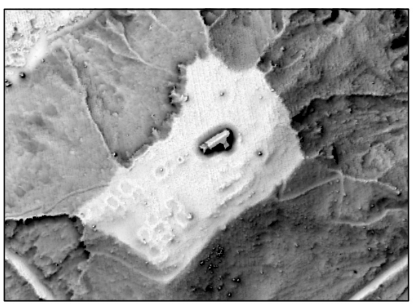

anisotropic sky-view factor
number of directions: 32
search radius: 10 m
0.55 1

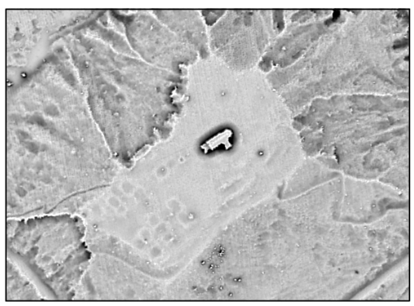

positive openness
number of directions: 32
search radius: 10 m
60° 95°

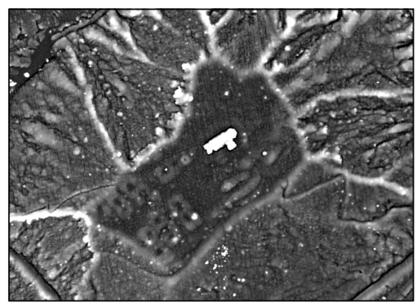

negative openness
number of directions: 32
search radius: 10 m
60° 95°

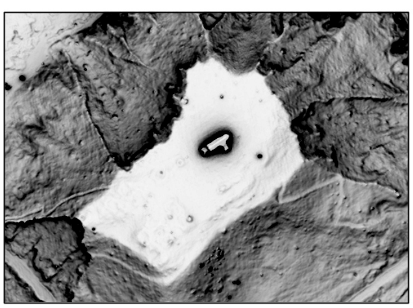

sky illumination model
model: overcast
max. distance: 50 m
0.45 0.59

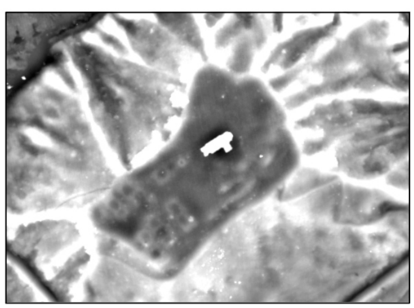

local dominance
search radius: 10-20 m
0.5 1.8

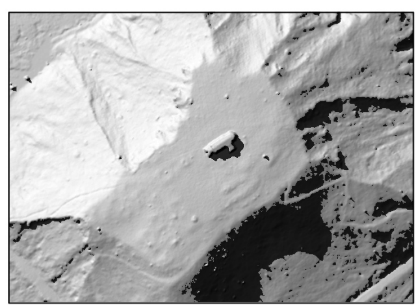

shadows on hillshading
azimuth: 315°
sun elevation: 35°

Lidar data © Walks of peace in the Soča river foundation
Average last and only returns per m² of a combined dataset: 11.2
Spatial resolution of the DEM: 0.5 m

0 50 100 m

CHAPTER

TWO

REFERENCES

When using the tools, please cite:

- Kokalj, Ž., Somrak, M. 2019. Why Not a Single Image? Combining Visualizations to Facilitate Fieldwork and On-Screen Mapping. Remote Sensing 11(7): 747.
- Zakšek, K., Oštir, K., Kokalj, Ž. 2011. Sky-View Factor as a Relief Visualization Technique. Remote Sensing 3: 398-415.
- Kokalj, Ž., Zakšek, K., Oštir, K. 2011. Application of Sky-View Factor for the Visualization of Historic Landscape Features in Lidar-Derived Relief Models. Antiquity 85, 327: 263-273.

CHAPTER THREE

FURTHER READING

- Kokalj, Žiga, Ralf Hesse. 2017. Airborne laser scanning raster data visualization: A Guide to Good Practice. Ljubljana: Založba ZRC. (a comparative guide describing each method)

CHAPTER

FOUR

CONTRIBUTING

The project source code is available at GitHub. Pull requests are welcome. For major changes, please open an issue first to discuss what you would like to change.

Please report any bugs and suggestions for improvements.

CHAPTER FIVE

ACKNOWLEDGMENT

Development of RVT was part financed by the European Commission's Culture Programme through the ArchaeoLandscapes Europe project and by the Slovenian Research Agency core funding No. P2-0406, and by research projects No. J2-9251, No. J6-7085 and No. J6-9395.

Development of RVT QGIS plugin was part financed by PTS Consultancy via the UK Government Culture Recovery Fund.

CHAPTER

SIX

LICENSE

This project is licensed under the terms of the Apache License.

6.1 Installation

RVT can be installed as a package for Python, where it can be used in Python scripts, Jupyter Notebooks and ArcGIS Pro.

RVT can also be installed as a set of custom raster functions for ArcGIS, and a plugin for QGIS.

You can also clone the repository (GitHub rvt_py).

6.1.1 Requirements

Required libraries (specified versions have been tested, other versions may also work):

- numpy 1.19.2
- scipy 1.5.2
- gdal 3.0.2

We recommend using Python 3.6 or higher and a Conda environment (this works best with `gdal`).

CONTENTS

Python installation

Conda

The `rvt` package is available from the Anaconda Cloud repository. Using Conda to install the `rvt` package will include all required libraries.

First install Anaconda and Conda.

Then open Anaconda Prompt (Windows) or Terminal (MacOS) and run:

```
conda install -c rvtpy rvt_py
```

PyPI

Another option is to install the `rvt-py` package and required libraries using the Python Package Index (PyPI).

PyPI usually has problems installing `gdal`, so install gdal first.

Then open Command Prompt (Windows) or Terminal (MacOS) and run:

```
pip install rvt-py
```

ArcGIS installation

To use RVT in ArcGIS Pro, download the ArcGIS Raster Functions repository by selecting `Code` → `Download ZIP`.

Unzip the downloaded repository folder and *rename* it to `rvt-arcgis-pro`, then copy the whole repository folder to: `<ArcGIS Pro install path>/Resources/Raster/Functions/Custom`

Usually the path is: `c:/Program Files/ArcGIS/Pro/Resources/Raster/Functions/Custom`

For ArcGIS Server use, copy the whole repository folder (`rvt-arcgis-pro`) to every federated server machine of your enterprise setup: `<ArcGIS Server install path>/framework/runtime/ArcGIS/Resources/Raster/Functions/Custom`

Open or restart ArcGIS Pro. Select `Imagery` → `Raster Functions` to open the Raster Functions pane.

In the `Raster Functions` pane, select the `Custom` tab to access the `rvt-arcgis-pro` group containing the raster functions.

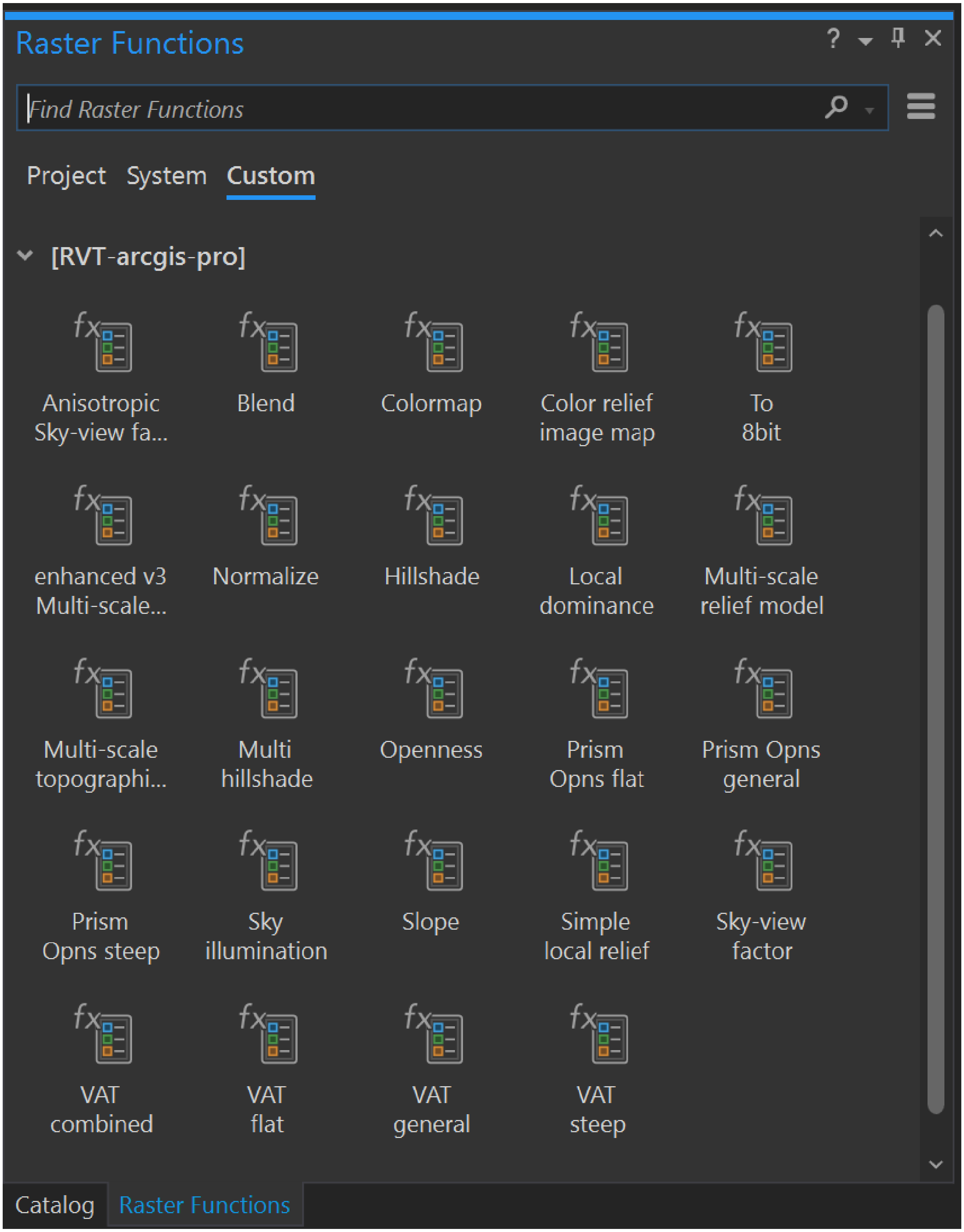
Raster Functions
Find Raster Functions
Project
System
Custom
[RVT-arcgis-pro]
Anisotropic Sky-view fa...
Blend
Colormap
Color relief image map
To 8bit
enhanced v3 Multi-scale...
Normalize
Hillshade
Local dominance
Multi-scale relief model
Multi-scale topographi...
Multi hillshade
Openness
Prism Opns flat
Prism Opns general
Prism Opns steep
Sky illumination
Slope
Simple local relief
Sky-view factor
VAT combined
VAT flat
VAT general
VAT steep
Catalog
Raster Functions

QGIS installation

To use RVT in QGIS, first open QGIS and select `Plugins` → `Manage and Install Plugins` → `All`.

Search for `RVT` or `Relief Visualization Toolbox` and select `Install Plugin`.

Once the plugin is installed, it can be accessed from the `Raster menu` or by selecting the icon that will appear on the toolbar. All the visualization functions are also available as processing functions in the `Processing toolbox`.

The RVT QGIS plugin can also be downloaded from the QGIS Python Plugins Repository.

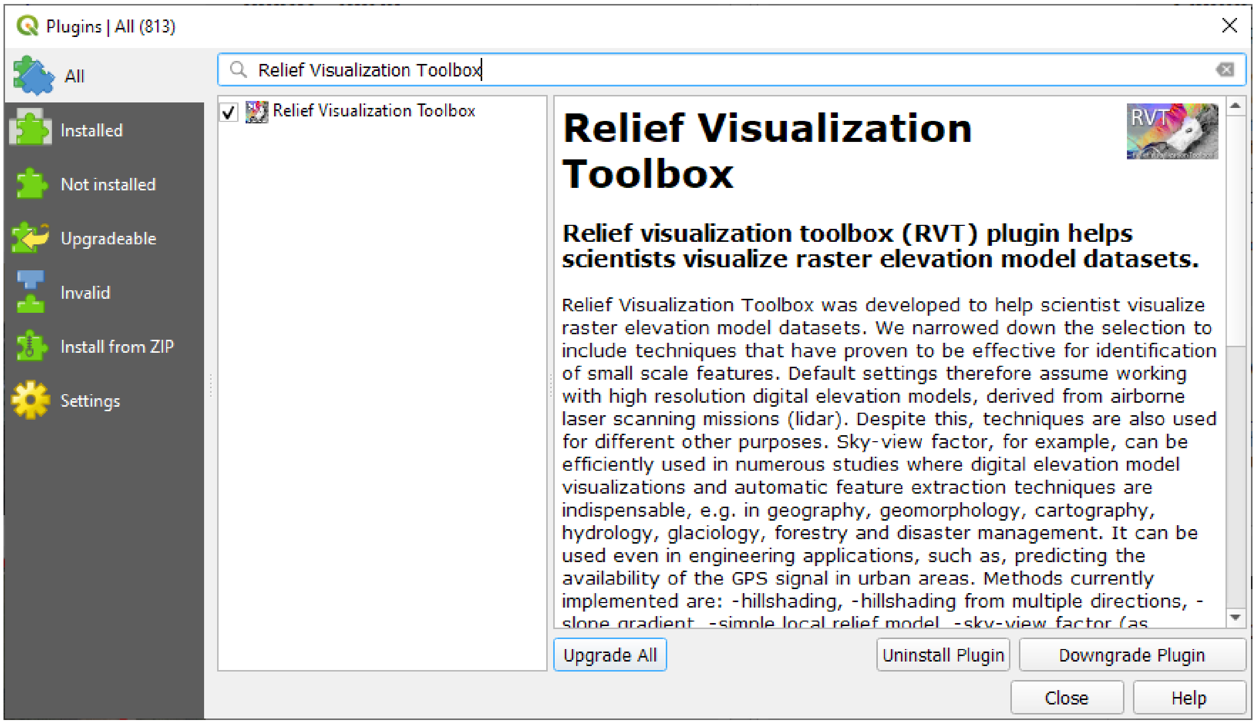

6.2 Getting started

The `rvt` Python package contains three modules:

- **vis** (*rvt.vis*) for computing visualizations
- **blend** (*rvt.blend*) for blending visualizations together
- **default** (*rvt.default*) for defining default parameters with methods to compute and save visualization functions using set parameters

This section explains how to complete some basic visualisation tasks using these modules, as well as some information on how to choose which visualizations to use.

If you need some data to get started, a small sample dataset (2.43 MB) and a larger sample dataset (152 MB) are available for download.

See also:

For more detailed explanations of how to use `rvt` visit *RVT for Python*

Tip: Carlos Carbajal has written an excellent two-part blog post on the use of RVT in Python and QGIS (in Spanish). You can check it out here: Part 1 & Part 2.

CONTENTS

6.2.1 Reading and saving raster data

For reading raster data (DEMs) from files (GeoTIFFs) to a numpy array we suggest using the `rvt.default` module (which uses `gdal`). You can also use `rasterio`, `gdal` or any other module for reading and saving geo rasters.

Reading raster data

Example

To read a raster with `rvt.default`:

```
# import the module
import rvt.default

# change this to the path to your GeoTIFF
dem_path = r"C:/data/dem.tif"

# call the function rvt.default.get_raster_arr() to return a dictionary with keys:
#   array (contains numpy array of raster),
#   resolution (contains the tuple(x resolution, y resolution)),
#   no_data (contains the value of no_data)
dem_dict = rvt.default.get_raster_arr(dem_path)

# numpy array
dem_arr = dem_dict["array"]

# resolution tuple (x-direction resolution, y-direction resolution)
dem_resolution_tuple = dem_dict["resolution"]

# first element of the resolution tuple (the x-direction resolution)
dem_x_resolution = dem_resolution_tuple[0]

# second element of resolution tuple (the y-direction resolution)
dem_y_resolution = dem_resolution_tuple[1]

# the value of no_data stored in DEM
dem_no_data = dem_dict["no_data"]
```

Saving raster data

Example

Let's say we wanted to use a DEM stored in `dem_path` to compute a hillshade (using `rvt.vis`) stored in `hillshade_arr`, and then save this hillshade visualization to `hillshade_path`:

```
# import the required modules
import rvt.default
import numpy as np

# call the function rvt.default.save_raster() and define the function parameters:
#   src_raster_path: source raster path (dem_path) to copy metadata,
#   out_raster_path: path to new file (visualization tif),
#   out_raster_arr: vizualization numpy array,
#   no_data: value of no_data (visualizations return no data as np.nan)
rvt.default.save_raster(
    src_raster_path=dem_path,
    out_raster_path=hillshade_path,
    out_raster_arr=hillshade_arr,
    no_data=np.nan
    )
```

See also:

Find out more about defining default values in *rvt.default*.

6.2.2 Creating a visualization

Visualizations can be created with both the `rvt.vis` and `rvt.default` modules.

Visualizations with rvt.vis

The module `rvt.vis` contains the `rvt` visualization functions.

Every function takes a DEM (as a 2D numpy array) with parameters, and outputs a visualization (as a 2D numpy array).

Example

Let's say we need to calculate a hillshade with sun azimuth 315° and sun elevation 35°:

```
# import the module
import rvt.vis

# read the DEM
# Follow the steps in `Reading raster data`

# call the rvt.vis.hillshade() function with its parameters
hillshade_arr = rvt.vis.hillshade(
    dem=dem_arr,
    sun_azimuth=315,
    sun_elevation=35,
    resolution_x=dem_x_resolution,
```

(continues on next page)

(continued from previous page)

```
    resolution_y=dem_y_resolution,
    no_data=dem_no_data
    )

# save the visualization
# Follow the steps in `Saving raster data`
```

See also:

Find out more about visualization functions and their parameters in *rvt.vis*.

Visualizations with rvt.default (beginner)

For beginner Python users we suggest using `rvt.default` instead of `rvt.vis` to calculate and store visualizations.

As well as containing functions to read and save rasters, `rvt.default` also contains the class `DefaultValues()` where we can store our visualization functions parameters. We can call the methods of this class for saving and computing visualizations with those parameters (these methods use `rvt.vis` for computing visualizations).

Example

To calculate, get or save a hillshade using `rvt.default`:

```
#  import the module
import rvt.default

# create a DefaultValues() class instance
default = rvt.default.DefaultValues()

# change hillshade parameters default values to our needs
# (they are attributes of DefaultValues(), their name starts with hs_)
default.hs_sun_el = 45
default.hs_sun_azi = 300

# call the method default.get_hillshade() which uses the set parameters and
# returns the hillshade numpy array
hillshade_arr = default.get_hillshade(
    dem_arr=dem_arr,
    resolution_x=dem_x_resolution,
    resolution_y=dem_y_resolution,
    no_data=dem_no_data
    )

# if we don't need the hillshade array and we just want to save the hillshade, we
# can directly call the default.save_hillshade() method. this method also uses the
# set hillshade parameters and saves the visualization as a GeoTIFF in dem_path
default.save_hillshade(
    dem_path=dem_path,
    save_float=True,
    save_8bit=True # to save the 8bit version of the result, set save_8bit=True
    )
```

Configuring visualization parameters

Parameters of a DefaultValues() instance can be saved to a JSON configuration file which can be edited. You can then load this file back and overwrite the attribute values (or visualization functions parameters).

Example

```python
# import the module
import rvt.default

# create a DefaultValues() class instance
default = rvt.default.DefaultValues()

# change this path to where you would like to save the config file
config_json_path = r"C:/rvt_default_values.json"

# save set attributes values to a JSON configuration file
default.save_default_to_file(file_path=config_json_path)

# overwrite the DefaultValues() instance (default) attributes values
# from the config file
default.read_default_from_file(file_path=config_json_path)
```

DefaultValues() class methods

The DefaultValues() class also contains the methods: get_slope(), save_slope(), get_multi_hillshade(), save_multi_hillshade(), get_slrm(), save_slrm(), get_sky_view_factor(), save_sky_view_factor(), get_neg_opns(), save_neg_opns(), get_local_dominance(), save_local_dominance(), get_sky_illumination(), save_sky_illumination().

See also:

Find out more about the methods and attributes of the DefaultValues() class in *rvt.default*.

6.2.3 Blending visualizations

You can blend manually or automatically.

Manual blending allows you to use visualizations that are not part of rvt. When blending manually you have to define each layer (visualization) in Python.

Automatic blending automatically computes rvt visualizations and blends them together according to a configuration JSON file, which can be edited.

The main class of the rvt.blend module for blending is BlenderCombination, which has the list attribute layers where instances of class BlenderLayer are stored. In BlenderLayer instances in layers we store a specific visualization and its parameters for blending.

The BlenderCombination class has the method render_all_images(), which blends together all BlenderLayer instances (visualizations) in the BlenderCombination.layers list and outputs the blended image.

You can blend as many layers as you want.

Manual blending

Example

Let's say we have already calculated the simple local relief model (slrm_arr), slope (slope_arr) and hillshade (hillshade_arr), and now need to blend all the calculated visualizations together:

```
# import the module
import rvt.blend

# create the BlenderCombination() class instance which will hold the layers␣
↪(visualizations)
combination_manual = rvt.blend.BlenderCombination()

# call BlenderCombination.create_layer() to add a layer
# this creates a BlenderLayer instance and adds it to BlenderCombination.layers

# 1st layer
# add slrm layer with 2% perc cuttoff on both sides, multiply blend mode and 25% opacity
combination_manual.create_layer(
    vis_method="Simple local relief model",
    normalization="perc",
    minimum=2,
    maximum=2,
    blend_mode="multiply",
    opacity=25,
    image=slrm_arr
    )

# 2nd layer
# add slope layer with value stretch from 0 to 51, luminosity blend mode and 50% opacity
combination_manual.create_layer(
    vis_method="Slope gradient",
    normalization="value",
    minimum=0,
    maximum=51,
    blend_mode="luminosity",
    opacity=50,
    image=slope_arr
    )

# 3rd layer
# add hillshade layer with value stretch from 0 to 1, normal blend mode and 100% opacity
combination_manual.create_layer(
    vis_method="Hillshade",
    normalization="value",
    minimum=0,
    maximum=1,
    blend_mode="normal",
    opacity=100,
    image=hillshade_arr
    )

# if we want to save the blended image to a file, we need to add dem_path to the
```

(continues on next page)

(continued from previous page)

```
# combination (for metadata, geodata)
combination_manual.add_dem_path(dem_path=input_dem_path)

# blend them all together
# you can save the blend to GeoTIFF if save_render_path presented
# (and dem_path is added), otherwise it only returns array
render_arr = combination_manual.render_all_images(save_render_path=output_blend_path)
```

Example

You can also let the `BlenderCombination` class automatically compute the visualization or give the path to a visualization.

If you **don't** provide the **image** parameter, and the vis_method parameter is correct (an existing `rvt.vis` function), blender automatically calculates the visualization.

If you **don't** provide the **image** parameter, but **do** provide the **image_path** parameter (if you provide both image will be used), blender will read the visualization from image_path.

If you **don't** provide the **image and image_path** parameters, you have to add an `rvt.default.DefaultValues` instance as a parameter to `BlenderCombination.render_all_images()`. Blender then takes the parameters set in this class when calculating specific visualizations. You also have to add dem array and its resolution.

The example below uses all three methods:

```
# import all required modules
import rvt.blend
import rvt.default

# create the BlenderCombination() class instance which will hold the layers␣
↪(visualizations)
combination_manual = rvt.blend.BlenderCombination()

# we will let blender compute the slrm visualization. so, we need to create
# rvt.default.DefaultValues() and change the parameters for slrm. we will later
# add default to the combination_manual.render_all_images() method
default = rvt.default.DefaultValues()
default.slrm_rad_cell = 15

# 1st layer
# add slrm layer with 2% perc cuttoff on both sides, multiply blend mode and 25% opacity
# image and image_path parameters both not provided, so slrm is calculated automatically
combination_manual.create_layer(
    vis_method="Simple local relief model",
    normalization="perc",
    minimum=2,
    maximum=2,
    blend_mode="multiply",
    opacity=25
    )

# 2nd layer
# add slope layer with value stretch from 0 to 51, luminosity blend mode and 50% opacity
# image_path parameter provided to slope, so slope is read from file
combination_manual.create_layer(
```

(continues on next page)

(continued from previous page)

```
    vis_method="Slope gradient",
    normalization="value",
    minimum=0,
    maximum=51,
    blend_mode="luminosity",
    opacity=50,
    image_path=slope_path
    )

# 3rd layer
# add hillshade layer with value stretch from 0 to 1, normal blend mode and 100% opacity
# image parameter provided
combination_manual.create_layer(
    vis_method="Hillshade",
    normalization="value",
    minimum=0,
    maximum=1,
    blend_mode="normal",
    opacity=100,
    image=hillshade_arr
    )

# we have to add dem array and resolution so that slrm can be computed
combination_manual.add_dem_arr(dem_arr=input_dem_arr, dem_resolution=resolution)

# blend them all together and add default where slrm parameters are defined
render_arr = combination_manual.render_all_images(default=default)
```

Automatic blending

Automatic blending is blending from a configuration `JSON` file. You can create a `JSON` file and change it to suit your needs.

Example

```
# import the module
import rvt.blend

# create the BlenderCombination() class
combination_auto = rvt.blend.BlenderCombination()

# to create the JSON blender combination configuration file example, change the
# path to where you wish to save the file
blender_combination_path = r"settings\blender_file_example.txt"
rvt.blend.create_blender_file_example(file_path=blender_combination_path)

# set the parameters of the visualizations you will be using
default = rvt.default.DefaultValues()
# for example default.hs_sun_el=40
```

(continues on next page)

(continued from previous page)

```
# read the JSON combination configuration file
combination_auto.read_from_file(file_path=blender_combination_path)

# needed when save_visualizations is True and save_render_path is not None
layers_auto.add_dem_path(input_dem_path)

# call the method render_all_images() and its parameters
# we can save a specific visualization (to dem_path directory) if we set the
# parameter ``save_visualization`` to True
layers_auto.render_all_images(
    default=default,
    save_visualizations=True,
    save_render_path=output_blend_path,
    save_float=True,
    save_8bit=True # set save_8bit=True if you also wish to save an 8bit version
    )
```

See also:

Find out more about blending in *rvt.blend*.

6.2.4 Choosing a visualization

When choosing a visualization, it is recommended to always begin by looking at a hillshade of the area under investigation. Hillshading provides the most ‘natural’ visual appearance of the topography and can help you decide which other techniques could work well.

See also:

Find out more about the visualizations that RVT can produce in *List of visualizations*.

By feature type

If you need some help to get started after trying a hillshade, consider the type of feature you're working with:

	mining pits	former field boundaries	burial mounds	terraces	hollow ways	ridge and furrow
shaded relief	-	-	+	o	o	-
slope	-	o	o	+	+	++
principal components analysis	-	-	+	o	+	++
trend removal and LRM	++	+	++	+	+	++
sky-view factor	++	+	o	++	++	++
openness	++	+	+	+	++	++
local dominance	++	++	++	+	++	++
cumulative visibility	-	-	+	o	+	o
accessibility	-	o	-	o	o	-
multi-scale integral invariants	+	+	o	+	+	+
Laplacian-of-Gaussian	+	+	++	+	+	++

- not suitable; o indistinct; + suitable; ++ very suitable

Table 1: Suitability of visualisation techniques for representing selected archaeological topographical features.

By topography type

You can also try adding techniques from Table 2, in order from left to right, based on the topography of the area under investigation.

flat terrain	Shaded relief (sun elevation < 10°)	Trend removal / LRM (filter radius ~ 20 m)	Local dominance (radius 10-20 m)	Openness or MSII (radius 10 m)	
gentle slopes	Shaded relief (sun elevation ~ 30°)	Sky-view factor (radius ~ 10 m)	Trend removal / LRM (filter radius ~ 20 m)	Local dominance (radius 10-20 m)	Openness or MSII (radius 10 m)
moderate slopes	Shaded relief (sun elevation ~ 45°)	SVF (& LoG) (radius ~ 10 m)	Trend removal / LRM (filter radius ~ 20 m)	LD (&LoG) (radius 10-20 m)	Openness or MSII (radius 10 m)
complex topography	Shaded relief (sun elevation > 45°)	SVF (& LoG) (radius ~ 10 m)	LD (&LoG) (radius 10-20 m)	Openness or MSII (radius 10 m)	

Table 2: Matrix for the suitability of visualisation techniques for selected archaeological relief features in different topographic settings.

See below for visual examples of the methods suggested in Table 2.

Flat terrain

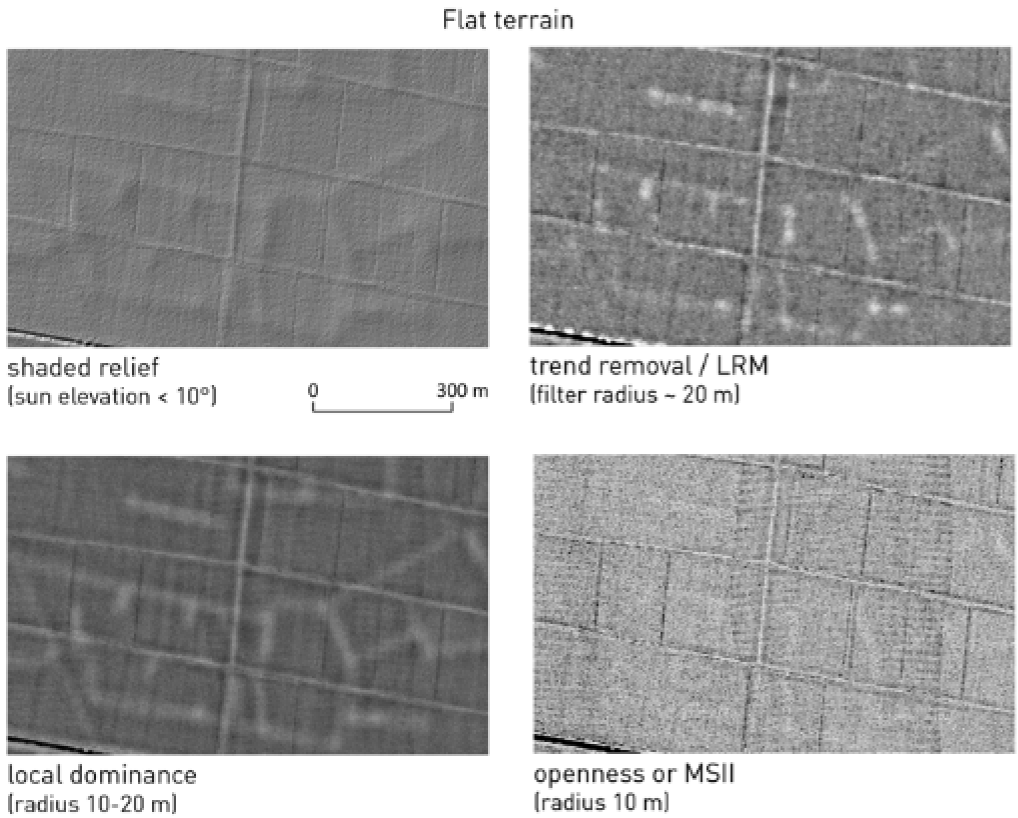

Gentle slopes

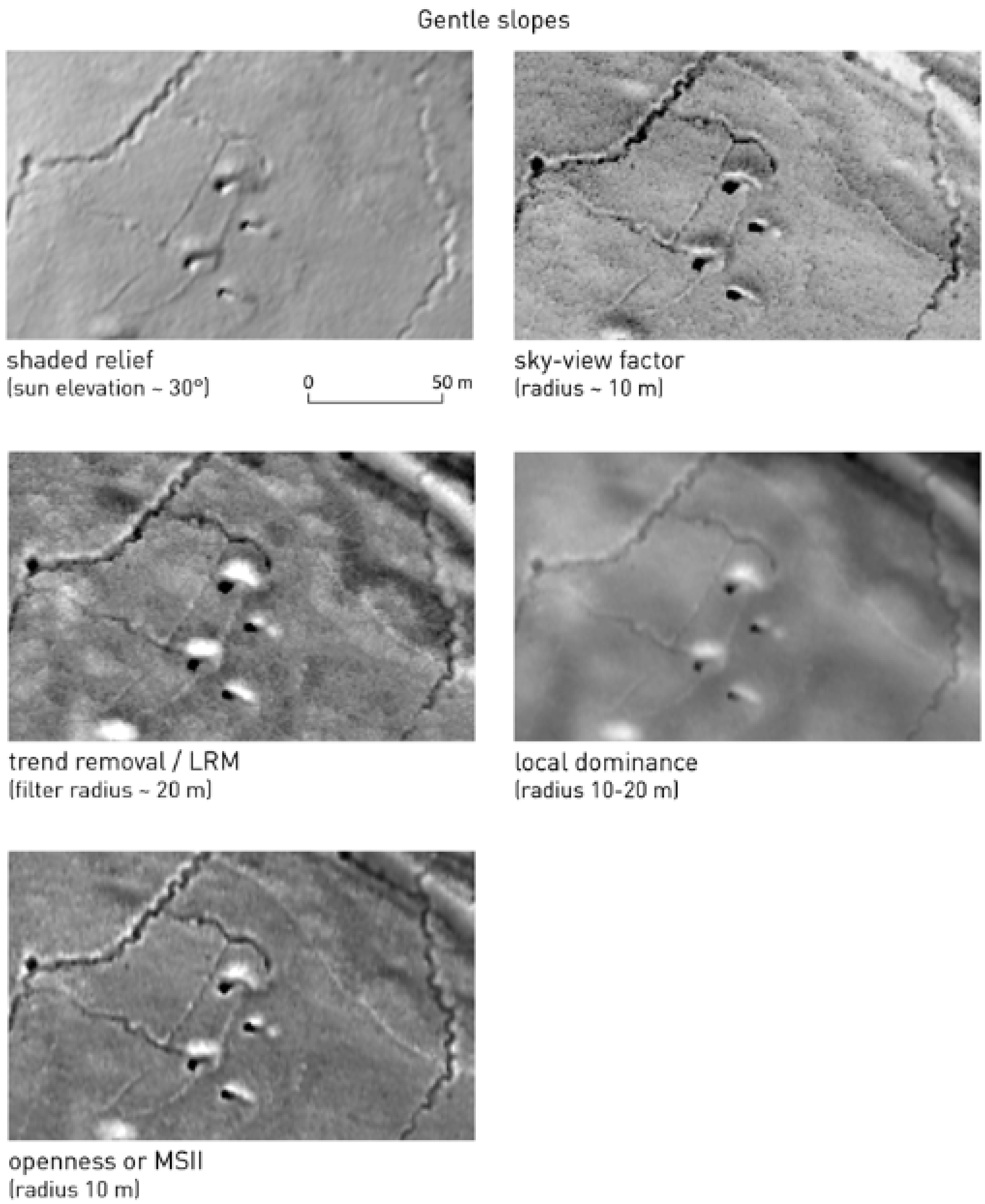

Moderate slopes

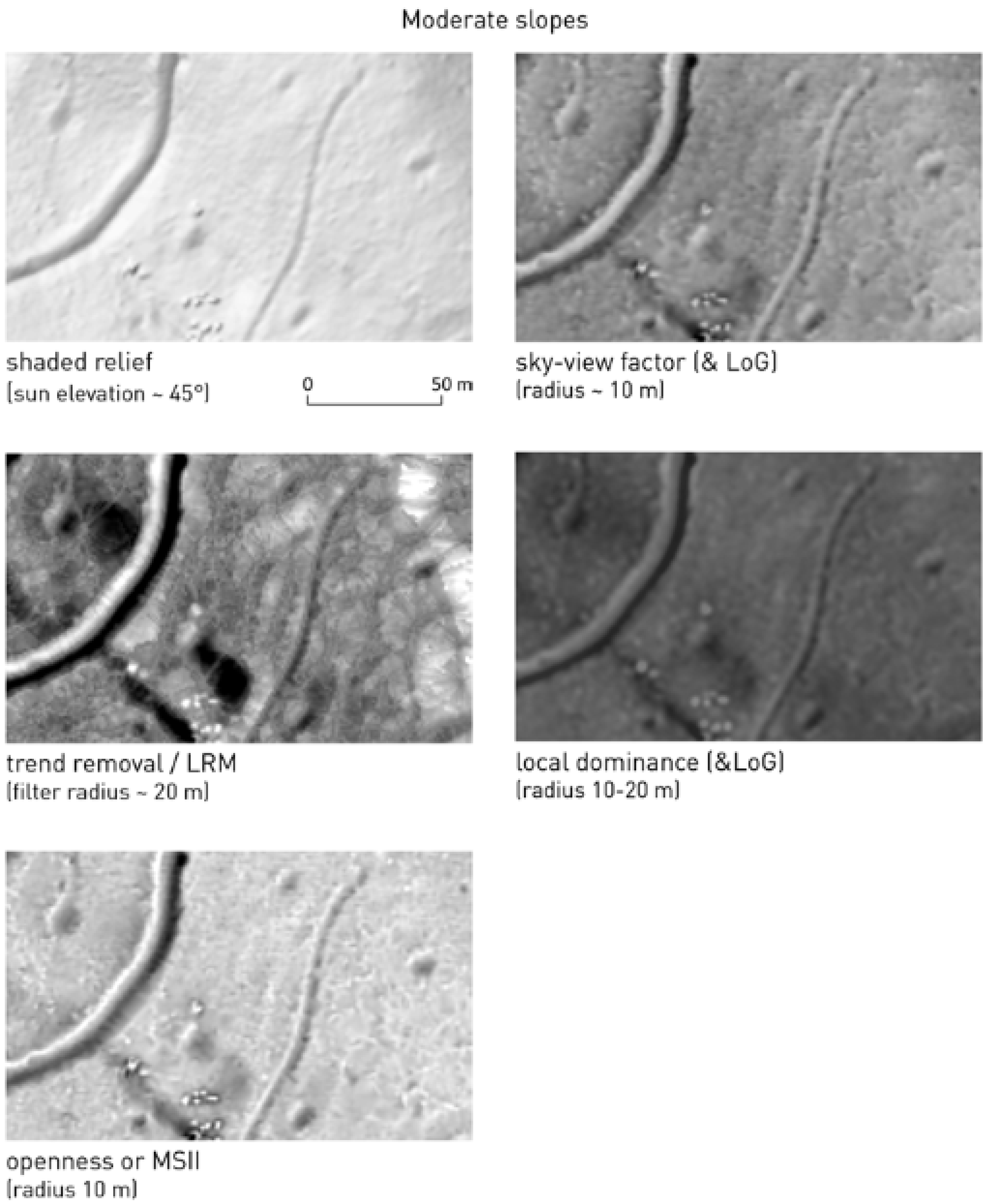

Steep slopes or complex topography

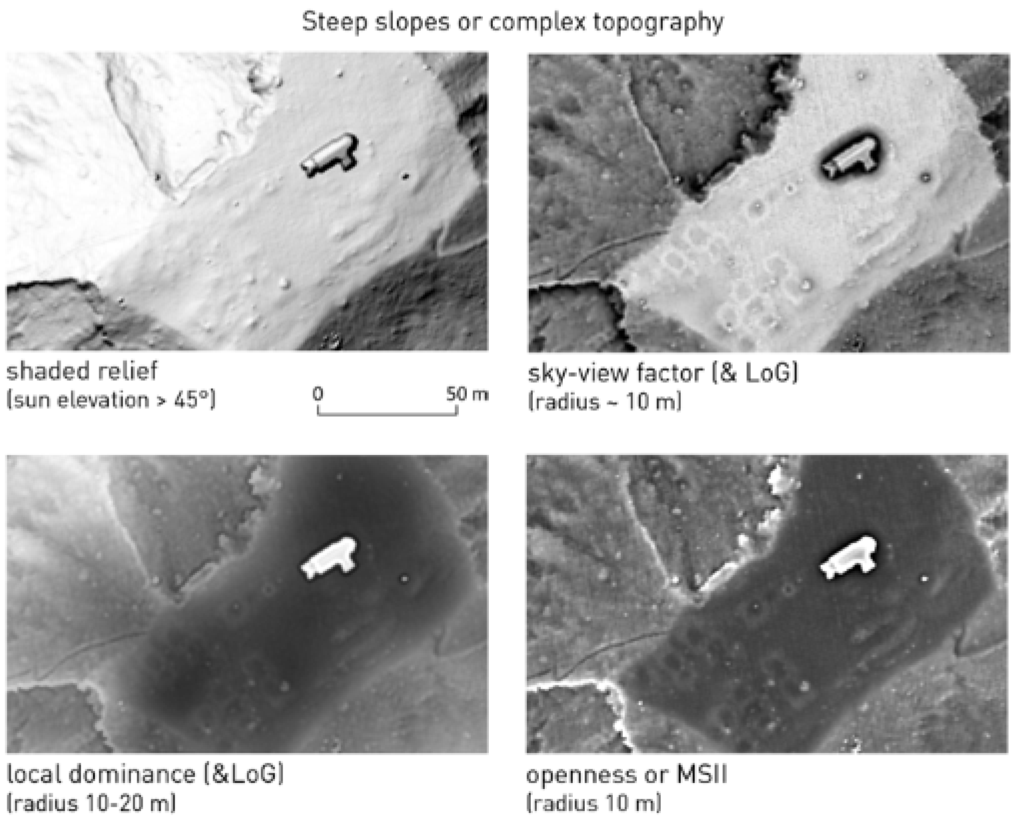

See also:

Find out more about choosing visualizations in Kokalj, Žiga, Ralf Hesse. 2017. Airborne laser scanning raster data visualization: A Guide to Good Practice. Ljubljana: Založba ZRC.

6.3 List of visualizations

This section contains a list of the visualizations that RVT can produce with introductory descriptions.

Unless otherwise referenced, the descriptions are simplified versions of the information available in Kokalj, Žiga, Ralf Hesse. 2017. Airborne laser scanning raster data visualization: A Guide to Good Practice. Ljubljana: Založba ZRC.

See also:

For example code showing how to create these visualizations visit *Example notebooks*.

CONTENTS

6.3.1 Slope

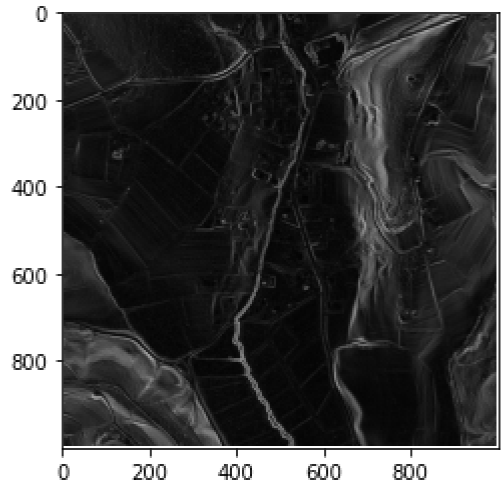

Slope (gradient) represents the maximum rate of change between each cell and its neighbours. It can be calculated either as percentage of slope or degree of slope. It is the first derivative of a DEM and is aspect independent.

Additional information is needed to distinguish between positive/convex (e.g. banks) and negative/concave (e.g. ditches) features, since slopes of the same gradient, regardless of rising or falling, are presented with the same colour.

6.3.2 Hillshading

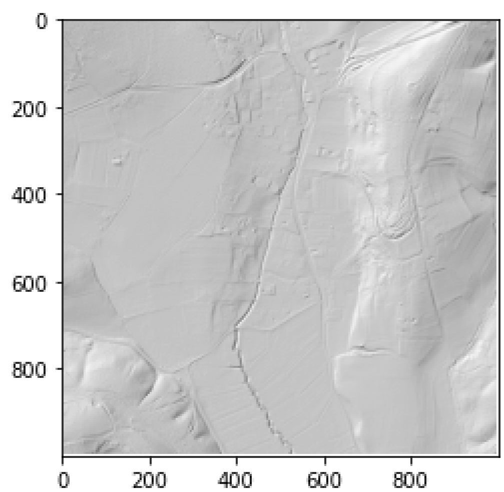

Hillshading (also known as relief shading or shaded relief) provides the most 'natural', i.e. intuitively readable, visual impression of all techniques.

It has a basic assumption that the relief is a Lambertian surface (equally bright from all viewing directions) illuminated by direct light from a fictive light source at an infinitive distance. The light beam has a constant azimuth and elevation angle for the entire area.

Applying several illumination directions can help to avoid the drawbacks of shaded relief, such as poor representation of linear features parallel to illumination azimuth, low contrast in areas facing towards (homogeneously bright) or away from (homogeneously dark) the light source, as well as optical illusions (e.g. inverted relief).

While very low illumination elevation angles (< 10°) can and should be used to highlight low relief features in areas of low slopes and flat terrain, higher illumination elevation angles (> 35°) are required in steeper topography.

To investigate features on moderate to steep slopes, shaded relief should be used with (almost) vertical illumination to minimize saturated bright/dark areas on slopes facing towards/away from the illumination. In such cases, shaded relief images become similar to slope images, which can be a useful alternative in moderate to steep topography.

Multiple direction hillshading

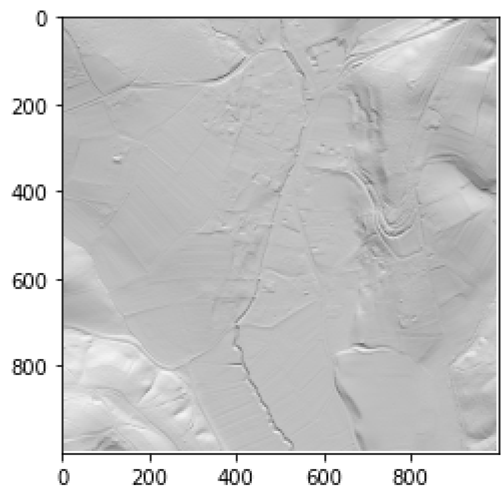

Producing multiple hillshading outputs by illuminating a surface from multiple directions enhances the visualization of topography.

Multi-directional hillshading reduces the need to compare multiple images, but the added complexity means they can be tricky to interpret. A step towards an improved understanding of the results is combining multiple shadings by considering only the mean, the maximum, or the range of values, for each pixel.

See also:

Slope.

6.3.3 Simple local relief model

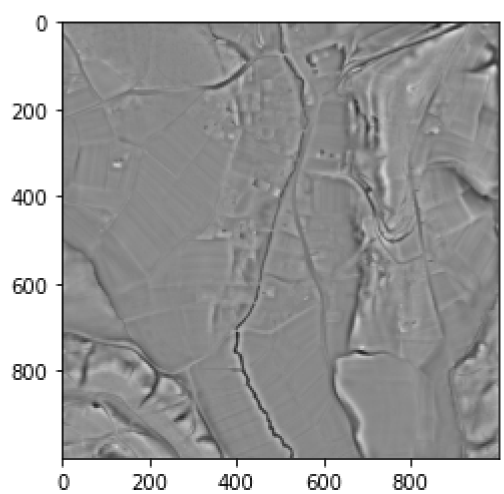

Simple local relief models use a procedure called trend removal that separates local small-scale features from large-scale landscape forms.

When working with a DEM, the trend (i.e. the larger landscape forms) is represented by a smoothed (generalized) version of that DEM. Trend removal is then accomplished by subtracting the smoothed DEM from the original DEM. The resulting difference map contains only the local deviations from the overall landscape forms.

In areas with flat or very gentle to moderate topography, local relief model and local dominance are very helpful to highlight very low relief features such as former field boundaries or levelled burial mounds.

Local relief model and local dominance are interchangeable to a certain extent. Local relief model produces more realistic relative elevation values of relief anomalies. Local dominance retains a (limited) visual impression of the overall landscape forms as it produces higher values on slopes than on horizontal planes.

See also:

Local dominance.

6.3.4 Sky-view factor

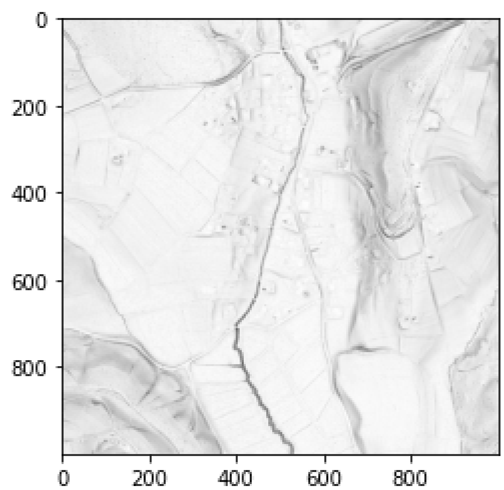

Sky-view factor (SVF) can be used as an alternative method of relief shading in order to overcome the directional problems of hillshading (see also: openness).

SVF represents the portion of the sky visible from a certain point. An imaginary light source illuminates the relief from the celestial hemisphere centred at the point being illuminated. It ignores any direction below the mathematical horizon (see also: openness). In contrast to shading techniques based on directional illumination, features visualized by SVF (or by openness) do not contain any horizontal displacements.

In areas of moderate to steep topography, sky-view factor works best to highlight surface depressions and features on slopes. Depending on the range of slopes in a given area under study, different histogram stretches may be necessary to avoid bright saturation in gentle topography and dark saturation on steep slopes.

In areas with flat or very gentle topography, sky-view factor is generally limited to the presentation of negative relief features (e.g. pits, ditches, quarries, erosion areas, dolines) and becomes very sensitive to DEM noise. A good general rule is to use a histogram stretch of 0.65 to 1.0 for diverse terrain and 0.9 to 1.0 for very flat terrain.

Anisotropic sky-view factor

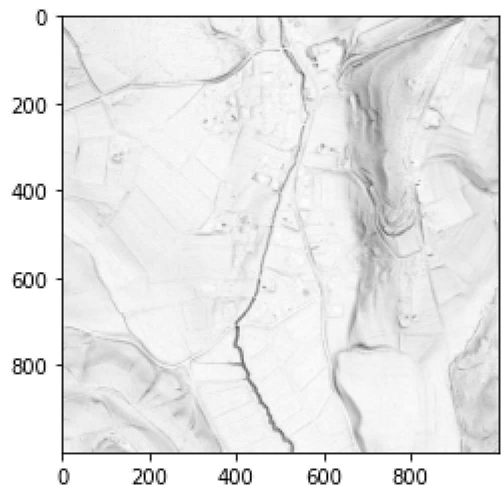

Anisotropic (directional) SVF assumes that the sky is brighter in some directions than in others. The brightness can depend on the azimuth and solar distance from the imaginary light source. This brings back some of the 'plasticity' of hill shading and gives better details on very flat areas.

See also:

Openness.

6.3.5 Openness

Positive openness

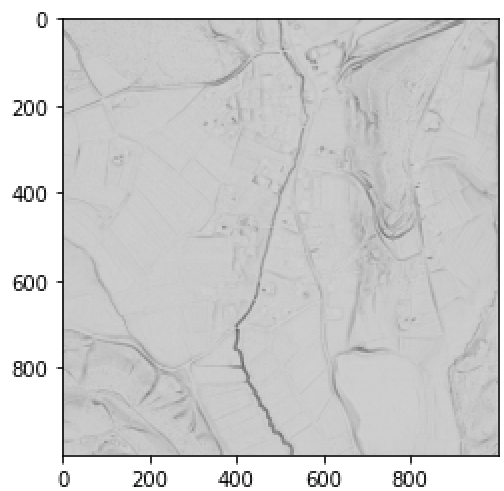

Openness is another proxy for relief shading (see also: sky-view factor). The method is based on estimating the mean horizon elevation angle within a defined search radius. The mean value of all zenith angles gives positive openness, while the mean nadir value gives negative openness.

Openness considers the whole sphere for calculation, not just the celestial hemisphere as SVF does. The result of this is a much 'flatter' image, devoid of general topography—a kind of trend-removed image. As the visual impression of the general topography is lost, interpretation becomes a bit trickier.

However, openness has big advantage for automatic feature detection because 'signatures' of features are more homogeneous because they are the same irrespectively of their location on a plane or slope.

Negative openness

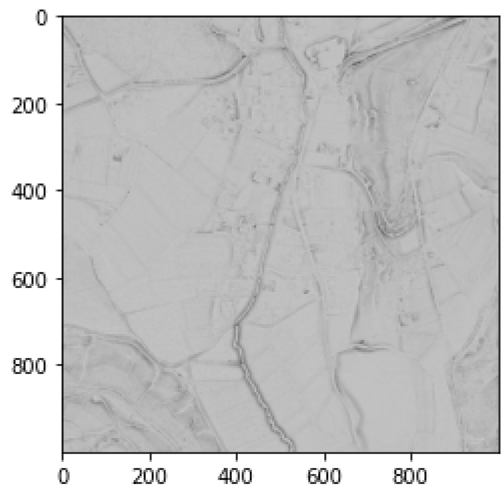

Negative openness is not the inverse of positive openness and it provides additional information. While positive openness highlights topographic convexities (e.g. ridges between hollow ways and rims of bomb craters), negative openness emphasizes the lowest parts of concavities, (e.g. the actual hollow ways, the lowest parts of gorges and the lower edges of cliffs).

For consistent readability, it is recommended that negative openness is displayed with inverted greyscale (i.e. darker for higher values), so that concave features are always presented by dark tones.

Positive and negative openness are very useful to highlight positive and negative relief features, respectively. As openness removes the visual impression of overall landscape forms, it is not affected by saturation due to gentle or steep slopes and may be used in a varied topography. Because of the ability to differentially highlight positive and negative relief features, it is particularly suitable for targeted detection of these features.

See also:

Sky-view factor.

6.3.6 Local dominance

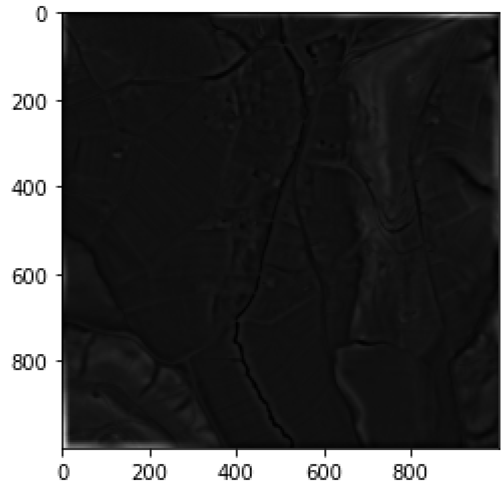

Local dominance is based on computing how dominant an observer standing on each pixel would be for a local surrounding area.

Dominance is the average steepness of the angle at which the observer looks down at the surrounding land surface. It is higher for points on local elevations as well as on slopes and lower for points in local depressions.

In areas with flat or very gentle to moderate topography, local dominance and local relief model are very helpful to highlight very low relief features such as former field boundaries or levelled burial mounds. Local dominanace also delivers very good results for topographic depressions such as dolines, mining traces, or hollow ways.

Local relief model and local dominance are interchangeable to a certain extent. Local relief model produces more realistic relative elevation values of relief anomalies. Local dominance retains a (limited) visual impression of the overall landscape forms as it produces higher values on slopes than on horizontal planes.

See also:

Simple local relief model.

6.3.7 Sky illumination

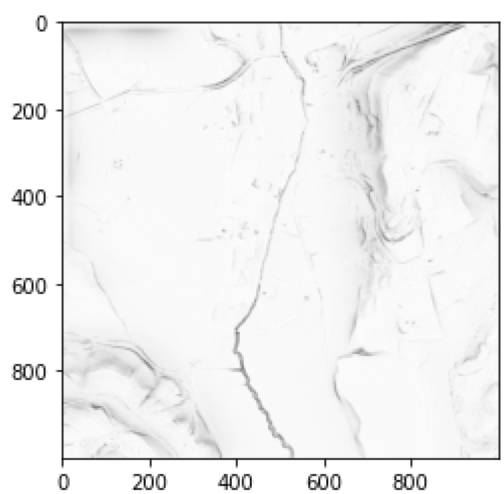

Sky illumination models quantitatively represent natural luminance of the sky under various atmospheric conditions.

Uniform and overcast sky models are implemented as they both disregard directional shadowing effects. Mode details in shadows can be seen using the overcast sky model.

Calculations last much longer than for other visualizations especially with large maximum shadow modelling distance.

Source: Relief Visualization Toolbox ver. 2.2.1 Manual

6.3.8 Multi-scale topographic position

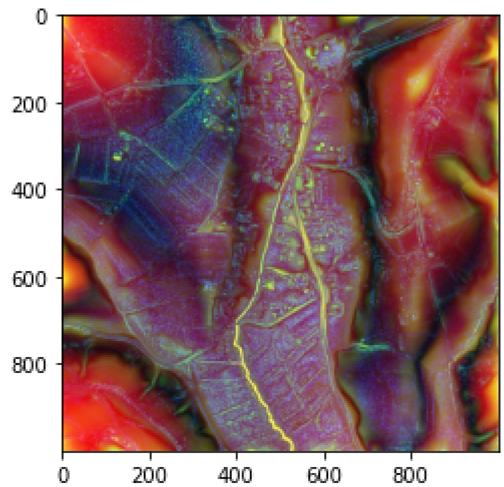

A multi-scale topographic position (MSTP) visualization is an effective means of visualising and interpreting the multi-scale topographic character of a landscape.

MSTP simultaneously summarizes the relative topographic position of sites across three defined ranges of spatial scales (local, meso, and broad).

The density of topographic information in an MSTP visualization is very high; on par with or exceeding that of commonly used methods such as hillshading.

Some practice is required to train the eye to recognize colors as the summation of relative topographic position across three scale ranges, rather than, for example, as the raw elevation observed in a DEM.

Source: Lindsay, Cockburn & Russell (2015), An integral image approach to performing multi-scale topographic position analysis

6.4 RVT for Python

The `rvt` Python package contains three modules:

- **vis** (*rvt.vis*) for computing visualizations
- **blend** (*rvt.blend*) for blending visualizations together
- **default** (*rvt.default*) for defining default parameters with methods to compute and save visualization functions using set parameters

This section contains full documentation of each of the `rvt` modules.

Two notebooks with examples for using the `rvt.vis` and `rvt.default` modules can be found in *Example notebooks*.

See also:

For beginner-friendly explanations of how to use `rvt` visit *Getting started*

CONTENTS

6.4.1 rvt.vis

Relief Visualization Toolbox – Visualization Functions

Contains functions for computing the visualizations.

`rvt.vis.`**`byte_scale`**(*data*, *c_min=None*, *c_max=None*, *high=255*, *low=0*, *no_data=None*)

Remade old scipy function. Byte scales an array (image). Linear scale.

Byte scaling means converting the input image to uint8 dtype and scaling the range to `(low, high)` (default 0-255).

Parameters

- **`data`** (*`numpy.ndarray`*) – Input data (visualization) as 2D or multi-D numpy array.
- **`c_min`** (*`int or float`*) – Scalar, Bias scaling of small values. Default is `data.min()`.
- **`c_max`** (*`int or float`*) – Scalar, Bias scaling of large values. Default is `data.max()`.
- **`high`** (*`int`*) – Scalar, Scale max value to *high*. Default is 255.
- **`low`** (*`int`*) – Scalar, Scale min value to *low*. Default is 0.
- **`no_data`** (*`int or float`*) – Value that represents no_data, it is changed to np.nan .

Returns
img_array – The byte-scaled array.

Return type
uint8 numpy.ndarray

`rvt.vis.`**`slope_aspect`**(*dem*, *resolution_x=1*, *resolution_y=1*, *output_units='radian'*, *ve_factor=1*, *no_data=None*)

Procedure can return terrain slope and aspect in radian units (default) or in alternative units (if specified). Available alternative units are ‘degree’ and ‘percent’. Slope is defined as 0 for horizontal plane and pi/2 for vertical plane. Aspect is defined as geographic azimuth: clockwise increasing, 0 or 2pi for the North direction.

0

270 90
180

Currently applied finite difference method.

Parameters

- **`dem`** (*`numpy.ndarray`*) – Input digital elevation model as 2D numpy array.
- **`resolution_x`** (*`int`*) – DEM resolution in X direction.
- **`resolution_y`** (*`int`*) – DEM resolution in Y direction.
- **`output_units`** (*`str`*) – Output units, you can choose between: percent, degree, radian. Default value is radian.

- **ve_factor** (*int or float*) – Vertical exaggeration factor.
- **no_data** (*int or float*) – Value that represents no_data, all pixels with this value are changed to np.nan. Only has to be specified if a numerical value is used for nodata (e.g. -9999).

Returns
dict_out – Returns {"slope": slope_out, "aspect": aspect_out}; slope_out, slope gradient : 2D numpy array (numpy.ndarray) of slope; aspect_out, aspect : 2D numpy array (numpy.ndarray) of aspect.

Return type
dict

rvt.vis.**roll_fill_nans**(*dem*, *shift*, *axis*)

Uses numpy.roll() function to roll array, then checks element-wise if new array has NaN value, but there was a numerical value in the source array, then use the original value instead of NaN. It is equivalent to edge padding.

https://numpy.org/doc/stable/reference/generated/numpy.roll.html#numpy.roll

rvt.vis.**hillshade**(*dem*, *resolution_x*, *resolution_y*, *sun_azimuth=315*, *sun_elevation=35*, *slope=None*, *aspect=None*, *ve_factor=1*, *no_data=None*)

Compute hillshade.

Parameters

- **dem** (*numpy.ndarray*) – Input digital elevation model as 2D numpy array.
- **resolution_x** (*int*) – DEM resolution in X direction.
- **resolution_y** (*int*) – DEM resolution in Y direction.
- **sun_azimuth** (*int or float*) – Solar azimuth angle (clockwise from North) in degrees.
- **sun_elevation** (*int or float*) – Solar vertical angle (above the horizon) in degrees.
- **slope** (*numpy.ndarray*) – Slope arr in radians if you don't input it, it is calculated.
- **aspect** (*numpy.ndarray*) – Aspect arr in radians if you don't input it, it is calculated.
- **ve_factor** (*int or float*) – Vertical exaggeration factor.
- **no_data** (*int or float*) – Value that represents no_data, all pixels with this value are changed to np.nan.

Returns
hillshade_out – Result hillshade 2D numpy array.

Return type
numpy.ndarray

rvt.vis.**multi_hillshade**(*dem*, *resolution_x*, *resolution_y*, *nr_directions=16*, *sun_elevation=35*, *slope=None*, *aspect=None*, *ve_factor=1*, *no_data=None*)

Calculates hillshades from multiple directions.

Parameters

- **dem** (*numpy.ndarray*) – Input digital elevation model as 2D numpy array.
- **resolution_x** (*int*) – DEM resolution in X direction.
- **resolution_y** (*int*) – DEM resolution in Y direction.
- **nr_directions** (*int*) – Number of solar azimuth angles (clockwise from North).
- **sun_elevation** (*int or float*) – Solar vertical angle (above the horizon) in degrees.

- **slope** (*numpy.ndarray*) – Slope in radians if you don't input it, it is calculated.
- **aspect** (*numpy.ndarray*) – Aspect in radians if you don't input it, it is calculated.
- **ve_factor** (*int or float*) – Vertical exaggeration factor.
- **no_data** (*int or float*) – Value that represents no_data, all pixels with this value are changed to np.nan .

Returns
multi_hillshade_out – Result multiple direction hillshade multidimensional (nr_directions=dimensions) numpy array.

Return type
numpy.ndarray

rvt.vis.**mean_filter**(*dem*, *kernel_radius*)

Applies mean filter (low pass filter) on DEM. Kernel radius is in pixels. Kernel size is 2 * kernel_radius + 1. It uses matrix shifting (roll) instead of convolutional approach (works faster). It returns mean filtered dem as numpy.ndarray (2D numpy array).

rvt.vis.**slrm**(*dem*, *radius_cell=20*, *ve_factor=1*, *no_data=None*)

Calculates Simple local relief model.

Parameters

- **dem** (*numpy.ndarray*) – Input digital elevation model as 2D numpy array.
- **radius_cell** (*int*) – Radius for trend assessment in pixels.
- **ve_factor** (*int or float*) – Vertical exaggeration factor.
- **no_data** (*int or float*) – Value that represents no_data, all pixels with this value are changed to np.nan .

Returns
slrm_out – Simple local relief model 2D numpy array.

Return type
numpy.ndarray

rvt.vis.**horizon_shift_vector**(*num_directions=16*, *radius_pixels=10*, *min_radius=1*)

Calculates Sky-View determination movements.

Parameters

- **num_directions** (*int*) – Number of directions as input.
- **radius_pixels** (*int*) – Radius to consider in pixels (not in meters).
- **min_radius** (*int*) – Radius to start searching for horizon in pixels (not in meters).

Returns

shift –

Dict with keys corresponding to the directions of search azimuths rounded to 1 decimal number

- **for each key, a subdict contains a key "shift":**
  values for this key is a list of tuples prepared for np.roll - shift along lines and columns
- **the second key is "distance":**
  values for this key is a list of search radius used for the computation of the elevation angle

Return type
dict

`rvt.vis.`**`sky_view_factor_compute`**(*height_arr*, *radius_max=10*, *radius_min=1*, *num_directions=16*, *compute_svf=True*, *compute_opns=False*, *compute_asvf=False*, *a_main_direction=315.0*, *a_poly_level=4*, *a_min_weight=0.4*)

Calculates horizon based visualizations: Sky-view factor, Anisotropic SVF and Openness.

SVF processing is using search radius, that looks at values beyond the edge of an array. Consider using a buffered array as an input, with the buffer size equal to the radius_max. To prevent erosion of the edge, function applies mirrored padding in all four directions, however, this means that edge values are "averaged over half of the hemisphere". Similarly, the edges of the dataset (i.e. areas with NaN values), will be considered as fully open (SFV angle 0, Openness angle -90).

Input array should use np.nan as nodata value.

Parameters

- **height_arr** (*numpy.ndarray*) – Elevation (DEM) as 2D numpy array.
- **radius_max** (*int*) – Maximal search radius in pixels/cells (not in meters).
- **radius_min** (*int*) – Minimal search radius in pixels/cells (not in meters), for noise reduction.
- **num_directions** (*int*) – Number of directions as input.
- **compute_svf** (*bool*) – If true it computes and outputs svf.
- **compute_asvf** (*bool*) – If true it computes and outputs asvf.
- **compute_opns** (*bool*) – If true it computes and outputs opns.
- **a_main_direction** (*int or float*) – Main direction of anisotropy.
- **a_poly_level** (*int*) – Level of polynomial that determines the anisotropy.
- **a_min_weight** (*float*) –

  Weight to consider anisotropy:
  0 - low anisotropy, 1 - high anisotropy (no illumination from the direction opposite the main direction)

Returns
dict_out – Return {"svf": svf_out, "asvf": asvf_out, "opns": opns_out}; svf_out, skyview factor : 2D numpy array (numpy.ndarray) of skyview factor; asvf_out, anisotropic skyview factor : 2D numpy array (numpy.ndarray) of anisotropic skyview factor; opns_out, openness : 2D numpy array (numpy.ndarray) openness (elevation angle of horizon).

Return type
dictionary

`rvt.vis.`**`sky_view_factor`**(*dem*, *resolution*, *compute_svf=True*, *compute_opns=False*, *compute_asvf=False*, *svf_n_dir=16*, *svf_r_max=10*, *svf_noise=0*, *asvf_dir=315*, *asvf_level=1*, *ve_factor=1*, *no_data=None*)

Prepare the data, call sky_view_factor_compute, reformat and return back 2D arrays.

Parameters

- **dem** (*numpy.ndarray*) – Input digital elevation model as 2D numpy array.
- **compute_svf** (*bool*) – Compute SVF (True) or not (False).
- **compute_opns** (*bool*) – Compute OPENNESS (True) or not (False).

- **resolution** (*float*) – Pixel resolution.
- **svf_n_dir** (*int*) – Number of directions.
- **svf_r_max** (*int*) – Maximal search radius in pixels.
- **svf_noise** (*int*) – The level of noise remove (0-don't remove, 1-low, 2-med, 3-high).
- **compute_asvf** (*bool*) – Compute anisotropic SVF (True) or not (False).
- **asvf_level** (*int*) – Level of anisotropy, 1-low, 2-high.
- **asvf_dir** (*int or float*) – Direction of anisotropy.
- **ve_factor** (*int or float*) – Vertical exaggeration factor.
- **no_data** (*int or float*) – Value that represents no_data, all pixels with this value are changed to np.nan. Use this parameter when nodata is not np.nan.

Returns
dict_out – Return {"svf": svf_out, "asvf": asvf_out, "opns": opns_out}; svf_out, skyview factor : 2D numpy array (numpy.ndarray) of skyview factor; asvf_out, anisotropic skyview factor : 2D numpy array (numpy.ndarray) of anisotropic skyview factor; opns_out, openness : 2D numpy array (numpy.ndarray) openness (elevation angle of horizon).

Return type
dictionary

rvt.vis.**local_dominance**(*dem*, *min_rad=10*, *max_rad=20*, *rad_inc=1*, *angular_res=15*, *observer_height=1.7*, *ve_factor=1*, *no_data=None*)

Compute Local Dominance dem visualization. Adapted from original version that is part of the Lidar Visualisation Toolbox LiVT developed by Ralf Hesse.

Parameters

- **dem** (*numpy.ndarray*) – Input digital elevation model as 2D numpy array.
- **min_rad** (*int*) – Minimum radial distance (in pixels) at which the algorithm starts with visualization computation.
- **max_rad** (*int*) – Maximum radial distance (in pixels) at which the algorithm ends with visualization computation.
- **rad_inc** (*int*) – Radial distance steps in pixels.
- **angular_res** (*int*) – Angular step for determination of number of angular directions.
- **observer_height** (*int or float*) – Height at which we observe the terrain.
- **ve_factor** (*int or float*) – Vertical exaggeration factor.
- **no_data** (*int or float*) – Value that represents no_data, all pixels with this value are changed to np.nan .

Returns
local_dom_out – 2D numpy array of local dominance

Return type
numpy.ndarray

rvt.vis.**horizon_generate_coarse_dem**(*dem_fine*, *pyramid_scale*, *conv_from*, *conv_to*, *max_radius*)

rvt.vis.**horizon_generate_pyramids**(*dem*, *num_directions=4*, *max_fine_radius=100*, *max_pyramid_radius=7*, *pyramid_scale=3*) rvt.vis.**sky_illumination**(*dem*, *resolution*, *sky_model='overcast'*, *compute_shadow=False*, *shadow_horizon_only=False*, *max_fine_radius=100*, *num_directions=32*, *shadow_az=315*, *shadow_el=35*, *ve_factor=1*, *no_data=None*)

Compute topographic corrections for sky illumination.

Parameters

- **dem** (*numpy.ndarray*) – Input digital elevation model as 2D numpy array.
- **resolution** (*float*) – DEM pixel size.
- **sky_model** (*str*) – Sky model, it can be 'overcast' or 'uniform'.
- **compute_shadow** (*bool*) – If True it computes and adds shadow.
- **shadow_horizon_only** (*bool*) – Returns dict {"shadow": shadow, "horizon": horizon}
- **max_fine_radius** (*int*) – Max shadow modeling distance in pixels.
- **num_directions** (*int*) – Number of directions to search for horizon.
- **shadow_az** (*int or float*) – Shadow azimuth.
- **shadow_el** (*int or float*) – Shadow elevation.
- **ve_factor** (*int or float*) – Vertical exaggeration factor.
- **no_data** (*int or float*) – Value that represents no_data, all pixels with this value are changed to np.nan .

Returns

sky_illumination – 2D numpy result array of Sky illumination.

Return type

numpy.ndarray

rvt.vis.**shadow_horizon**(*dem*, *resolution*, *shadow_az=315*, *shadow_el=35*, *ve_factor=1*, *no_data=None*)

Compute shadow and horizon.

Parameters

- **dem** (*numpy.ndarray*) – Input digital elevation model as 2D numpy array.
- **resolution** (*float*) – DEM pixel size.
- **shadow_az** (*int or float*) – Shadow azimuth.
- **shadow_el** (*int or float*) – Shadow elevation.
- **ve_factor** (*int or float*) – Vertical exaggeration factor.
- **no_data** (*int or float*) – Value that represents no_data, all pixels with this value are changed to np.nan .

Returns

dict_out – Returns {"shadow": shadow, "horizon": horizon}; shadow : 2D binary numpy array (numpy.ndarray) of shadows; horizon; 2D numpy array (numpy.ndarray) of horizon.

Return type

dict

rvt.vis.**msrm**(*dem*, *resolution*, *feature_min*, *feature_max*, *scaling_factor*, *ve_factor=1*, *no_data=None*)

Compute Multi-scale relief model (MSRM).

Parameters

- **dem** (*numpy.ndarray*) – Input digital elevation model as 2D numpy array.

- **resolution** (*float*) – DEM pixel size.
- **feature_min** (*float*) – Minimum size of the feature you want to detect in meters.
- **feature_max** (*float*) – Maximum size of the feature you want to detect in meters.
- **scaling_factor** (*int*) – Scaling factor, if larger than 1 it provides larger range of MSRM values (increase contrast and visibility), but could result in a loss of sensitivity for intermediate sized features.
- **ve_factor** (*int or float*) – Vertical exaggeration factor.
- **no_data** (*int or float*) – Value that represents no_data, all pixels with this value are changed to np.nan .

Returns
msrm_out – 2D numpy result array of Multi-scale relief model.

Return type
numpy.ndarray

rvt.vis.**integral_image**(*dem*, *data_type=<class 'numpy.float64'>*)

Calculates integral image (summed-area table), where origin is left upper corner.

Parameters

- **dem** (*numpy.ndarray*) – Input digital elevation model as 2D numpy array.
- **data_type** (*np.__class__*) – dtype as numpy data type class (np.float64, np.int8, etc.)

Returns
msrm_out – Cumulative sum of the elements along each axis of a 2D array.

Return type
numpy.ndarray

References

https://en.wikipedia.org/wiki/Summed-area_table

Examples

In: print(integral_image(np.array([[7, 4, 7, 2], … [6, 9, 9, 5], … [6, 6, 7, 6]])))

Out: [[7. 11. 18. 20.]
[13. 26. 42. 49.] [19. 38. 61. 74.]]

rvt.vis.**topographic_dev**(*dem*, *dem_i_nr_pixels*, *dem_i1*, *dem_i2*, *kernel_radius*)

Calculates topographic DEV - Deviation from mean elevation. DEV(D) = (z0 - zmD) / sD. Where D is radius of kernel, z0 is center pixel value, zmD is mean of all kernel values, sD is standard deviation of kernel.

Parameters

- **dem** (*numpy.ndarray*) – Input digital elevation model as 2D numpy array.
- **dem_i_nr_pixels** (*numpy.ndarray*) – Summed area table (integral image) of number of pixels.
- **dem_i1** (*numpy.ndarray*) – Summed area table (integral image) of dem.
- **dem_i2** (*numpy.ndarray*) – Summed area table (integral image) of dem squared (dem**2).
- **kernel_radius** (*int*) – Kernel radius (D).

Returns
dev_out – 2D numpy result array of topographic DEV - Deviation from mean elevation.

Return type
numpy.ndarray

`rvt.vis.max_elevation_deviation`(*dem*, *minimum_radius*, *maximum_radius*, *step*)

Calculates maximum deviation from mean elevation, dev_max (Maximum Deviation from mean elevation) for each grid cell in a digital elevation model (DEM) across a range specified spatial scales.

Parameters

- **dem** (*numpy.ndarray*) – Input digital elevation model as 2D numpy array.
- **minimum_radius** (*int*) – Minimum radius to calculate DEV (topographic_dev).
- **maximum_radius** (*int*) – Maximum radius to calculate DEV (topographic_dev).
- **step** (*int*) – Step from minimum to maximum radius to calc DEV (topographic_dev).

Returns
dev_out – 2D numpy result array of maxDEV - Maximum Deviation from mean elevation.

Return type
numpy.ndarray

`rvt.vis.mstp`(*dem*, *local_scale=(3, 21, 2)*, *meso_scale=(23, 203, 18)*, *broad_scale=(223, 2023, 180)*, *lightness=1.2*, *ve_factor=1*, *no_data=None*)

Compute Multi-scale topographic position (MSTP).

Parameters

- **dem** (*numpy.ndarray*) – Input digital elevation model as 2D numpy array.
- **local_scale** (*tuple(int, int, int)*) – Input local scale minimum radius (local_scale[0]), maximum radius (local_scale[1]), step (local_scale[2]).
- **meso_scale** (*tuple(int, int, int)*) – Input meso scale minimum radius (meso_scale[0]), maximum radius (meso_scale[1]), step (meso_scale[2]).
- **broad_scale** (*tuple(int, int, int)*) – Input broad scale minimum radius (broad_scale[0]), maximum radius (broad_scale[1]), step (broad_scale[2]).
- **lightness** (*float*) – Lightness of image.
- **ve_factor** (*int or float*) – Vertical exaggeration factor.
- **no_data** (*int or float*) – Value that represents no_data, all pixels with this value are changed to np.nan .

Returns
msrm_out – 3D numpy RGB result array of Multi-scale topographic position.

Return type
numpy.ndarray

`rvt.vis.fill_where_nan`(*dem*, *method='idw'*)

Replaces np.nan values, with interpolation (extrapolation).

Parameters

- **dem** (*numpy.ndarray*) – Input digital elevation model as 2D numpy array.

- **method** (*{'linear_row', 'idw_r_p', 'kd_tree', 'nearest_neighbour'}*) – 'linear_row', Linear row interpolation, array is flattened and then linear interpolation is performed. This method is fast but very inaccurate. 'idw_r_p', Inverse Distance Weighting interpolation. If you only input idw it will take default parameters (r=20, p=2). You can also input interpolation radius (r) and power (p) for weights. (Example: idw_5_2 means radius = 5, power = 2.) 'kd_tree', K-D Tree interpolation. 'nearest_neighbour', Nearest neighbour interpolation.

6.4.2 rvt.blend

Relief Visualization Toolbox – Visualization Functions

Contains classes and methods for blending.

`rvt.blend.`**`create_blender_file_example`**(*file_path=None*)

Create blender .json file example (can be changed and read). Example is VAT - Archaeological combination

class `rvt.blend.`**`BlenderLayer`**(*vis_method=None, normalization='value', minimum=None, maximum=None, blend_mode='normal', opacity=100, colormap=None, min_colormap_cut=None, max_colormap_cut=None, image=None, image_path=None*)

Bases: `object`

Class which define layer for blending. BlenderLayer is basic element in BlenderCombination.layers list.

`vis`

Visualization method.

Type
str

`normalization`

Normalization type, could be "Value" or "Percent".

Type
str

`min`

Normalization minimum.

Type
float

`max`

Normalization maximum.

Type
float

`opacity`

Image (visualization) opacity.

Type
integer

`colormap`

Colormap form matplotlib (https://matplotlib.org/3.3.2/tutorials/colors/colormaps.html).

Type
str

`min_colormap_cut`

What lower part of colormap to cut to select part of colormap. Valid values are between 0 and 1, if 0.2 it cuts off (deletes) 20% of lower colors in colormap. If None cut is not applied.

Type
float

`max_colormap_cut`

What upper part of colormap to cut to select part of colormap. Valid values are between 0 and 1, if 0.8 it cuts off (deletes) 20% of upper colors in colormap. If None cut is not applied.

Type
float

`image_path`

Path to DEM. Doesn't matter if image is not None. Leave None if you would like for blender to compute it.

Type
str

`image`

Visualization raster. Leave None if you would like for blender to compute it.

Type
numpy.array (2D)

`check_data()`

Check Attributes

`class rvt.blend.BlenderCombination(`*dem_arr=None*, *dem_resolution=None*, *dem_path=None*`)`

Bases: `object`

Class for storing layers (rasters, parameters for blending) and rendering(blending) into blended raster.

`dem_arr`

Array with DEM data, needed for calculating visualization functions in memory.

Type
np.array (2D)

`dem_path`

Path to DEM, needed for calculating visualization functions and saving them.

Type
str

`name`

Name of BlenderCombination combination.

Type
str

`layers`

List of BlenderLayer instances which will be blended together.

Type
[*BlenderLayer*]

add_dem_arr(*dem_arr*, *dem_resolution*)

Add or change dem_arr attribute and its resolution dem_resolution attribute.

add_dem_path(*dem_path*)

Add or change dem_path attribute.

create_layer(*vis_method=None*, *normalization='value'*, *minimum=None*, *maximum=None*, *blend_mode='normal'*, *opacity=100*, *colormap=None*, *min_colormap_cut=None*, *max_colormap_cut=None*, *image=None*, *image_path=None*)

Create BlenderLayer and adds it to layers attribute.

add_layer(*layer:* BlenderLayer)

Add BlenderLayer instance to layers attribute.

remove_all_layers()

Empties layers attribute.

layers_info()

read_from_file(*file_path*)

Reads class attributes from .json file.

read_from_json(*json_data*)

Fill class attributes with json data.

save_to_file(*file_path*)

Save layers (manually) to .json file. Parameters image and image_path in each layer have to be None, visualization has to be correct!

to_json()

Outputs class attributes as json.

check_data()

render_all_images(*default=None*, *save_visualizations=False*, *save_render_path=None*, *save_float=True*, *save_8bit=False*, *no_data=None*)

Render all layers and returns blended image. If specific layer (BlenderLayer) in layers has image (is not None), method uses this image, if image is None and layer has image_path method reads image from path. If both image and image_path are None method calculates visualization. If save_visualization is True method needs dem_path and saves each visualization (if it doesn't exists) in directory of dem_path, else (save_visualization=False) method needs dem_arr, dem_resolution and calculates each visualization simultaneously (in memory). Be careful save_visualisation applies only if specific BlenderLayer image and image_path are None. Parameter no_data changes all pixels with this values to np.nan, if save_visualizations is Ture it is not needed.

create_log_file(*dem_path*, *combination_name*, *render_path*, *default:* DefaultValues, *terrain_sett_name=None*, *custom_dir=None*, *computation_time=None*)

Creates log file in custom_dir, if custom_dir=None it creates it in dem directory (dem_path).

`rvt.blend.`**compare_2_combinations**(*combination1:* BlenderCombination, *combination2:* BlenderCombination)

class `rvt.blend.`**BlenderCombinations**

Bases: `object`

Class for storing combinations.

combinations

List of BlenderCombination instances.

Type
[*BlenderCombination*]

add_combination(*combination: BlenderCombination*, *name=None*)

Adds combination if parameter name not None it renames combination.

remove_all_combinations()

Removes all combinations from self.combinations.

select_combination_by_name(*name*)

Select first combination where self.combinations.BlenderCombination.name = name.

remove_combination_by_name(*name*)

Removes all combinations where self.combinations.BlenderCombination.name = name. If combinations list is empty function returns 0, else 1.

read_from_file(*file_path*)

Reads combinations from .json file.

save_to_file(*file_path*)

Saves combination to .json file.

combination_in_combinations(*input_combination: BlenderCombination*)

If input_combination (BlenderCombination) has same attributes as one of the combinations (self), method returns name of the combination (from combinations). If there is no equal one it returns None.

combinations_names()

Returns list of combinations names.

class rvt.blend.**TerrainSettings**

Bases: `object`

Terrain settings for GUI.

read_from_file(*file_path*)

Reads combinations from .json file.

read_from_json(*json_data*)

Reads json dict and fills self attributes.

apply_terrain(*default: DefaultValues*, *combination: BlenderCombination*)

It overwrites default (DefaultValues) and combination (BlenderCombination), with self values that are not None.

class rvt.blend.**TerrainsSettings**

Bases: `object`

Multiple Terrain settings.

read_from_file(*file_path*)

Reads combinations from .json file.

select_terrain_settings_by_name(*name*)

Select first combination where self.combinations.BlenderCombination.name = name.

`rvt.blend.color_relief_image_map`(*dem*, *resolution*, *default: ~rvt.default.DefaultValues = <rvt.default.DefaultValues object>*, *colormap='OrRd'*, *min_colormap_cut=0*, *max_colormap_cut=1*, *no_data=None*)

RVT Color relief image map (CRIM) Blending combination where layers are: 1st: Openness positive - Openness negative, overlay, 50% opacity 2nd: Openness positive - Openness negative, luminosity, 50% opacity 3rd: Slope gradient, colored with matplotlib colormap

Parameters

- **dem** (*numpy.ndarray*) – Input digital elevation model as 2D numpy array.
- **resolution** (*float*) – DEM pixel size.
- **default** (rvt.default.DefaultValues) – Default values for visualization functions.
- **colormap** (*str*) – Colormap form matplotlib (https://matplotlib.org/3.3.2/tutorials/colors/colormaps.html).
- **min_colormap_cut** (*float*) – What lower part of colormap to cut. Between 0 and 1, if 0.2 it cuts off (deletes) 20% of lower colors in colormap. If None cut is not applied.
- **max_colormap_cut** (*float*) – What upper part of colormap to cut. Between 0 and 1, if 0.8 it cuts off (deletes) 20% of upper colors in colormap. If None cut is not applied.
- **no_data** (*int or float*) – Value that represents no_data, all pixels with this value are changed to np.nan .

Returns

crim_out – 2D numpy result array of Color relief image map.

Return type

numpy.ndarray

`rvt.blend.e3mstp`(*dem*, *resolution*, *default: ~rvt.default.DefaultValues = <rvt.default.DefaultValues object>*, *no_data=None*)

RVT enhanced version 3 Multi-scale topographic position (e3MSTP) Blending combination where layers are: 1st: Simple local relief model (SLRM), screen, 25% opacity 2nd: Color relief image map where cmap=Reds_r(0.5-1) (CRIM_Reds_r), soft_light, 70% opacity 3rd: Multi-scale topographic position (MSTP)

Parameters

- **dem** (*numpy.ndarray*) – Input digital elevation model as 2D numpy array.
- **resolution** (*float*) – DEM pixel size.
- **default** (rvt.default.DefaultValues) – Default values for visualization functions.
- **no_data** (*int or float*) – Value that represents no_data, all pixels with this value are changed to np.nan .

Returns

crim_out – 2D numpy result array of Color relief image map.

Return type

numpy.ndarray

6.4.3 rvt.default

Relief Visualization Toolbox – Visualization Functions

Contains all default values for visualisation functions, which can be changed. Allows computing from rvt.visualization with using defined default values and saving output rasters with default names (dependent on default values).

`class rvt.default.RVTVisualization(value, names=None, *values, module=None, qualname=None, type=None, start=1, boundary=None)`

Bases: `Enum`

`SLOPE = 'slp'`

`HILLSHADE = 'hs'`

`SHADOW = 'shd'`

`MULTI_HILLSHADE = 'mhs'`

`SIMPLE_LOCAL_RELIEF_MODEL = 'slrm'`

`SKY_VIEW_FACTOR = 'svf'`

`ANISOTROPIC_SKY_VIEW_FACTOR = 'asvf'`

`POSITIVE_OPENNESS = 'pos_opns'`

`NEGATIVE_OPENNESS = 'neg_opns'`

`SKY_ILLUMINATION = 'sim'`

`LOCAL_DOMINANCE = 'ld'`

`MULTI_SCALE_RELIEF_MODEL = 'msrm'`

`MULTI_SCALE_TOPOGRAPHIC_POSITION = 'mstp'`

`class rvt.default.DefaultValues`

Bases: `object`

Class which define layer for blending. BlenderLayer is basic element in BlenderCombination.layers list.

`overwrite`

When saving visualisation functions and file already exists, if 0 it doesn't compute it, if 1 it overwrites it.

Type
bool

`ve_factor`

For all visualization functions. Vertical exaggeration.

Type
float

`slp_compute`

If compute Slope. Parameter for GUIs.

Type
bool

`slp_output_units`
Slope. Output units [radian, degree, percent].

Type
str

`hs_compute`
If compute Hillshade. Parameter for GUIs.

Type
bool

`hs_sun_azi`
Hillshade. Solar azimuth angle (clockwise from North) in degrees.

Type
int

`hs_sun_el`
Hillshade. Solar vertical angle (above the horizon) in degrees.

Type
int

`hs_shadow`
Hillshade. If 1 (Ture) computes binary shadow raster, if 0 (False) it doesn't.

Type
bool

`mhs_compute`
If compute Multi directional hillshade. Parameter for GUIs.

Type
bool

`mhs_nr_dir`
Multi directional hillshade. Number of solar azimuth angles (clockwise from North).

Type
int

`mhs_sun_el`
Multi directional hillshade. Solar vertical angle (above the horizon) in degrees.

Type
int

`slrm_compute`
If compute Simple local relief model. Parameter for GUIs.

Type
bool

`slrm_rad_cell`
Simple local relief model. Radius for trend assessment in pixels.

Type
int

`svf_compute`

If compute Sky-View Factor. Parameter for GUIs.

Type
bool

`svf_n_dir`

Sky-View Factor (Anisotropic Sky-View Factor, Openness). Number of directions.

Type
int

`svf_r_max`

Sky-View Factor (Anisotropic Sky-View Factor, Openness). Maximal search radius in pixels.

Type
int

`svf_noise`

Sky-View Factor (Anisotropic Sky-View Factor, Openness). The level of noise remove [0-don't remove, 1-low, 2-med , 3-high].

Type
int

`asvf_compute`

If compute Anisotropic Sky-View Factor. Parameter for GUIs.

Type
bool

`asvf_dir`

Anisotropic Sky-View Factor. Direction of anisotropy in degrees.

Type
int

`asvf_level`

Anisotropic Sky-View Factor. Level of anisotropy [1-low, 2-high].

Type
int

`pos_opns_compute`

If compute Positive Openness. Parameter for GUIs.

Type
bool

`neg_opns_compute`

If compute Negative Openness. Parameter for GUIs.

Type
bool

`sim_compute`

If compute Sky illumination. Parameter for GUIs.

Type
bool

`sim_sky_mod`
Sky illumination. Sky model [overcast, uniform].

Type
str

`sim_compute_shadow`
Sky illumination. If 1 it computes shadows, if 0 it doesn't.

Type
bool

`sim_nr_dir`
Sky illumination. Number of directions.

Type
int

`sim_shadow_dist`
Sky illumination. Max shadow modeling distance in pixels.

Type
int

`sim_shadow_az`
Sky illumination. Shadow azimuth in degrees.

Type
int

`sim_shadow_el`
Sky illumination. Shadow elevation in degrees.

Type
int

`ld_compute`
If compute Local dominance. Parameter for GUIs.

Type
bool

`ld_min_rad`
Local dominance. Minimum radial distance (in pixels) at which the algorithm starts with visualization computation.

Type
int

`ld_max_rad`
Local dominance. Maximum radial distance (in pixels) at which the algorithm ends with visualization computation.

Type
int

`ld_rad_inc`
Local dominance. Radial distance steps in pixels.

Type
int

`ld_anglr_res`

Local dominance. Angular step for determination of number of angular directions.

Type
int

`ld_observer_h`

Local dominance. Height at which we observe the terrain.

Type
float

`msrm_compute`

If compute Multi-scale relief model. Parameter for GUIs.

Type
bool

`msrm_feature_min`

Minimum size of the feature you want to detect in meters.

Type
float

`msrm_feature_max`

Maximum size of the feature you want to detect in meters.

Type
float

`msrm_scaling_factor`

Scaling factor.

Type
int

`mstp_compute`

If compute Multi-scale topographic position (MSTP).

Type
bool

`mstp_local_scale`

Local scale minimum radius, maximum radius and step in pixels to calculate maximum mean deviation from elevation. All have to be integers!

Type
tuple(min_radius, max_radius, step)

`mstp_meso_scale`

Meso scale minimum radius, maximum radius and step in pixels to calculate maximum mean deviation from elevation. All have to be integers!

Type
tuple(min_radius, max_radius, step)

`mstp_broad_scale`

Broad scale minimum radius, maximum radius and step in pixels to calculate maximum mean deviation from elevation. All have to be integers!

Type
tuple(min_radius, max_radius, step)

`mstp_lightness`
Lightness of image.

Type
float

`slp_save_float`
Slope. If 1 (True) it saves float, if 0 (False) it doesn't.

Type
bool

`hs_save_float`
Hillshade. If 1 (True) it saves float, if 0 (False) it doesn't.

Type
bool

`mhs_save_float`
Multi hillshade. If 1 (True) it saves float, if 0 (False) it doesn't.

Type
bool

`slrm_save_float`
Simplified local relief model. If 1 (True) it saves float, if 0 (False) it doesn't.

Type
bool

`svf_save_float`
Sky-view factor (asvf, pos_opns). If 1 (True) it saves float, if 0 (False) it doesn't.

Type
bool

`neg_opns_save_float`
Negative openness. If 1 (True) it saves float, if 0 (False) it doesn't.

Type
bool

`sim_save_float`
Sky illumination. If 1 (True) it saves float, if 0 (False) it doesn't.

Type
bool

`ld_save_float`
Local dominance. If 1 (True) it saves float, if 0 (False) it doesn't.

Type
bool

`msrm_save_float`
Multi-scale relief model. If 1 (True) it saves float, if 0 (False) it doesn't.

Type
bool

`slp_save_8bit`

Slope. If 1 (True) it saves 8bit, if 0 (False) it doesn't.

Type
bool

`hs_save_8bit`

Hillshade. If 1 (True) it saves 8bit, if 0 (False) it doesn't.

Type
bool

`mhs_save_8bit`

Multi hillshade. If 1 (True) it saves 8bit, if 0 (False) it doesn't.

Type
bool

`slrm_save_8bit`

Simplified local relief model. If 1 (True) it saves 8bit, if 0 (False) it doesn't.

Type
bool

`svf_save_8bit`

Sky-view factor (asvf, pos_opns). If 1 (True) it saves 8bit, if 0 (False) it doesn't.

Type
bool

`neg_opns_save_8bit`

Negative openness. If 1 (True) it saves 8bit, if 0 (False) it doesn't.

Type
bool

`sim_save_8bit`

Sky illumination. If 1 (True) it saves 8bit, if 0 (False) it doesn't.

Type
bool

`ld_save_8bit`

local dominance. If 1 (True) it saves 8bit, if 0 (False) it doesn't.

Type
bool

`msrm_save_8bit`

Multi-scale relief model. If 1 (True) it saves 8bit, if 0 (False) it doesn't.

Type
bool

`slp_bytscl`

Slope, bytescale (0-255) for 8bit raster. Mode can be 'value' (linear stretch) or 'percent' (histogram equalization, cut-off). Values min and max define stretch/cut-off borders.

Type
tuple(mode, min, max)

`hs_bytscl`

Hillshade, linear stretch, bytescale (0-255) for 8bit raster. Mode can be 'value' or 'percent' (cut-off units). Values min and max define stretch borders (in mode units).

Type
tuple(mode, min, max)

`mhs_bytscl`

Multi directional hillshade, linear stretch, bytescale (0-255) for 8bit raster. Mode can be 'value' or 'percent' (cut-off units). Values min and max define stretch borders (in mode units).

Type
tuple(mode, min, max)

`slrm_bytscl`

Simplified local relief model, linear stretch, bytescale (0-255) for 8bit raster. Mode can be 'value' or 'percent' (cut-off units). Values min and max define stretch borders (in mode units).

Type
tuple(mode, min, max)

`svf_bytscl`

Sky-view factor, linear stretch, bytescale (0-255) for 8bit raster. Mode can be 'value' or 'percent' (cut-off units). Values min and max define stretch borders (in mode units).

Type
tuple(mode, min, max)

`asvf_bytscl`

Anisotropic Sky-view factor, linear stretch, bytescale (0-255) for 8bit raster. Mode can be 'value' or 'percent' (cut-off units). Values min and max define stretch borders (in mode units).

Type
tuple(mode, min, max)

`pos_opns_bytscl`

Positive Openness, linear stretch, bytescale (0-255) for 8bit raster. Mode can be 'value' or 'percent' (cut-off units). Values min and max define stretch borders (in mode units).

Type
tuple(mode, min, max)

`neg_opns_bytscl`

Negative Openness, linear stretch, bytescale (0-255) for 8bit raster. Mode can be 'value' or 'percent' (cut-off units). Values min and max define stretch borders (in mode units).

Type
tuple(mode, min, max)

`sim_bytscl`

Sky illumination, linear stretch, bytescale (0-255) for 8bit raster. Mode can be 'value' or 'percent' (cut-off units). Values min and max define stretch borders (in mode units).

Type
tuple(mode, min, max)

`ld_bytscl`

Local dominance, linear stretch, bytescale (0-255) for 8bit raster. Mode can be 'value' or 'percent' (cut-off units). Values min and max define stretch borders (in mode units).

Type
tuple(mode, min, max)

`msrm_bytscl`
Multi-scale relief model, linear stretch, bytescale (0-255) for 8bit raster. Mode can be 'value' or 'percent' (cut-off units). Values min and max define stretch borders (in mode units).

Type
tuple(mode, min, max)

`tile_size_limit`
If array size bigger than tile_size_limit it uses saving tile by tile (rvt.tile module).

Type
int

`tile_size`
Size of single tile when saving tile by tile.

Type
tuple(x_size, y_size)

`save_default_to_file`(*file_path=None*)
Saves default attributes into .json file.

`read_default_from_file`(*file_path*)
Reads default attributes from file.

`get_shadow_file_name`(*dem_path*)
Returns shadow name, with added hillshade parameters (hs_sun_azi == shadow azimuth, hs_sun_el == shadow_elevation).

`get_shadow_path`(*dem_path*)
Returns path to Shadow. Generates shadow name (uses default attributes and dem name from dem_path) and adds dem directory (dem_path) to it.

`get_hillshade_file_name`(*dem_path*, *bit8=False*)
Returns Hillshade name, dem name (from dem_path) with added hillshade parameters. If bit8 it returns 8bit file name.

`get_hillshade_path`(*dem_path*, *bit8=False*)
Returns path to Hillshade. Generates hillshade name (uses default attributes and dem name from dem_path) and adds dem directory (dem_path) to it. If bit8 it returns 8bit file path.

`get_slope_file_name`(*dem_path*, *bit8=False*)
Returns Slope name, dem name (from dem_path) with added slope parameters. If bit8 it returns 8bit file name.

`get_slope_path`(*dem_path*, *bit8=False*)
Returns path to slope. Generates slope name and adds dem directory (dem_path) to it. If bit8 it returns 8bit file path.

`get_multi_hillshade_file_name`(*dem_path*, *bit8=False*)
Returns Multiple directions hillshade name, dem name (from dem_path) with added multi hillshade parameters. If bit8 it returns 8bit file name.

`get_multi_hillshade_path`(*dem_path*, *bit8=False*)
Returns path to Multiple directions hillshade. Generates multi hillshade name (uses default attributes and dem name from dem_path) and adds dem directory (dem_path) to it. If bit8 it returns 8bit file path.

`get_slrm_file_name`(*dem_path*, *bit8=False*)

Returns Simple local relief model name, dem name (from dem_path) with added slrm parameters. If bit8 it returns 8bit file name.

`get_slrm_path`(*dem_path*, *bit8=False*)

Returns path to Simple local relief model. Generates slrm name (uses default attributes and dem name from dem_path) and adds dem directory (dem_path) to it. If bit8 it returns 8bit file path.

`get_svf_file_name`(*dem_path*, *bit8=False*)

Returns Sky-view factor name, dem name (from dem_path) with added svf parameters. If bit8 it returns 8bit file name.

`get_svf_path`(*dem_path*, *bit8=False*)

Returns path to Sky-view factor. Generates svf name (uses default attributes and dem name from dem_path) and adds dem directory (dem_path) to it. If bit8 it returns 8bit file path.

`get_asvf_file_name`(*dem_path*, *bit8=False*)

Returns Anisotropic Sky-view factor name, dem name (from dem_path) with added asvf parameters. If bit8 it returns 8bit file name.

`get_asvf_path`(*dem_path*, *bit8=False*)

Returns path to Anisotropic Sky-view factor. Generates asvf name (uses default attributes and dem name from dem_path) and adds dem directory (dem_path) to it. If bit8 it returns 8bit file path.

`get_opns_file_name`(*dem_path*, *bit8=False*)

Returns Positive Openness name, dem name (from dem_path) with added pos opns parameters. If bit8 it returns 8bit file name.

`get_opns_path`(*dem_path*, *bit8=False*)

Returns path to Positive Openness. Generates pos opns name (uses default attributes and dem name from dem_path) and adds dem directory (dem_path) to it. If bit8 it returns 8bit file path.

`get_neg_opns_file_name`(*dem_path*, *bit8=False*)

Returns Negative Openness name, dem name (from dem_path) with added neg opns parameters. If bit8 it returns 8bit file name.

`get_neg_opns_path`(*dem_path*, *bit8=False*)

Returns path to Negative Openness. Generates pos neg name (uses default attributes and dem name from dem_path) and adds dem directory (dem_path) to it. If bit8 it returns 8bit file path.

`get_sky_illumination_file_name`(*dem_path*, *bit8=False*)

Returns Sky illumination name, dem name (from dem_path) with added sim parameters. If bit8 it returns 8bit file name.

`get_sky_illumination_path`(*dem_path*, *bit8=False*)

Returns path to Sky illumination. Generates sim name (uses default attributes and dem name from dem_path) and adds dem directory (dem_path) to it. If bit8 it returns 8bit file path.

`get_local_dominance_file_name`(*dem_path*, *bit8=False*)

Returns Local dominance name, dem name (from dem_path) with added ld parameters. If bit8 it returns 8bit file name.

`get_local_dominance_path`(*dem_path*, *bit8=False*)

Returns path to Local dominance. Generates ld name (uses default attributes and dem name from dem_path) and adds dem directory (dem_path) to it. If bit8 it returns 8bit file path.

get_msrm_file_name(*dem_path*, *bit8=False*)

Returns Multi-scale relief model name, dem name (from dem_path) with added msrm parameters. If bit8 it returns 8bit file name.

get_msrm_path(*dem_path*, *bit8=False*)

Returns path to Multi-scale relief model. Generates msrm name (uses default attributes and dem name from dem_path) and adds dem directory (dem_path) to it. If bit8 it returns 8bit file path.

get_mstp_file_name(*dem_path*, *bit8=False*)

Returns Multi-scale topographic position name, dem name (from dem_path) with added mstp parameters. If bit8 it returns 8bit file name.

get_mstp_path(*dem_path*, *bit8=False*)

get_visualization_file_name(*rvt_visualization: RVTVisualization*, *dem_path: Path*, *path_8bit: bool*) → str

“Return visualization path.

get_visualization_path(*rvt_visualization: RVTVisualization*, *dem_path: Path*, *output_dir_path: Path*, *path_8bit: bool*) → Path

“Return visualization path.

float_to_8bit(*float_arr: array*, *visualization: RVTVisualization*, *x_res: float = None*, *y_res: float = None*, *no_data: float | None = None*)

Converts (byte scale) float visualization to 8bit. Resolution (x_res, y_res) and no_data needed only for multiple directions hillshade! Method first normalize then byte scale (0-255).

get_slope(*dem_arr*, *resolution_x*, *resolution_y*, *no_data=None*)

save_slope(*dem_path*, *custom_dir=None*, *save_float=None*, *save_8bit=None*)

Calculates and saves Slope from dem (dem_path) with default parameters. If custom_dir is None it saves in dem directory else in custom_dir. If path to file already exists we can overwrite file (overwrite=0) or not (overwrite=1). If save_float is True method creates Gtiff with real values, if save_8bit is True method creates GTiff with bytescaled values (0-255).

get_shadow(*dem_arr*, *resolution*, *no_data=None*)

get_hillshade(*dem_arr*, *resolution_x*, *resolution_y*, *no_data=None*)

save_hillshade(*dem_path*, *custom_dir=None*, *save_float=None*, *save_8bit=None*, *save_shadow=None*)

Calculates and saves Hillshade from dem (dem_path) with default parameters. If custom_dir is None it saves in dem directory else in custom_dir. If path to file already exists we can overwrite file (overwrite=1) or not (overwrite=0). If save_float is True method creates Gtiff with real values, if save_8bit is True method creates GTiff with bytescaled values (0-255).

get_multi_hillshade(*dem_arr*, *resolution_x*, *resolution_y*, *no_data=None*)

save_multi_hillshade(*dem_path*, *custom_dir=None*, *save_float=None*, *save_8bit=None*)

Calculates and saves Multidirectional hillshade from dem (dem_path) with default parameters. If custom_dir is None it saves in dem directory else in custom_dir. If path to file already exists we can overwrite file (overwrite=1) or not (overwrite=0). If save_float is True method creates Gtiff with real values, if save_8bit is True method creates GTiff with bytescaled values (0-255).

get_slrm(*dem_arr*, *no_data=None*)

`save_slrm`(*dem_path*, *custom_dir=None*, *save_float=None*, *save_8bit=None*)

Calculates and saves Simple local relief model from dem (dem_path) with default parameters. If custom_dir is None it saves in dem directory else in custom_dir. If path to file already exists we can overwrite file (overwrite=1) or not (overwrite=0). If save_float is True method creates Gtiff with real values, if save_8bit is True method creates GTiff with bytescaled values (0-255).

`get_sky_view_factor`(*dem_arr*, *resolution*, *compute_svf=True*, *compute_asvf=False*, *compute_opns=False*, *no_data=None*)

`save_sky_view_factor`(*dem_path*, *save_svf=True*, *save_asvf=False*, *save_opns=False*, *custom_dir=None*, *save_float=None*, *save_8bit=None*)

Calculates and saves Sky-view factor(save_svf=True), Anisotropic Sky-view factor(save_asvf=True) and Positive Openness(save_opns=True) from dem (dem_path) with default parameters. If custom_dir is None it saves in dem directory else in custom_dir. If path to file already exists we can overwrite file (overwrite=1) or not (overwrite=0). If save_float is True method creates Gtiff with real values, if save_8bit is True method creates GTiff with bytescaled values (0-255).

`get_neg_opns`(*dem_arr*, *resolution*, *no_data=None*)

`save_neg_opns`(*dem_path*, *custom_dir=None*, *save_float=None*, *save_8bit=None*)

Calculates and saves Negative Openness from dem (dem_path) with default parameters. If custom_dir is None it saves in dem directory else in custom_dir. If path to file already exists we can overwrite file (overwrite=1) or not (overwrite=0). If save_float is True method creates Gtiff with real values, if save_8bit is True method creates GTiff with bytescaled values (0-255).

`get_sky_illumination`(*dem_arr*, *resolution*, *no_data=None*)

`save_sky_illumination`(*dem_path*, *custom_dir=None*, *save_float=None*, *save_8bit=None*)

Calculates and saves Sky illumination from dem (dem_path) with default parameters. If custom_dir is None it saves in dem directory else in custom_dir. If path to file already exists we can overwrite file (overwrite=1) or not (overwrite=0). If save_float is True method creates Gtiff with real values, if save_8bit is True method creates GTiff with bytescaled values (0-255).

`get_local_dominance`(*dem_arr*, *no_data=None*)

`save_local_dominance`(*dem_path*, *custom_dir=None*, *save_float=None*, *save_8bit=None*)

Calculates and saves Local dominance from dem (dem_path) with default parameters. If custom_dir is None it saves in dem directory else in custom_dir. If path to file already exists we can overwrite file (overwrite=1) or not (overwrite=0). If save_float is True method creates Gtiff with real values, if save_8bit is True method creates GTiff with bytescaled values (0-255).

`get_msrm`(*dem_arr*, *resolution*, *no_data=None*)

`save_msrm`(*dem_path*, *custom_dir=None*, *save_float=None*, *save_8bit=None*)

Calculates and saves Multi-scale relief model from dem (dem_path) with default parameters. If custom_dir is None it saves in dem directory else in custom_dir. If path to file already exists we can overwrite file (overwrite=1) or not (overwrite=0). If save_float is True method creates Gtiff with real values, if save_8bit is True method creates GTiff with bytescaled values (0-255).

`get_mstp`(*dem_arr*, *no_data=None*)

`save_mstp`(*dem_path*, *custom_dir=None*, *save_float=None*, *save_8bit=None*)

Calculates and saves Multi-scale topographic position from dem (dem_path) with default parameters. If custom_dir is None it saves in dem directory else in custom_dir. If path to file already exists we can overwrite file (overwrite=1) or not (overwrite=0).

save_visualizations(*dem_path*, *custom_dir=None*)

Save all visualizations where self.'visualization'_compute = True also saves float where self.'visualization' _save_float = True and 8bit where self.'visualization'_save_8bit = True. In the end method creates log file.

calculate_visualization(*visualization: RVTVisualization*, *dem: array*, *resolution_x: float*, *resolution_y: float*, *no_data: float | None = None*, *save_float: bool = True*, *save_8bit: bool = False*) → Tuple[array, array] | None

create_log_file(*dem_path*, *custom_dir=None*, *compute_time=None*)

Creates log file in custom_dir, if custom_dir=None it creates it in dem directory (dem_path). Be aware, all default parameters have to be right! Parameter compute_time is in seconds.

rvt.default.**get_raster_arr**(*raster_path*)

Reads raster from raster_path and returns its array(value) and resolution.

Parameters
raster_path (*str*) – Path to raster

Returns
dict_out – Returns {"array": array, "resolution": (x_res, y_res), "no_data": no_data} : dict("array": np.array, "resolution": tuple(float, float), "no_data": float). Returns dictionary with keys: array, resolution and no_data. Key resolution is tuple where first element is x resolution and second is y resolution. Key no_data represent value of no data.

Return type
dict

rvt.default.**get_raster_size**(*raster_path*, *band=1*)

Opens raster path and returns selected band size.

Parameters

- **raster_path** (*str*) – Path to raster.
- **band** (*int*) – Selected band number.

Return type
tuple(x_size, y_size)

rvt.default.**save_raster**(*src_raster_path*, *out_raster_path*, *out_raster_arr: ndarray*, *no_data=None*, *e_type=6*)

Saves raster array (out_rast_arr) to out_raster_path (GTiff), using src_rast_path information.

Parameters

- **src_raster_path** (*str*) – Path to source raster.
- **out_raster_path** (*str*) – Path to new file, where to save raster (GTiff).
- **out_raster_arr** (*np.array (2D - one band, 3D - multiple bands)*) – Array with raster data.
- **no_data** (*float*) – Value that represents no data pixels.
- **e_type** (*GDALDataType*) – https://gdal.org/api/raster_c_api.html#_CPPv412GDALDataType, (GDT_Float32 = 6, GDT_UInt8 = 1, …)

6.5 RVT for ArcGIS Pro

RVT can be used in ArcGIS Pro as a set of custom raster functions.

As described in the ArcGIS Pro documentation:

> Raster functions are operations that apply processing directly to the pixels of imagery and raster datasets, as opposed to geoprocessing tools, which write out a new raster to disk. Calculations are applied to the pixels of the original data as displayed, so only pixels that are visible on your screen are processed. As you zoom and/or pan around, the calculations are performed on the fly. Because no intermediate datasets are created, processes can be applied quickly, as opposed to the time it would take to create a processed file on disk.

See also:

Find out how to install RVT for ArcGIS in *ArcGIS installation*.

6.5.1 Setting up

1. Start ArcGIS Pro, open a project, and add a DEM layer.

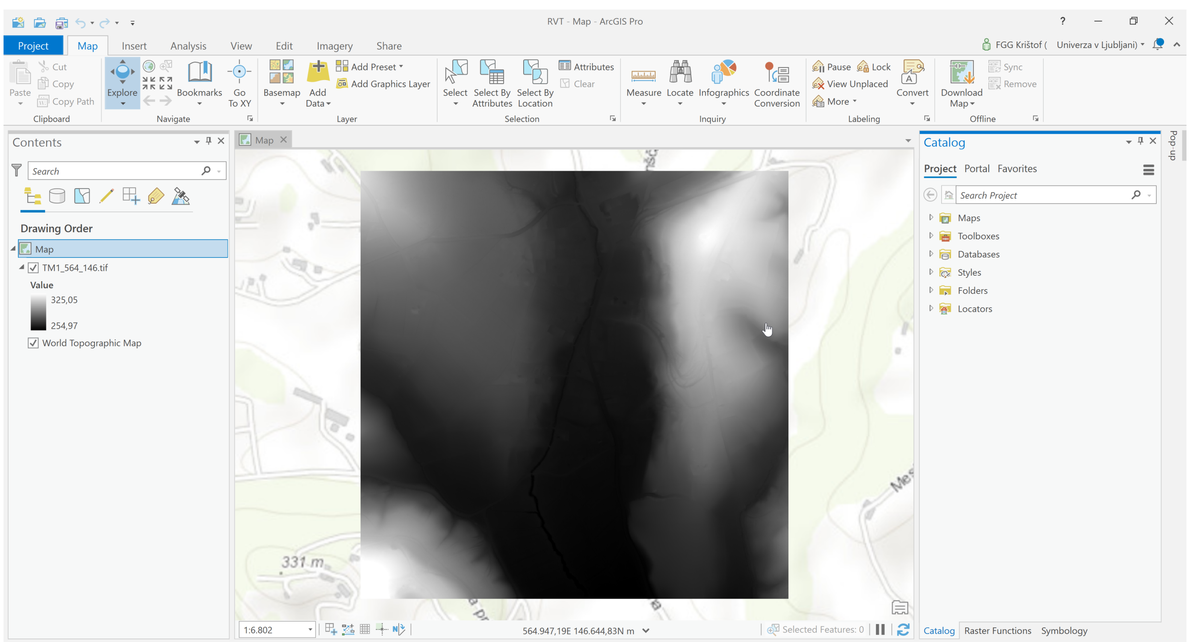

2. Select `Imagery` → `Raster Functions`.

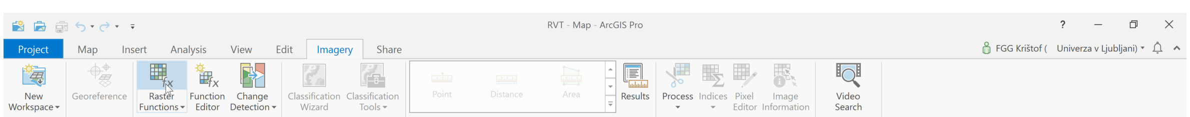

3. Select `Custom` and open the group `rvt-arcgis-pro`.

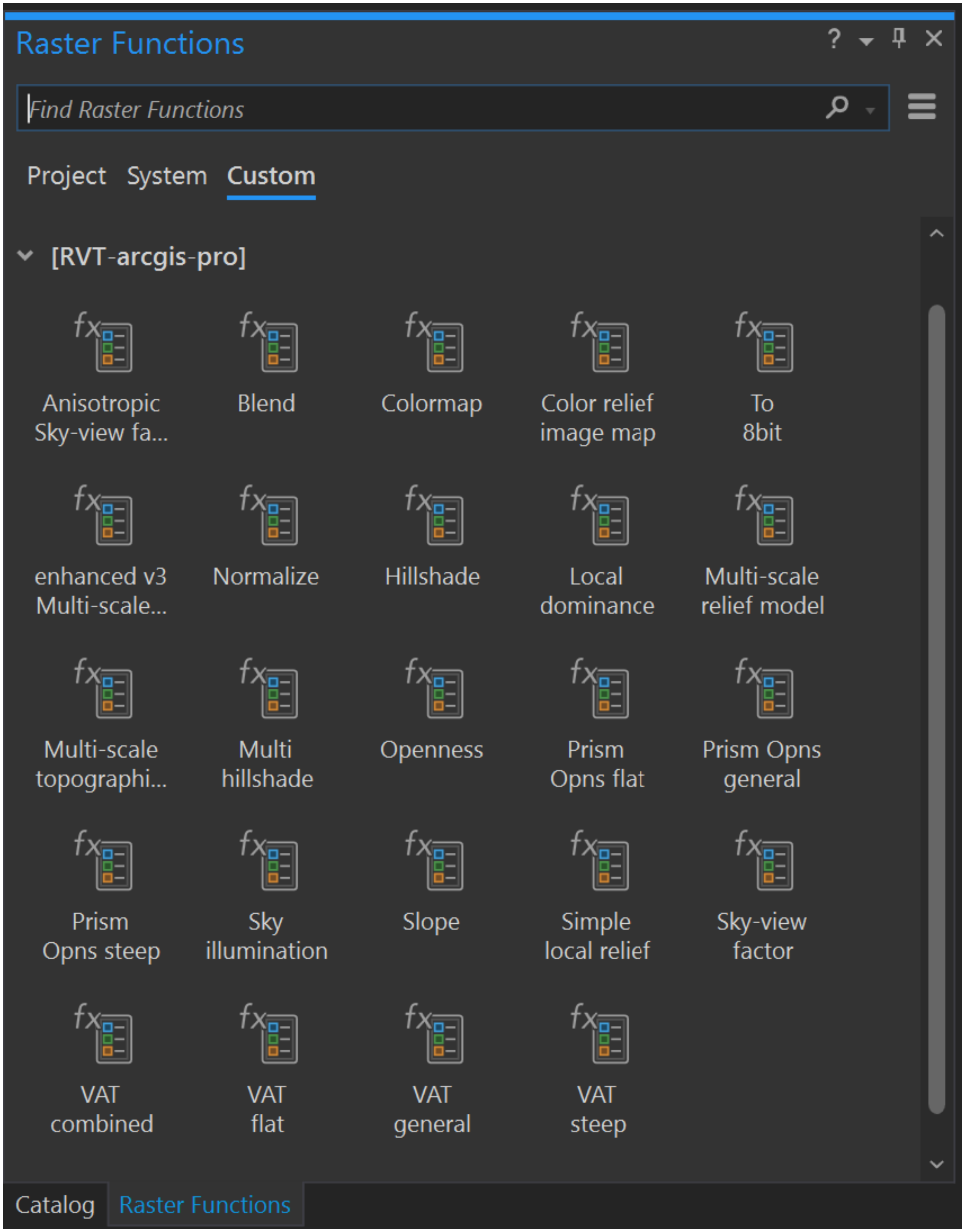
Raster Functions
Find Raster Functions
Project
System
Custom
[RVT-arcgis-pro]
Anisotropic Sky-view fa...
Blend
Colormap
Color relief image map
To 8bit
enhanced v3 Multi-scale...
Normalize
Hillshade
Local dominance
Multi-scale relief model
Multi-scale topographi...
Multi hillshade
Openness
Prism Opns flat
Prism Opns general
Prism Opns steep
Sky illumination
Slope
Simple local relief
Sky-view factor
VAT combined
VAT flat
VAT general
VAT steep
Catalog
Raster Functions

6.5.2 Computing visualizations

1. Select the appropriate function, e.g. `svf`, specify the processing parameters and select `Create new layer` (or `Save As`).

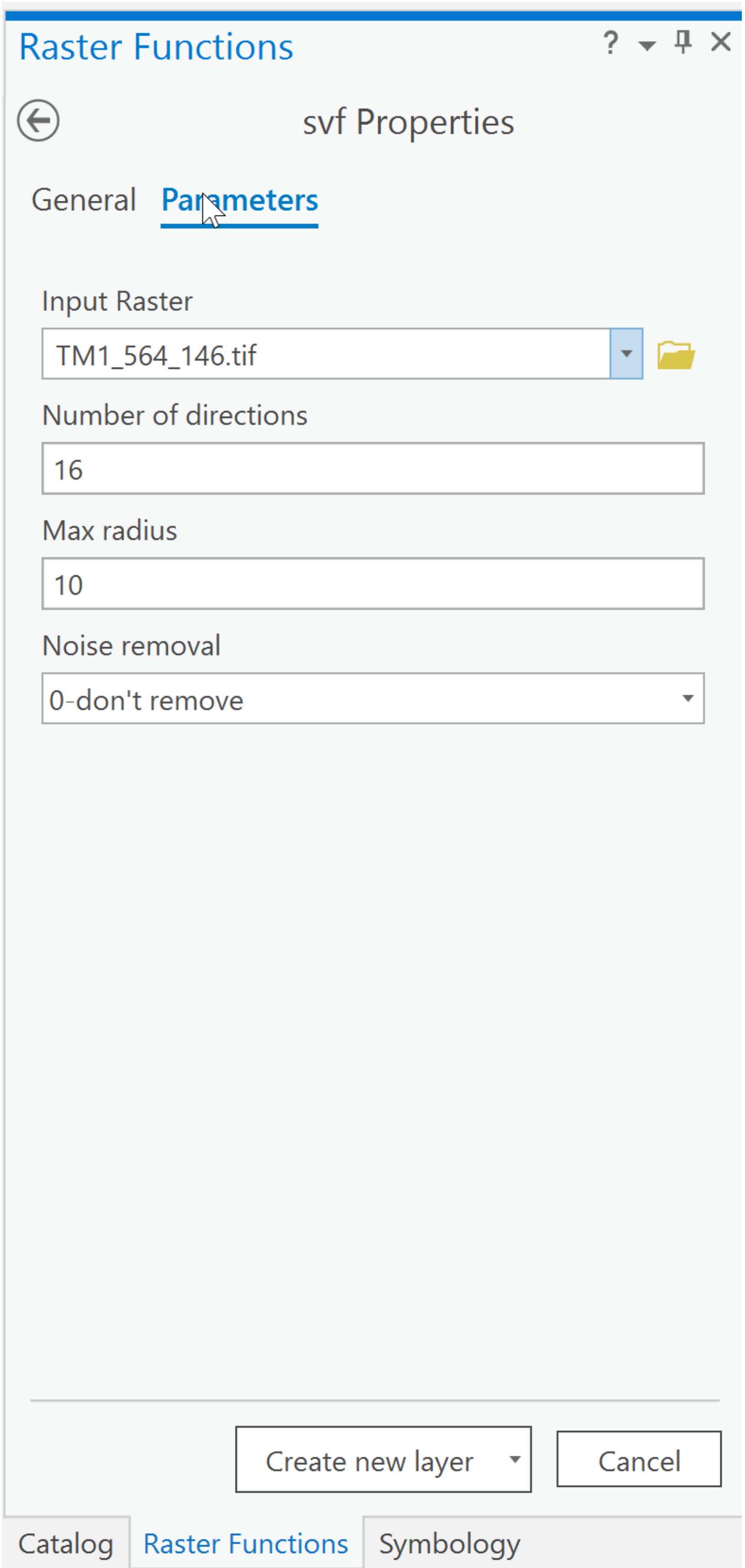
Raster Functions
svf Properties
General
Parameters
Input Raster
TM1_564_146.tif
Number of directions
16
Max radius
10
Noise removal
0-don't remove
Create new layer
Cancel
Catalog
Raster Functions
Symbology

2. The visualization is computed and displayed as a layer in the main window.

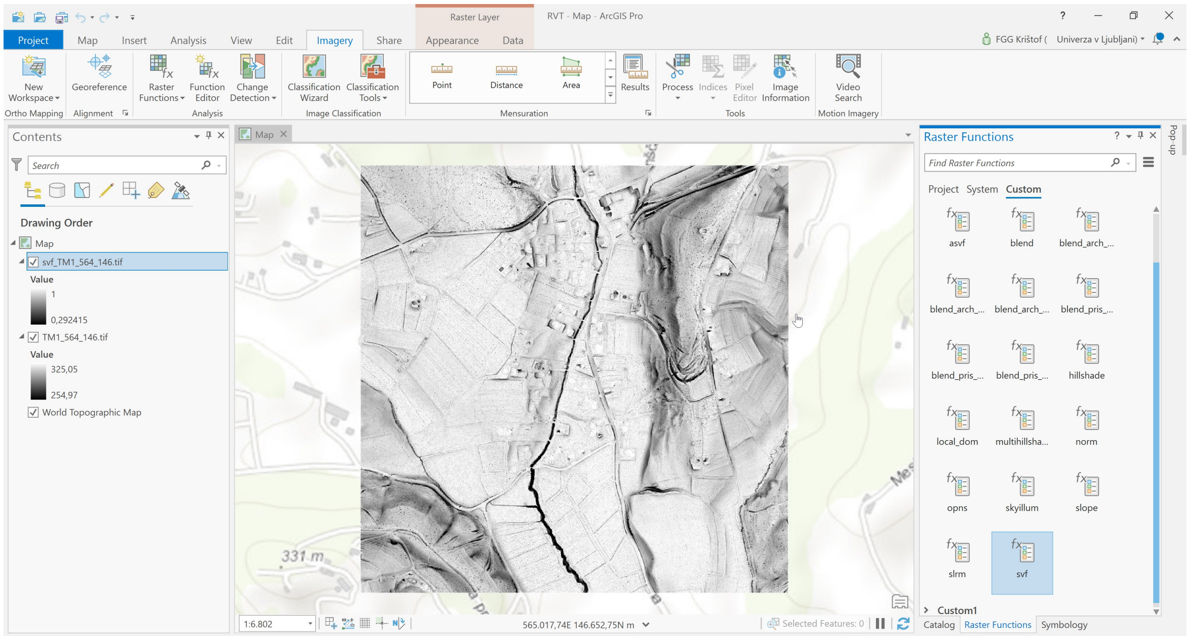

6.5.3 Using the blender

1. The blender in ArcGIS is slightly different from the blender in the QGIS plugin and the Python package. The same blend mode options exist, but only two raster layers can be blended at one time.

Use the blender in the same way as a visualization function, by specifying the processing parameters and selecting `Save As`.

6.6 RVT for QGIS

The RVT QGIS plugin uses the core RVT Python package. The plugin interface offers a user-friendly way to access all the functionality of the Python package.

See also:

Find out how to install RVT for QGIS in *QGIS installation*.

6.6.1 Setting up

1. Open a DEM file to be visualized.

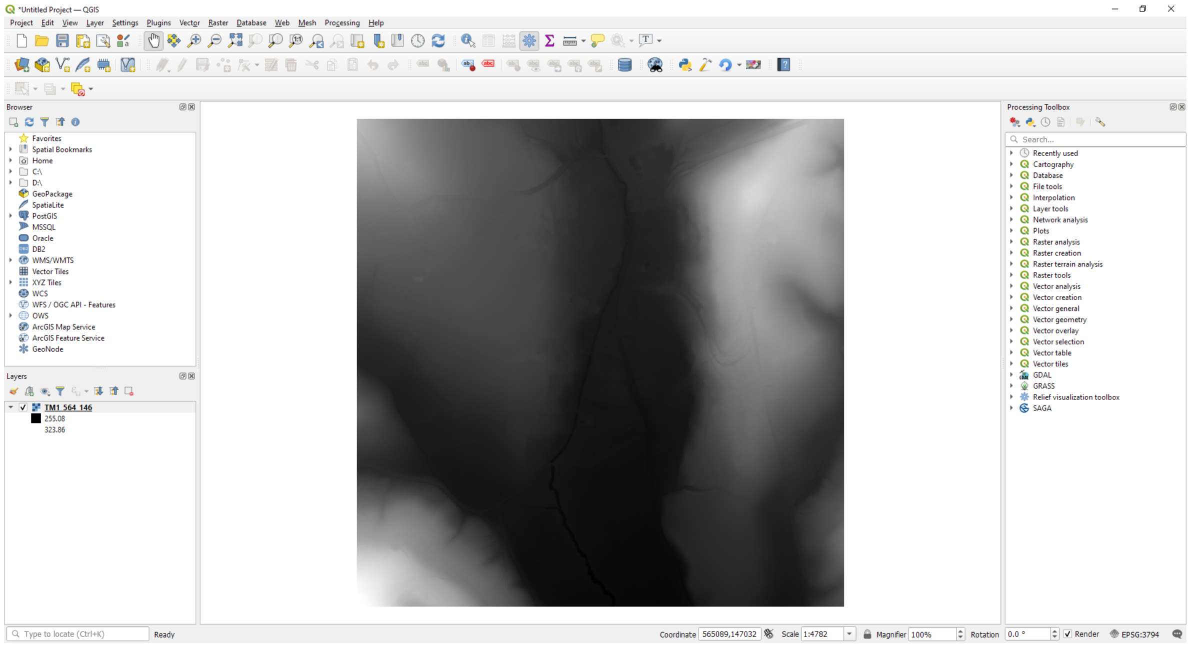

2. Select `Raster` → `Relief Visualization Toolbox` or the RVT icon in the toolbar.

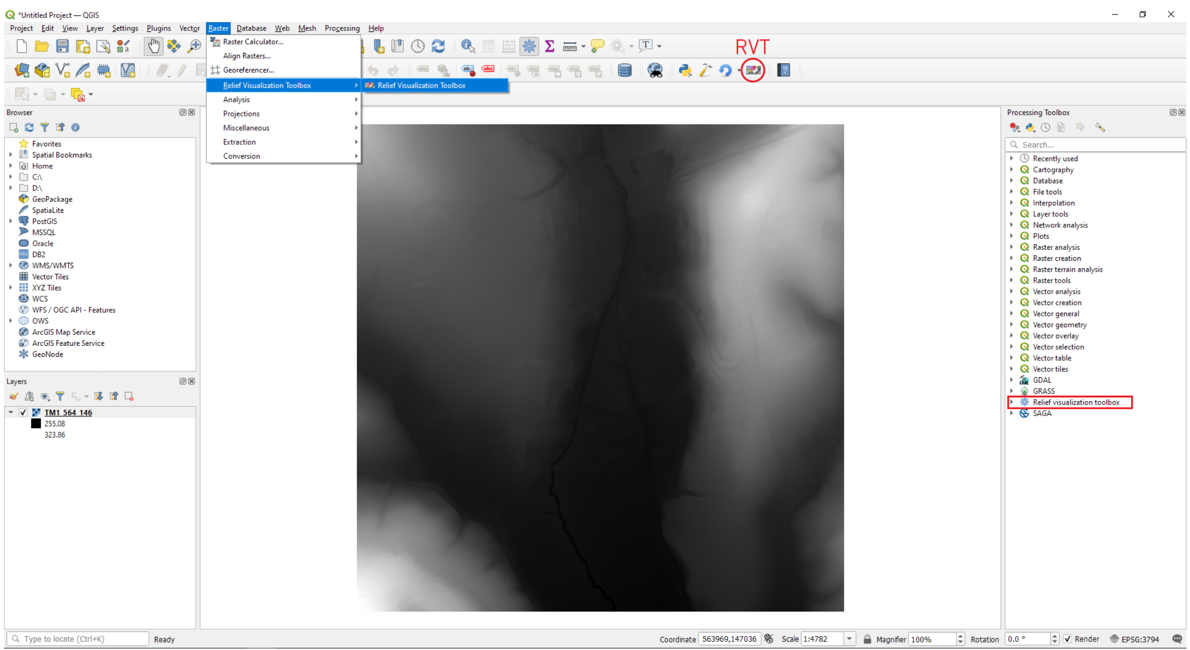

6.6.2 Computing visualizations

1. Select the DEM in `List of currently selected files:`, then select the `Visualizations` tab. In the `Visualization` tab select `preferred visualizations` and set their parameters (options).

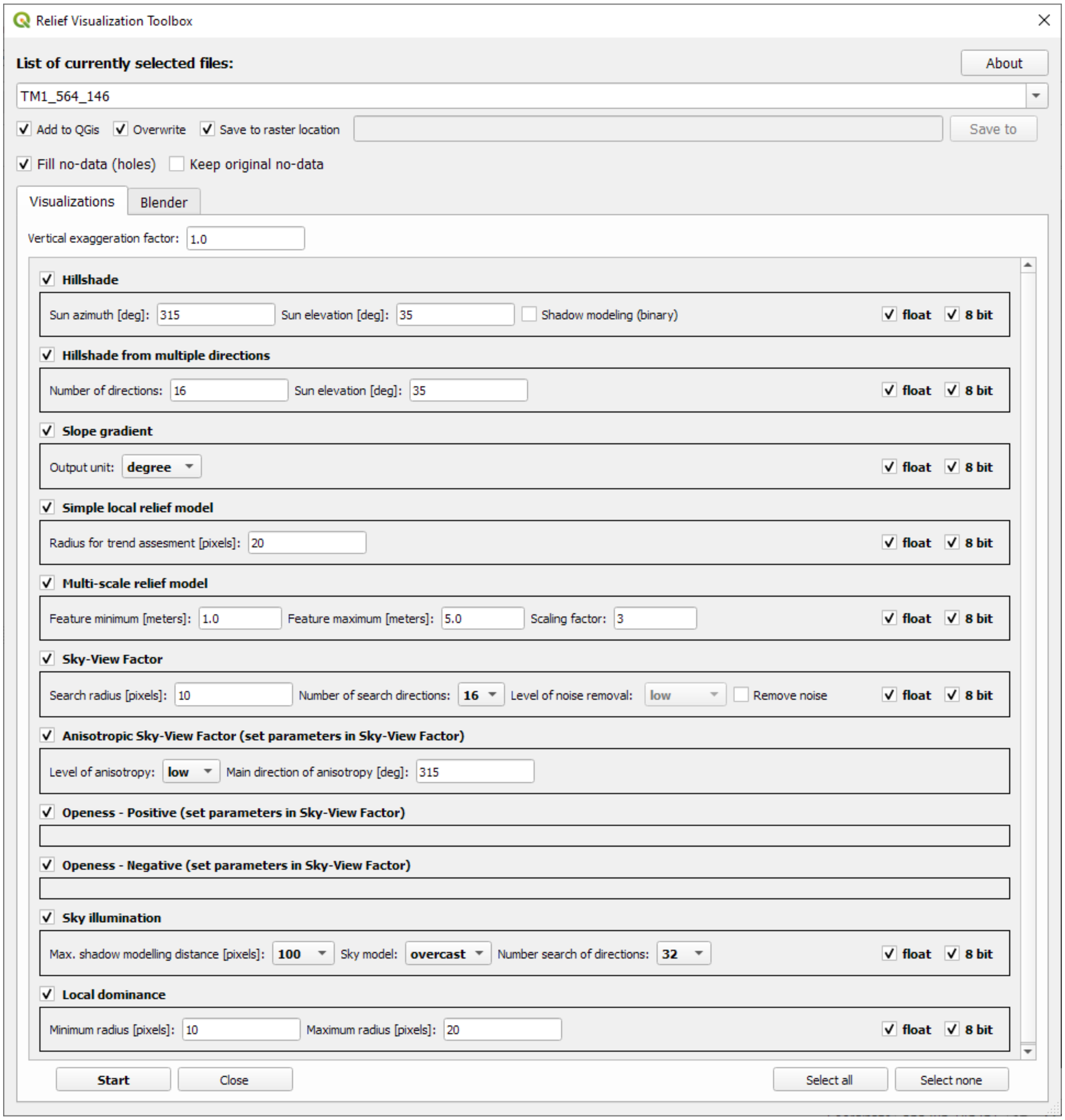

2. Select `Start` to calculate the visualizations.

The visualizations are stored as GeoTIFFs in the same folder as the input file, or to a custom location (if the `Save to raster location` check box is unchecked, and the `Save to` directory is set).

Visualizations are also added to the main window of QGIS if the `Add to QGIS` check box is checked. If the `Overwrite` check box is checked, the program overwrites any existing visualization files.

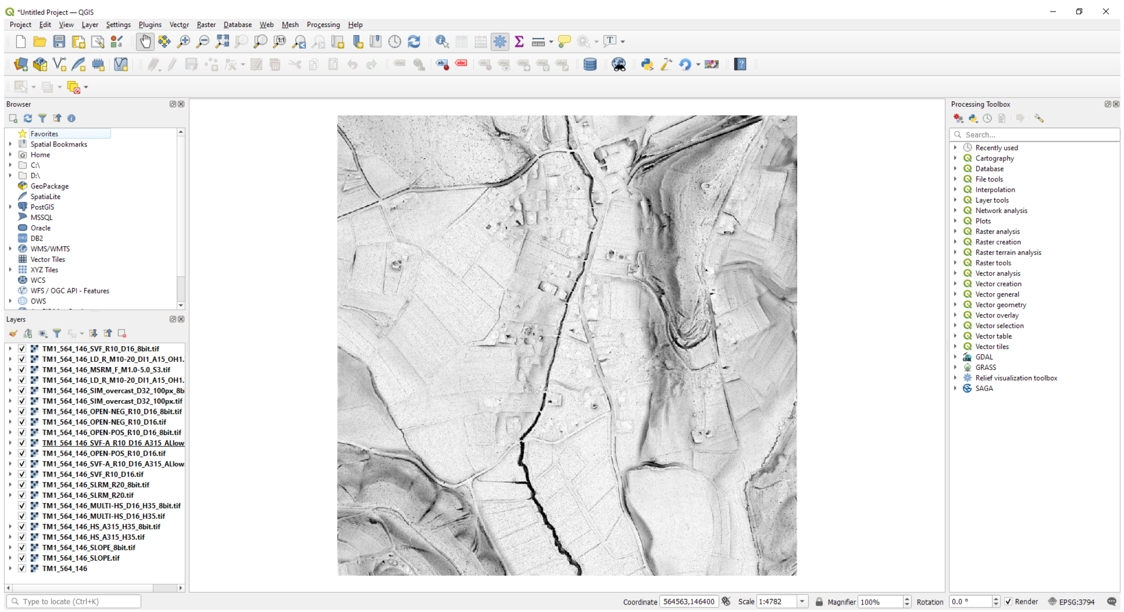

See also:

Find out more about visualizations and their parameters in *rvt.vis*.

6.6.3 Using the blender

1. Chose a DEM in `List of currently selected files:`, then choose the `Blender` tab. In the `Blender` tab select your `Blend combination:` or build your own in layers.

You can add your own custom combination to the list. Write a name in the `Combination name` text field and select `Add`. To remove it, just select it in the (`Blend combination` list) and select `Remove`.

You can also save a specific combination to a JSON file (if you want to share it, for example). To do this, input its name (in the `Combination name` text field) and select `Save ...` (then select the location and name of the file).

Saved JSON combinations can be added by selecting the `Load ...` button (select file). You can change the parameters for each visualization method in the blend combination in the Visualizations tab.

If you check the `Use preset values for terrain type` it applies the selected terrain type settings (this changes the normalization min and max, and visualizations parameters). If you check `Save visualizations`, all the visualization parameters used in the blender combination will be saved.

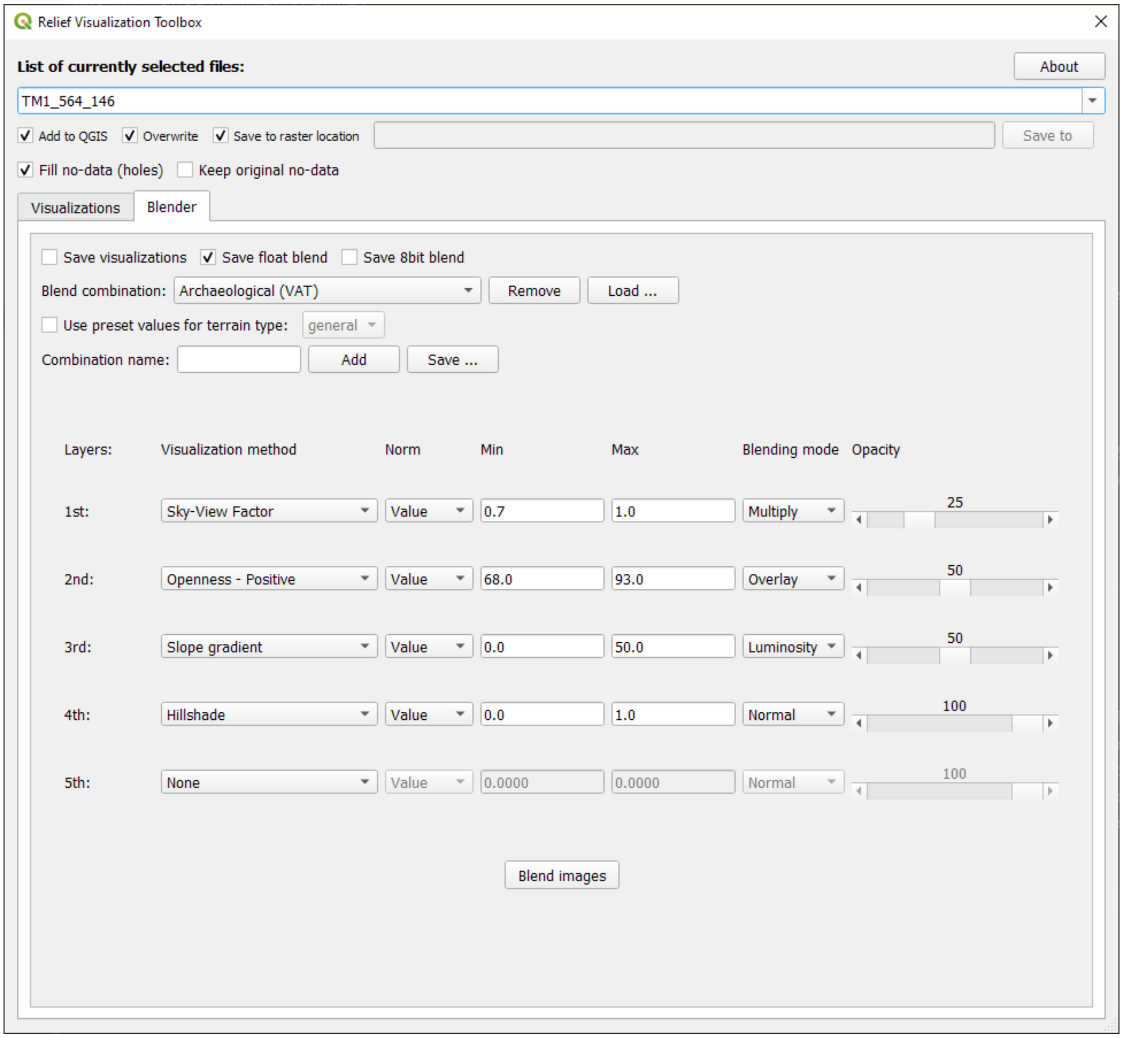

1. Select `Blend images` to calculate the blended (fused, combined) image.

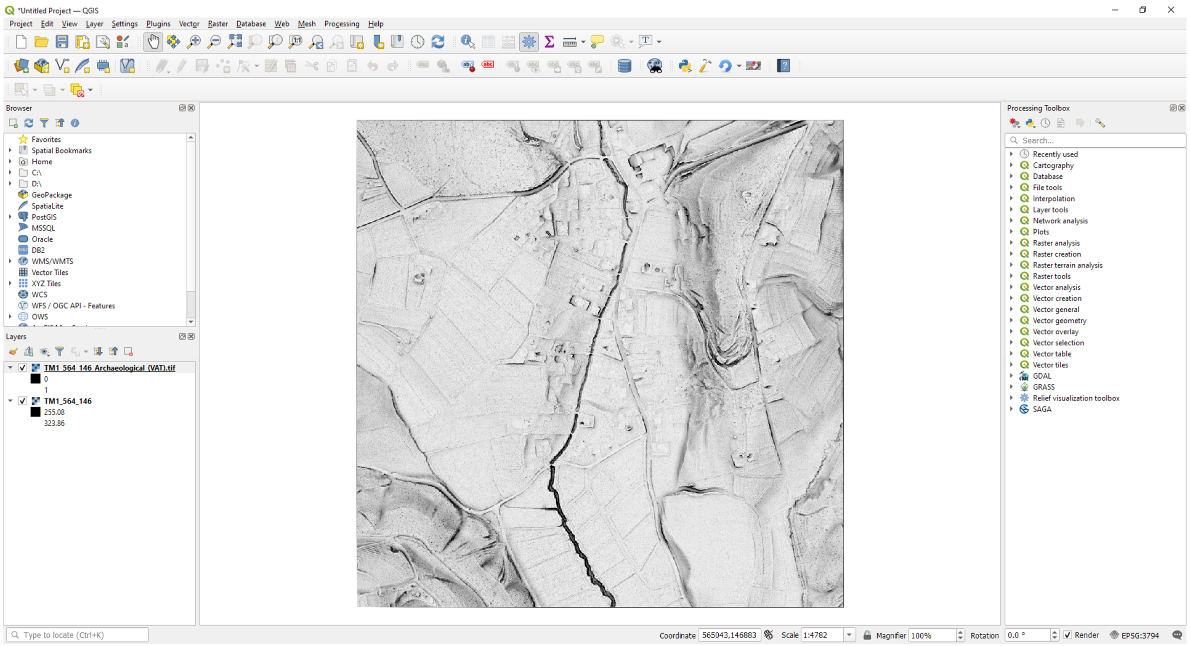

The blended image is stored as a GeoTIFF in the same folder as the input file or to a custom location (if `Save to raster location` check box is unchecked and a directory is set in the text field next to it).

6.6.4 Using the processing functions

1. Go to the `Processing Toolbox` → `Relief visualization toolbox` to access all the RVT visualization functions.

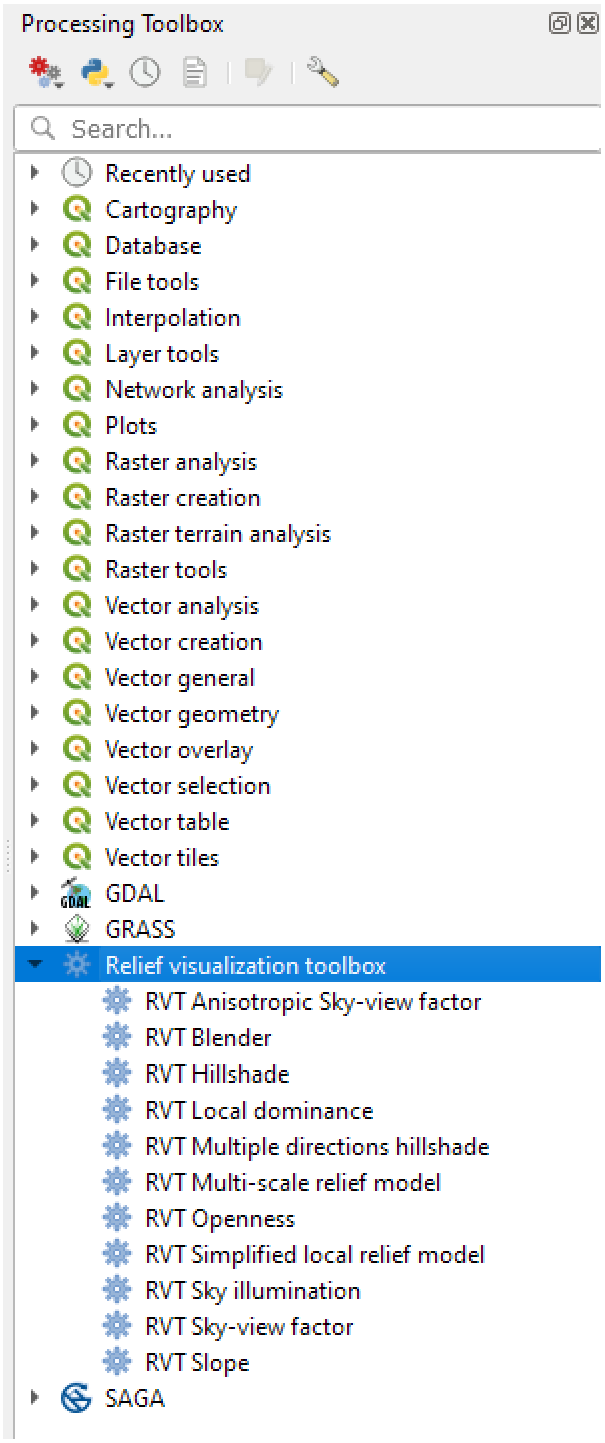
Processing Toolbox
Search...
Recently used
Cartography
Database
File tools
Interpolation
Layer tools
Network analysis
Plots
Raster analysis
Raster creation
Raster terrain analysis
Raster tools
Vector analysis
Vector creation
Vector general
Vector geometry
Vector overlay
Vector selection
Vector table
Vector tiles
GDAL
GRASS
Relief visualization toolbox
RVT Anisotropic Sky-view factor
RVT Blender
RVT Hillshade
RVT Local dominance
RVT Multiple directions hillshade
RVT Multi-scale relief model
RVT Openness
RVT Simplified local relief model
RVT Sky illumination
RVT Sky-view factor
RVT Slope
SAGA

6.7 Example notebooks

This section contains example code for using the `rvt.vis` and `rvt.default` modules in two Jupyter Notebooks.

Both notebooks are available in the examples folder in the repository .

CONTENTS

6.7.1 RVT vis module

This example notebook shows how to create visualizations with the rvt.vis module.

Before you start

You'll need a DEM to work through this notebook.

Download the test data from Getting started, or have some of your own data ready to work with.

Save your data in a directory called test_data. You'll need to set a path to this test data in cell [2].

First, let's import the required modules.

To load the DEM file into a numpy array and to store visualizations back to GeoTIFF, we will be using rvt.default module (which is based on the Python gdal library).

You can also use rasterio, gdal or any other Python library.

[1]:
```
import rvt.vis  # fro calculating visualizations
import rvt.default  # for loading/saving rasters
import numpy as np
import matplotlib.pyplot as plt  # to plot visualizations
```

In the test_data directory is a file called "TM1_564_146.tif". This will be our test DEM, from which we will be calculating visualizations.

Define a string with the path to this file (input_dem_path).

[2]:
```
dem_path = r"../test_data/TM1_564_146.tif"
```

This module has the function get_raster_arr() which reads a raster from a raster path and returns a dictionary with the keys "array", "resolution" and "no_data":

- "array" is the numpy array of the raster
- "resolution" is a tuple representing the raster's size in pixels, where the first element is the pixel size in x direction and the second is in y direction.
- "no_data" is the value which represents noData in the raster (array).

[3]:
```
dict_dem = rvt.default.get_raster_arr(dem_path)
dem_arr = dict_dem["array"]  # numpy array of DEM
dem_resolution = dict_dem["resolution"]
dem_res_x = dem_resolution[0]  # resolution in X direction
dem_res_y = dem_resolution[1]  # resolution in Y direction
```

(continues on next page)

(continued from previous page)

```
dem_no_data = dict_dem["no_data"]

plt.imshow(dem_arr, cmap='gray')
```

[3]:
```
<matplotlib.image.AxesImage at 0x1923a694108>
```

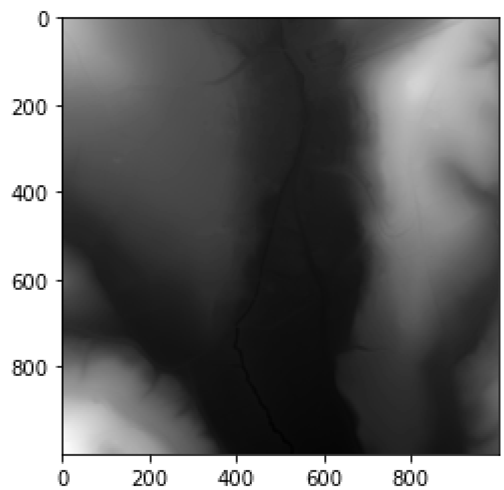

Visualization functions

All of the visualization functions take a DEM array as an input parameter.

They also take some parameters which are specific for each visualization, as well as common parameters: - ve_factor (vertical exaggeration factor, multipy factor) - no_data (value that represents no_data, every function replace all no_data value in array with np.nan)

The no_data parameter is represented as np.nan. Before every visualization function starts computing a visualization it changes no_data to np.nan.

Some visualization functions return a dictionary which contains the numpy array of visualization, some return the numpy array of visualization directly.

Slope

To calculate slope use the rvt.vis.slope_aspect() function.

This function takes the parameters:

- dem
- resolution_x
- resolution_y
- output_units (can be: percent, degree, radian)
- ve_factor
- no_data.

This function outputs a dictonary with the keys "slope" and "aspect". Each key contains a numpy array.

[4]:
```
dict_slope_aspect = rvt.vis.slope_aspect(dem=dem_arr, resolution_x=dem_res_x, resolution_
↪y=dem_res_y,
                                         output_units="degree", ve_factor=1, no_data=dem_
↪no_data)
slope_arr = dict_slope_aspect["slope"]

plt.imshow(slope_arr, cmap='gray')
```

[4]:
```
<matplotlib.image.AxesImage at 0x1923ca44048>
```

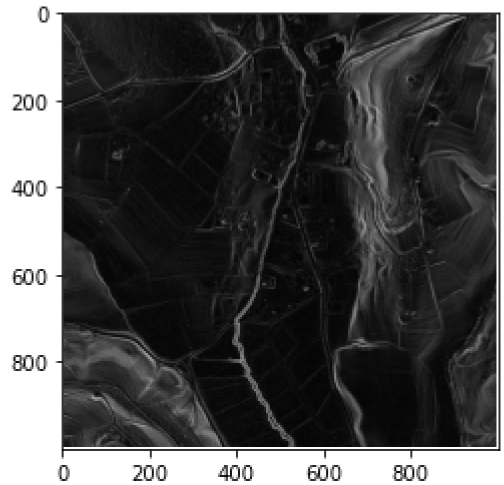

To save the visualization use the rvt.default.save_raster() function.

This function takes the parameters:

- src_raster_path (dem path to copy geodata)
- out_raster_path (visualization path)
- out_raster_arr (visualization numpy array)
- no_data (how is no data stored, all the visualizations no_data is stored as np.nan)
- e_type (GDALDataType, for example 6 is for float32 and 1 is for uint8)

[5]:
```
slope_path = r"../test_data/TM1_564_146_slope.tif"
rvt.default.save_raster(src_raster_path=dem_path, out_raster_path=slope_path, out_raster_
↪arr=slope_arr, no_data=np.nan,
                        e_type=6)
```

Hillshade

To calculate a hillshade use the rvt.vis.hillshade() function.

This function takes the parameters:

- dem
- resolution_x
- resolution_y
- sun_azimuth

- sun_elevation
- ve_factor
- no_data.

This function outputs a numpy array of the hillshade.

[6]:
```
sun_azimuth = 315  # Solar azimuth angle (clockwise from North) in degrees
sun_elevation = 45  # Solar vertical angle (above the horizon) in degrees
hillshade_arr = rvt.vis.hillshade(dem=dem_arr, resolution_x=dem_res_x, resolution_y=dem_
↪res_y,
                                  sun_azimuth=sun_azimuth, sun_elevation=sun_elevation,␣
↪ve_factor=1)

plt.imshow(hillshade_arr, cmap='gray')
```

[6]:
```
<matplotlib.image.AxesImage at 0x1923cebfbc8>
```

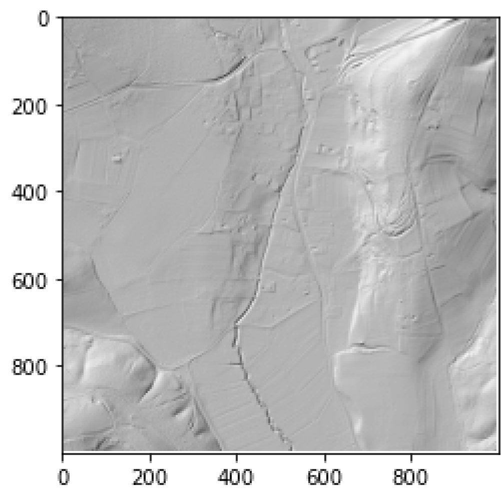

[7]:
```
hillshade_path = r"../test_data/TM1_564_146_hillshade.tif"
rvt.default.save_raster(src_raster_path=dem_path, out_raster_path=hillshade_path, out_
↪raster_arr=hillshade_arr, no_data=np.nan,
                        e_type=6)
```

Multiple direction hillshade

To calculate a multiple direction hillshade use the rvt.vis.multi_hillshade() function.

This function takes the parameters:

- dem
- resolution_x
- resolution_y
- nr_directions
- sun_elevation
- ve_factor

- no_data

This function ouputs a 3D numpy array, where the first dimension represents each direction (nr_directions), e.g. arr[0] is the first direction.To calculate multiple directions hillshade use rvt.vis.multi_hillshade() function. Parameters are: dem, resolution_x, resolution_y, nr_directions, sun_elevation, ve_factor, no_data. Function ouputs 3D numpy array (where first dimension represents each direction (nr_directions), for example arr[0] is first direction).

[8]:
```
nr_directions = 16  # Number of solar azimuth angles (clockwise from North) (number of␣
↪directions, number of bands)
sun_elevation = 45  # Solar vertical angle (above the horizon) in degrees
multi_hillshade_arr = rvt.vis.multi_hillshade(dem=dem_arr, resolution_x=dem_res_x,␣
↪resolution_y=dem_res_y,
                                              nr_directions=nr_directions, sun_
↪elevation=sun_elevation, ve_factor=1,
                                              no_data=dem_no_data)

plt.imshow(multi_hillshade_arr[0], cmap='gray')  # plot first direction where solar␣
↪azimuth = 22.5 (360/16=22.5)
```

[8]:
```
<matplotlib.image.AxesImage at 0x1923d3221c8>
```

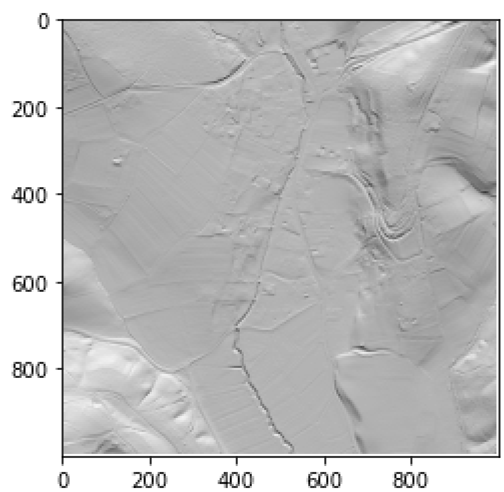

When saving multiple direction hillshade array, each direction (solar azimuth) will be saved in one band.

[9]:
```
multi_hillshade_path = r"../test_data/TM1_564_146_multi_hillshade.tif"
rvt.default.save_raster(src_raster_path=dem_path, out_raster_path=multi_hillshade_path,␣
↪out_raster_arr=multi_hillshade_arr,
                        no_data=np.nan, e_type=6)
```

Simple Local Relief Model (SLRM)

To calculate a Simple Local Relief Model (SLRM) use the rvt.vis.slrm() function.

This function takes the parameters:

- dem
- radius_cell
- ve_factor

- no_data.

This function returns a numpy array of the SLRM.

[10]:
```
radius_cell = 15  # radius to consider in pixels (not in meters)
slrm_arr = rvt.vis.slrm(dem=dem_arr, radius_cell=radius_cell, ve_factor=1, no_data=dem_
↪no_data)

plt.imshow(slrm_arr, cmap='gray')
```

[10]:
```
<matplotlib.image.AxesImage at 0x1923db59308>
```

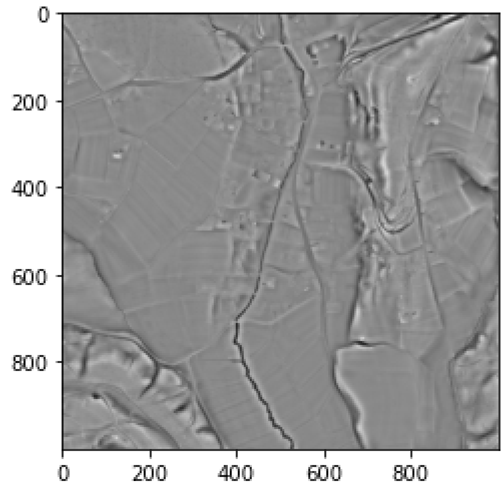

[11]:
```
slrm_path = r"../test_data/TM1_564_146_slrm.tif"
rvt.default.save_raster(src_raster_path=dem_path, out_raster_path=slrm_path, out_raster_
↪arr=slrm_arr,
                        no_data=np.nan, e_type=6)
```

Multi-Scale Relief Model (MSRM)

To calculate a Multi-Scale Relief Model (MSRM) use the rvt.vis.msrm() function.

This function takes the parameters:

- dem
- resolution
- feature_min
- feature_max
- scaling_factor
- ve_factor
- no_data.

This function returns a numpy array of the MSRM.

[12]:
```
feature_min = 1  # minimum size of the feature you want to detect in meters
feature_max = 5  # maximum size of the feature you want to detect in meters
```

(continues on next page)

(continued from previous page)

```
scaling_factor = 3  # scaling factor
msrm_arr = rvt.vis.msrm(dem=dem_arr, resolution=dem_res_x, feature_min=feature_min,␣
↪feature_max=feature_max,
                        scaling_factor=scaling_factor, ve_factor=1, no_data=dem_no_data)

plt.imshow(msrm_arr, cmap='gray')
```

[12]:
```
<matplotlib.image.AxesImage at 0x1923dbbaf88>
```

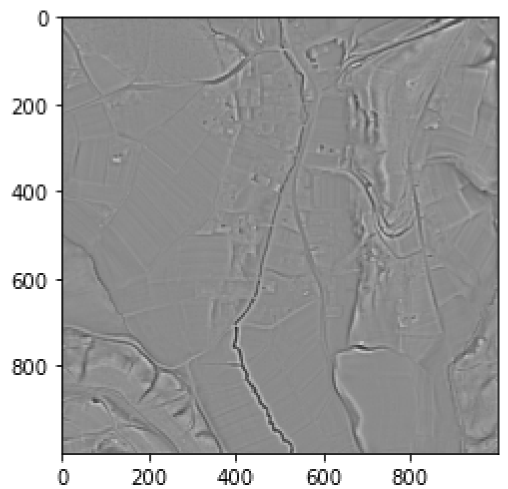

[13]:
```
msrm_path = r"../test_data/TM1_564_146_msrm.tif"
rvt.default.save_raster(src_raster_path=dem_path, out_raster_path=msrm_path, out_raster_
↪arr=msrm_arr,
                        no_data=np.nan, e_type=6)
```

Sky-view factor, anisotropic sky-view factor & positive openness

Sky-view factor, anisotropic sky-view factor and positive openness are all calculated with the same function: rvt.vis.sky_view_factor().

This function takes the parameters:

- dem
- resolution
- compute_svf (bool, if true it computes sky-view factor)
- compute_asvf (bool, if true it computes anisotropic svf)
- copmute_opns (bool, if true it computes positive openness)
- svf_n_dir (number of directions)
- svf_r_max (maximal search radius in pixels)
- svf_noise (level of noise remove (0-don't remove, 1-low, 2-med, 3-high))
- asvf_level (level of anisotropy, 1-low, 2-high)
- asvf_dir (direction of anisotropy), ve_factor, no_data.

This function outputs a dictionary with the keys:

- "svf" (if copute_svf is true)
- "asvf" (if copute_asvf is true)
- "opns" (if copute_opns is true)

Each key contains a numpy array of the visualization.

[14]:
```
# svf, sky-view factor parameters which also applies to asvf and opns
svf_n_dir = 16  # number of directions
svf_r_max = 10  # max search radius in pixels
svf_noise = 0  # level of noise remove (0-don't remove, 1-low, 2-med, 3-high)
# asvf, anisotropic svf parameters
asvf_level = 1  # level of anisotropy (1-low, 2-high)
asvf_dir = 315  # dirction of anisotropy in degrees
dict_svf = rvt.vis.sky_view_factor(dem=dem_arr, resolution=dem_res_x, compute_svf=True,␣
↪compute_asvf=True, compute_opns=True,
                                   svf_n_dir=svf_n_dir, svf_r_max=svf_r_max, svf_
↪noise=svf_noise,
                                   asvf_level=asvf_level, asvf_dir=asvf_dir,
                                   no_data=dem_no_data)
svf_arr = dict_svf["svf"]  # sky-view factor
asvf_arr = dict_svf["asvf"]  # anisotropic sky-view factor
opns_arr = dict_svf["opns"]  # positive openness
```

[15]:
```
plt.imshow(svf_arr, cmap='gray')
```

[15]:
```
<matplotlib.image.AxesImage at 0x1923dc318c8>
```

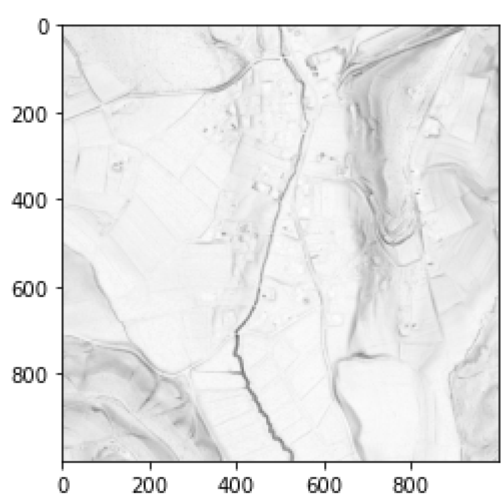

[16]:
```
plt.imshow(asvf_arr, cmap='gray')
```

[16]:
```
<matplotlib.image.AxesImage at 0x1923dca7488>
```

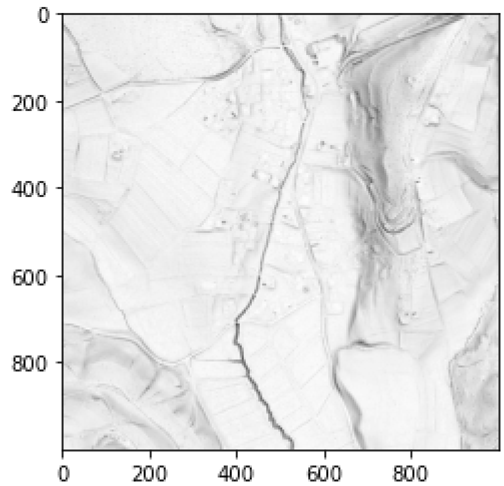

[17]:
```
plt.imshow(opns_arr, cmap="gray")
```

[17]: <matplotlib.image.AxesImage at 0x1923dd16cc8>

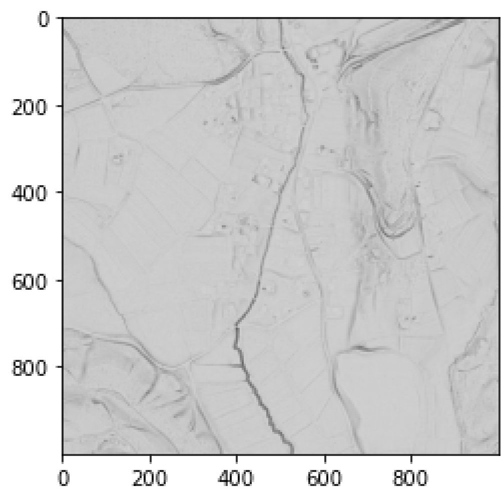

To save:

[18]:
```
svf_path = r"../test_data/TM1_564_146_svf.tif"
rvt.default.save_raster(src_raster_path=dem_path, out_raster_path=svf_path, out_raster_
↪arr=svf_arr,
                        no_data=np.nan, e_type=6)
asvf_path = r"../test_data/TM1_564_146_asvf.tif"
rvt.default.save_raster(src_raster_path=dem_path, out_raster_path=asvf_path, out_raster_
↪arr=asvf_arr,
                        no_data=np.nan, e_type=6)
opns_path = r"../test_data/TM1_564_146_pos_opns.tif"
rvt.default.save_raster(src_raster_path=dem_path, out_raster_path=opns_path, out_raster_
↪arr=opns_arr,
                        no_data=np.nan, e_type=6)
```

Negative openness

Negative openness is calculated the same as postive openness, but we have to multiply the input DEM by -1.

[19]:
```
# svf, sky-view factor parameters which also applies to asvf and opns
svf_n_dir = 16  # number of directions
svf_r_max = 10  # max search radius in pixels
svf_noise = 0  # level of noise remove (0-don't remove, 1-low, 2-med, 3-high)
dem_arr_neg_opns = dem_arr * -1  # dem * -1 for neg opns
# we don't need to calculate svf and asvf (compute_svf=False, compute_asvf=False)
dict_svf = rvt.vis.sky_view_factor(dem=dem_arr_neg_opns, resolution=dem_res_x, compute_
↪svf=False, compute_asvf=False, compute_opns=True,
                                   svf_n_dir=svf_n_dir, svf_r_max=svf_r_max, svf_
↪noise=svf_noise,
                                   no_data=dem_no_data)
neg_opns_arr = dict_svf["opns"]

plt.imshow(neg_opns_arr, cmap='gray')
```

[19]:
```
<matplotlib.image.AxesImage at 0x1924343f308>
```

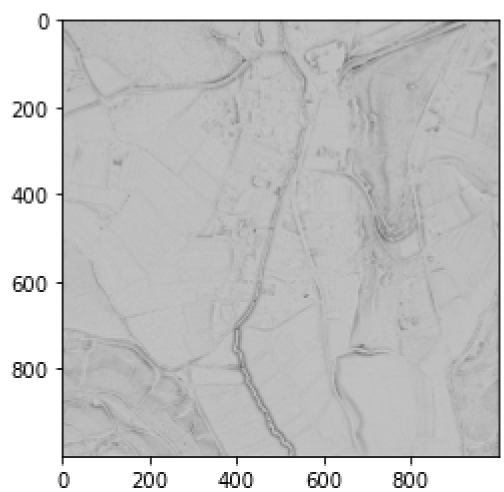

[20]:
```
neg_opns_path = r"../test_data/TM1_564_146_neg_opns.tif"
rvt.default.save_raster(src_raster_path=dem_path, out_raster_path=neg_opns_path, out_
↪raster_arr=neg_opns_arr,
                        no_data=np.nan, e_type=6)
```

Local dominance

To calculate local dominance use the rvt.vis.local_dominance() function.

This function takes the parameters:

- dem
- min_rad (minimum radial distance (in pixels) at which the algorithm starts with visualization computation)
- max_rad (maximum radial distance (in pixels) at which the algorithm starts with visualization computation)
- rad_inc (radial distance steps in pixels)

- angular_res (angular step for determination of number of angular directions)
- observer_height (height at which we observe the terrain)
- ve_factor
- no_data.

This function outputs a numpy array of local dominance.

[21]:
```
min_rad = 10  # minimum radial distance
max_rad = 20  # maximum radial distance
rad_inc = 1  # radial distance steps in pixels
angular_res = 15 # angular step for determination of number of angular directions
observer_height = 1.7  # height at which we observe the terrain
local_dom_arr = rvt.vis.local_dominance(dem=dem_arr, min_rad=min_rad, max_rad=max_rad,␣
↪rad_inc=rad_inc, angular_res=angular_res,
                                       observer_height=observer_height, ve_factor=1,
                                       no_data=dem_no_data)

plt.imshow(local_dom_arr, cmap='gray')
```

[21]:
```
<matplotlib.image.AxesImage at 0x192434a0dc8>
```

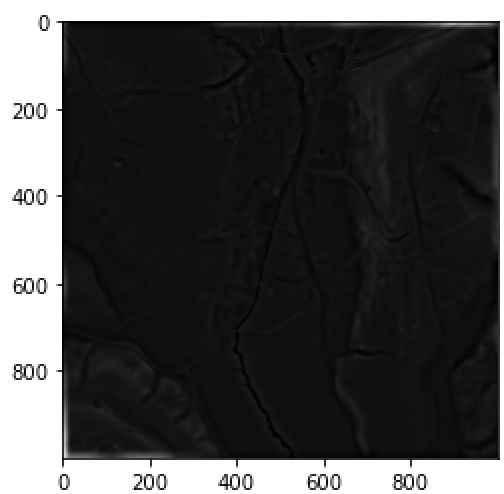

[22]:
```
local_dom_path = r"../test_data/TM1_564_146_local_dominance.tif"
rvt.default.save_raster(src_raster_path=dem_path, out_raster_path=local_dom_path, out_
↪raster_arr=local_dom_arr,
                        no_data=np.nan, e_type=6)
```

Sky illumination

To calculate sky illumination use the rvt.vis.sky_illumination() function.

This function takes the parameters:

- dem
- resolution
- sky_model ("overcast" or "uniform")

- compute_shadow (boolean if true it adds shadow)
- max_fine_radius (max shadow modeling distance in pixels)
- num_directions (number of directions to search for horizon)
- shadow_az (shadow azimuth if copute_shadow is true)
- shadow_el (shadow elevation if compute_shadow is true)
- ve_factor
- no_data.

This function outputs the numpy array of sky illumination.

[23]:
```
sky_model = "overcast"  # could also be uniform
max_fine_radius = 100
num_directions = 32
compute_shadow = True
shadow_az = 315
shadow_el = 35
sky_illum_arr = rvt.vis.sky_illumination(dem=dem_arr, resolution=dem_res_x, sky_
↪model=sky_model,
                                         max_fine_radius=max_fine_radius, num_
↪directions=num_directions,
                                         shadow_az=shadow_az, shadow_el=shadow_el, ve_
↪factor=1,
                                         no_data=dem_no_data)

plt.imshow(sky_illum_arr, cmap='gray')
```

[23]:
```
<matplotlib.image.AxesImage at 0x192435189c8>
```

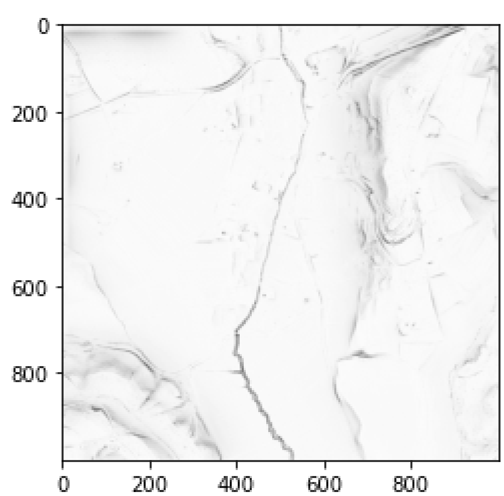

[24]:
```
sky_illum_path = r"../test_data/TM1_564_146_sky_illumination.tif"
rvt.default.save_raster(src_raster_path=dem_path, out_raster_path=sky_illum_path, out_
↪raster_arr=sky_illum_arr,
                        no_data=np.nan, e_type=6)
```

Multi-Scale Topographic Position (MSTP)

To calculate Multi-Scale Topographic Position (MSTP) use the rvt.vis.mstp() function.

This function takes the parameters: - dem - local_scale (tuple where first element is local scale min, second is local scale max and third is local scale step) - meso scale (tuple of min, max, step for meso scale) - broad scale (tuple of min, max, step for broad scale) - lightness (parameter to control visualization lightness) - ve_factor - no_data

This function outputs a 3D RGB 8bit numpy array of MSTP.

[25]:
```
local_scale=(1, 5, 1)  # min, max, step
meso_scale=(5, 50, 5)  # min, max, step
broad_scale=(50, 500, 50)  # min, max, step
lightness=1.2  # best results from 0.8 to 1.6
mstp_arr = rvt.vis.mstp(dem=dem_arr, local_scale=local_scale, meso_scale=meso_scale,
                        broad_scale=broad_scale, lightness=lightness, ve_factor=1, no_
↪data=dem_no_data)

# to show image in matplotlib we have to normalize visualization and rearrange it
# import blend_func modulte which contain function for noramlization
import rvt.blend_func
# normalize visualization from 0-255 to 0-1
mstp_floar_arr = rvt.blend_func.normalize_lin(image=mstp_arr, minimum=0, maximum=255)
# rearrange visualization from np.array([r, g, b]) to form that is supported by␣
↪matplotlib and display it
plt.imshow(np.dstack((mstp_floar_arr[0],mstp_floar_arr[1],mstp_floar_arr[2])))
```

[25]:
```
<matplotlib.image.AxesImage at 0x1924359db88>
```

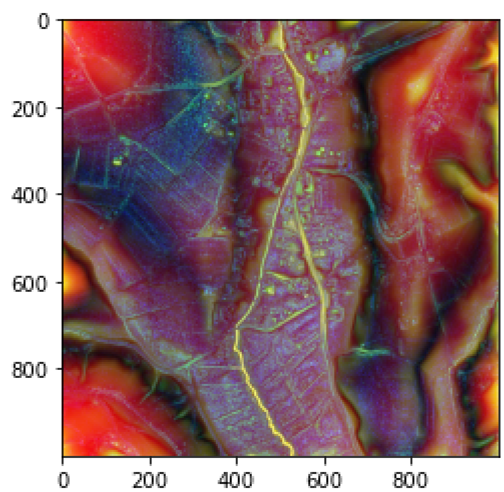

[26]:
```
mstp_path = r"../test_data/TM1_564_146_MSTP.tif"
rvt.default.save_raster(src_raster_path=dem_path, out_raster_path=mstp_path, out_raster_
↪arr=mstp_arr,
                        no_data=np.nan, e_type=1)  # e_type has to be 1 because␣
↪visualization is 8-bit (0-255)
```

6.7.2 RVT default module

This example notebook shows how the rvt.default module can quickly calculate or save any rvt visualization.

This notebook is suitable for beginner python users.

Before you start

You'll need a DEM to work through this notebook.

Download the test data from Getting started, or have some of your own data ready to work with.

Save your data in a directory called test_data. You'll need to set a path to this test data in cell [2].

Working with visualization parameters

To calculate a visualization we need to use visualization parameters (e.g. hillshade sun azimuth).

The default module has the rvt.default.DefultValues() class. All visualization parameters are stored as **attributes** of this class.

This class also contains **methods** to calculate the numpy array of a specific visualization, or to calculate and save a specific visualization as a GeoTIFF. All methods use class atributes (or set parameters).

For **get** methods we need the DEM numpy array, for **save** methods we need the DEM path.

If you call a save method for a specific visualization (e.g. default.save_hillshade()) it will be saved in the DEM directory (dem_path). To change the output directory, input the output directory as a string in custom_dir (save methods parameter).

Save methods also have two boolean parameters: save_float and save_8bit. If save_float is True, the method will save the visulization as float. If save_8bit is True, the method will bytescale visualization (0-255) and save it. Both can be True, if you want to save both.

Ok, let's import the required modules:

[1]:
```
import matplotlib.pyplot as plt
import rvt.default
```

To get the visualization array we need to input the DEM numpy array.

We will use the default module function get_raster_arr() to read it.

[2]:
```
dem_path = r"../test_data/TM1_564_146.tif"  # set path to your dem
```

[3]:
```
dict_dem = rvt.default.get_raster_arr(dem_path)
```

[4]:
```
dem_arr = dict_dem["array"]  # numpy array of DEM
dem_resolution = dict_dem["resolution"]
dem_res_x = dem_resolution[0]  # resolution in X direction
dem_res_y = dem_resolution[1]  # resolution in Y direction
dem_no_data = dict_dem["no_data"]

plt.imshow(dem_arr, cmap='gray')  # show DEM
```

[4]: <matplotlib.image.AxesImage at 0x17d9c68c888>

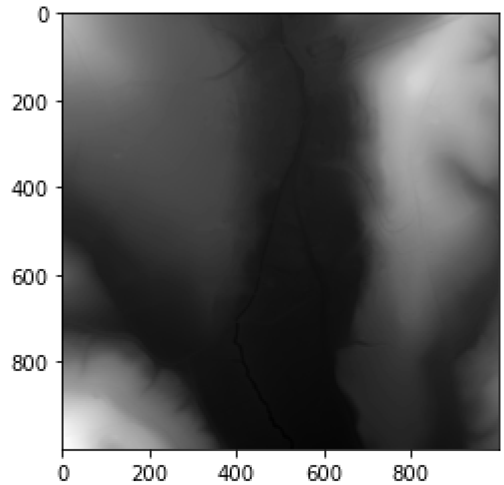

Create rvt.default.DefaultValues() class:

[5]:
```
default = rvt.default.DefaultValues()  # we created instance of class and stored it in␣
↪default variable
```

Slope

Set parameters:

[6]:
```
default.slp_output_units = "degree"
```

Calculate numpy array:

[7]:
```
slope_arr = default.get_slope(dem_arr=dem_arr, resolution_x=dem_res_x, resolution_y=dem_
↪res_y)
plt.imshow(slope_arr, cmap='gray')
```

[7]: <matplotlib.image.AxesImage at 0x17d9d656c08>

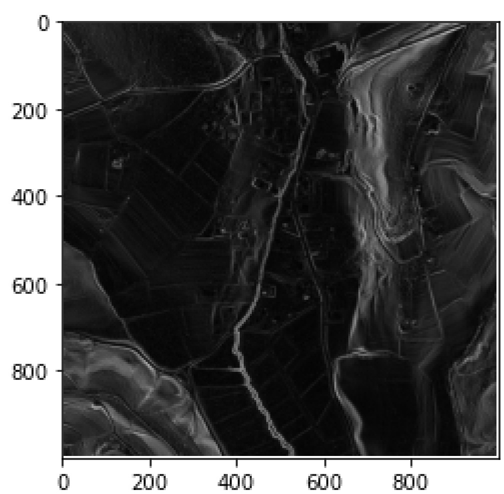

Calculate and save as GeoTIFF in DEM directory:

```
[8]: default.save_slope(dem_path=dem_path, custom_dir=None, save_float=True, save_8bit=True)
```

```
[8]: 1
```

Hillshade

Set parameters:

```
[9]: default.hs_sun_el = 35
     default.hs_sun_azi = 315
```

Calculate numpy array:

```
[10]: hillshade_arr = default.get_hillshade(dem_arr=dem_arr, resolution_x=dem_res_x,␣
      ↪resolution_y=dem_res_y)
      plt.imshow(hillshade_arr, cmap='gray')
```

```
[10]: <matplotlib.image.AxesImage at 0x17d9dacb988>
```

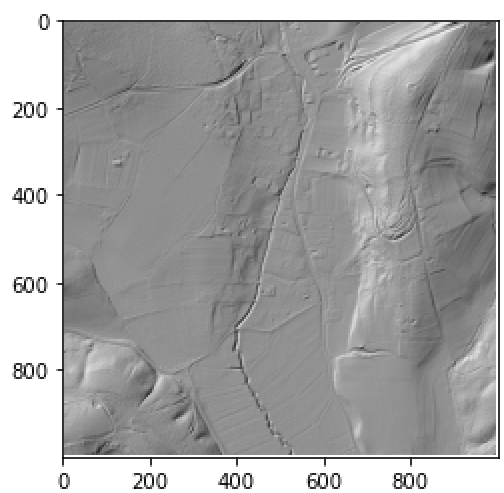

Calculate and save as GeoTIFF in DEM directory:

```
[11]: default.save_hillshade(dem_path=dem_path, custom_dir=None, save_float=True, save_
      ↪8bit=True)
```

```
[11]: 1
```

Multiple directions hillshade

Set parameters:

```
[12]: default.mhs_nr_dir = 16
      default.mhs_sun_el = 35
```

Calculate numpy array:

[13]:
```
mhs_arr = default.get_multi_hillshade(dem_arr=dem_arr, resolution_x=dem_res_x,␣
↪resolution_y=dem_res_y)
```

Calculate and save as GeoTIFF in DEM directory:

[14]:
```
default.save_multi_hillshade(dem_path=dem_path, custom_dir=None, save_float=True, save_
↪8bit=True)
```

[14]:
```
1
```

Simple Local Relief Model (SLRM)

Set parameters:

[15]:
```
default.slrm_rad_cell = 20
```

Calculate numpy array:

[16]:
```
slrm_arr = default.get_slrm(dem_arr=dem_arr)
plt.imshow(slrm_arr, cmap='gray')
```

[16]:
```
<matplotlib.image.AxesImage at 0x17d9e2f6808>
```

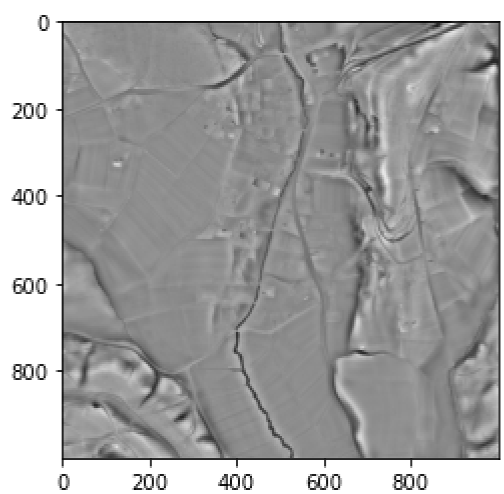

Calculate and save as GeoTIFF in DEM directory:

[17]:
```
default.save_slrm(dem_path=dem_path, custom_dir=None, save_float=True, save_8bit=True)
```

[17]:
```
1
```

Multi-Scale Relief Model (MSRM)

Set parameters:

[18]:
```
default.msrm_feature_min = 1
default.msrm_feature_max = 5
default.msrm_scaling_factor = 3
```

Calculate numpy array:

[19]:
```
msrm_arr = default.get_msrm(dem_arr=dem_arr, resolution=dem_res_x)
plt.imshow(msrm_arr, cmap='gray')
```

[19]:
```
<matplotlib.image.AxesImage at 0x17d9e74b688>
```

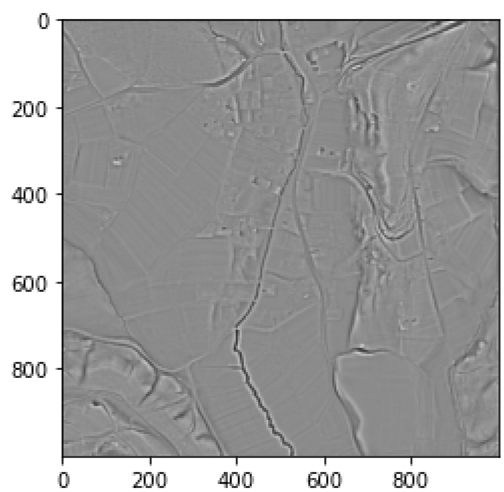

Calculate and save as GeoTIFF in DEM directory:

[20]:
```
default.save_msrm(dem_path=dem_path, custom_dir=None, save_float=True, save_8bit=True)
```

[20]:
```
1
```

Sky-view factor, Anisotropic sky-view factor, Positive openness

Set parameters:

[21]:
```
# parameters for all three
default.svf_n_dir = 16
default.svf_r_max = 10
default.svf_noise = 0
# parameters for asvf
default.asvf_dir = 315
default.asvf_level = 1
```

Calculate numpy array:

[22]:
```
svf_asvf_opns_dict = default.get_sky_view_factor(dem_arr=dem_arr, resolution=dem_res_x,
                                                  compute_svf=True, compute_asvf=True,
↪compute_opns=True)
```

[23]:
```
svf_arr = svf_asvf_opns_dict["svf"]
plt.imshow(svf_arr, cmap='gray')
```

[23]:
```
<matplotlib.image.AxesImage at 0x17d9e7d0ac8>
```

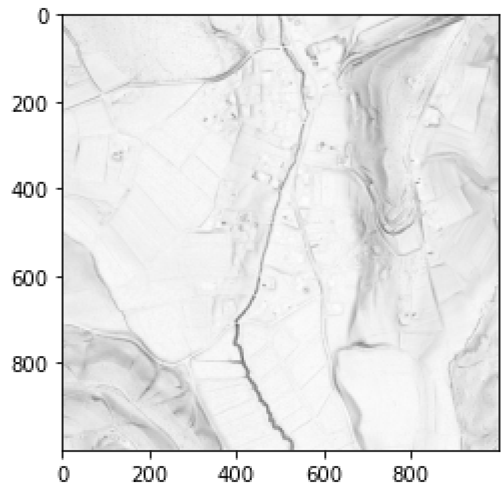

[24]:
```
asvf_arr = svf_asvf_opns_dict["asvf"]
plt.imshow(asvf_arr, cmap='gray')
```

[24]:
```
<matplotlib.image.AxesImage at 0x17d9e8334c8>
```

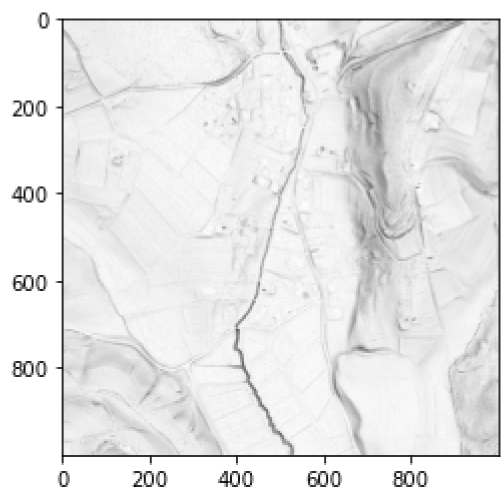

[25]:
```
opns_arr = svf_asvf_opns_dict["opns"]
plt.imshow(opns_arr, cmap='gray')
```

[25]:
```
<matplotlib.image.AxesImage at 0x17d9e8b4a08>
```

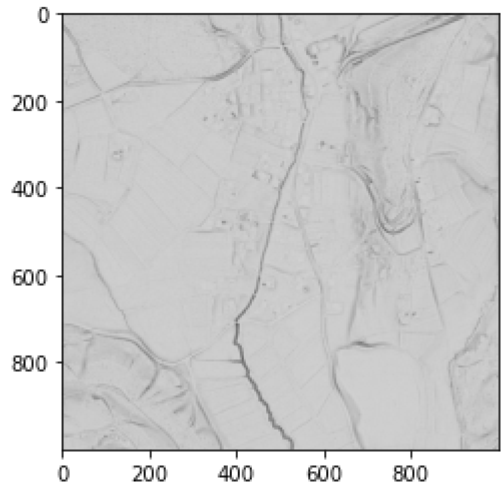

Calculate and save as GeoTIFF in DEM directory:

[26]:
```
default.save_sky_view_factor(dem_path=dem_path, save_svf=True, save_asvf=True, save_
↪opns=True,
                             custom_dir=None, save_float=True, save_8bit=True)
```

[26]:
```
1
```

Negative openness

Set parameters (svf_parameters):

[27]:
```
default.svf_n_dir = 16
default.svf_r_max = 10
default.svf_noise = 0
```

Calculate numpy array:

[28]:
```
neg_opns_arr = default.get_neg_opns(dem_arr=dem_arr, resolution=dem_res_x)
plt.imshow(neg_opns_arr, cmap='gray')
```

[28]:
```
<matplotlib.image.AxesImage at 0x17d9e91d1c8>
```

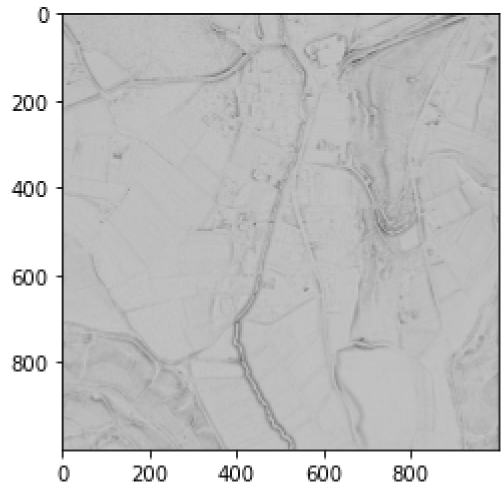

Calculate and save as GeoTIFF in DEM directory:

[29]:
```
default.save_neg_opns(dem_path=dem_path, custom_dir=None, save_float=True, save_
↪8bit=True)
```

[29]: 1

Local dominance

Set parameters:

[30]:
```
default.ld_min_rad = 10
default.ld_max_rad = 20
default.ld_rad_inc = 1
default.ld_anglr_res = 15
default.ld_observer_h = 1.7
```

Calculate numpy array:

[31]:
```
local_dom_arr = default.get_local_dominance(dem_arr=dem_arr)
plt.imshow(local_dom_arr, cmap='gray')
```

[31]: <matplotlib.image.AxesImage at 0x17da0cd0f88>

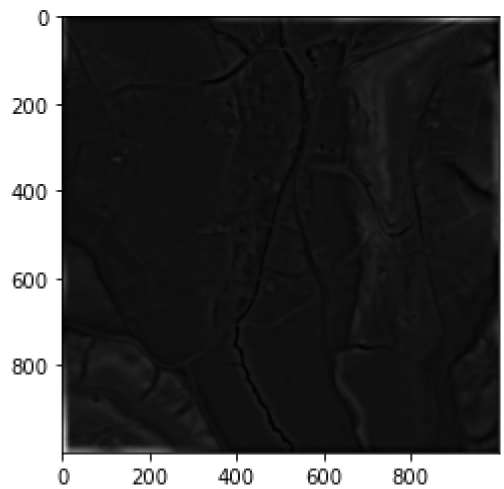

Calculate and save as GeoTIFF in DEM directory:

[32]:
```
default.save_local_dominance(dem_path=dem_path, custom_dir=None, save_float=True, save_
↪8bit=True)
```

[32]:
```
1
```

Sky illumination

Set parameters:

[33]:
```
default.sim_sky_mod = "overcast"
default.sim_compute_shadow = 0
default.sim_shadow_dist = 100
default.sim_nr_dir = 32
default.sim_shadow_az = 315
default.sim_shadow_el = 35
```

Calculate numpy array:

[34]:
```
sky_illum_arr = default.get_sky_illumination(dem_arr=dem_arr, resolution=dem_res_x)
plt.imshow(sky_illum_arr, cmap='gray')
```

[34]:
```
<matplotlib.image.AxesImage at 0x17da0f84e88>
```

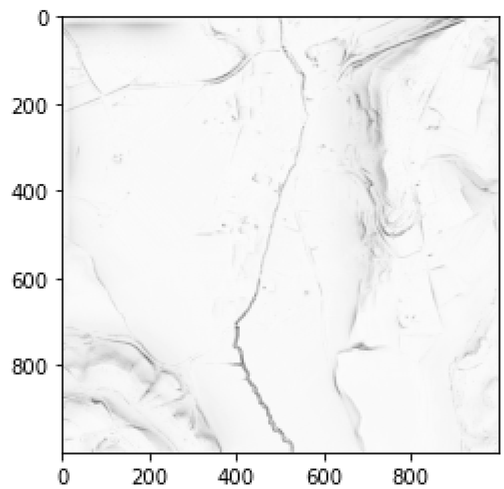

Calculate and save as GeoTIFF in DEM directory:

[35]:
```
default.save_sky_illumination(dem_path=dem_path, custom_dir=None, save_float=True, save_
↪8bit=True)
```

[35]: 1

Multi-Scale Topographic Position (MSTP)

Set parameters:

[36]:
```
default.mstp_local_scale = (1, 5, 1)
default.mstp_meso_scale = (5, 50, 5)
default.mstp_broad_scale = (50, 500, 50)
default.mstp_lightness = 1.2
```

Calculate numpy array:

[37]:
```
mstp_arr = default.get_mstp(dem_arr=dem_arr)
```

Calculate and save as GeoTIFF in DEM directory:

[38]:
```
default.save_mstp(dem_path=dem_path, custom_dir=None)
```

[38]: 1

6.8 Release history

6.8.1 Python package release history

UNRELEASED

2.2.1

- Fixed bug in blending.

RELEASE

May 23, 2023

2.2.0

- Added 1 pixel edge padding before the calculation of hillshade and slope, to avoid no data edge in the final results.
- Added float option for MSTP visualization.
- Changed default parameters of MSTP visualization.
- Changed nodata handling when calculating slope visualization. When calculating slope in the specific pixel if any of neighbour pixels are nodata use middle value in the calculation instead.

RELEASE

May 22, 2023

2.1.0

- Changed 8bit (bytescale) parameters of some visualizations (all changed to value mode, to avoid tiling effect when using tile module).
- Float to 8bit bug fix.

RELEASE

March 6, 2022

2.0.0

- Module multiproc.py replaced with tile.py.

RELEASE

February 5, 2022

1.0.0

- Added soft light blending mode.
- Added Color Relief Image Map (CRIM) blending combination visualization.
- Added enhance Multi-Scale Topographic Position (e3MSTP) blending combination visualization.
- Fixed luminosity blending bug.
- Fixed summed area table algorithm (used in SLRM, MSRM, MSTP) no data bug.

RELEASE

September 14, 2021

1.0.0a11

- Blending with Multiple directions hillshade bug fixed. Now MHS 8-bit is used.
- Fixed SVF, ASVF, OPNS file name, added noise remove parameter in the output name.

PRE-RELEASE

May 20, 2021

1.0.0a10

- Added fill no data methods (IDW, Nearest neighbor, K-D Tree)
- Fixed Negative Openness 8bit image (reverted colors).
- Added Multi-scale topographic position (MSTP)

PRE-RELEASE

Apr 16, 2021

1.0.0a9

PRE-RELEASE

Mar 9, 2021

1.0.0a8

PRE-RELEASE

Jan 29, 2021

1.0.0a7

PRE-RELEASE

Jan 19, 2021

1.0.0a6

PRE-RELEASE

Jan 11, 2021

1.0.0a5

PRE-RELEASE

Jan 10, 2021

1.0.0a4

PRE-RELEASE

Jan 8, 2021

1.0.0a3

PRE-RELEASE

Jan 8, 2021

1.0.0a2

PRE-RELEASE

Jan 8, 2021

1.0.0a1

PRE-RELEASE

Jan 8, 2021

6.8.2 QGIS plugin release history

v0.9.6

- Use rvt-py v2.2.1.

v0.9.5

- Use rvt-py v2.2.0.

v0.9.4

- Fixed paths to processing functions.

v0.9.3

- Added MSTP float and 8bit option.

v0.9.2

- Try to install scipy if it doesn't exist.
- Added processing functions for filling no-data.

v0.9.1

- Added 1 pixel edge padding before the calculation of hillshade and slope, to avoid no data edge in the final results.

v0.9.0

- Added tiling module, visualizations on huge rasters are now calculated tile by tile.
- Changed bytescale to 8bit parameters of all the visualizations to value mode (value ranges are different on each tile, this is why percent mode is not suitable).

v0.8.1

- Hillshade negative values set to 0.
- Changed vertical exaggeration factor limit from [-1000, 1000] to [-10000, 10000].

v0.8.0

- Luminosity blending bug fix.
- Added soft light blending mode.
- Added enhanced Multi-Scale Topographic Position (e3MSTP).
- Fixed summed area table (used in MSTP, SLRM, MSRM) bug when DEM contains nodata.
- Removed fill no-data option from visualizations (is still available under Other tab).

v0.7.1

- Buttons "Select all" and "Select none" to select/deselect all DEMs.

v0.7.0

- Enabled qgis_process command line utility.

v0.6.4

- Blending with Multiple directions hillshade bug fixed. Now MHS 8-bit is used.
- Fixed SVF, ASVF, OPNS file name, added noise remove parameter in the output name.
- Added Multi-scale topographic position (MSTP) processing algorithm (function).

v0.6.3

- Negative-Openness 8bit reversed colors bug fix.
- Added Multi-scale topographic position (MSTP) visualization.

v0.6.2.1

- Changed RVT QGIS plugin documentation link in About.

v0.6.2

- Added fill no-data methods (Inverse Distance Weighting, K-D Tree, Nearest Neighbour).

v0.6.1

- Multi-scale relief model fixed and added back. Sky illumination is still not working as it should (will be fixed soon). Read the Docs sites (RVT python library rvt_py, RVT QGIS plugin, RVT ArcGIS raster fn) were merged into one.

v0.5.3

- Multi-scale relief model and Sky illumination visualizations temporarily removed, because they don't work as they should. They will be fixed soon.

v0.5.2

- 8-bit no data values changed from 0 to 255 (white).
- Added from osgeo import gdal to default module.

v0.5.1

- Blender tab Blend images button position changed.

v0.5.0

- Added Other tab where you can cut-off raster values, normalize raster and change raster to 8 bit.
- Plugin saves all output raster files as LZW compressed GeoTIFFs (previously it was saving without compression).

6.9 Bibliography

RVT has been used in a variety of applications, from archaeology to urban heat island modelling, landscape recognition and analysis, and ceramic imaging.

Here is a list of journal articles that originated from the Scopus database. If you have used RVT and your publication is not listed, please contact us.

BIBLIOGRAPHY

[1] D. Abate, M. Faka, C. Keleshis, C. Constantinides, A. Leonidou, and A. Papageorgiou. Aerial image-based documentation and monitoring of illegal archaeological excavations. *Heritage*, 6(5):4302–4319, 2023. URL: https://www.scopus.com/inward/record.uri?eid=2-s2.0-85160320524&doi=10.3390%2fheritage6050228&partnerID=40&md5=67763b1331c3cae2d08ced4acc5f6e20, doi:10.3390/heritage6050228.

[2] J. Hollesen, M. S. Jepsen, and H. Harmsen. The application of rgb, multispectral, and thermal imagery to document and monitor archaeological sites in the arctic: a case study from south greenland. *Drones*, 2023. URL: https://www.scopus.com/inward/record.uri?eid=2-s2.0-85149152652&doi=10.3390%2fdrones7020115&partnerID=40&md5=4b0e0dad5645479f863d8481b053fded, doi:10.3390/drones7020115.

[3] J. Ikäheimo. Detecting pitfall systems in the suomenselkä watershed, finland, with airborne laser scanning and artificial intelligence. *Journal of Archaeological Science: Reports*, 2023. URL: https://www.scopus.com/inward/record.uri?eid=2-s2.0-85171758750&doi=10.1016%2fj.jasrep.2023.104216&partnerID=40&md5=3124991d43ebf217d1773ad2e7e09005, doi:10.1016/j.jasrep.2023.104216.

[4] I. Kadhim and F. M. Abed. A critical review of remote sensing approaches and deep learning techniques in archaeology. *Sensors*, 2023. URL: https://www.scopus.com/inward/record.uri?eid=2-s2.0-85151188371&doi=10.3390%2fs23062918&partnerID=40&md5=3cdefe50228f23505a5b252365d0a6eb, doi:10.3390/s23062918.

[5] I. Kadhim, F. M. Abed, J. M. Vilbig, V. Sagan, and C. DeSilvey. Combining remote sensing approaches for detecting marks of archaeological and demolished constructions in cahokia's grand plaza, southwestern illinois. *Remote Sensing*, 2023. URL: https://www.scopus.com/inward/record.uri?eid=2-s2.0-85149260920&doi=10.3390%2frs15041057&partnerID=40&md5=381b54b9da7a4c39ee67e3db349c785d, doi:10.3390/rs15041057.

[6] B. Kazimi and M. Sester. Self-supervised learning for semantic segmentation of archaeological monuments in dtms. *Journal of Computer Applications in Archaeology*, 6(1):155–173, 2023. URL: https://www.scopus.com/inward/record.uri?eid=2-s2.0-85179966569&doi=10.5334%2fjcaa.110&partnerID=40&md5=96f1b1aa02a0e05cd40bca52c3ceef24, doi:10.5334/jcaa.110.

[7] D. Kobiałka, M. Kostyrko, A. Lokś, K. Karski, V. Rezler-Wasielewska, P. Stanek, A. Wickiewicz, E. Góra, S. Tomczak, and M. Pawleta. “hell camp” hidden in the forest–the materiality of stalag viii b (344) lamsdorf. *Journal of Conflict Archaeology*, 2023. URL: https://www.scopus.com/inward/record.uri?eid=2-s2.0-85178203285&doi=10.1080%2f15740773.2023.2288959&partnerID=40&md5=7de4351c9ed2ae39d7b1645dfcc56de4, doi:10.1080/15740773.2023.2288959.

[8] M. H. Hofmann, N. W. Hinman, M. Phillips, M. McInenly, G. Chong-Diaz, K. Warren-Rhodes, and N. A. Cabrol. Gypsum-lined degassing holes in tumuli. *Earth Surface Processes and Landforms*, 2023. URL: https://www.scopus.com/inward/record.uri?eid=2-s2.0-85169690692&doi=10.1002%2fesp.5692&partnerID=40&md5=230488b7714b9c8c3e5548284f9386f0, doi:10.1002/esp.5692.

[9] D. Kobiałka, M. Pawleta, K. Karski, M. Kostyrko, A. Lokś, V. Rezler-Wasielewska, P. Stanek, A. Czerner, E. Góra, M. Michalski, S. Tomczak, Z. Kowalczyk, S. Ważyński, and P. Wroniecki. Camp archaeology at the site of national remembrance in Łambinowice (formerly lamsdorf), poland. *International Journal of Historical Archaeology*, 2023. URL: https://www.scopus.com/inward/record.uri?eid=2-s2.0-85159267534&doi=10.1007%

2fs10761-023-00700-y&partnerID=40&md5=e66649136a4fb1940e223b927a4a712e, doi:10.1007/s10761-023-00700-y.

[10] C. Koski, P. Kettunen, J. Poutanen, L. Zhu, and J. Oksanen. Mapping small watercourses from dems with deep learning—exploring the causes of false predictions. *Remote Sensing*, 2023. URL: https://www.scopus.com/inward/record.uri?eid=2-s2.0-85161605652&doi=10.3390%2frs15112776&partnerID=40&md5=a55f29f0bfef186cfcb96a25da78891b, doi:10.3390/rs15112776.

[11] A. Łabuz, N. Borowiec, and U. Marmol. Automatic detection of lusatian culture fortified settlement based on data from airborne laser scanning. *International Journal of Conservation Science*, 14(1):83–98, 2023. URL: https://www.scopus.com/inward/record.uri?eid=2-s2.0-85159812092&doi=10.36868%2fIJCS.2023.01.07&partnerID=40&md5=615a7d54810b489bebb1bfad773f4d3e, doi:10.36868/IJCS.2023.01.07.

[12] J. Lehner, P. Wernette, A. Smith, and C. Houser. Multi-dimensional approach for interpreting the structure of barrier island morphology. *Geomorphology*, 2024. URL: https://www.scopus.com/inward/record.uri?eid=2-s2.0-85180489539&doi=10.1016%2fj.geomorph.2023.109006&partnerID=40&md5=e5bef2db8542e7eee7933c102eccf240, doi:10.1016/j.geomorph.2023.109006.

[13] Z. Li. New opportunities for archaeological research in the greater ghingan range, china: application of uav lidar in the archaeological survey of the shenshan mountain. *Journal of Archaeological Science: Reports*, 2023. URL: https://www.scopus.com/inward/record.uri?eid=2-s2.0-85168536765&doi=10.1016%2fj.jasrep.2023.104182&partnerID=40&md5=34606d64485c3193caba948fcb5f9ef7, doi:10.1016/j.jasrep.2023.104182.

[14] Y. Liang, S. Cao, M. Du, L. Lu, J. Jiang, J. Quan, and M. Yang. Local climate zone mapping using remote sensing: a synergetic use of daytime multi-view ziyuan-3 stereo imageries and luojia-1 nighttime light data. *International Journal of Digital Earth*, 16(1):3456–3488, 2023. URL: https://www.scopus.com/inward/record.uri?eid=2-s2.0-85169549632&doi=10.1080%2f17538947.2023.2251437&partnerID=40&md5=9a759d0bf655810f4fc67d95850dbad2, doi:10.1080/17538947.2023.2251437.

[15] X. Zhong, L. Zhao, X. Zhang, J. Wang, H. Zhao, and P. Ren. Analysis of the adjacency effect on retrieval of land surface temperatures based on multimodal images from unmanned aerial vehicles. *URBAN CLIMATE*, 2023. URL: https://www.scopus.com/inward/record.uri?eid=2-s2.0-85169046528&doi=10.1016%2fj.uclim.2023.101664&partnerID=40&md5=1a83587e1d501c687789cdd3f38cdfff, doi:10.1016/j.uclim.2023.101664.

[16] Ž. Kokalj, S. Džeroski, I. Šprajc, J. Štajdohar, A. Draksler, and M. Somrak. Machine learning-ready remote sensing data for maya archaeology. *Scientific Data*, 2023. URL: https://www.scopus.com/inward/record.uri?eid=2-s2.0-85168596294&doi=10.1038%2fs41597-023-02455-x&partnerID=40&md5=019116c68e2a3bd254ae201fa52f05c2, doi:10.1038/s41597-023-02455-x.

[17] V. Yordanov, Q. X. Truong, and M. A. Brovelli. Estimating landslide surface displacement by combining low-cost uav setup, topographic visualization and computer vision techniques. *Drones*, 2023. URL: https://www.scopus.com/inward/record.uri?eid=2-s2.0-85149243740&doi=10.3390%2fdrones7020085&partnerID=40&md5=355b5e849d6d22fabb6f7be4c29f2d92, doi:10.3390/drones7020085.

[18] Z.-W. He and B.-H. Tang. Retrieval of rugged mountainous areas land surface temperature from high-spatial-resolution thermal infrared remote sensing data. *IEEE TRANSACTIONS ON GEOSCIENCE AND REMOTE SENSING*, 61:1–16, 2023. URL: https://www.scopus.com/inward/record.uri?eid=2-s2.0-85176787359&doi=10.1109%2fTGRS.2023.3316624&partnerID=40&md5=2faa62726c7f37d08dd13d4c34b760ec, doi:10.1109/TGRS.2023.3316624.

[19] L. Han, P. Duan, J. Liu, and J. Li. Research on landslide trace recognition by fusing uav-based lidar dem multi-feature information. *Remote Sensing*, 2023. URL: https://www.scopus.com/inward/record.uri?eid=2-s2.0-85174193640&doi=10.3390%2frs15194755&partnerID=40&md5=a44a623335873af2af92a0c621f104bc, doi:10.3390/rs15194755.

[20] J. Czerniec, K. Kozioł, M. Jankowski, P. Lewińska, C.A.G. Santos, and K. Maciuk. How to find the undiscovered? anthropogenic objects in forest areas: a critical assessment of current methods. *International Journal of Conservation Science*, 14(1):115–130, 2023. URL: https://www.scopus.com/

inward/record.uri?eid=2-s2.0-85159809487&doi=10.36868%2fIJCS.2023.01.09&partnerID=40&md5=37fe00372a1a3853dd104d512bfeb26f, doi:10.36868/IJCS.2023.01.09.

[21] L. Čapek and M. Chalánek. The deserted medieval village of zábdiší on the estate of Žebrák castle. *Archaeologia Historica*, 48(2):587–609, 2023. URL: https://www.scopus.com/inward/record.uri?eid=2-s2.0-85182893965&doi=10.5817%2fAH2023-2-13&partnerID=40&md5=dd2c9825365df9caeeff9468fecfa6f4, doi:10.5817/AH2023-2-13.

[22] C. A. Delaney, K. Adamson, L. D. Linch, S. Davis, and S. McCarron. Reconstructing terrestrial ice sheet retreat dynamics from hummocky topography using multiscale evidence: an example from central ireland. *Quaternary Science Reviews*, 2023. URL: https://www.scopus.com/inward/record.uri?eid=2-s2.0-85151661987&doi=10.1016%2fj.quascirev.2023.108041&partnerID=40&md5=cb589001bc69c77f7b50a0b5fd856ab3, doi:10.1016/j.quascirev.2023.108041.

[23] X. Dong, B. Deng, F. Yuan, X. Fu, W. Zhang, Y. Ju, and X. Ren. Application of aerial remote sensing in geological hazards: current situation and prospects. *Wuhan Daxue Xuebao (Xinxi Kexue Ban)/Geomatics and Information Science of Wuhan University*, 48(12):1897–1913, 2023. URL: https://www.scopus.com/inward/record.uri?eid=2-s2.0-85179888137&doi=10.13203%2fj.whugis20220151&partnerID=40&md5=8755e8b751d0f10ef243affa9587f3e6, doi:10.13203/j.whugis20220151.

[24] G. Dotta, A. Fornaciai, G. Bertolini, I. Isola, L. Nannipieri, M. Favalli, P. Burrato, R. Devoti, G. Gigli, L. Mucchi, E. Intrieri, M. Pizziolo, T. Gracchi, and N. Casagli. Geomorphology of the upper sector of the roncovetro active landslide (emilia-romagna region, italy). *Journal of Maps*, 19(1):1–11, 2023. URL: https://www.scopus.com/inward/record.uri?eid=2-s2.0-85177579012&doi=10.1080%2f17445647.2023.2277898&partnerID=40&md5=21ae25eccae8ff93a55d2d3d1d71b7de, doi:10.1080/17445647.2023.2277898.

[25] E. Draganits, B. Moshammer, G. Kremer, and M. Doneus. Geoarchaeological remote sensing prospection of miocene limestone quarries in the hinterland of roman carnuntum and vindobona(vienna basin, austria). *Austrian Journal of Earth Sciences*, 116(1):39–83, 2023. URL: https://www.scopus.com/inward/record.uri?eid=2-s2.0-85162077596&doi=10.17738%2fajes.2023.0003&partnerID=40&md5=bf4b471a5cfc1edf648829e6b30f3b71, doi:10.17738/ajes.2023.0003.

[26] D. Han, X. Xu, Z. Qiao, F. Wang, H. Cai, H. An, K. Jia, Y. Liu, Z. Sun, S. Wang, and W. Han. The roles of surrounding 2d/3d landscapes in park cooling effect: analysis from extreme hot and normal weather perspectives. *BUILDING AND ENVIRONMENT*, 2023. URL: https://www.scopus.com/inward/record.uri?eid=2-s2.0-85147191100&doi=10.1016%2fj.buildenv.2023.110053&partnerID=40&md5=d5c4a0a72b49903c9522915a048379dc, doi:10.1016/j.buildenv.2023.110053.

[27] Y. Fang, L. Zhao, B. Dou, Y. Li, and S. Wang. Circuit vrc: a circuit theory-based ventilation corridor model for mitigating the urban heat islands. *BUILDING AND ENVIRONMENT*, 2023. URL: https://www.scopus.com/inward/record.uri?eid=2-s2.0-85169575358&doi=10.1016%2fj.buildenv.2023.110786&partnerID=40&md5=f9874ce846220dd918f45a9798085818, doi:10.1016/j.buildenv.2023.110786.

[28] J. Fernández-Lozano, V. Turu, R. M. Carrasco, R. L. Soteres, J. Sánchez-Vizcaino, T. Karampaglidis, X. Ros, O. Merlo, and J. Pedraza. The mid-latitude hydrolaccolith of the spanish central system (southern europe): a top-to-bottom integration of geomatic, geophysical and sedimentary datasets for characterising a singular periglacial landform. *Land Degradation and Development*, 2023. URL: https://www.scopus.com/inward/record.uri?eid=2-s2.0-85178231575&doi=10.1002%2fldr.4968&partnerID=40&md5=29223185478a2c630f9d085e565760ca, doi:10.1002/ldr.4968.

[29] S. Field. Lidar-derived road profiles. *Advances in Archaeological Practice*, 11(2):184–197, 2023. URL: https://www.scopus.com/inward/record.uri?eid=2-s2.0-85162147550&doi=10.1017%2faap.2022.31&partnerID=40&md5=8679f98422931be787b3f8ff504442aa, doi:10.1017/aap.2022.31.

[30] J. Fonte, A. L. Rodrigues, M. I. Dias, D. Russo, T. D. Pereiro, J. Carvalho, S. Amorim, C. Jorge, P. Monteiro, C. Ferro-Vázquez, J. M. Costa-García, M. Gago, and I. Oltean. Reassessing roman military activity through an interdisciplinary approach: myth and archaeology in laboreiro mountain (northwestern iberia). *Journal of Archaeological Science: Reports*, 2023. URL: https://www.scopus.com/

inward/record.uri?eid=2-s2.0-85151638668&doi=10.1016%2fj.jasrep.2023.103993&partnerID=40&md5=caaebce3528a4c21cba6864b556fa86e, doi:10.1016/j.jasrep.2023.103993.

[31] Y. Mo, Z. Guo, R. Zhong, W. Song, and S. Cao. Urban functional zone classification using light-detection-and-ranging point clouds, aerial images, and point-of-interest data. *Remote Sensing*, 2024. URL: https://www.scopus.com/inward/record.uri?eid=2-s2.0-85183327352&doi=10.3390%2frs16020386&partnerID=40&md5=4a57673d9636a8abbf4cbb570bc6b91e, doi:10.3390/rs16020386.

[32] A. Ghosh and B. Bera. Landform classification and geomorphological mapping of the chota nagpur plateau, india. *Quaternary Science Advances*, 2023. URL: https://www.scopus.com/inward/record.uri?eid=2-s2.0-85151021095&doi=10.1016%2fj.qsa.2023.100082&partnerID=40&md5=8cc250a0d2064fb53144d0619c41c1e9, doi:10.1016/j.qsa.2023.100082.

[33] D. Han, H. An, H. Cai, F. Wang, X. Xu, Z. Qiao, K. Jia, Z. Sun, and Y. An. How do 2d/3d urban landscapes impact diurnal land surface temperature: insights from block scale and machine learning algorithms. *SUSTAINABLE CITIES AND SOCIETY*, 2023. URL: https://www.scopus.com/inward/record.uri?eid=2-s2.0-85171171735&doi=10.1016%2fj.scs.2023.104933&partnerID=40&md5=dee537370861226e36110848ae324e96, doi:10.1016/j.scs.2023.104933.

[34] R. C. Fernández, M. R. Velasco, I. H. Uceda, and J. Martínez-González. La marañosa-albende (san martín de la vega, madrid): late antique castled settlement and andalusian ḥiṣn. results of the application of lidar technology to archaeological prospection. *Cuadernos de Prehistoria y Arqueologia de la Universidad Autonoma de Madrid*, 49(2):241–261, 2023. URL: https://www.scopus.com/inward/record.uri?eid=2-s2.0-85182632782&doi=10.15366%2fCUPAUAM2023.49.2.009&partnerID=40&md5=ceb0e71ced57ebf59af589da9498f7d0, doi:10.15366/CUPAUAM2023.49.2.009.

[35] N. Crabb, C. Carey, A. J. Howard, and M. Brolly. Lidar visualization techniques for the construction of geoarchaeological deposit models: an overview and evaluation in alluvial environments. *Geoarchaeology*, 2023. URL: https://www.scopus.com/inward/record.uri?eid=2-s2.0-85150938546&doi=10.1002%2fgea.21959&partnerID=40&md5=00cadf145d7813860842de15be2534cb, doi:10.1002/gea.21959.

[36] J. S. Lim and G. J. Linares Matás. Dunes, death, and datasets: modelling funerary monument construction in remote arid landscapes using spaceborne stereo imagery. *Journal of Archaeological Science*, 2023. URL: https://www.scopus.com/inward/record.uri?eid=2-s2.0-85162139332&doi=10.1016%2fj.jas.2023.105815&partnerID=40&md5=f48fed450e7754fa38f078f5fa2a42b4, doi:10.1016/j.jas.2023.105815.

[37] Q. Xu, B. Zhao, K. Dai, X. Dong, W. Li, X. Zhu, Y. Yang, X. Xiao, X. Wang, J. Huang, H. Lu, B. Deng, and D. Ge. Remote sensing for landslide investigations: a progress report from china. *Engineering Geology*, 2023. URL: https://www.scopus.com/inward/record.uri?eid=2-s2.0-85159186201&doi=10.1016%2fj.enggeo.2023.107156&partnerID=40&md5=ed3a9da2477e86a42f5043a4c2c2fabb, doi:10.1016/j.enggeo.2023.107156.

[38] M. Sánchez-Fernández, L. Arenas-García, and J. A. Gutiérrez Gallego. Detection of construction and demolition illegal waste using photointerpretation of dem models of lidar data. *Land*, 2023. URL: https://www.scopus.com/inward/record.uri?eid=2-s2.0-85180689325&doi=10.3390%2fland12122119&partnerID=40&md5=9494553b4b11676e01d04fc5c4b7c23f, doi:10.3390/land12122119.

[39] C. Ru, S.-B. Duan, X.-G. Jiang, Z.-L. Li, C. Huang, and M. Liu. An extended sw-tes algorithm for land surface temperature and emissivity retrieval from ecostress thermal infrared data over urban areas. *REMOTE SENSING OF ENVIRONMENT*, 2023. URL: https://www.scopus.com/inward/record.uri?eid=2-s2.0-85150191258&doi=10.1016%2fj.rse.2023.113544&partnerID=40&md5=14db35da06fa7484119a81262023a6ed, doi:10.1016/j.rse.2023.113544.

[40] O. Risbøl, J.S.P. Eidshaug, H. B. Bjerck, M. M. Gran, K. R. Rantala, A. M. Tivoli, and A.F.J. Zangrando. Uav lidar in coastal environments: archaeological case studies from tierra del fuego, argentina, and vega, norway. *Archaeological Prospection*, 2023. URL: https://www.scopus.com/inward/record.uri?eid=2-s2.0-85176271512&doi=10.1002%2farp.1918&partnerID=40&md5=45a4fdf028b26214b67e2499a9ea41b9, doi:10.1002/arp.1918.

[41] A. M. Rekemová, R. Čambal, and I. Bazovský. Aplikácia nedeštruktívnych metód na lokalite tvrdošovce (predbežné výsledky). *Zbornik Slovenskeho Narodneho Muzea Archeologia*, 33:115–129, 2023. URL: https://www.scopus.com/inward/record.uri?eid=2-s2.0-85183009938&doi=10.55015%2fXHTO2250&partnerID=40&md5=155d8427c7d0a2ac64cb4951b842f7cc, doi:10.55015/XHTO2250.

[42] G. Poggi, L. Dallai, and V. Volpi. Mining under the canopy: unveiling the archaeo-mining record in the colline metallifere with lidar analysis and multidisciplinary studies. *Quaternary International*, 2023. URL: https://www.scopus.com/inward/record.uri?eid=2-s2.0-85169507176&doi=10.1016%2fj.quaint.2023.08.006&partnerID=40&md5=9140af7f4cb09442a464cbb385539af9, doi:10.1016/j.quaint.2023.08.006.

[43] V. Petras, A. Petrasova, J. B. McCarter, H. Mitasova, and R. K. Meentemeyer. Point density variations in airborne lidar point clouds. *Sensors*, 2023. URL: https://www.scopus.com/inward/record.uri?eid=2-s2.0-85147846600&doi=10.3390%2fs23031593&partnerID=40&md5=bf6f5827896b448bf209fbca3b18392c, doi:10.3390/s23031593.

[44] K.F.-C. Sit, C.-H. Pun, W.W.L. Lai, D.K.-W. Chung, and C.-M. Kwong. Unfolding wwii heritages with airborne and ground-based laser scanning. *Heritage*, 6(9):6189–6212, 2023. URL: https://www.scopus.com/inward/record.uri?eid=2-s2.0-85172266745&doi=10.3390%2fheritage6090325&partnerID=40&md5=1116484d2f00e74d7d0b0e4f8542e77f, doi:10.3390/heritage6090325.

[45] A. Pețan and A. Hegyi. Freely available lidar-derived digital terrain model (dtm) uncovers the heartland of the dacian kingdom. *Digital Applications in Archaeology and Cultural Heritage*, 2023. URL: https://www.scopus.com/inward/record.uri?eid=2-s2.0-85172879468&doi=10.1016%2fj.daach.2023.e00292&partnerID=40&md5=813bb9f375baf864ce8787ff17be07ac, doi:10.1016/j.daach.2023.e00292.

[46] B. T. Pandolpho, M. Urlaub, C. Berndt, and J. Bialas. Identification and differentiation of vertical movement through morphological changes and stratigraphic imprint: two distinct uplifting mechanisms in the upper calabrian accretionary wedge, western ionian sea. *Basin Research*, 2023. URL: https://www.scopus.com/inward/record.uri?eid=2-s2.0-85169667614&doi=10.1111%2fbre.12819&partnerID=40&md5=adf40d17facd2b0895f12eca9e199857, doi:10.1111/bre.12819.

[47] A. J. Ortiz Villarejo, J. M. Delgado Barrado, G. Casagrande, and J. M. Valderrama Zafra. Remote sensing and archaeology in modern age: the study case of the aldea de buenos aires in sierra morena. *Journal of Archaeological Science: Reports*, 2023. URL: https://www.scopus.com/inward/record.uri?eid=2-s2.0-85171803018&doi=10.1016%2fj.jasrep.2023.104205&partnerID=40&md5=460c3009cf0a71db94f100a782cae058, doi:10.1016/j.jasrep.2023.104205.

[48] A. J. Ortiz Villarejo and J. M. Delgado Barrado. Digitalescape project—aerial remote sensing, hbim, and archaeology for the preservation and dissemination of the cultural heritage at risk in the sierra sur and sierra morena regions. *Remote Sensing*, 2023. URL: https://www.scopus.com/inward/record.uri?eid=2-s2.0-85164917795&doi=10.3390%2frs15133315&partnerID=40&md5=19c47320b6c89390662dafc911a45d27, doi:10.3390/rs15133315.

[49] A. Novak, S. Poglajen, and M. Vrabec. Not another hillshade: alternatives which improve visualizations of bathymetric data. *Frontiers in Marine Science*, 2023. URL: https://www.scopus.com/inward/record.uri?eid=2-s2.0-85179350233&doi=10.3389%2ffmars.2023.1266364&partnerID=40&md5=4f387de777e07960f56f34577b062e91, doi:10.3389/fmars.2023.1266364.

[50] J. M. Niebylski, D. Stefański, and P. Wierzbicki. The formation of the units of the polish people's army (1944-1945) in eastern poland. the lidar evidence. *Archaeologia Polona*, 61:269–287, 2023. URL: https://www.scopus.com/inward/record.uri?eid=2-s2.0-85183053228&doi=10.23858%2fAPA61.2023.3499&partnerID=40&md5=733c095969e546d837c2ad348f327746, doi:10.23858/APA61.2023.3499.

[51] M. G. Mohlehli, E. Adam, and M. H. Schoeman. The potential for lidar using support vector machine (svm) to detect archaeological stone-walled structures in khutwaneng, bokoni. *South African Archaeological Bulletin*, 78(218):33–42, 2023. URL: https://www.scopus.com/inward/record.uri?eid=2-s2.0-85175016526&partnerID=40&md5=d18fd7e9259aa5432976dca962e59b41.

[52] M. E. Pérez Rivas, A. López Corral, H.A.G. Silva, T. W. Stanton, A. Daniel Urías Lugo, and S. M. Acevedo. Hallazgos con lidar en el tren maya. *Arqueologia Mexicana*, pages 84–89, 2023. URL: https://www.scopus.com/inward/record.uri?eid=2-s2.0-85181710034&partnerID=40&md5=27b0f24d222d145724a9d39ccd9638e3.

[53] J. Yang, Z. Wu, M. Menenti, M. S. Wong, Y. Xie, R. Zhu, S. Abbas, and Y. Xu. Impacts of urban morphology on sensible heat flux and net radiation exchange. *URBAN CLIMATE*, 2023. URL: https://www.scopus.com/inward/record.uri?eid=2-s2.0-85163554047&doi=10.1016%2fj.uclim.2023.101588&partnerID=40&md5=41168b51b186a0231aa52548978e29e4, doi:10.1016/j.uclim.2023.101588.

[54] R. M. Soares, M. Nabais, T. D. Pereiro, R. Dias, J. Hipólito, J. Fonte, L. G. Seco, F. Menéndez-Marsh, and A. Neves. New plan of the velho de safara castle: integration of archaeological data with high-resolution topography derived from drone-lidar survey. *Estudos do Quaternario*, 2023(23):66–75, 2023. URL: https://www.scopus.com/inward/record.uri?eid=2-s2.0-85181735499&doi=10.30893%2feq.v0i23.217&partnerID=40&md5=9e8ff6e959fd3edfae757d70551fb454, doi:10.30893/eq.v0i23.217.

[55] M. Sobala. Detection of past landscape elements in marginal mountain areas—the example of the western carpathians. *ARCHAEOLOGICAL AND ANTHROPOLOGICAL SCIENCES*, 2023. URL: https://www.scopus.com/inward/record.uri?eid=2-s2.0-85150923804&doi=10.1007%2fs12520-023-01750-3&partnerID=40&md5=03de54da9af6e39b032f69ab901cf6a7, doi:10.1007/s12520-023-01750-3.

[56] P. Wroniecki, M. Furmanek, and Wł. Raczkowski. Revealing the extent of neolithic rondel enclosures in lower silesia using non-invasive prospection. *Antiquity*, 97(395):1100–1118, 2023. URL: https://www.scopus.com/inward/record.uri?eid=2-s2.0-85175460417&doi=10.15184%2faqy.2023.24&partnerID=40&md5=0bfd4451e1cb428c864dbe3c93792d7a, doi:10.15184/aqy.2023.24.

[57] Y. Liu, Q. Hu, S. Wang, F. Zou, M. Ai, and P. Zhao. Discovering the ancient tomb under the forest using machine learning with timing-series features of sentinel images: taking baling mountain in jingzhou as an example. *Remote Sensing*, 2023. URL: https://www.scopus.com/inward/record.uri?eid=2-s2.0-85147947286&doi=10.3390%2frs15030554&partnerID=40&md5=e62ad7bcd02e328d917977d64ec35fdb, doi:10.3390/rs15030554.

[58] L. Liu, M. Lin, Z. Du, J. Liu, G. Chen, and J. Du. Developing a cnn-based, block-scale oriented local climate zone mapping approach: a case study in guangzhou. *BUILDING AND ENVIRONMENT*, 2023. URL: https://www.scopus.com/inward/record.uri?eid=2-s2.0-85161054980&doi=10.1016%2fj.buildenv.2023.110414&partnerID=40&md5=0df787474bfdbcdee5ea2a512e9a37af, doi:10.1016/j.buildenv.2023.110414.

[59] Y. Liu and H. Wang. The effects of 2d and 3d urban morphology on air quality. *Water, Air, and Soil Pollution*, 2023. URL: https://www.scopus.com/inward/record.uri?eid=2-s2.0-85169571522&doi=10.1007%2fs11270-023-06592-2&partnerID=40&md5=514880dbca94b1b1766c719c93fb2b1c, doi:10.1007/s11270-023-06592-2.

[60] M. Weber, D. G. Passmore, D. Capps-Tunwell, and H.G.W. Davie. The battle of the seelow heights, april 1945: conflict archaeology in the forests of eastern brandenburg, germany. *Journal of Conflict Archaeology*, 2023. URL: https://www.scopus.com/inward/record.uri?eid=2-s2.0-85150706754&doi=10.1080%2f15740773.2023.2183784&partnerID=40&md5=bf34425a88dea27baa92a3818fc22012, doi:10.1080/15740773.2023.2183784.

[61] Q. Wang, X. Wang, Y. Meng, Y. Zhou, and H. Wang. Exploring the impact of urban features on the spatial variation of land surface temperature within the diurnal cycle. *SUSTAINABLE CITIES AND SOCIETY*, 2023. URL: https://www.scopus.com/inward/record.uri?eid=2-s2.0-85147092355&doi=10.1016%2fj.scs.2023.104432&partnerID=40&md5=2afcae58d21f1c83bf6c435ac9de61fd, doi:10.1016/j.scs.2023.104432.

[62] M. Sobala. Assessment of the traditional landscapes' state in mountain areas as the basis for their restoration (the western beskids, poland). *APPLIED GEOGRAPHY*, 2023. URL: https://www.scopus.com/inward/record.uri?eid=2-s2.0-85174011725&doi=10.1016%2fj.apgeog.2023.103123&partnerID=40&md5=2e0acc0837bf56fe4b140569cdd2e1fc, doi:10.1016/j.apgeog.2023.103123.

[63] M. Vojtas, J. Těsnohlídek, M. Prišťáková, J. Petřík, M. Fojtík, J. Zubalík, R. Kapavík, and P. Tajkov. Battlefield archaeology of the first world war in northeastern slovakia. *Archaeologia Polona*, 61:31–59, 2023. URL: https://www.scopus.com/inward/record.uri?eid=2-s2.0-85184217325&doi=10.23858%2fAPA61.2023.3362&partnerID=40&md5=a8e691aea7bcb7e5752dc7211e301ea7, doi:10.23858/APA61.2023.3362.

[64] Y. Tian, A. Wang, S. Mora, P. Desouza, X. Yao, F. Duarte, H. Lin, and C. Ratti. Improving no2 prediction by integrating tree diversity, urban form, and scale sensitivity through mobile monitoring. *APPLIED GEOGRAPHY*, 2023. URL: https://www.scopus.com/inward/record.uri?eid=2-s2.0-85150833136&doi=10.1016%2fj.apgeog.2023.102943&partnerID=40&md5=62a2fc2418921b6a43e8dbf17335104b, doi:10.1016/j.apgeog.2023.102943.

[65] Victor D. Thompson. Considering urbanism at mound key (caalus), the capital of the calusa in the 16th century, southwest florida, usa. *JOURNAL OF ANTHROPOLOGICAL ARCHAEOLOGY*, 2023. URL: https://www.scopus.com/inward/record.uri?eid=2-s2.0-85171803228&doi=10.1016%2fj.jaa.2023.101546&partnerID=40&md5=74fa72430d762c1894974654732ecf43, doi:10.1016/j.jaa.2023.101546.

[66] B. Štular, E. Lozić, and S. Eichert. Interpolation of airborne lidar data for archaeology. *Journal of Archaeological Science: Reports*, 2023. URL: https://www.scopus.com/inward/record.uri?eid=2-s2.0-85146733762&doi=10.1016%2fj.jasrep.2023.103840&partnerID=40&md5=e1d89f8fb42a82d15e66d713a08fec59, doi:10.1016/j.jasrep.2023.103840.

[67] J. W. Suh and W. Ouimet. Mapping stone walls in northeastern usa using deep learning and lidar data. *GIScience and Remote Sensing*, 2023. URL: https://www.scopus.com/inward/record.uri?eid=2-s2.0-85152389672&doi=10.1080%2f15481603.2023.2196117&partnerID=40&md5=47989de82abec39c6a64f79e2d5792b3, doi:10.1080/15481603.2023.2196117.

[68] J. G. Stauffer, S. B. Grooms, L. W. Hu, J. Mersmann, T. R. Kidder, and E. R. Henry. Reimagining the development of downtown cahokia using remote sensing visualizations from the western edge of the grand plaza. *Land*, 2023. URL: https://www.scopus.com/inward/record.uri?eid=2-s2.0-85149252683&doi=10.3390%2fland12020342&partnerID=40&md5=20ea4e56ee70b207c1a16f22a20d94e8, doi:10.3390/land12020342.

[69] L. Lu, P. Fu, A. Dewan, and Q. Li. Contrasting determinants of land surface temperature in three megacities: implications to cool tropical metropolitan regions. *SUSTAINABLE CITIES AND SOCIETY*, 2023. URL: https://www.scopus.com/inward/record.uri?eid=2-s2.0-85150878965&doi=10.1016%2fj.scs.2023.104505&partnerID=40&md5=667701031c2fb23f3dbe56977858b6cf, doi:10.1016/j.scs.2023.104505.

[70] Y. Tian, X. A. Yao, M. Madden, and A. Grundstein. Synergic effects of meteorological factors on urban form-outdoor exercise relationship: a study with crowdsourced data. *Journal of Geographical Systems*, 2023. URL: https://www.scopus.com/inward/record.uri?eid=2-s2.0-85169606163&doi=10.1007%2fs10109-023-00424-x&partnerID=40&md5=714e0713dd97898091c11ca68feace9a, doi:10.1007/s10109-023-00424-x.

[71] J. A. Comer, D. C. Comer, I. A. Dumitru, C. E. Priebe, and J. L. Patsolic. Sampling methods for archaeological predictive modeling: spatial autocorrelation and model performance. *Journal of Archaeological Science: Reports*, 2023. URL: https://www.scopus.com/inward/record.uri?eid=2-s2.0-85148351272&doi=10.1016%2fj.jasrep.2022.103824&partnerID=40&md5=1f37ef7dacc0fcbd4441c5c86ac47434, doi:10.1016/j.jasrep.2022.103824.

[72] M. Meliho, A. Khattabi, D. Zejli, and C. A. Orlando. Spatiotemporal prediction of daily air temperature using remote sensing and machine learning in morocco. *THEORETICAL AND APPLIED CLIMATOLOGY*, 2023. URL: https://www.scopus.com/inward/record.uri?eid=2-s2.0-85178144757&doi=10.1007%2fs00704-023-04759-9&partnerID=40&md5=6eb6152123320cd3a52ec38a9847edd9, doi:10.1007/s00704-023-04759-9.

[73] N. Abate, D. Ronchi, V. Vitale, N. Masini, A. Angelini, F. Giuri, A. Minervino Amodio, A. M. Gennaro, and D. Ferdani. Integrated close range remote sensing techniques for detecting, documenting, and interpreting lost medieval settlements under canopy: the case of altanum (rc, italy). *Land*, 2023. URL: https://www.scopus.com/inward/record.uri?eid=2-s2.0-85149237338&doi=10.3390%2fland12020310&partnerID=40&md5=3a0e63b298d62569bae744cd1969579b, doi:10.3390/land12020310.

[74] S. Asadzadeh and C. R. Souza Filho. Numerical modeling of land surface temperature over complex geologic terrains: a remote sensing approach. *Remote Sensing*, 2023. URL: https://www.scopus.com/inward/record.uri?eid=2-s2.0-85174165895&doi=10.3390%2frs15194877&partnerID=40&md5=559de0395303f310047f250ef2956b7a, doi:10.3390/rs15194877.

[75] J. Berthe, A. Devos, O. Lejeune, N. Bollot, G. Fronteau, R. Perarnau, and S. Ortonovi. Contribution of airborne lidar on the understanding of exokarstification factors in a low plateau context, example of the montagne de reims (france). *Geomorphologie: Relief, Processus, Environnement*, 28(4):207–221, 2022. URL: https://www.scopus.com/inward/record.uri?eid=2-s2.0-85161188319&doi=10.4000%2fgeomorphologie.16829&partnerID=40&md5=881f16077e25c70d1362ecf0a5150707, doi:10.4000/geomorphologie.16829.

[76] F. Bernardini, M. Pipan, E. Forte, E. Leghissa, M. Calosi, S. Furlani, S. Hunter Broking, R. Loiacono, and V. Macovaz. Trmun (north-eastern italy): multi-scale remote and ground-based sensing of a bronze age and post-roman fortification. *Journal of Archaeological Science: Reports*, 2023. URL: https://www.scopus.com/inward/record.uri?eid=2-s2.0-85167985398&doi=10.1016%2fj.jasrep.2023.104108&partnerID=40&md5=afd3f1b72af031bdfd382d4ae057d6a6, doi:10.1016/j.jasrep.2023.104108.

[77] R. Brancato, C. Lamanna, V. Mirto, and L. Manganelli. Digital technologies and the archaeological topography of castellito (sicily): the reconstruction of a roman villa. *ARCHEOLOGIA E CALCOLATORI*, 34(2):185–206, 2023. URL: https://www.scopus.com/inward/record.uri?eid=2-s2.0-85182773692&doi=10.19282%2fac.34.2.2023.10&partnerID=40&md5=e522644bb1b24768a750463de126d12d, doi:10.19282/ac.34.2.2023.10.

[78] C. Brașoveanu, A. Mihu-Pintilie, and R.-A. Brunchi. Inside late bronze age settlements in ne romania: gis-based surface characterization of ashmound structures using airborne laser scanning and aerial photography techniques. *Remote Sensing*, 2023. URL: https://www.scopus.com/inward/record.uri?eid=2-s2.0-85170361622&doi=10.3390%2frs15174124&partnerID=40&md5=5da8e0e087709c087ad195eba27e8e32, doi:10.3390/rs15174124.

[79] N. Anttiroiko, F. J. Groesz, J. Ikäheimo, A. Kelloniemi, R. Nurmi, S. Rostad, and O. Seitsonen. Detecting the archaeological traces of tar production kilns in the northern boreal forests based on airborne laser scanning and deep learning. *Remote Sensing*, 2023. URL: https://www.scopus.com/inward/record.uri?eid=2-s2.0-85152768915&doi=10.3390%2frs15071799&partnerID=40&md5=745da963383a7199506dbab6b42714f9, doi:10.3390/rs15071799.

[80] C. Chen, H. Bagan, and T. Yoshida. Multiscale mapping of local climate zones in tokyo using airborne lidar data, gis vectors, and sentinel-2 imagery. *GIScience and Remote Sensing*, 2023. URL: https://www.scopus.com/inward/record.uri?eid=2-s2.0-85159805853&doi=10.1080%2f15481603.2023.2209970&partnerID=40&md5=48599be89e10c90beef66143a0dd8a38, doi:10.1080/15481603.2023.2209970.

[81] Z. Cheng, J. M. Chen, Z. Guo, G. Miao, H. Zeng, R. Wang, Z. Huang, and Y. Wang. Improving uav-based lai estimation for forests over complex terrain by reducing topographic effects on multispectral reflectance. *IEEE TRANSACTIONS ON GEOSCIENCE AND REMOTE SENSING*, 62:1–19, 2024. URL: https://www.scopus.com/inward/record.uri?eid=2-s2.0-85179083406&doi=10.1109%2fTGRS.2023.3337177&partnerID=40&md5=a9fb790affaaa5de6a0db56c0594f15e, doi:10.1109/TGRS.2023.3337177.

[82] J. Aldrighettoni and M. G. D'Urso. Military archaeology and lidar data visualizations: a non-invasive approach to detect historical remains. *Acta IMEKO*, 2023. URL: https://www.scopus.com/inward/record.uri?eid=2-s2.0-85164967947&doi=10.21014%2factaimeko.v12i2.1395&partnerID=40&md5=b138062be54a012e8d659fb480b56ac3, doi:10.21014/actaimeko.v12i2.1395.

[83] H.-K. Ahn, K.-J. Oh, and Y.-J. Cho. Case study of a korean archaeological survey using lidar. *International Journal of Korean History*, 28(1):99–141, 2023. URL: https://www.scopus.com/inward/record.uri?eid=2-s2.0-85151429675&doi=10.22372%2fijkh.2023.28.1.99&partnerID=40&md5=43cb250936c4d2193c4a640bdc780661, doi:10.22372/ijkh.2023.28.1.99.

[84] F. Bernardini. Rediscovering the lost roman landscape in the southern trieste karst (north-eastern italy): road network, land divisions, rural buildings and new hints on the avesica road station. *Remote Sensing*, 2023. URL: https://www.scopus.com/inward/record.uri?eid=2-s2.0-85151146311&doi=10.3390%2frs15061506&partnerID=40&md5=755355c10629dafd9e716e06d4779171, doi:10.3390/rs15061506.

[85] I. Berganzo-Besga, H. A. Orengo, J. Canela, and M. C. Belarte. Potential of multitemporal lidar for the detection of subtle archaeological features under perennial dense forest. *Land*, 2022. URL: https://www.scopus.com/inward/record.uri?eid=2-s2.0-85149491459&doi=10.3390%2fland11111964&partnerID=40&md5=952319f22d54cfb1d3e86222a7d5c3b4, doi:10.3390/land11111964.

[86] A. Campiani, S. McAvoy, N. Lercari, R. Liendo Stuardo, G. Jiménez Delgado, J. López Mejía, D. Rissolo, and F. Kuester. Developing an interoperable cloud-based visualization workflow for 3d archaeological heritage data: the palenque 3d archaeological atlas. *Digital Applications in Archaeology and Cultural Heritage*, 2023. URL: https://www.scopus.com/inward/record.uri?eid=2-s2.0-85173528903&doi=10.1016%2fj.daach.2023.e00293&partnerID=40&md5=4b39867516ee7edd364beed922d851fc, doi:10.1016/j.daach.2023.e00293.

[87] G. Caspari. The potential of new lidar datasets for archaeology in switzerland. *Remote Sensing*, 2023. URL: https://www.scopus.com/inward/record.uri?eid=2-s2.0-85151479441&doi=10.3390%2frs15061569&partnerID=40&md5=3626989291e8da718c0cef1735c64e11, doi:10.3390/rs15061569.

[88] I. Basista, E. Dębińska, K. Kozioł, J. Czerniec, and M. Sosnowski. Micro-morphological analyses of digital terrain model in search of traces of ploughing on archaeological objects. *International Journal of Conservation Science*, 14(1):131–158, 2023. URL: https://www.scopus.com/inward/record.uri?eid=2-s2.0-85159810751&doi=10.36868%2fIJCS.2023.01.10&partnerID=40&md5=1a9da056f8efb580f672be350b4efd1a, doi:10.36868/IJCS.2023.01.10.

[89] R. Bi, S. Gan, X. Yuan, R. Li, S. Gao, M. Yang, W. Luo, and L. Hu. Multi-view analysis of high-resolution geomorphic features in complex mountains based on uav–lidar and sfm–mvs: a case study of the northern pit rim structure of the mountains of lufeng, china. *Applied Sciences (Switzerland)*, 2023. URL: https://www.scopus.com/inward/record.uri?eid=2-s2.0-85146644920&doi=10.3390%2fapp13020738&partnerID=40&md5=b5c3b6fe578ec0b85e94a638a5cc475e, doi:10.3390/app13020738.

[90] Andrzej Affek. Past carpathian landscapes recorded in the microtopography. *GEOGRAPHIA POLONICA*, 89(3):415–424, 2016. URL: https://www.scopus.com/inward/record.uri?eid=2-s2.0-84989283172&doi=10.7163%2fGPol.0062&partnerID=40&md5=47c41674f6516fba0c9e78377ba9b2e5, doi:10.7163/GPol.0062.

[91] Andrzej Norbert Affek, Maria Zachwatowicz, Agnieszka Sosnowska, Alina Gerlée, and Krzysztof Kiszka. Impacts of modern mechanised skidding on the natural and cultural heritage of the polish carpathian mountains. *FOREST ECOLOGY AND MANAGEMENT*, 405:391–403, 2017. URL: https://www.scopus.com/inward/record.uri?eid=2-s2.0-85030472101&doi=10.1016%2fj.foreco.2017.09.047&partnerID=40&md5=19ad50c4bc2f2318a4b70c90f20ec59b, doi:10.1016/j.foreco.2017.09.047.

[92] A. N. Affek, J. Wolski, A. Latocha, M. Zachwatowicz, and M. Wieczorek. The use of lidar in reconstructing the pre-world war ii landscapes of abandoned mountain villages in southern poland. *Archaeological Prospection*, 2021. URL: https://www.scopus.com/inward/record.uri?eid=2-s2.0-85115824622&doi=10.1002%2farp.1846&partnerID=40&md5=8bddc14f7ff3498041059fd406f3a263, doi:10.1002/arp.1846.

[93] Z. Alvyar, F. Shahbazi, S. Oustan, O. Dengiz, and B. Minasny. Digital mapping of potentially toxic elements enrichment in soils of urmia lake due to water level decline. *SCIENCE OF THE TOTAL ENVIRONMENT*, 2022. URL: https://www.scopus.com/inward/record.uri?eid=2-s2.0-85120804478&doi=10.1016%2fj.scitotenv.2021.152086&partnerID=40&md5=a692ce37f50cabd4cf40015fee4f35e4, doi:10.1016/j.scitotenv.2021.152086.

[94] S. M. An, B. S. Kim, H. Y. Lee, C. H. Kim, C. Y. Yi, J. H. Eum, and J. H. Woo. Three-dimensional point cloud based sky view factor analysis in complex urban settings. *International Journal of Climatology*, 34(8):2685–2701, 2014. URL: https://www.scopus.com/inward/record.uri?eid=2-s2.0-84902658594&doi=10.1002%2fjoc.3868&partnerID=40&md5=ff05eb4ec4882da15b4a218b30d27d4d, doi:10.1002/joc.3868.

[95] B. Antunes, C. Figueiredo-Vázquez, K. Dudek, M. Liana, M. Pabijan, P. Zieliński, and W. Babik. Landscape genetics reveals contrasting patterns of connectivity in two newt species (lissotriton montandoni and l. vulgaris). *Molecular Ecology*, 2022. URL: https://www.scopus.com/inward/record.uri?eid=2-s2.0-85131638691&doi=10.1111%2fmec.16543&partnerID=40&md5=fbf23c83995bfe32eed6d16dc792a411, doi:10.1111/mec.16543.

[96] Anahita Asadi, Hossein Arefi, and Hafez Fathipoor. Simulation of green roofs and their potential mitigating effects on the urban heat island using an artificial neural network: a case study in austin, texas. *Advances in Space Research*, 66(8):1846–1862, 2020. URL: https://www.scopus.com/inward/record.uri?eid=2-s2.0-85089143121&doi=10.1016%2fj.asr.2020.06.039&partnerID=40&md5=bd55a0bc3dfb48d46187b2026c1c018b, doi:10.1016/j.asr.2020.06.039.

[97] Andrei Asăndulesei. Inside a cucuteni settlement: remote sensing techniques for documenting an unexplored eneolithic site from northeastern romania. *Remote Sensing*, 9(1):41, 2017. doi:10.3390/rs9010041.

[98] Nigel Atkinson, Daniel J. Utting, and Steven M. Pawley. Landform signature of the laurentide and cordilleran ice sheets across alberta during the last glaciation. *CANADIAN JOURNAL OF EARTH SCIENCES*, 51(12):1067–1083, 2014. URL: https://www.scopus.com/inward/record.uri?eid=2-s2.0-84919388104&doi=10.1139%2fcjes-2014-0112&partnerID=40&md5=9c2c9dde68caa88daa55153f51a857c7, doi:10.1139/cjes-2014-0112.

[99] Łukasz Banaszek, Dave Cowley, and Mike Middleton. Towards national archaeological mapping. assessing source data and methodology—a case study from scotland. *Geosciences (Switzerland)*, 8(8):272, 2018. URL: https://www.scopus.com/inward/record.uri?eid=2-s2.0-85051021501&doi=10.3390%2fgeosciences8080272&partnerID=40&md5=e8bcac74228741cc8fc1479bc0cf189b, doi:10.3390/geosciences8080272.

[100] Łukasz Banaszek. It takes all kinds of trees to make a forest. using historic maps and forestry data to inform airborne laser scanning based archaeological prospection in woodland. *Archaeological Prospection*, 27(4):377–392, 2020. URL: https://www.scopus.com/inward/record.uri?eid=2-s2.0-85085603988&doi=10.1002%2farp.1780&partnerID=40&md5=3ee77cb73d221e0879c22967507d1bd6, doi:10.1002/arp.1780.

[101] Elena Barbierato, Iacopo Bernetti, Irene Capecchi, and Claudio Saragosa. Quantifying the impact of trees on land surface temperature: a downscaling algorithm at city-scale. *European Journal of Remote Sensing*, 52(sup4):74–83, 2019. URL: https://www.scopus.com/inward/record.uri?eid=2-s2.0-85070261286&doi=10.1080%2f22797254.2019.1646104&partnerID=40&md5=261e3cdda3cf1e8459b81ffa8d1b368d, doi:10.1080/22797254.2019.1646104.

[102] P. Barruezo-Vaquero, A. Dorado Alejos, J. A. Cámara Serrano, A. M. Ruíz, and F. M. González. Digitizing los millares (santa fe de mondujar, almería, spain) through 3-d and geospatial technologies: preserving and disseminating the archaeological heritage. *Digital Applications in Archaeology and Cultural Heritage*, 2022. URL: https://www.scopus.com/inward/record.uri?eid=2-s2.0-85142180817&doi=10.1016%2fj.daach.2022.e00247&partnerID=40&md5=6db2940d4ff1236675efd21e244d6bf0, doi:10.1016/j.daach.2022.e00247.

[103] Carlos Bartesaghi Koc, Paul Osmond, Alan Peters, and Matthias Irger. Understanding land surface temperature differences of local climate zones based on airborne remote sensing data. *IEEE Journal of Selected Topics in Applied Earth Observations and Remote Sensing*, 11(8):2724–2730, 2018. URL: https://www.scopus.com/inward/record.uri?eid=2-s2.0-85045676804&doi=10.1109%2fJSTARS.2018.2815004&partnerID=40&md5=cdee346a9d5a03f9e113f14523d9378a, doi:10.1109/JSTARS.2018.2815004.

[104] C. Bartesaghi-Koc, P. Osmond, and A. Peters. Innovative use of spatial regression models to predict the effects of green infrastructure on land surface temperatures. *Energy and Buildings*, 2022. URL: https://www.scopus.com/inward/record.uri?eid=2-s2.0-85119070057&doi=10.1016%2fj.enbuild.2021.111564&partnerID=40&md5=34c8a81fc09fcfa00070b1a2a39b84e3, doi:10.1016/j.enbuild.2021.111564.

[105] Timothy Beach, Sheryl Luzzadder-Beach, Samantha Krause, Tom Guderjan, Fred Valdez, Juan Carlos Fernandez-Diaz, Sara Eshleman, and Colin Doyle. Ancient maya wetland fields revealed under tropical forest canopy from laser scanning and multiproxy evidence. *Proceedings of the National Academy of Sciences of the United States of America*, 116(43):21469–21477, 2019. URL: https://www.scopus.com/inward/record.uri?eid=2-s2.0-85073738764&doi=10.1073%2fpnas.1910553116&partnerID=40&md5=88a1859f49a1c0727d48b1fc7bd08d86, doi:10.1073/pnas.1910553116.

[106] Anton Beloconi, Yiannis Kamarianakis, and Nektarios Chrysoulakis. Estimating urban pm10 and pm2.5 concentrations, based on synergistic meris/aatsr aerosol observations, land cover and morphology data. *REMOTE SENSING OF ENVIRONMENT*, 172:148–164, 2016. URL: https://www.scopus.com/inward/record.uri?eid=2-s2.0-84947551513&doi=10.1016%2fj.rse.2015.10.017&partnerID=40&md5=917dbe554523f6c4421dbb74a1161d27, doi:10.1016/j.rse.2015.10.017.

[107] Rebecca Bennett, Kate Welham, Ross a. Hill, and Andrew Ford. A comparison of visualization techniques for models created from airborne laser scanned data. *Archaeological Prospection*, 19(1):41–48, 2012. URL:

https://www.scopus.com/inward/record.uri?eid=2-s2.0-84858007655&doi=10.1002%2farp.1414&partnerID=40&md5=c1a0000033a95a27a346e3819cc81432, doi:10.1002/arp.1414.

[108] V. Berezowski, I. Moffat, Y. Shendryk, D. MacGregor, J. Ellis, and X. Mallett. A multidisciplinary approach to locating clandestine gravesites in cold cases: combining geographic profiling, lidar, and near surface geophysics. *Forensic Science International: Synergy*, 2022. URL: https://www.scopus.com/inward/record.uri?eid=2-s2.0-85135712785&doi=10.1016%2fj.fsisyn.2022.100281&partnerID=40&md5=0a9674f686650934c2e4a2525ff64e22, doi:10.1016/j.fsisyn.2022.100281.

[109] I. Berganzo-Besga, H. A. Orengo, F. Lumbreras, M. Carrero-Pazos, J. Fonte, and B. Vilas-Estévez. Hybrid msrm-based deep learning and multitemporal sentinel 2-based machine learning algorithm detects near 10k archaeological tumuli in north-western iberia. *Remote Sensing*, 2021. URL: https://www.scopus.com/inward/record.uri?eid=2-s2.0-85118223117&doi=10.3390%2frs13204181&partnerID=40&md5=145d31b220e2978f6c8f17190e3ea28d, doi:10.3390/rs13204181.

[110] C. Berger, J. Rosentreter, M. Voltersen, C. Baumgart, C. Schmullius, and S. Hese. Spatio-temporal analysis of the relationship between 2d/3d urban site characteristics and land surface temperature. *REMOTE SENSING OF ENVIRONMENT*, 193:225–243, 2017. URL: https://www.scopus.com/inward/record.uri?eid=2-s2.0-85015377927&doi=10.1016%2fj.rse.2017.02.020&partnerID=40&md5=acad91e4335a7f918f78925c0d0912e1, doi:10.1016/j.rse.2017.02.020.

[111] Federico Bernardini and Giacomo Vinci. Archaeological landscape in central northern istria (croatia) revealed by airborne lidar: from prehistoric sites to roman centuriation. *ARCHAEOLOGICAL AND ANTHROPOLOGICAL SCIENCES*, 2020. URL: https://www.scopus.com/inward/record.uri?eid=2-s2.0-85086372298&doi=10.1007%2fs12520-020-01070-w&partnerID=40&md5=5610c090479e0d7367ea21e31c38ecc5, doi:10.1007/s12520-020-01070-w.

[112] Miloud Bessafi, Vishwamitra Oree, Abdel Khoodaruth, Guillaume Jumaux, François Bonnardot, Patrick Jeanty, Mathieu Delsaut, Jean-Pierre Chabriat, and Muhammad Zaid Dauhoo. Downscaling solar irradiance using dem-based model in young volcanic islands with rugged topography. *RENEWABLE ENERGY*, 126:584–593, 2018. URL: https://www.scopus.com/inward/record.uri?eid=2-s2.0-85047501513&doi=10.1016%2fj.renene.2018.03.071&partnerID=40&md5=7ae87804c6ae7c1868b392d366c139ce, doi:10.1016/j.renene.2018.03.071.

[113] C. Bettineschi, L. Magnini, G. Azzalin, and A. de Guio. Clearence cairnfields forever: combining ai and lidar data in the marcesina upland (northern italy). *European Journal of Post-Classical Archaeologies*, 12:49–68, 2022. URL: https://www.scopus.com/inward/record.uri?eid=2-s2.0-85140493250&partnerID=40&md5=ecd1dcd7575ab5e61b4c080f1c8dfe8f.

[114] P. Bisták, J. Zachar, A. Rášová, T. Lieskovský, I. Kravjanská, M. Orosová, K. Krocková, and M. Felcan. Archaeological digital archiving in heritage management in slovakia. *Internet Archaeology*, 2021. URL: https://www.scopus.com/inward/record.uri?eid=2-s2.0-85122590914&doi=10.11141%2fia.58.16&partnerID=40&md5=5a495d9e933220bf211b8bd06091f922, doi:10.11141/ia.58.16.

[115] Peter Bobáľ, Slavomír Sipina, and Filip Škultéty. Aspects of aerial laser scanning when exploring unknown archaeological sites (case study). *Transportation Research Procedia*, 28:37–44, 2017. doi:10.1016/j.trpro.2017.12.166.

[116] Alexander Bonhage, Florian Hirsch, Thomas Raab, Anna Schneider, Alexandra Raab, and Will Ouimet. Characteristics of small anthropogenic landforms resulting from historical charcoal production in western connecticut, usa. *CATENA*, 195:104896, 2020. URL: https://www.scopus.com/inward/record.uri?eid=2-s2.0-85091390891&doi=10.1016%2fj.catena.2020.104896&partnerID=40&md5=50352ae4eeee95e9cc2bba52926ba12a, doi:10.1016/j.catena.2020.104896.

[117] Alexander Bonhage, Mahmoud Eltaher, Thomas Raab, Michael Breuß, Alexandra Raab, and Anna Schneider. A modified mask region–based convolutional neural network approach for the automated detection of archaeological sites on high–resolution light detection and ranging–derived digital elevation models in the north german lowland. *Archaeological Prospection*, 28(2):177–186, 2021. URL: https://www.scopus.com/inward/record.uri?eid=2-s2.0-85100307716&doi=10.1002%2farp.1806&partnerID=40&md5=b07a74dcc9585d2088fe2bd717f2af9d, doi:10.1002/arp.1806.

[118] Marek Bundzel, Miroslav Jaščur, Milan Kováč, Tibor Lieskovský, Peter Sinčák, and Tomáš Tkáčik. Semantic segmentation of airborne lidar data in maya archaeology. *Remote Sensing*, 12(22):3685, 2020. URL: https://www.scopus.com/inward/record.uri?eid=2-s2.0-85096102892&doi=10.3390%2frs12223685&partnerID=40&md5=163897c439ef6ea5f95161ec89125efe, doi:10.3390/rs12223685.

[119] J. Buridant, C. Pichard, and E. Gallet-Moron. Use of lidar technology for archaeological and geo-historical knowledge: french examples. *Transylvanian Review*, 29:291–305, 2020. URL: https://www.scopus.com/inward/record.uri?eid=2-s2.0-85090783893&partnerID=40&md5=ff19034bc57750bf2caa562e038d3de3.

[120] Laura Burigana and Luigi Magnini. Image processing and analysis of radar and lidar data: new discoveries in verona southern lowland (italy). *SCIENCE AND TECHNOLOGY OF ARCHAEOLOGICAL RESEARCH*, 3(2):490–509, 2017. URL: https://www.scopus.com/inward/record.uri?eid=2-s2.0-85057157061&doi=10.1080%2f20548923.2018.1426273&partnerID=40&md5=ef065b5f3558219ef6c67c6dd1a8ccaa, doi:10.1080/20548923.2018.1426273.

[121] J. Caha. Line of sight analyst: arcgis python toolbox for visibility analyses. *Geographia Cassoviensis*, 12(1):5–15, 2018. URL: https://www.scopus.com/inward/record.uri?eid=2-s2.0-85050815135&partnerID=40&md5=f4fb740c76f5e4ff31c592be07d39ab9.

[122] Marcello A. Canuto, Francisco Estrada-Belli, Thomas G. Garrison, Stephen D. Houston, Mary Jane Acuña, Milan Kováč, Damien Marken, Philippe Nondédéo, Luke Auld-Thomas, Cyril Castanet, David Chatelain, Carlos R. Chiriboga, Tomáš Drápela, Tibor Lieskovský, Alexandre Tokovinine, Antolín Velasquez, Juan C. Fernández-Díaz, and Ramesh Shrestha. Ancient lowland maya complexity as revealed by airborne laser scanning of northern guatemala. *Science*, 2018. doi:10.1126/science.aau0137.

[123] Shisong Cao, Mingyi Du, Wenji Zhao, Yungang Hu, You Mo, Shanshan Chen, Yile Cai, Ziqiang Peng, and Chaoyi Zhang. Multi-level monitoring of three-dimensional building changes for megacities: trajectory, morphology, and landscape. *ISPRS JOURNAL OF PHOTOGRAMMETRY AND REMOTE SENSING*, 167:54–70, 2020. URL: https://www.scopus.com/inward/record.uri?eid=2-s2.0-85087859016&doi=10.1016%2fj.isprsjprs.2020.06.020&partnerID=40&md5=f05a3e2d711a6a72c1c3fc53da38723a, doi:10.1016/j.isprsjprs.2020.06.020.

[124] Shisong Cao, Qihao Weng, Mingyi Du, Bing Li, Ruofei Zhong, and You Mo. Multi-scale three-dimensional detection of urban buildings using aerial lidar data. *GIScience and Remote Sensing*, 57(8):1125–1143, 2020. URL: https://www.scopus.com/inward/record.uri?eid=2-s2.0-85096343023&doi=10.1080%2f15481603.2020.1847453&partnerID=40&md5=33292fce35508bacb370c517b1e2c8b2, doi:10.1080/15481603.2020.1847453.

[125] Qian Cao, Qingzu Luan, Yupeng Liu, and Renqing Wang. The effects of 2d and 3d building morphology on urban environments: a multi-scale analysis in the beijing metropolitan region. *BUILDING AND ENVIRONMENT*, 192:107635, 2021. URL: https://www.scopus.com/inward/record.uri?eid=2-s2.0-85099859571&doi=10.1016%2fj.buildenv.2021.107635&partnerID=40&md5=0fa381f562b32269602a8694b9a651e0, doi:10.1016/j.buildenv.2021.107635.

[126] Rosa M. Carrasco, Rodrigo L. Soteres, Javier Pedraza, Javier Fernández-Lozano, Valentí Turu, José Antonio López-Sáez, Theodoros Karampaglidis, José Luis Granja-Bruña, and Alfoso Muñoz-Martín. Glacial geomorphology of the high gredos massif: gredos and pinar valleys (iberian central system, spain). *Journal of Maps*, 16(2):790–804, 2020. URL: https://www.scopus.com/inward/record.uri?eid=2-s2.0-85094869879&doi=10.1080%2f17445647.2020.1833768&partnerID=40&md5=924e56a9df9fd13442721541a59f282c, doi:10.1080/17445647.2020.1833768.

[127] Miguel Carrero-Pazos, Alia Vázquez-Martínez, and Benito Vilas-Estévez. Astrend: towards a new method for the study of ancient carvings. *Journal of Archaeological Science: Reports*, 9:105–119, 2016. URL: https://www.scopus.com/inward/record.uri?eid=2-s2.0-84979030916&doi=10.1016%2fj.jasrep.2016.06.044&partnerID=40&md5=7e3f6a5199d78b97535730f3fe42c4c2, doi:10.1016/j.jasrep.2016.06.044.

[128] M. Carrero-Pazos. Visibility as a locational factor in the megaliths of southern galicia. *Zephyrus*, 87:63–81, 2021. URL: https://www.scopus.com/inward/record.uri?eid=2-s2.0-85109601394&doi=10.14201%2fZEPHYRUS2021876381&partnerID=40&md5=677846b944619b1a67cd90a51a44b5cc, doi:10.14201/ZEPHYRUS2021876381.

[129] Jesse Casana, Elise Jakoby Laugier, Austin Chad Hill, and Donald Blakeslee. A council circle at etzanoa? multi-sensor drone survey at an ancestral wichita settlement in southeastern kansas. *American Antiquity*, 85(4):761–780, 2020. URL: https://www.scopus.com/inward/record.uri?eid=2-s2.0-85093525387&doi=10.1017%2faaq.2020.49&partnerID=40&md5=30e39072aa0907904c0d9f336259a7f9, doi:10.1017/aaq.2020.49.

[130] J. Casana, E. J. Laugier, A. C. Hill, K. M. Reese, C. Ferwerda, M. D. McCoy, and T. Ladefoged. Exploring archaeological landscapes using drone-acquired lidar: case studies from hawai'i, colorado, and new hampshire, usa. *Journal of Archaeological Science: Reports*, 2021. URL: https://www.scopus.com/inward/record.uri?eid=2-s2.0-85113661723&doi=10.1016%2fj.jasrep.2021.103133&partnerID=40&md5=86ffbd37fb7bdbfbf8273f91e223e9b7, doi:10.1016/j.jasrep.2021.103133.

[131] Keith Challis, Paolo Forlin, and Mark Kincey. A generic toolkit for the visualization of archaeological features on airborne lidar elevation data. *Archaeological Prospection*, 18(4):279–289, 2011. URL: https://www.scopus.com/inward/record.uri?eid=2-s2.0-80051887600&doi=10.1002%2farp.421&partnerID=40&md5=388cac4342c58b79fbf0bf49cbaf685c, doi:10.1002/arp.421.

[132] Samuel N. Chambers, Geoffrey Alan Boyce, and W. Jake Jacobs. Constructing a desert labyrinth: the psychological and emotional geographies of deterrence strategy on the u.s. / mexico border. *Emotion, Space and Society*, 38:100764, 2021. URL: https://www.scopus.com/inward/record.uri?eid=2-s2.0-85100197874&doi=10.1016%2fj.emospa.2021.100764&partnerID=40&md5=663c9726044eb266218db5b291726a3e, doi:10.1016/j.emospa.2021.100764.

[133] Adrian S. Z. Chase. Beyond elite control: residential reservoirs at caracol, belize. *Wiley Interdisciplinary Reviews: Water*, 3(6):885–897, 2016. URL: https://www.scopus.com/inward/record.uri?eid=2-s2.0-85016780545&doi=10.1002%2fwat2.1171&partnerID=40&md5=de52dd07f90007589d579902cf5c1512, doi:10.1002/wat2.1171.

[134] Chuanfa Chen and Yanyan Li. A fast global interpolation method for digital terrain model generation from large lidar-derived data. *Remote Sensing*, 11(11):1324, 2019. URL: https://www.scopus.com/inward/record.uri?eid=2-s2.0-85067388732&doi=10.3390%2frs11111324&partnerID=40&md5=bf621b1b897b59b7f8e80ee57669d658, doi:10.3390/rs11111324.

[135] Q. Chen, Q. Cheng, Y. Chen, K. Li, D. Wang, and S. Cao. The influence of sky view factor on daytime and nighttime urban land surface temperature in different spatial-temporal scales: a case study of beijing. *Remote Sensing*, 2021. URL: https://www.scopus.com/inward/record.uri?eid=2-s2.0-85117267569&doi=10.3390%2frs13204117&partnerID=40&md5=03fff992554335d8e3e251a5c652cdb9, doi:10.3390/rs13204117.

[136] C. Chen, H. Bagan, T. Yoshida, H. Borjigin, and J. Gao. Quantitative analysis of the building-level relationship between building form and land surface temperature using airborne lidar and thermal infrared data. *URBAN CLIMATE*, 2022. URL: https://www.scopus.com/inward/record.uri?eid=2-s2.0-85135578613&doi=10.1016%2fj.uclim.2022.101248&partnerID=40&md5=d60d41cf19ea8726ef090d5768bfdc4b, doi:10.1016/j.uclim.2022.101248.

[137] X. Chen, Z. Wang, Y. Bao, Q. Luo, and W. Wei. Combined impacts of buildings and urban remnant mountains on thermal environment in multi-mountainous city. *SUSTAINABLE CITIES AND SOCIETY*, 2022. URL: https://www.scopus.com/inward/record.uri?eid=2-s2.0-85139596343&doi=10.1016%2fj.scs.2022.104247&partnerID=40&md5=8a51406ce38fee60f78dfb3b03d808a5, doi:10.1016/j.scs.2022.104247.

[138] Emmanuel Chevigny, Laure Saligny, Ludovic Granjon, Dominique Goguey, Alexandra Cordier, Yves Pautrat, and Alain Giosa. Identifier et enregistrer des vestiges archéologiques sous couvert forestier à partir de données lidar : méthode et limites. *ArcheoSciences*, 42(2018):31–43, 2018. URL: https://www.scopus.com/inward/record.uri?eid=2-s2.0-85064679283&doi=10.4000%2farcheosciences.5727&partnerID=40&md5=3d3816bece0feadbf66b20f40c2d0915, doi:10.4000/archeosciences.5727.

[139] Francis Choi, Tarik Gouhier, Fernando Lima, Gil Rilov, Rui Seabra, and Brian Helmuth. Mapping physiology: biophysical mechanisms define scales of climate change impacts. *CONSERVATION PHYSIOLOGY*, 7(1):coz028, 2019. URL: https://www.scopus.com/inward/record.uri?eid=2-s2.0-85082705736&doi=10.1093%2fconphys%2fcoz028&partnerID=40&md5=6c4b258e7f65914a06ab650de96bacc3, doi:10.1093/conphys/coz028.

[140] František Chudý, Martina Slámová, Julián Tomaštík, Roberta Prokešová, and Martin Mokroš. Identification of micro-scale landforms of landslides using precise digital elevation models. *Geosciences (Switzerland)*, 9(3):117, 2019. URL: https://www.scopus.com/inward/record.uri?eid=2-s2.0-85065247438&doi=10.3390%2fgeosciences9030117&partnerID=40&md5=8c0f2c4f54ccb238c77b87d451e3b210, doi:10.3390/geosciences9030117.

[141] Bumseok Chun and Subhrajit Guhathakurta. Daytime and nighttime urban heat islands statistical models for atlanta. *Environment and Planning B: Urban Analytics and City Science*, 44(2):308–327, 2017. URL: https://www.scopus.com/inward/record.uri?eid=2-s2.0-85028619116&doi=10.1177%2f0265813515624685&partnerID=40&md5=c6841ec4e5d4a53f9c59a47dde9447f7, doi:10.1177/0265813515624685.

[142] Bumseok Chun and Subhrajit Guhathakurta. The impacts of three-dimensional surface characteristics on urban heat islands over the diurnal cycle. *PROFESSIONAL GEOGRAPHER*, 69(2):191–202, 2017. URL: https://www.scopus.com/inward/record.uri?eid=2-s2.0-84983507774&doi=10.1080%2f00330124.2016.1208102&partnerID=40&md5=1611b9f9dba565bbc3ad08b64d2141c5, doi:10.1080/00330124.2016.1208102.

[143] Bumseok Chun and Jean-Michel Guldmann. Impact of greening on the urban heat island: seasonal variations and mitigation strategies. *Computers, Environment and Urban Systems*, 71:165–176, 2018. URL: https://www.scopus.com/inward/record.uri?eid=2-s2.0-85047260094&doi=10.1016%2fj.compenvurbsys.2018.05.006&partnerID=40&md5=8a8ebdac70527c5b876a9a33035c0f80, doi:10.1016/j.compenvurbsys.2018.05.006.

[144] Douglas C. Comer, Jacob A. Comer, Ioana A. Dumitru, William S. Ayres, Maureece J. Levin, Katherine A. Seikel, Devin A. White, and Michael J. Harrower. Airborne lidar reveals a vast archaeological landscape at the nan madol world heritage site. *Remote Sensing*, 11(18):2152, 2019. URL: https://www.scopus.com/inward/record.uri?eid=2-s2.0-85072648611&doi=10.3390%2frs11182152&partnerID=40&md5=594bf680634884d70a644d81e5e5eba7, doi:10.3390/rs11182152.

[145] Š. Čonč, T. Oliveira, R. Portas, R. Černe, M. B. Valjavec, and M. Krofel. Dolines and cats: remote detection of karst depressions and their application to study wild felid ecology. *Remote Sensing*, 2022. URL: https://www.scopus.com/inward/record.uri?eid=2-s2.0-85123702795&doi=10.3390%2frs14030656&partnerID=40&md5=fa61a352955ae147b9a2323aca372721, doi:10.3390/rs14030656.

[146] J-M. Costa-García, J. Fonte, and M. Gago. The reassessment of the roman military presence in galicia and northern portugal through digital tools: archaeological diversity and historical problems. *Mediterranean Archaeology and Archaeometry*, 19(3):17–49, 2019. URL: https://www.scopus.com/inward/record.uri?eid=2-s2.0-85074189897&doi=10.5281%2fzenodo.3457524&partnerID=40&md5=8fbe14f86150f46777e56be25efb4abb, doi:10.5281/zenodo.3457524.

[147] Dave Cowley, Geert Verhoeven, and Arianna Traviglia. Editorial for special issue: "archaeological remote sensing in the 21st century: (re)defining practice and theory". *Remote Sensing*, 13(8):1431, 2021. URL: https://www.scopus.com/inward/record.uri?eid=2-s2.0-85104670340&doi=10.3390%2frs13081431&partnerID=40&md5=518bb3c88f1b052cf1c2409d520e2e26, doi:10.3390/rs13081431.

[148] Kieran F. Craven, Stephen McCarron, Xavier Monteys, and Dayton Dove. Interaction of multiple ice streams on the malin shelf during deglaciation of the last british–irish ice sheet. *JOURNAL OF QUATERNARY SCIENCE*, 36(2):153–168, 2021. URL: https://www.scopus.com/inward/record.uri?eid=2-s2.0-85099651939&doi=10.1002%2fjqs.3266&partnerID=40&md5=0ad35407676525443a250b2775d9c86d, doi:10.1002/jqs.3266.

[149] B. X. Currás Refojos, E. Martín-Hernández, L. F. López-González, and J. G. Castro. Two possible roman camps in the province of lugo: criticism and praise of the archaeological news. *Archivo Espanol de Arqueologia*, 2021. URL: https://www.scopus.com/inward/record.uri?eid=2-s2.0-85113800928&doi=10.3989%2fAESPA.094.021.13&partnerID=40&md5=fd7bdce6de10b016a5d1771c4f0cbeb5, doi:10.3989/AESPA.094.021.13.

[150] M. Danese, D. Gioia, V. Vitale, N. Abate, A. M. Amodio, R. Lasaponara, and N. Masini. Pattern recognition approach and lidar for the analysis and mapping of archaeological looting: application to an etruscan site. *Remote Sensing*, 2022. URL: https://www.scopus.com/inward/record.uri?eid=2-s2.0-85127741392&doi=10.3390%2frs14071587&partnerID=40&md5=a7634fd995d7d3629c3dee35ddd64082, doi:10.3390/rs14071587.

[151] B. Dang, Y. Liu, H. Lyu, X. Zhou, W. Du, C. Xuan, P. Xing, R. Yang, and F. Xiong. Assessment of urban climate environment and configuration of ventilation corridor: a refined study in xi'an. *Journal of Meteorological Research*, 36(6):914–930, 2022. URL: https://www.scopus.com/inward/record.uri?eid=2-s2.0-85146134905&doi=10.1007%2fs13351-022-2035-0&partnerID=40&md5=73e43497ceda7896c2bba97ca3834b92, doi:10.1007/s13351-022-2035-0.

[152] Peter Davies, Jodi Turnbull, and Susan Lawrence. Remote sensing landscapes of water management on the victorian goldfields, australia. *Journal of Archaeological Science*, 76:48–55, 2016. URL: https://www.scopus.com/inward/record.uri?eid=2-s2.0-84994663246&doi=10.1016%2fj.jas.2016.10.009&partnerID=40&md5=c577d9e1b96dd43304276c11ce2d34a2, doi:10.1016/j.jas.2016.10.009.

[153] John R. Davis, Erik Brubaker, and Kai Vetter. Fast neutron background characterization with the radiological multi-sensor analysis platform (radmap). *Nuclear Instruments and Methods in Physics Research, Section A: Accelerators, Spectrometers, Detectors and Associated Equipment*, 858:106–112, 2017. URL: https://www.scopus.com/inward/record.uri?eid=2-s2.0-85017129383&doi=10.1016%2fj.nima.2017.03.042&partnerID=40&md5=705ae606823a39d9f58dcf3ec3ef84e1, doi:10.1016/j.nima.2017.03.042.

[154] Catherine A. Delaney, Stephen McCarron, and Stephen Davis. Irish ice sheet dynamics during deglaciation of the central irish midlands: evidence of ice streaming and surging from airborne lidar. *Geomorphology*, 306:235–253, 2018. URL: https://www.scopus.com/inward/record.uri?eid=2-s2.0-85044651596&doi=10.1016%2fj.geomorph.2018.01.011&partnerID=40&md5=0e1c4919b923da605c88253fbe533ccb, doi:10.1016/j.geomorph.2018.01.011.

[155] C. Delaney. The development and impact of an ice-contact proglacial lake during the last glacial termination, palaeolake riada, central ireland. *JOURNAL OF QUATERNARY SCIENCE*, 2022. URL: https://www.scopus.com/inward/record.uri?eid=2-s2.0-85125837349&doi=10.1002%2fjqs.3412&partnerID=40&md5=610dc3fc2a57a8dd7cf7204f362c0dff, doi:10.1002/jqs.3412.

[156] Y. Di, D. Hu, M. Liu, S. Chen, C. Yu, and Y. Wang. Radiation correction considering geometric effect of urban area and its application in temperature retrieval through remote sensing. *Yaogan Xuebao/Journal of Remote Sensing*, 25(8):1821–1835, 2021. URL: https://www.scopus.com/inward/record.uri?eid=2-s2.0-85115274404&doi=10.11834%2fjrs.20211167&partnerID=40&md5=01c94ac1907b381a770eb10ca50c89f4, doi:10.11834/jrs.20211167.

[157] Ana Djuricic, Peter Dorninger, Clemens Nothegger, Mathias Harzhauser, Balázs Székely, Sascha Rasztovits, Oleg Mandic, Gábor Molnár, and Norbert Pfeifer. High-resolution 3d surface modeling of a fossil oyster reef. *GEOSPHERE*, 12(5):1457–1477, 2016. URL: https://www.scopus.com/inward/record.uri?eid=2-s2.0-85053361419&doi=10.1130%2fGES01282.1&partnerID=40&md5=1ba8a2c2c29c691cbc1ceb15153f6871, doi:10.1130/GES01282.1.

[158] S. Dominika, Bartłomiej, W. Krzysztof, P. B. Dąbek, J. M. Bastante, and W. Izabela. Inca water channel flow analysis based on 3d models from terrestrial and uav laser scanning at the chachabamba archaeological site (machu picchu national archaeological park, peru). *Journal of Archaeological Science*, 2022. URL: https://www.scopus.com/inward/record.uri?eid=2-s2.0-85119251321&doi=10.1016%2fj.jas.2021.105515&partnerID=40&md5=edf3ec5060d8eea62a3ba195cd81c91e, doi:10.1016/j.jas.2021.105515.

[159] Michael Doneus. Openness as visualization technique for interpretative mapping of airborne lidar derived digital terrain models. *Remote Sensing*, 5(12):6427–6442, 2013. URL: https://www.scopus.com/inward/record.uri?eid=2-s2.0-84891448248&doi=10.3390%2frs5126427&partnerID=40&md5=a055024abca69dff73bbc0f580d7ec71, doi:10.3390/rs5126427.

[160] Michael Doneus, Nives Doneus, Christian Briese, Michael Pregesbauer, Gottfried Mandlburger, and Geert Verhoeven. Airborne laser bathymetry – detecting and recording submerged archaeological sites from the air. *Journal of Archaeological Science*, 40(4):2136–2151, 2013. URL: https://www.scopus.com/inward/record.uri?eid=2-s2.0-84873815454&doi=10.1016%2fj.jas.2012.12.021&partnerID=40&md5=e7da88b92dcf5698a43eed2278a9f9f1, doi:10.1016/j.jas.2012.12.021.

[161] Nives Doneus, Michael Doneus, and Zrinka Ettinger-Starčić. The ancient city of osor, northern adriatic, in integrated archaeological prospection. *Hortus Artium Mediaevalium*, 23(2):761–775, 2017. URL:

https://www.scopus.com/inward/record.uri?eid=2-s2.0-85021902028&doi=10.1484%2fJ.HAM.5.113761&partnerID=40&md5=21c706c1bbcadfd08ef13416816dfe0a, doi:10.1484/J.HAM.5.113761.

[162] M. Doneus, Ł. Banaszek, and G. J. Verhoeven. The impact of vegetation on the visibility of archaeological features in airborne laser scanning datasets from different acquisition dates. *Remote Sensing*, 2022. URL: https://www.scopus.com/inward/record.uri?eid=2-s2.0-85124792518&doi=10.3390%2frs14040858&partnerID=40&md5=2cfc63f82dc8e698677afe209be0d0ad, doi:10.3390/rs14040858.

[163] M. Doneus, B. Höfle, D. Kempf, G. Daskalakis, and M. Shinoto. Human-in-the-loop development of spatially adaptive ground point filtering pipelines—an archaeological case study. *Archaeological Prospection*, 2022. URL: https://www.scopus.com/inward/record.uri?eid=2-s2.0-85137461623&doi=10.1002%2farp.1873&partnerID=40&md5=b6bcf6912a152ea0438202b083b65bef, doi:10.1002/arp.1873.

[164] M. Doneus, N. Doneus, and D. Cowley. Confronting complexity: interpretation of a dry stone walled landscape on the island of cres, croatia. *Land*, 2022. URL: https://www.scopus.com/inward/record.uri?eid=2-s2.0-85140871755&doi=10.3390%2fland11101672&partnerID=40&md5=480fbaf219a730575eec4c2abb1f5a5d, doi:10.3390/land11101672.

[165] A. Dorison. Ancient agriculture on lava flows: using lidar and soil science to reassess pre-hispanic farming on malpaís landforms in west mexico. *Journal of Ethnobiology*, 42(2):131–151, 2022. URL: https://www.scopus.com/inward/record.uri?eid=2-s2.0-85134747852&doi=10.2993%2f0278-0771-42.2.131&partnerID=40&md5=0fb71713444f7a12045c73b4b3c63ef1, doi:10.2993/0278-0771-42.2.131.

[166] N.A.K. Douglass and C. S. Fish. That's a relief: assessing beauty, realism, and landform clarity in multilayer terrain maps. *Cartographic Perspectives*, 2022(100):45–66, 2022. URL: https://www.scopus.com/inward/record.uri?eid=2-s2.0-85146219407&doi=10.14714%2fCP100.1727&partnerID=40&md5=9146501aa984aa9a9879368c1bdf3201, doi:10.14714/CP100.1727.

[167] C. Doyle, S. Luzzadder-Beach, and T. Beach. Advances in remote sensing of the early anthropocene in tropical wetlands: from biplanes to lidar and machine learning. *Progress in Physical Geography*, 2022. URL: https://www.scopus.com/inward/record.uri?eid=2-s2.0-85140657894&doi=10.1177%2f03091333221134185&partnerID=40&md5=ece6b05c8c6866e015c756aa571e28ff, doi:10.1177/03091333221134185.

[168] E. Draganits, M. Doneus, T. Gansum, L. Gustavsen, E. Nau, C. Tonning, I. Trinks, and W. Neubauer. The late nordic iron age and viking age royal burial site of borre in norway: als- and gpr-based landscape reconstruction and harbour location at an uplifting coastal area. *Quaternary International*, 367:96–110, 2015. URL: https://www.scopus.com/inward/record.uri?eid=2-s2.0-84928780285&doi=10.1016%2fj.quaint.2014.04.045&partnerID=40&md5=618aa461ccd08c150ea4fbe845fbaa81, doi:10.1016/j.quaint.2014.04.045.

[169] Lia Duarte, Ana Teodoro, Dalmiro Maia, and Domingos Barbosa. Radio astronomy demonstrator: assessment of the appropriate sites through a gis open source application. *ISPRS INTERNATIONAL JOURNAL OF GEO-INFORMATION*, 5(11):209, 2016. URL: https://www.scopus.com/inward/record.uri?eid=2-s2.0-85032345197&doi=10.3390%2fijgi5110209&partnerID=40&md5=bc82a36c10aa324dc12d7dce8cb786e9, doi:10.3390/ijgi5110209.

[170] Steve Dübel and Heidrun Schumann. Visualization of features in 3d terrain. *ISPRS INTERNATIONAL JOURNAL OF GEO-INFORMATION*, 6(11):357, 2017. URL: https://www.scopus.com/inward/record.uri?eid=2-s2.0-85044603354&doi=10.3390%2fijgi6110357&partnerID=40&md5=09703073e5c5051662a0e3bbb0f0a7c2, doi:10.3390/ijgi6110357.

[171] Gary Duckers. Bridging the 'geospatial divide' in archaeology: community based interpretation of lidar data. *Internet Archaeology*, 2013. URL: https://www.scopus.com/inward/record.uri?eid=2-s2.0-85088181177&doi=10.11141%2fia.35.2&partnerID=40&md5=7f991ecb0dcda722181d0dff6767f5e3, doi:10.11141/ia.35.2.

[172] Hamid Ebrahimy and Mohsen Azadbakht. Downscaling modis land surface temperature over a heterogeneous area: an investigation of machine learning techniques, feature selection, and impacts of mixed pixels. *Computers and Geosciences*, 124:93–102, 2019. URL: https://www.scopus.com/inward/record.uri?eid=2-s2.0-85059840570&doi=10.1016%2fj.cageo.2019.01.004&partnerID=40&md5=15bc0c7273205836c2f27c2c0932a606, doi:10.1016/j.cageo.2019.01.004.

[173] Pastor Fábrega-Álvarez and César Parcero-Oubiña. Now you see me. an assessment of the visual recognition and control of individuals in archaeological landscapes. *Journal of Archaeological Science*, 104:56–74, 2019. URL: https://www.scopus.com/inward/record.uri?eid=2-s2.0-85062017957&doi=10.1016%2fj.jas.2019.02.002&partnerID=40&md5=5fb0eadc78f04982dec2d0023070d950, doi:10.1016/j.jas.2019.02.002.

[174] Xiao-Yi Fang, Chen Cheng, Yong-Hong Liu, Wu-Peng Du, Xiao-Jun Xiao, and Bing Dang. A climatic environmental performance assessment method for ecological city construction: application to beijing yanqi lake. *ADVANCES IN CLIMATE CHANGE RESEARCH*, 6(1):23–35, 2015. URL: https://www.scopus.com/inward/record.uri?eid=2-s2.0-84945284998&doi=10.1016%2fj.accre.2015.08.001&partnerID=40&md5=949c6179a82cd41ed8e03ce695be6d45, doi:10.1016/j.accre.2015.08.001.

[175] Y. Fang and L. Zhao. Assessing the environmental benefits of urban ventilation corridors: a case study in hefei, china. *BUILDING AND ENVIRONMENT*, 2022. URL: https://www.scopus.com/inward/record.uri?eid=2-s2.0-85123679247&doi=10.1016%2fj.buildenv.2022.108810&partnerID=40&md5=06cb327d9bd5c0a8933aab040a82c165, doi:10.1016/j.buildenv.2022.108810.

[176] Marianna Farmakis-Serebryakova and Lorenz Hurni. Comparison of relief shading techniques applied to landforms. *ISPRS INTERNATIONAL JOURNAL OF GEO-INFORMATION*, 9(4):253, 2020. URL: https://www.scopus.com/inward/record.uri?eid=2-s2.0-85083790955&doi=10.3390%2fijgi9040253&partnerID=40&md5=45b27f539c07d2ad19d8f44baaed4337, doi:10.3390/ijgi9040253.

[177] Massimiliano Favalli and Alessandro Fornaciai. Visualization and comparison of dem-derived parameters. application to volcanic areas. *Geomorphology*, 290:69–84, 2017. URL: https://www.scopus.com/inward/record.uri?eid=2-s2.0-85017618865&doi=10.1016%2fj.geomorph.2017.02.029&partnerID=40&md5=b2bcd7b5128765a45ded2aa6fa635b7c, doi:10.1016/j.geomorph.2017.02.029.

[178] Massimiliano Favalli, Alessandro Fornaciai, Luca Nannipieri, Andrew Harris, Sonia Calvari, and Charline Lormand. Uav-based remote sensing surveys of lava flow fields: a case study from etna's 1974 channel-fed lava flows. *BULLETIN OF VOLCANOLOGY*, 2018. URL: https://www.scopus.com/inward/record.uri?eid=2-s2.0-85042530326&doi=10.1007%2fs00445-018-1192-6&partnerID=40&md5=7a43bc72c7a44db3bf1afbb07d92f646, doi:10.1007/s00445-018-1192-6.

[179] D. R. Feldman, M. Worden, N. Falco, P. J. Dennedy-Frank, J. Chen, B. Dafflon, and H. Wainwright. Three-dimensional surface downwelling longwave radiation clear-sky effects in the upper colorado river basin. *Geophysical Research Letters*, 2022. URL: https://www.scopus.com/inward/record.uri?eid=2-s2.0-85125954892&doi=10.1029%2f2021GL094605&partnerID=40&md5=740c2705c1c87dfff95849bbbb6192ab, doi:10.1029/2021GL094605.

[180] Juan Fernandez-Diaz, William Carter, Ramesh Shrestha, and Craig Glennie. Now you see it$…$ now you don't: understanding airborne mapping lidar collection and data product generation for archaeological research in mesoamerica. *Remote Sensing*, 6(10):9951–10001, 2014. URL: https://www.scopus.com/inward/record.uri?eid=2-s2.0-84912141883&doi=10.3390%2frs6109951&partnerID=40&md5=b2a3c57fd4570acc0108e88a5d9c786f, doi:10.3390/rs6109951.

[181] Javier Fernández-Lozano and Gabriel Gutiérrez-Alonso. Improving archaeological prospection using localized uavs assisted photogrammetry: an example from the roman gold district of the eria river valley (nw spain). *Journal of Archaeological Science: Reports*, 5:509–520, 2016. URL: https://www.scopus.com/inward/record.uri?eid=2-s2.0-84954115074&doi=10.1016%2fj.jasrep.2016.01.007&partnerID=40&md5=49cbc59f56492c249d46a67f710b9cfd, doi:10.1016/j.jasrep.2016.01.007.

[182] J. Fernández-Lozano, J. J. Palao-Vicente, J. A. Blanco-Sánchez, G. Gutiérrez-Alonso, J. Remondo, J. Bonachea, M. Morellón, and A. González-Díez. Gold-bearing plio-quaternary deposits: insights from airborne lidar technology into the landscape evolution during the early roman mining works in north-west spain. *Journal of Archaeological Science: Reports*, 24:843–855, 2019. URL: https://www.scopus.com/inward/record.uri?eid=2-s2.0-85063012446&doi=10.1016%2fj.jasrep.2019.03.001&partnerID=40&md5=4612132346d35d18c9692b57be3ee24c, doi:10.1016/j.jasrep.2019.03.001.

[183] Javier Fernández-Lozano, Rosa M. Carrasco, Javier Pedraza, and Antonio Bernardo-Sánchez. The anthropic landscape imprint around one of the largest roman hydraulic gold mines in europe: sierra

del teleno (nw spain). *Geomorphology*, 357:107094, 2020. URL: https://www.scopus.com/inward/record.uri?eid=2-s2.0-85081023239&doi=10.1016%2fj.geomorph.2020.107094&partnerID=40&md5=7835f795e25c8786a95dad852c261508, doi:10.1016/j.geomorph.2020.107094.

[184] J. Fernández-Lozano, G. Gutiérrez-Alonso, R. M. Carrasco, and J. Pedraza. Lidar datasets applied to roman gold mining studies in nw iberia. response to paper: roman gold mining at “las miédolas” (nw spain): lidar and photo interpretation in the analysis of “peines”. *Geoheritage*, 2022. URL: https://www.scopus.com/inward/record.uri?eid=2-s2.0-85126132440&doi=10.1007%2fs12371-022-00674-z&partnerID=40&md5=074f9f69da5b084a489d2f948ba9398f, doi:10.1007/s12371-022-00674-z.

[185] R. Filzwieser and S. Eichert. Towards an online database for archaeological landscapes. using the web based, open source software openatlas for the acquisition, analysis and dissemination of archaeological and historical data on a landscape basis. *Heritage*, 3(4):1385–1401, 2020. URL: https://www.scopus.com/inward/record.uri?eid=2-s2.0-85118808571&doi=10.3390%2fheritage3040077&partnerID=40&md5=1916c13470d4c5f8652f73afdd2d3b13, doi:10.3390/heritage3040077.

[186] Roland Filzwieser, Vujadin Ivanišević, Geert J. Verhoeven, Christian Gugl, Klaus Löcker, Ivan Bugarski, Hannes Schiel, Mario Wallner, Immo Trinks, Tanja Trausmuth, Alois Hinterleitner, Nemanja Marković, Roald Docter, Falko Daim, and Wolfgang Neubauer. Integrating geophysical and photographic data to visualize the quarried structures of the roman town of bassianae. *Remote Sensing*, 13(12):2384, 2021. doi:10.3390/rs13122384.

[187] R. Filzwieser, D. Ruß, M. Kucera, M. Doneus, G. Hasenhündl, G. J. Verhoeven, G. Zotti, A. Lenzhofer, G. Stüttler, M. Pisz, and W. Neubauer. History and archaeology in discourse on the dernberg–reconstructing the historical landscape of a medieval motte-and-bailey castle and deserted village. *Heritage*, 5(3):2123–2141, 2022. URL: https://www.scopus.com/inward/record.uri?eid=2-s2.0-85138596281&doi=10.3390%2fheritage5030111&partnerID=40&md5=176af675f5350c20b9ef4086ad5c64cb, doi:10.3390/heritage5030111.

[188] J. Flyckt, F. Andersson, N. Lavesson, L. Nilsson, and A. M. Å gren. Detecting ditches using supervised learning on high-resolution digital elevation models. *Expert Systems with Applications*, 2022. URL: https://www.scopus.com/inward/record.uri?eid=2-s2.0-85128240716&doi=10.1016%2fj.eswa.2022.116961&partnerID=40&md5=39b8ad28d9d19952c67346644ee5088b, doi:10.1016/j.eswa.2022.116961.

[189] G. Fontana. Italy's hidden hillforts: a large-scale lidar-based mapping of samnium. *Journal of Field Archaeology*, 47(4):245–261, 2022. URL: https://www.scopus.com/inward/record.uri?eid=2-s2.0-85127648048&doi=10.1080%2f00934690.2022.2031465&partnerID=40&md5=8a82c9ec3647b6ddefb6a308e86c59dc, doi:10.1080/00934690.2022.2031465.

[190] João Fonte, João Pimenta, Carlos Pereira, and Ana Margarida Arruda. Revisitando os chões de alpompé com técnicas de deteção remota: novas evidências sobre os sistemas defensivos romano-republicanos. *Cuadernos de Prehistoria y Arqueologia de la Universidad Autonoma de Madrid*, 2020(46):215–238, 2020. URL: https://www.scopus.com/inward/record.uri?eid=2-s2.0-85099099769&doi=10.15366%2fCUPAUAM2020.46.008&partnerID=40&md5=521f7ab253f4bdb7d7d9c0907ed2fc1e, doi:10.15366/CUPAUAM2020.46.008.

[191] J. Fonte, J. M. Costa-García, and M. Gago. O penedo dos lobos: roman military activity in the uplands of the galician massif (northwest iberia). *Journal of Conflict Archaeology*, 2021. URL: https://www.scopus.com/inward/record.uri?eid=2-s2.0-85115232812&doi=10.1080%2f15740773.2021.1980757&partnerID=40&md5=523bc821ee5d83460a7458185204748a, doi:10.1080/15740773.2021.1980757.

[192] J. Fonte, E. Meunier, J. A. Gonçalves, F. Dias, A. Lima, L. Gonçalves-Seco, and E. Figueiredo. An integrated remote-sensing and gis approach for mapping past tin mining landscapes in northwest iberia. *Remote Sensing*, 2021. URL: https://www.scopus.com/inward/record.uri?eid=2-s2.0-85114101887&doi=10.3390%2frs13173434&partnerID=40&md5=78824f1c002c4d7061705989cc55b986, doi:10.3390/rs13173434.

[193] Giuseppe Formetta, Giovanna Capparelli, Olaf David, Timothy Green, and Riccardo Rigon. Integration of a three-dimensional process-based hydrological model into the object modeling system. *Water (Switzerland)*, 8(1):12, 2016. URL: https://www.scopus.com/inward/record.uri?eid=2-s2.0-84958778331&doi=10.3390%2fw8010012&partnerID=40&md5=262593246e6e1793a2cd060cfb94eff7, doi:10.3390/w8010012.

[194] M.F.L. Gacha and M. Koch. Distributed energy balance flux modelling of mass balances in the artesonraju glacier and discharge in the basin of artesoncocha, cordillera blanca, peru. *Climate*, 2021. URL: https://www.scopus.com/inward/record.uri?eid=2-s2.0-85115782671&doi=10.3390%2fcli9090143&partnerID=40&md5=9d9b59d1adf116786e8e4ef14d672cbb, doi:10.3390/cli9090143.

[195] Gallwey, Eyre, Tonkins, and Coggan. Bringing lunar lidar back down to earth: mapping our industrial heritage through deep transfer learning. *Remote Sensing*, 11(17):1994, 2019. URL: https://www.scopus.com/inward/record.uri?eid=2-s2.0-85071983589&doi=10.3390%2frs11171994&partnerID=40&md5=9b0df73be60e89bab802eedc17bb4771, doi:10.3390/rs11171994.

[196] T. G. Garrison, A. E. Thompson, S. Krause, S. Eshleman, J. C. Fernandez-Diaz, J. D. Baldwin, and R. Cambranes. Assessing the lidar revolution in the maya lowlands: a geographic approach to understanding feature classification accuracy. *Progress in Physical Geography*, 2022. URL: https://www.scopus.com/inward/record.uri?eid=2-s2.0-85142027448&doi=10.1177%2f03091333221138050&partnerID=40&md5=dff68af9cb092fa1a6d9aa1314b5b9a3, doi:10.1177/03091333221138050.

[197] N. Gazzán, C. Cancela-Cereijo, C. Gianotti, P. Fábrega-álvarez, L. Del Puerto, and F. Criado-Boado. From mounds to villages: the social construction of the landscape during the middle and late holocene in the india muerta lowlands, uruguay. *Land*, 2022. URL: https://www.scopus.com/inward/record.uri?eid=2-s2.0-85127558753&doi=10.3390%2fland11030441&partnerID=40&md5=db3941c7db6fb3a2ed4077b25542825e, doi:10.3390/land11030441.

[198] Wouter Gheyle, Birger Stichelbaut, Timothy Saey, Nicolas Note, Hanne van den Berghe, Veerle van Eetvelde, Marc van Meirvenne, and Jean Bourgeois. Scratching the surface of war. airborne laser scans of the great war conflict landscape in flanders (belgium). *APPLIED GEOGRAPHY*, 90:55–68, 2018. URL: https://www.scopus.com/inward/record.uri?eid=2-s2.0-85037356797&doi=10.1016%2fj.apgeog.2017.11.011&partnerID=40&md5=bdb92ec5ea62f94b6c6bc84ce63600d0, doi:10.1016/j.apgeog.2017.11.011.

[199] A. González-Díez, J. A. Barreda-Argüeso, L. Rodríguez-Rodríguez, and J. Fernández-Lozano. The use of filters based on the fast fourier transform applied to dems for the objective mapping of karstic features. *Geomorphology*, 385:107724, 2021. URL: https://www.scopus.com/inward/record.uri?eid=2-s2.0-85104388090&doi=10.1016%2fj.geomorph.2021.107724&partnerID=40&md5=3b3aa2fcff626cde7d3a775fc3d9a822, doi:10.1016/j.geomorph.2021.107724.

[200] Benedikt Grammer, Erich Draganits, Martin Gretscher, and Ulrike Muss. Lidar-guided archaeological survey of a mediterranean landscape: lessons from the ancient greek polis of kolophon (ionia, western anatolia). *Archaeological Prospection*, 24(4):311–333, 2017. URL: https://www.scopus.com/inward/record.uri?eid=2-s2.0-85018713268&doi=10.1002%2farp.1572&partnerID=40&md5=7992f22f19572919df52301244cc2525, doi:10.1002/arp.1572.

[201] G. Grau, J. Vicent, and J. Moreno. Análisis del efecto topográfico en la corrección radiométrica de imágenes meris. *Revista de Teledeteccion*, pages 99, 2014. URL: https://www.scopus.com/inward/record.uri?eid=2-s2.0-84918784195&doi=10.4995%2fraet.2014.2299&partnerID=40&md5=773417d684690a672751734b67ce69df, doi:10.4995/raet.2014.2299.

[202] Y. Gu and X.-Y. You. A spatial quantile regression model for driving mechanism of urban heat island by considering the spatial dependence and heterogeneity: an example of beijing, china. *SUSTAINABLE CITIES AND SOCIETY*, 2022. URL: https://www.scopus.com/inward/record.uri?eid=2-s2.0-85123029131&doi=10.1016%2fj.scs.2022.103692&partnerID=40&md5=754969c4b3674b02da5b33bda9474770, doi:10.1016/j.scs.2022.103692.

[203] N. Gumede, O. Mutanga, and M. Sibanda. Mapping leaf area index of the yellowwood tree species in an afromontane mistbelt forest of southern africa using topographic variables. *Remote Sensing Applications: Society and Environment*, 2022. URL: https://www.scopus.com/inward/record.uri?eid=2-s2.0-85131145146&doi=10.1016%2fj.rsase.2022.100778&partnerID=40&md5=aec1477bd6af146d52a134e39fdd18e6, doi:10.1016/j.rsase.2022.100778.

[204] Andong Guo, Jun Yang, Xiangming Xiao, Jianhong Xia, Cui Jin, and Xueming Li. Influences of urban spatial form on urban heat island effects at the community level in china. *SUSTAINABLE CITIES AND SO-*

CIETY, 53:101972, 2020. URL: https://www.scopus.com/inward/record.uri?eid=2-s2.0-85075378667&doi=10.1016%2fj.scs.2019.101972&partnerID=40&md5=49d3c06109a4800fa03aaebf0c5ecfcb, doi:10.1016/j.scs.2019.101972.

[205] C. Guo, Q. Xu, X. Dong, W. Li, K. Zhao, H. Lu, and Y. Ju. Geohazard recognition and inventory mapping using airborne lidar data in complex mountainous areas. *Journal of Earth Science*, 32(5):1079–1091, 2021. URL: https://www.scopus.com/inward/record.uri?eid=2-s2.0-85116257858&doi=10.1007%2fs12583-021-1467-2&partnerID=40&md5=e134486ac25e8ea46d1e3fe665c8a524, doi:10.1007/s12583-021-1467-2.

[206] C. Guo, Q. Xu, X. Dong, X. Pan, X. Liu, and J. She. Landslide recognition based on svf terrain visualization method: a case study of a typical landslide in danba, sichuan, china. *Journal of Chengdu University of Technology (Science and Technology Edition)*, 48(6):705–713, 2021. URL: https://www.scopus.com/inward/record.uri?eid=2-s2.0-85131373560&doi=10.3969%2fj.issn.1671-9727.2021.06.07&partnerID=40&md5=baf6eee132df79398620388926651 3f6, doi:10.3969/j.issn.1671-9727.2021.06.07.

[207] Alexandre Guyot, Laurence Hubert-Moy, and Thierry Lorho. Detecting neolithic burial mounds from lidar-derived elevation data using a multi-scale approach and machine learning techniques. *Remote Sensing*, 10(2):225, 2018. URL: https://www.scopus.com/inward/record.uri?eid=2-s2.0-85042553801&doi=10.3390%2frs10020225&partnerID=40&md5=96e2ada7be607bfac11b221ff01e79ef, doi:10.3390/rs10020225.

[208] Alexandre Guyot, Marc Lennon, and Laurence Hubert-Moy. Objective comparison of relief visualization techniques with deep cnn for archaeology. *Journal of Archaeological Science: Reports*, 38:103027, 2021. URL: https://www.scopus.com/inward/record.uri?eid=2-s2.0-85106463536&doi=10.1016%2fj.jasrep.2021.103027&partnerID=40&md5=edd8737fe9f8aebc4660be18e01438ef, doi:10.1016/j.jasrep.2021.103027.

[209] D. Han, H. An, F. Wang, X. Xu, Z. Qiao, M. Wang, X. Sui, S. Liang, X. Hou, H. Cai, and Y. Liu. Understanding seasonal contributions of urban morphology to thermal environment based on boosted regression tree approach. *BUILDING AND ENVIRONMENT*, 2022. URL: https://www.scopus.com/inward/record.uri?eid=2-s2.0-85141539025&doi=10.1016%2fj.buildenv.2022.109770&partnerID=40&md5=8e5fe17f2124971151d816354a8193cf, doi:10.1016/j.buildenv.2022.109770.

[210] Dalei Hao, Jianguang Wen, Qing Xiao, Shengbiao Wu, Xingwen Lin, Dongqin You, and Yong Tang. Modeling anisotropic reflectance over composite sloping terrain. *IEEE TRANSACTIONS ON GEOSCIENCE AND REMOTE SENSING*, 56(7):3903–3923, 2018. URL: https://www.scopus.com/inward/record.uri?eid=2-s2.0-85045219411&doi=10.1109%2fTGRS.2018.2816015&partnerID=40&md5=6f996f40fba94f93814ad2392c92dc45, doi:10.1109/TGRS.2018.2816015.

[211] Dalei Hao, Jianguang Wen, Qing Xiao, Shengbiao Wu, Xingwen Lin, Baocheng Dou, Dongqin You, and Yong Tang. Simulation and analysis of the topographic effects on snow-free albedo over rugged terrain. *Remote Sensing*, 10(2):278, 2018. URL: https://www.scopus.com/inward/record.uri?eid=2-s2.0-85042541287&doi=10.3390%2frs10020278&partnerID=40&md5=b36740ab1a8111c20321d35f5bd4251d, doi:10.3390/rs10020278.

[212] D. Hao, J. Wen, Q. Xiao, D. You, X. Wu, X. Lin, and S. Wu. An accuracy assessment method for dem upscaling based on energy factor. *Wuhan Daxue Xuebao (Xinxi Kexue Ban)/Geomatics and Information Science of Wuhan University*, 44(4):570–577, 2019. URL: https://www.scopus.com/inward/record.uri?eid=2-s2.0-85068071663&doi=10.13203%2fj.whugis20170126&partnerID=40&md5=694bc79c694e03cb40a44cb174f73b7b, doi:10.13203/j.whugis20170126.

[213] Dalei Hao, Jianguang Wen, Qing Xiao, Dongqin You, and Yong Tang. An improved topography-coupled kernel-driven model for land surface anisotropic reflectance. *IEEE TRANSACTIONS ON GEOSCIENCE AND REMOTE SENSING*, 58(4):2833–2847, 2020. URL: https://www.scopus.com/inward/record.uri?eid=2-s2.0-85082884008&doi=10.1109%2fTGRS.2019.2956705&partnerID=40&md5=f796c157c264285137f6714fe5f1c608, doi:10.1109/TGRS.2019.2956705.

[214] D. Hao, G. Bisht, Y. Gu, W.-L. Lee, K.-N. Liou, and L. R. Leung. A parameterization of sub-grid topographical effects on solar radiation in the e3sm land model (version 1.0): implementation and evaluation over the tibetan plateau. *Geoscientific Model Development*, 14(10):6273–6289, 2021. URL:

https://www.scopus.com/inward/record.uri?eid=2-s2.0-85117955625&doi=10.5194%2fgmd-14-6273-2021&partnerID=40&md5=22527feb9c011fff77bccc5d2af38c05, doi:10.5194/gmd-14-6273-2021.

[215] Umesh Haritashya, Jeffrey Kargel, Dan Shugar, Gregory Leonard, Katherine Strattman, C. Watson, David Shean, Stephan Harrison, Kyle Mandli, and Dhananjay Regmi. Evolution and controls of large glacial lakes in the nepal himalaya. *Remote Sensing*, 10(5):798, 2018. URL: https://www.scopus.com/inward/record.uri?eid=2-s2.0-85047532687&doi=10.3390%2frs10050798&partnerID=40&md5=13c7077325757b5ab9adc1da1b82c3ab, doi:10.3390/rs10050798.

[216] W. He, S. Cao, M. Du, D. Hu, Y. Mo, M. Liu, J. Zhao, and Y. Cao. How do two-and three-dimensional urban structures impact seasonal land surface temperatures at various spatial scales? a case study for the northern part of brooklyn, new york, usa. *Remote Sensing*, 2021. URL: https://www.scopus.com/inward/record.uri?eid=2-s2.0-85113398171&doi=10.3390%2frs13163283&partnerID=40&md5=f8ebc81602c0c0c82d33d9a6c52c9fb2, doi:10.3390/rs13163283.

[217] Edward R. Henry, Carl R. Shields, and Tristram R. Kidder. Mapping the adena-hopewell landscape in the middle ohio valley, usa: multi-scalar approaches to lidar-derived imagery from central kentucky. *Journal of Archaeological Method and Theory*, 26(4):1513–1555, 2019. URL: https://www.scopus.com/inward/record.uri?eid=2-s2.0-85075556738&doi=10.1007%2fs10816-019-09420-2&partnerID=40&md5=2caa9fada64148257b76cfcc823e2683, doi:10.1007/s10816-019-09420-2.

[218] Edward R. Henry, Alice P. Wright, Sarah C. Sherwood, Stephen B. Carmody, Casey R. Barrier, and Christopher van de Ven. Beyond never-never land: integrating lidar and geophysical surveys at the johnston site, pinson mounds state archaeological park, tennessee, usa. *Remote Sensing*, 12(15):2364, 2020. URL: https://www.scopus.com/inward/record.uri?eid=2-s2.0-85089693570&doi=10.3390%2fRS12152364&partnerID=40&md5=4baf750d77410461d626540ae9b96580, doi:10.3390/RS12152364.

[219] Edward R. Henry, Natalie G. Mueller, and Mica B. Jones. Ritual dispositions, enclosures, and the passing of time: a biographical perspective on the winchester farm earthwork in central kentucky, usa. *JOURNAL OF ANTHROPOLOGICAL ARCHAEOLOGY*, 62:101294, 2021. URL: https://www.scopus.com/inward/record.uri?eid=2-s2.0-85103970195&doi=10.1016%2fj.jaa.2021.101294&partnerID=40&md5=224888b1769e319db7501740d619314d, doi:10.1016/j.jaa.2021.101294.

[220] Jae Heo, Jaehoon Jung, Byungil Kim, and SangUk Han. Digital elevation model-based convolutional neural network modeling for searching of high solar energy regions. *APPLIED ENERGY*, 262:114588, 2020. URL: https://www.scopus.com/inward/record.uri?eid=2-s2.0-85078985189&doi=10.1016%2fj.apenergy.2020.114588&partnerID=40&md5=a01561b69fd26daa81714ecec5276871, doi:10.1016/j.apenergy.2020.114588.

[221] I. Herzog. Computational approaches towards the understanding of past boundaries: a case study based on archaeological and historical data in a hilly region in germany. *IT - Information Technology*, 64(6):261–283, 2022. URL: https://www.scopus.com/inward/record.uri?eid=2-s2.0-85143282936&doi=10.1515%2fitit-2022-0010&partnerID=40&md5=a1ecb7165a8588c3a51db8f700acb772, doi:10.1515/itit-2022-0010.

[222] Ralf Hesse. Geomorphological traces of conflict in high-resolution elevation models. *APPLIED GEOGRAPHY*, 46:11–20, 2014. URL: https://www.scopus.com/inward/record.uri?eid=2-s2.0-84887522080&doi=10.1016%2fj.apgeog.2013.10.004&partnerID=40&md5=9f35510bcde41f4ac31605ac83b75a0f, doi:10.1016/j.apgeog.2013.10.004.

[223] Hung Chak Ho, Man Sing Wong, Lin Yang, Wenzhong Shi, Jinxin Yang, Muhammad Bilal, and Ta-Chien Chan. Spatiotemporal influence of temperature, air quality, and urban environment on cause-specific mortality during hazy days. *ENVIRONMENT INTERNATIONAL*, 112:10–22, 2018. URL: https://www.scopus.com/inward/record.uri?eid=2-s2.0-85037857158&doi=10.1016%2fj.envint.2017.12.001&partnerID=40&md5=e97770ca8996300e93156b98cf0d9d10, doi:10.1016/j.envint.2017.12.001.

[224] Hung Chak Ho and Man Sing Wong. Urban environmental influences on the temperature-mortality relationship associated mental disorders and cardiorespiratory diseases during normal summer days in a subtropical city. *ENVIRONMENTAL SCIENCE AND POLLUTION RESEARCH*, 26(23):24272–24285, 2019. URL: https://www.scopus.com/inward/record.uri?eid=2-s2.0-85067847334&doi=10.1007%

2fs11356-019-05594-0&partnerID=40&md5=e909fbb8a2ae8c7980a78e2df8400102, doi:10.1007/s11356-019-05594-0.

[225] Hung Chak Ho, Man Sing Wong, Ho Yin Man, Yuan Shi, and Sawaid Abbas. Neighborhood-based subjective environmental vulnerability index for community health assessment: development, validation and evaluation. *SCIENCE OF THE TOTAL ENVIRONMENT*, 654:1082–1090, 2019. URL: https://www.scopus.com/inward/record.uri?eid=2-s2.0-85056631254&doi=10.1016%2fj.scitotenv.2018.11.136&partnerID=40&md5=e2c57da8ceb3f84fc7769dcaf878b65d, doi:10.1016/j.scitotenv.2018.11.136.

[226] Hung Chak Ho, Ho Yin Man, Man Sing Wong, Yuan Shi, and Blake Byron Walker. Perceived differences in the (re)production of environmental deprivation between sub-populations: a study combining citizens' perceptions with remote-sensed and administrative data. *BUILDING AND ENVIRONMENT*, 174:106769, 2020. URL: https://www.scopus.com/inward/record.uri?eid=2-s2.0-85081133587&doi=10.1016%2fj.buildenv.2020.106769&partnerID=40&md5=a2fe003eab619a73af072e9e82b5d8e2, doi:10.1016/j.buildenv.2020.106769.

[227] Matus Hodul, Anders Knudby, and Hung Ho. Estimation of continuous urban sky view factor from landsat data using shadow detection. *Remote Sensing*, 8(7):568, 2016. URL: https://www.scopus.com/inward/record.uri?eid=2-s2.0-85019847861&doi=10.3390%2frs8070568&partnerID=40&md5=3057fd86265e8821724dc700f556d95f, doi:10.3390/rs8070568.

[228] Lukáš Holata, Jindřich Plzák, Radek Světlík, and João Fonte. Integration of low-resolution als and ground-based sfm photogrammetry data. a cost-effective approach providing an `enhanced 3d model' of the hound tor archaeological landscapes (dartmoor, south-west england). *Remote Sensing*, 10(9):1357, 2018. URL: https://www.scopus.com/inward/record.uri?eid=2-s2.0-85053604506&doi=10.3390%2frs10091357&partnerID=40&md5=619bb1d18c536dae58b6e6532e32ad4a, doi:10.3390/rs10091357.

[229] Jan Horák, Martin Janovský, Michal Hejcman, Ladislav Šmejda, and Tomáš Klír. Soil geochemistry of medieval arable fields in lovětín near třešť, czech republic. *CATENA*, 162:14–22, 2018. URL: https://www.scopus.com/inward/record.uri?eid=2-s2.0-85034731982&doi=10.1016%2fj.catena.2017.11.014&partnerID=40&md5=3da163c1e60f5ef5ab790f8a6c0dd66b, doi:10.1016/j.catena.2017.11.014.

[230] Milan Horňák and Ján Zachar. Some examples of good practice in lidar prospection in preventive archaeology. *Interdisciplinaria Archaeologica*, VIII(2/2017):113–124, 2017. URL: https://www.scopus.com/inward/record.uri?eid=2-s2.0-85042793400&doi=10.24916%2fiansa.2017.2.1&partnerID=40&md5=d73ad2df7fb3615d158da7e99a300a5a, doi:10.24916/iansa.2017.2.1.

[231] Petr Hrubý, Martin Košťál, Karel Malý, and Jakub Těsnohlídek. Středověká úpravna rud u koječína na Českomoravské vrchovině : k poznání technologií produkce stříbra ve státě posledních přemyslovců. *Archaeologia Historica*, 44(2):949–981, 2019. URL: https://www.scopus.com/inward/record.uri?eid=2-s2.0-85072878562&doi=10.5817%2fAH2019-2-19&partnerID=40&md5=4b123941f7d28532e1e34910a9c01efe, doi:10.5817/AH2019-2-19.

[232] Pan Huang, Wei Zhao, and Ainong Li. The preliminary investigation on the uncertainties associated with surface solar radiation estimation in mountainous areas. *IEEE GEOSCIENCE AND REMOTE SENSING LETTERS*, 14(7):1071–1075, 2017. URL: https://www.scopus.com/inward/record.uri?eid=2-s2.0-85018899936&doi=10.1109%2fLGRS.2017.2696973&partnerID=40&md5=e6911fb2b130723edf426d6d9a31614c, doi:10.1109/LGRS.2017.2696973.

[233] Xin Huang and Ying Wang. Investigating the effects of 3d urban morphology on the surface urban heat island effect in urban functional zones by using high-resolution remote sensing data: a case study of wuhan, central china. *ISPRS JOURNAL OF PHOTOGRAMMETRY AND REMOTE SENSING*, 152:119–131, 2019. URL: https://www.scopus.com/inward/record.uri?eid=2-s2.0-85064550621&doi=10.1016%2fj.isprsjprs.2019.04.010&partnerID=40&md5=613b04ffdea0d162d737bd105181e7eb, doi:10.1016/j.isprsjprs.2019.04.010.

[234] Christopher Hutengs and Michael Vohland. Downscaling land surface temperatures at regional scales with random forest regression. *REMOTE SENSING OF ENVIRONMENT*, 178:127–141, 2016. URL: https://www.scopus.com/inward/record.uri?eid=2-s2.0-84961115074&doi=10.1016%2fj.rse.2016.03.006&partnerID=40&md5=0663696601bbdfebf44f666f9564bbff, doi:10.1016/j.rse.2016.03.006.

[235] Scott R. Hutson. Adapting lidar data for regional variation in the tropics: a case study from the northern maya lowlands. *Journal of Archaeological Science: Reports*, 4:252–263, 2015. URL: https://www.scopus.com/inward/record.uri?eid=2-s2.0-84942577018&doi=10.1016%2fj.jasrep.2015.09.012&partnerID=40&md5=da7e47e912c2168abc6faadce73de30a, doi:10.1016/j.jasrep.2015.09.012.

[236] S. R. Hutson, N. P. Dunning, B. Cook, T. Ruhl, N. C. Barth, and D. Conley. Ancient maya rural settlement patterns, household cooperation, and regional subsistence interdependency in the río bec area: contributions from g-liht. *Journal of Anthropological Research*, 77(4):550–579, 2021. URL: https://www.scopus.com/inward/record.uri?eid=2-s2.0-85118382089&doi=10.1086%2f716750&partnerID=40&md5=9c45dc7a4ccc88fbc01b3bb85e159e29, doi:10.1086/716750.

[237] S. R. Hutson, T. S. Hare, T. W. Stanton, M. A. Masson, N. C. Barth, T. Ardren, and A. Magnoni. A space of one's own: houselot size among the ancient maya. *JOURNAL OF ANTHROPOLOGICAL ARCHAEOLOGY*, 2021. URL: https://www.scopus.com/inward/record.uri?eid=2-s2.0-85117604470&doi=10.1016%2fj.jaa.2021.101362&partnerID=40&md5=4c085139e0977fbac13af3efd3cec32f, doi:10.1016/j.jaa.2021.101362.

[238] Takeshi Inomata, Flory Pinzón, José Luis Ranchos, Tsuyoshi Haraguchi, Hiroo Nasu, Juan Carlos Fernandez-Diaz, Kazuo Aoyama, and Hitoshi Yonenobu. Archaeological application of airborne lidar with object-based vegetation classification and visualization techniques at the lowland maya site of ceibal, guatemala. *Remote Sensing*, 9(6):563, 2017. URL: https://www.scopus.com/inward/record.uri?eid=2-s2.0-85021066279&doi=10.3390%2frs9060563&partnerID=40&md5=7a2e582100b22d3a303d6b8720a6be34, doi:10.3390/rs9060563.

[239] Takeshi Inomata, Daniela Triadan, Verónica A. Vázquez López, Juan Carlos Fernandez-Diaz, Takayuki Omori, María Belén Méndez Bauer, Melina García Hernández, Timothy Beach, Clarissa Cagnato, Kazuo Aoyama, and Hiroo Nasu. Monumental architecture at aguada fénix and the rise of maya civilization. *Nature*, 582(7813):530–533, 2020. doi:10.1038/s41586-020-2343-4.

[240] A. Jalandoni, M. Kottermair, B. Dixon, and V. H. Torres. Effectiveness of 2020 airborne lidar for identifying archaeological sites and features on guåhan (guam). *Journal of Computer Applications in Archaeology*, 5(1):255–270, 2022. URL: https://www.scopus.com/inward/record.uri?eid=2-s2.0-85143132887&doi=10.5334%2fjcaa.101&partnerID=40&md5=173b98faac91b832a5e0ff9c550d0533, doi:10.5334/jcaa.101.

[241] P. Jamšek Rupnik, M. Žebre, J. Jež, M. Zajc, F. Preusser, and G. Monegato. Deciphering the deformation mechanism in quaternary deposits along the idrija fault in the formerly glaciated soča valley, southeast european alps. *Engineering Geology*, 2022. URL: https://www.scopus.com/inward/record.uri?eid=2-s2.0-85122645440&doi=10.1016%2fj.enggeo.2021.106515&partnerID=40&md5=0b356a3731eae931bbd8ac3a2d1f6f0a, doi:10.1016/j.enggeo.2021.106515.

[242] Lukasz Janowski, Maria Kubacka, Andrzej Pydyn, Mateusz Popek, and Lukasz Gajewski. From acoustics to underwater archaeology: deep investigation of a shallow lake using high–resolution hydroacoustics—the case of lake lednica, poland. *Archaeometry*, 2021. URL: https://www.scopus.com/inward/record.uri?eid=2-s2.0-85101509547&doi=10.1111%2farcm.12663&partnerID=40&md5=b255d2bbb7a378be220d1ce94393b14b, doi:10.1111/arcm.12663.

[243] Zhong-Hu Jiao, Huazhong Ren, Xihan Mu, Jing Zhao, Tianxing Wang, and Jiaji Dong. Evaluation of four sky view factor algorithms using digital surface and elevation model data. *EARTH AND SPACE SCIENCE*, 6(2):222–237, 2019. URL: https://www.scopus.com/inward/record.uri?eid=2-s2.0-85061937049&doi=10.1029%2f2018EA000475&partnerID=40&md5=2dfa0054d97b0ceadd3851962795f4da, doi:10.1029/2018EA000475.

[244] Hester Jiskoot and Mark S. Mueller. Glacier fragmentation effects on surface energy balance and runoff: field measurements and distributed modelling. *HYDROLOGICAL PROCESSES*, 26(12):1861–1875, 2012. URL: https://www.scopus.com/inward/record.uri?eid=2-s2.0-84862021470&doi=10.1002%2fhyp.9288&partnerID=40&md5=af0422a6215f14e297e0c091e2e62a21, doi:10.1002/hyp.9288.

[245] Katharine M. Johnson and William B. Ouimet. Rediscovering the lost archaeological landscape of southern new england using airborne light detection and ranging (lidar). *Journal of Archaeological Science*, 43(1):9–20, 2014. URL: https://www.scopus.com/inward/record.uri?eid=2-s2.0-84891723190&doi=10.1016%2fj.jas.2013.12.004&partnerID=40&md5=2e71f021ec6aaf1de260676f19b3a4cf, doi:10.1016/j.jas.2013.12.004.

[246] Katharine M. Johnson and William B. Ouimet. Physical properties and spatial controls of stone walls in the northeastern usa: implications for anthropocene studies of 17th to early 20th century agriculture. *ANTHROPOCENE*, 15:22–36, 2016. URL: https://www.scopus.com/inward/record.uri?eid=2-s2.0-84994713290&doi=10.1016%2fj.ancene.2016.07.001&partnerID=40&md5=692dd03f75885096492eed5d25e5f0c7, doi:10.1016/j.ancene.2016.07.001.

[247] Katharine M. Johnson and William B. Ouimet. An observational and theoretical framework for interpreting the landscape palimpsest through airborne lidar. *APPLIED GEOGRAPHY*, 91:32–44, 2018. URL: https://www.scopus.com/inward/record.uri?eid=2-s2.0-85039979208&doi=10.1016%2fj.apgeog.2017.12.018&partnerID=40&md5=7dfba63707a5c1e95440197a7adcf3ab, doi:10.1016/j.apgeog.2017.12.018.

[248] Katharine M. Johnson and William B. Ouimet. Reconstructing historical forest cover and land use dynamics in the northeastern united states using geospatial analysis and airborne lidar. *Annals of the American Association of Geographers*, pages 1–23, 2021. URL: https://www.scopus.com/inward/record.uri?eid=2-s2.0-85102359764&doi=10.1080%2f24694452.2020.1856640&partnerID=40&md5=7fdce09a39016d67b166b42fbfa68ef9, doi:10.1080/24694452.2020.1856640.

[249] G. Jordanova and T. Verbovšek. Improved automatic classification of litho-geomorphological units by using raster image blending, vipava valley (sw slovenia). *Remote Sensing*, 2023. URL: https://www.scopus.com/inward/record.uri?eid=2-s2.0-85146427970&doi=10.3390%2frs15020531&partnerID=40&md5=1dd33000ef48e3d5d38f0eabf2d0a041, doi:10.3390/rs15020531.

[250] M. Y. Joshi, A. Rodler, M. Musy, S. Guernouti, M. Cools, and J. Teller. Identifying urban morphological archetypes for microclimate studies using a clustering approach. *BUILDING AND ENVIRONMENT*, 2022. URL: https://www.scopus.com/inward/record.uri?eid=2-s2.0-85137662382&doi=10.1016%2fj.buildenv.2022.109574&partnerID=40&md5=a7f6a0680996f68253c5924d0f7ae1e4, doi:10.1016/j.buildenv.2022.109574.

[251] M. Kałaska, R. Siuda, P. Sierpień, and D. H. Werra. Application of arsenic surveying for determining the position of former mining and metallurgical constructions: an example from the radzimowice area (lower silesia, sw poland). *ARCHAEOLOGICAL AND ANTHROPOLOGICAL SCIENCES*, 2022. URL: https://www.scopus.com/inward/record.uri?eid=2-s2.0-85137591457&doi=10.1007%2fs12520-022-01654-8&partnerID=40&md5=c0770031425036bf9eec8c34e208884d, doi:10.1007/s12520-022-01654-8.

[252] Israa Kadhim and Fanar M. Abed. The potential of lidar and uav-photogrammetric data analysis to interpret archaeological sites: a case study of chun castle in south-west england. *ISPRS INTERNATIONAL JOURNAL OF GEO-INFORMATION*, 10(1):41, 2021. URL: https://www.scopus.com/inward/record.uri?eid=2-s2.0-85105155726&doi=10.3390%2fijgi10010041&partnerID=40&md5=15c75a77f538877a14bf1cc9be936fb5, doi:10.3390/ijgi10010041.

[253] Maciej Kania and Mateusz Szczęch. Geometry and topology of tectonolineaments in the gorce mts. (outer carpathians) in poland. *JOURNAL OF STRUCTURAL GEOLOGY*, 141:104186, 2020. URL: https://www.scopus.com/inward/record.uri?eid=2-s2.0-85091675311&doi=10.1016%2fj.jsg.2020.104186&partnerID=40&md5=5cc220e90a62a994be4db1934313cd56, doi:10.1016/j.jsg.2020.104186.

[254] Zahra Karimidastenaei, Ali Torabi Haghighi, Omid Rahmati, Kabir Rasouli, Sajad Rozbeh, Abdollah Pirnia, Biswajeet Pradhan, and Bjørn Kløve. Fog-water harvesting capability index (fci) mapping for a semi-humid catchment based on socio-environmental variables and using artificial intelligence algorithms. *SCIENCE OF THE TOTAL ENVIRONMENT*, 708:135115, 2020. URL: https://www.scopus.com/inward/record.uri?eid=2-s2.0-85075989839&doi=10.1016%2fj.scitotenv.2019.135115&partnerID=40&md5=9ec0369391b6966a7089698ca5f7c1b0, doi:10.1016/j.scitotenv.2019.135115.

[255] Vladislav V. Kazakov, Aleksandr I. Simukhin, Vasiliy S. Kovalev, Pavel E. Marnuev, Dashinima V. Namsaraev, and Lyudmila V. Lbova. The tamchinskiy deer stone: documenting megalithic objects. *Siberian Historical Research*, 2019(3):141–167, 2019. URL: https://www.scopus.com/inward/record.uri?eid=2-s2.0-85082115685&doi=10.17223%2f2312461X%2f25%2f8&partnerID=40&md5=6bb1bd2c177243b68172f931e753cd40, doi:10.17223/2312461X/25/8.

[256] Grzegorz Kiarszys. The destroyer of worlds hidden in the forest: cold war nuclear warhead sites in poland. *Antiquity*, 93(367):236–255, 2019. URL: https://www.scopus.com/inward/record.uri?eid=2-s2.0-85061647150&doi=10.15184%2faqy.2018.173&partnerID=40&md5=60f79814c6ceb427bd966c33aac299f9, doi:10.15184/aqy.2018.173.

[257] Chris Kidd and Lee Chapman. Derivation of sky-view factors from lidar data. *INTERNATIONAL JOURNAL OF REMOTE SENSING*, 33(11):3640–3652, 2012. URL: https://www.scopus.com/inward/record.uri?eid=2-s2.0-84857012365&doi=10.1080%2f01431161.2011.635163&partnerID=40&md5=7d6fe57e4bdf20d95fd26a9b8e05a5f3, doi:10.1080/01431161.2011.635163.

[258] Drago Kladnik, Matjaž Geršič, Primož Pipan, and Manca Volk Bahun. Land-use changes in slovenian terraced landscapes. *Acta Geographica Slovenica*, 59(2):119–141, 2019. URL: https://www.scopus.com/inward/record.uri?eid=2-s2.0-85069227756&doi=10.3986%2fAGS.6988&partnerID=40&md5=1032f5b02148b23b9077c08e87608b77, doi:10.3986/AGS.6988.

[259] Raphael Knevels, Helene Petschko, Philip Leopold, and Alexander Brenning. Geographic object-based image analysis for automated landslide detection using open source gis software. *ISPRS INTERNATIONAL JOURNAL OF GEO-INFORMATION*, 8(12):551, 2019. URL: https://www.scopus.com/inward/record.uri?eid=2-s2.0-85076676014&doi=10.3390%2fijgi8120551&partnerID=40&md5=5548697aae228e104117ab9176f50f26, doi:10.3390/ijgi8120551.

[260] Žiga Kokalj, Klemen Zakšek, and Krištof Oštir. Application of sky-view factor for the visualisation of historic landscape features in lidar-derived relief models. *Antiquity*, 85(327):263–273, 2011. doi:10.1017/S0003598X00067594.

[261] Žiga Kokalj and Maja Somrak. Why not a single image? combining visualizations to facilitate fieldwork and on-screen mapping. *Remote Sensing*, 11(7):747, 2019. doi:10.3390/rs11070747.

[262] Žiga Kokalj and Johannes Mast. Space lidar for archaeology? reanalyzing gedi data for detection of ancient maya buildings. *Journal of Archaeological Science: Reports*, 36:102811, 2021. URL: https://www.scopus.com/inward/record.uri?eid=2-s2.0-85100318003&doi=10.1016%2fj.jasrep.2021.102811&partnerID=40&md5=86f43ef3878d78501192726a94f565f6, doi:10.1016/j.jasrep.2021.102811.

[263] F. Kong, J. Chen, A. Middel, H. Yin, M. Li, T. Sun, N. Zhang, J. Huang, H. Liu, K. Zhou, and J. Ma. Impact of 3-d urban landscape patterns on the outdoor thermal environment: a modelling study with solweig. *Computers, Environment and Urban Systems*, 2022. URL: https://www.scopus.com/inward/record.uri?eid=2-s2.0-85126137383&doi=10.1016%2fj.compenvurbsys.2022.101773&partnerID=40&md5=3a780fccda2cb478b2e66cc8de4ea989, doi:10.1016/j.compenvurbsys.2022.101773.

[264] Karin Kopetzky, Hermann Genz, Christoph Schwall, Jakob Rom, Florian Haas, Manuel Stark, Fabian Dremel, and Mario Börner. Between land and sea: tell mirhan and the chekka regional survey. *Agypten und Levante*, 29:105–124, 2020. URL: https://www.scopus.com/inward/record.uri?eid=2-s2.0-85097592361&doi=10.1553%2fAEUNDL29S105&partnerID=40&md5=128dfbba14169e123cefc66e2e5b6a96, doi:10.1553/AEUNDL29S105.

[265] Kathryn E. Krasinski, Brian T. Wygal, Joanna Wells, Richard L. Martin, and Fran Seager-Boss. Detecting late holocene cultural landscape modifications using lidar imagery in the boreal forest, susitna valley, southcentral alaska. *Journal of Field Archaeology*, 41(3):255–270, 2016. URL: https://www.scopus.com/inward/record.uri?eid=2-s2.0-84981240767&doi=10.1080%2f00934690.2016.1174764&partnerID=40&md5=f6cda62c5e23ca076b535138e1ad5943, doi:10.1080/00934690.2016.1174764.

[266] Shashi Kumar, S. Kandasamy Vignesh, Arun Babu, Praveen K. Thakur, and Shefali Agrawal. Psinsar-based surface deformation mapping of angkor wat cultural heritage site. *JOURNAL OF THE INDIAN SOCIETY OF REMOTE SENSING*, 49(4):827–842, 2021. URL: https://www.scopus.com/inward/record.uri?eid=2-s2.0-85096208103&doi=10.1007%2fs12524-020-01257-7&partnerID=40&md5=3353ea05a3f16d199a64aeeeb74e8586, doi:10.1007/s12524-020-01257-7.

[267] K. L. Kvamme. A filter for characterizing the ridge-drainage continuum in digital elevation models. *Journal of Archaeological Science*, 2021. URL: https://www.scopus.com/inward/record.uri?eid=2-s2.0-85118492400&

doi=10.1016%2fj.jas.2021.105510&partnerID=40&md5=399663539414c0ce08911915201d70ff, doi:10.1016/j.jas.2021.105510.

[268] Joshua J. Kwoka, Thomas H. Guderjan, Sara Eshleman, Thomas Ruhl, Justin Telepak, Timothy Beach, Sheryl Luzzadder-Beach, Will McClatchey, and Grace Bascopé. A multimethod approach to the study of classic maya houselots and land tenure: preliminary results from the three rivers region, belize. *Journal of Archaeological Science: Reports*, 38:103049, 2021. URL: https://www.scopus.com/inward/record.uri?eid=2-s2.0-85107689519&doi=10.1016%2fj.jasrep.2021.103049&partnerID=40&md5=50f62d59b5f24977fef023bdbcf46d3e, doi:10.1016/j.jasrep.2021.103049.

[269] Thegn N. Ladefoged, Mark D. McCoy, Gregory P. Asner, Patrick V. Kirch, Cedric O. Puleston, Oliver A. Chadwick, and Peter M. Vitousek. Agricultural potential and actualized development in hawai'i: an airborne lidar survey of the leeward kohala field system (hawai'i island). *Journal of Archaeological Science*, 38(12):3605–3619, 2011. URL: https://www.scopus.com/inward/record.uri?eid=2-s2.0-80054097091&doi=10.1016%2fj.jas.2011.08.031&partnerID=40&md5=290b92c124a4f83f9b4a852411bb53c4, doi:10.1016/j.jas.2011.08.031.

[270] S. Lai, Y. Zhao, Y. Fan, and J. Ge. Characteristics of daytime land surface temperature in wind corridor: a case study of a hot summer and warm winter city. *Journal of Building Engineering*, 2021. URL: https://www.scopus.com/inward/record.uri?eid=2-s2.0-85122289042&doi=10.1016%2fj.jobe.2021.103370&partnerID=40&md5=f8c67266dca3f334ee29c1fc090c642c, doi:10.1016/j.jobe.2021.103370.

[271] C.-F. Lee, H.-T. Chou, T.-C. Tsao, C.-H. Hsu, C.-H. Huang, and W.-S. Liao. Heliu debris flow induced by typhoon soudelor: failure mechanism and numerical simulation. *Journal of Chinese Soil and Water Conservation*, 47(4):171–184, 2016. URL: https://www.scopus.com/inward/record.uri?eid=2-s2.0-85013911937&partnerID=40&md5=ae5e2adbf2c30dc1d1d729c299d2f608.

[272] Ching-Fang Lee, Chia-Ming Lo, Hsien-Ter Chou, and Shu-Yeong Chi. Landscape evolution analysis of large scale landslides at don-ao peak, taiwan. *ENVIRONMENTAL EARTH SCIENCES*, 75(1):1–19, 2016. URL: https://www.scopus.com/inward/record.uri?eid=2-s2.0-84950325580&doi=10.1007%2fs12665-015-4817-5&partnerID=40&md5=99fbf890cb44ab696815dd5c8bcd1d30, doi:10.1007/s12665-015-4817-5.

[273] C.-F. Lee, T.-C. Tsao, W.-K. Huang, S.-C. Lin, and H.-Y. Yin. Landslide mapping and geomorphologic change based on a sky-view factor and local relief model: a case study in hongye village, taitung. *Journal of Chinese Soil and Water Conservation*, 49(1):27–39, 2018. URL: https://www.scopus.com/inward/record.uri?eid=2-s2.0-85049253222&doi=10.29417%2fJCSWC.201803_49%281%29.0003&partnerID=40&md5=407a804faef7c4b5a99ca65bec3f513d, doi:10.29417/JCSWC.201803{\textunderscore }49(1).0003.

[274] Doo-Il Lee, Ju-Wan Woo, and Sang-Hyun Lee. An analytically based numerical method for computing view factors in real urban environments. *THEORETICAL AND APPLIED CLIMATOLOGY*, 131(1-2):445–453, 2018. URL: https://www.scopus.com/inward/record.uri?eid=2-s2.0-84994246364&doi=10.1007%2fs00704-016-1966-8&partnerID=40&md5=1ba0e9b401275ece604f769d8e0f30d7, doi:10.1007/s00704-016-1966-8.

[275] Kwanho Lee and Geoff J. Levermore. Sky view factor and sunshine factor of urban geometry for urban heat island and renewable energy. *ARCHITECTURAL SCIENCE REVIEW*, 62(1):26–34, 2019. URL: https://www.scopus.com/inward/record.uri?eid=2-s2.0-85055440842&doi=10.1080%2f00038628.2018.1536601&partnerID=40&md5=a88080bb79484803917db488f02e647c, doi:10.1080/00038628.2018.1536601.

[276] Doo-Il Lee and Sang-Hyun Lee. The microscale urban surface energy (muse) model for real urban application. *ATMOSPHERE*, 11(12):1347, 2020. URL: https://www.scopus.com/inward/record.uri?eid=2-s2.0-85098091668&doi=10.3390%2fatmos11121347&partnerID=40&md5=586c9c080904c0d8f9d7fe89204754db, doi:10.3390/atmos11121347.

[277] Kwanho Lee and Geoff J. Levermore. Estimation of surface solar irradiation using sky view factor, sunshine factor and solar irradiation models according to geometry and buildings. *ADVANCES IN BUILDING ENERGY RESEARCH*, 14(2):189–201, 2020. URL: https://www.scopus.com/inward/record.uri?eid=2-s2.0-85062942817&doi=10.1080%2f17512549.2019.1591299&partnerID=40&md5=526a59590c073e135232d8043f700d14, doi:10.1080/17512549.2019.1591299.

[278] Michał Leloch, Michał Jakubczak, Marcin Przybyła, Katarzyna Pyżewicz, Marcin Szeliga, Michał Wojenka, Grzegorz Czajka, and Małgorzata Kot. A multiproxy approach to studying a large prehistoric enclosure in ojców, kraków upland, poland. *Archaeological Prospection*, 2021. URL: https://www.scopus.com/inward/record.uri?eid=2-s2.0-85105284664&doi=10.1002%2farp.1824&partnerID=40&md5=98704c586af96a6b040589d9101c69bd, doi:10.1002/arp.1824.

[279] Jingxin Li, Hongqi Zhang, and Erqi Xu. A two-level nested model for extracting positive and negative terrains combining morphology and visualization indicators. *ECOLOGICAL INDICATORS*, 109:105842, 2020. URL: https://www.scopus.com/inward/record.uri?eid=2-s2.0-85073717153&doi=10.1016%2fj.ecolind.2019.105842&partnerID=40&md5=09b82b5fbb99285ed44f0af5dcb4892b, doi:10.1016/j.ecolind.2019.105842.

[280] T. Li, D. Hu, Y. Wang, Y. Di, and M. Liu. Correcting remote-sensed shaded image with urban surface radiative transfer model. *INTERNATIONAL JOURNAL OF APPLIED EARTH OBSERVATION AND GEOINFORMATION*, 2022. URL: https://www.scopus.com/inward/record.uri?eid=2-s2.0-85122535486&doi=10.1016%2fj.jag.2021.102654&partnerID=40&md5=f3b9b35979c77d72b73b88e9f62c27ee, doi:10.1016/j.jag.2021.102654.

[281] Jianming Liang, Jianhua Gong, Jun Sun, Jieping Zhou, Wenhang Li, Yi Li, Jin Liu, and Shen Shen. Automatic sky view factor estimation from street view photographs—a big data approach. *Remote Sensing*, 9(5):411, 2017. URL: https://www.scopus.com/inward/record.uri?eid=2-s2.0-85019964303&doi=10.3390%2frs9050411&partnerID=40&md5=86093d9456c93dd68a98563c538778e8, doi:10.3390/rs9050411.

[282] Jonathan Lim, James Clark, and Gonzalo Linares-Matás. Subsurface delineation of doline features associated with pleistocene clay-with-flints deposits in the chilterns: implications for british palaeolithic archaeology. *Journal of Archaeological Science: Reports*, 34:102665, 2020. URL: https://www.scopus.com/inward/record.uri?eid=2-s2.0-85096687648&doi=10.1016%2fj.jasrep.2020.102665&partnerID=40&md5=9dd72027aa01027491b56d2fbcd396a7, doi:10.1016/j.jasrep.2020.102665.

[283] J. A. Linares-Catela, C. M. Molina, A. L. López, T. D. Romero, J. C. Vera-Rodríguez, and P. B. Ramírez. The megalithic site of la torre-la janera (huelva): prehistoric monumentalities in the lower guadiana. *Trabajos de Prehistoria*, 79(1):115–130, 2022. URL: https://www.scopus.com/inward/record.uri?eid=2-s2.0-85133435252&doi=10.3989%2ftp.2022.12290&partnerID=40&md5=a445bd5df6c203eccaa5254d54fabebf, doi:10.3989/tp.2022.12290.

[284] Yonghong Liu, Xiaoyi Fang, Chen Cheng, Qingzu Luan, Wupeng Du, Xiaojun Xiao, and Huaisheng Wang. Research and application of city ventilation assessments based on satellite data and gis technology: a case study of the yanqi lake eco-city in huairou district, beijing. *METEOROLOGICAL APPLICATIONS*, 23(2):320–327, 2016. URL: https://www.scopus.com/inward/record.uri?eid=2-s2.0-84962861039&doi=10.1002%2fmet.1557&partnerID=40&md5=9bb675269f39a468a3284bcc8245665d, doi:10.1002/met.1557.

[285] Yonghong Liu, Pengfei Cheng, Peng Chen, and Shuo Zhang. Detection of wind corridors based on "climatopes": a study in central ji'nan. *THEORETICAL AND APPLIED CLIMATOLOGY*, 142(3-4):869–884, 2020. URL: https://www.scopus.com/inward/record.uri?eid=2-s2.0-85089454522&doi=10.1007%2fs00704-020-03323-z&partnerID=40&md5=253381c481cc320b390624efebb6dd9f, doi:10.1007/s00704-020-03323-z.

[286] Yonghong Liu, Yongming Xu, Fangmin Zhang, and Wenjun Shu. A preliminary study on the influence of beijing urban spatial morphology on near-surface wind speed. *URBAN CLIMATE*, 34:100703, 2020. URL: https://www.scopus.com/inward/record.uri?eid=2-s2.0-85091596898&doi=10.1016%2fj.uclim.2020.100703&partnerID=40&md5=efe48be9701e4a63e63ee1437d14bd0d, doi:10.1016/j.uclim.2020.100703.

[287] Yonghong Liu, Yongming Xu, Fuzhong Weng, Fangmin Zhang, and Wenjun Shu. Impacts of urban spatial layout and scale on local climate: a case study in beijing. *SUSTAINABLE CITIES AND SOCIETY*, 68:102767, 2021. URL: https://www.scopus.com/inward/record.uri?eid=2-s2.0-85101370514&doi=10.1016%2fj.scs.2021.102767&partnerID=40&md5=25f3e04bbdd5e19f26abae80ea13d192, doi:10.1016/j.scs.2021.102767.

[288] Y. Liu, Y. Xu, F. Zhang, and W. Shu. Influence of beijing spatial morphology on the distribution of urban heat island. *Dili Xuebao/Acta Geographica Sinica*, 76(7):1662–1679, 2021. URL:

https://www.scopus.com/inward/record.uri?eid=2-s2.0-85113808214&doi=10.11821%2fdlxb202107007&partnerID=40&md5=ee27142e14d5d829da001facebc00a4b, doi:10.11821/dlxb202107007.

[289] Yonghong Liu, Yongming Xu, Xiuzhen Han, Wenjun Shu, and Fuzhong Weng. Influence of the urban spatial layout of central beijing on the atmospheric humidity field. *THEORETICAL AND APPLIED CLIMATOLOGY*, 145(1-2):455–471, 2021. URL: https://www.scopus.com/inward/record.uri?eid=2-s2.0-85105525825&doi=10.1007%2fs00704-021-03621-0&partnerID=40&md5=5c9fa6eac38d875822cd9a4bde87f66d, doi:10.1007/s00704-021-03621-0.

[290] Y. Liu, C. Xuan, Y. Xu, N. Fu, F. Xiong, and L. Gan. Local climate effects of urban wind corridors in beijing. *URBAN CLIMATE*, 2022. URL: https://www.scopus.com/inward/record.uri?eid=2-s2.0-85129476496&doi=10.1016%2fj.uclim.2022.101181&partnerID=40&md5=4d92dd239e74ef8ecd0d9de7e0d00ff8, doi:10.1016/j.uclim.2022.101181.

[291] Y. Liu, Y. Xu, Y. Zhang, X. Han, F. Weng, C. Xuan, and W. Shu. Impacts of the urban spatial landscape in beijing on surface and canopy urban heat islands. *Journal of Meteorological Research*, 36(6):882–899, 2022. URL: https://www.scopus.com/inward/record.uri?eid=2-s2.0-85146128576&doi=10.1007%2fs13351-022-2045-y&partnerID=40&md5=b2675070e3a1e0c1ecfb29b36c304f0b, doi:10.1007/s13351-022-2045-y.

[292] Noura Lkebir, Tanguy Rolland, Fabrice Monna, Moussa Masrour, Lhoussaine Bouchaou, Emmanuel Fara, Nicolas Navarro, Josef Wilczek, El Hassan Beraaouz, Carmela Chateau-Smith, and Félix Pérez-Lorente. Anza palaeoichnological site, late cretaceous, morocco. part iii: comparison between traditional and photogrammetric records. *JOURNAL OF AFRICAN EARTH SCIENCES*, 172:103985, 2020. URL: https://www.scopus.com/inward/record.uri?eid=2-s2.0-85089798851&doi=10.1016%2fj.jafrearsci.2020.103985&partnerID=40&md5=d930b4842c4fd7ae84d51469c5d3b36e, doi:10.1016/j.jafrearsci.2020.103985.

[293] Chia-Ming Lo, Ching-Fang Lee, and Jeff Keck. Application of sky view factor technique to the interpretation and reactivation assessment of landslide activity. *ENVIRONMENTAL EARTH SCIENCES*, 2017. URL: https://www.scopus.com/inward/record.uri?eid=2-s2.0-85019711584&doi=10.1007%2fs12665-017-6705-7&partnerID=40&md5=0e77d62e2174cd5b97610a817c5668c8, doi:10.1007/s12665-017-6705-7.

[294] Edisa Lozić and Benjamin Štular. Documentation of archaeology-specific workflow for airborne lidar data processing. *Geosciences (Switzerland)*, 11(1):26, 2021. URL: https://www.scopus.com/inward/record.uri?eid=2-s2.0-85099651658&doi=10.3390%2fgeosciences11010026&partnerID=40&md5=7efcbb9dc1116f7f0d0b3b62eee2404b, doi:10.3390/geosciences11010026.

[295] Lei Luo, Xinyuan Wang, Huadong Guo, Rosa Lasaponara, Xin Zong, Nicola Masini, Guizhou Wang, Pilong Shi, Houcine Khatteli, Fulong Chen, Shahina Tariq, Jie Shao, Nabil Bachagha, Ruixia Yang, and Ya Yao. Airborne and spaceborne remote sensing for archaeological and cultural heritage applications: a review of the century (1907–2017). *REMOTE SENSING OF ENVIRONMENT*, 232:111280, 2019. doi:10.1016/j.rse.2019.111280.

[296] Florence Magnin, Alexander Brenning, Xavier Bodin, Philip Deline, and Ludovic Ravanel. Modélisation statistique de la distribution du permafrost de paroi : application au massif du mont blanc. *Geomorphologie: Relief, Processus, Environnement*, 21(2):145–162, 2015. URL: https://www.scopus.com/inward/record.uri?eid=2-s2.0-84939800928&doi=10.4000%2fgeomorphologie.10965&partnerID=40&md5=7bbde0a391191e2408dd89057aff05ca, doi:10.4000/geomorphologie.10965.

[297] Luigi Magnini, Cinzia Bettineschi, and Armando de Guio. Object-based shell craters classification from lidar-derived sky-view factor. *Archaeological Prospection*, 24(3):211–223, 2017. URL: https://www.scopus.com/inward/record.uri?eid=2-s2.0-85007047555&doi=10.1002%2farp.1565&partnerID=40&md5=acb1de5478a03dca9016770059d8f7be, doi:10.1002/arp.1565.

[298] L. Magnini, C. Bettineschi, A. de Guio, L. Burigana, G. Colombatti, C. Bettanini, and A. Aboudan. Multisensor-multiscale approach in studying the proto-historic settlement of bostel in northern italy. *ARCHEOLOGIA E CALCOLATORI*, 30:347–365, 2019. URL: https://www.scopus.com/inward/record.uri?eid=2-s2.0-85080084858&doi=10.19282%2fac.30.2019.20&partnerID=40&md5=7779ceb13d46f89cb4f1a1d3c46ea788, doi:10.19282/ac.30.2019.20.

[299] Luigi Magnini and Cinzia Bettineschi. Object-based predictive modeling (obpm) for archaeology: finding control places in mountainous environments. *Remote Sensing*, 13(6):1197, 2021. URL: https://www.scopus.com/inward/record.uri?eid=2-s2.0-85103520317&doi=10.3390%2frs13061197&partnerID=40&md5=98d8cc8c52b2963915d94533feadb813, doi:10.3390/rs13061197.

[300] Emanuele Mandanici, Paolo Conte, and Valentina Girelli. Integration of aerial thermal imagery, lidar data and ground surveys for surface temperature mapping in urban environments. *Remote Sensing*, 8(10):880, 2016. URL: https://www.scopus.com/inward/record.uri?eid=2-s2.0-85019059558&doi=10.3390%2frs8100880&partnerID=40&md5=a84655b54ac3b35e9dbe60106bafdf7c, doi:10.3390/rs8100880.

[301] Nicola Masey, Scott Hamilton, and Iain J. Beverland. Development and evaluation of the rapidair\circledR dispersion model, including the use of geospatial surrogates to represent street canyon effects. *Environmental Modelling and Software*, 108:253–263, 2018. URL: https://www.scopus.com/inward/record.uri?eid=2-s2.0-85053195806&doi=10.1016%2fj.envsoft.2018.05.014&partnerID=40&md5=73e4b263d9aa1bdae3b213a57ae51b3b, doi:10.1016/j.envsoft.2018.05.014.

[302] Nicola Masini, Fabrizio Gizzi, Marilisa Biscione, Vincenzo Fundone, Michele Sedile, Maria Sileo, Antonio Pecci, Biagio Lacovara, and Rosa Lasaponara. Medieval archaeology under the canopy with lidar. the (re)discovery of a medieval fortified settlement in southern italy. *Remote Sensing*, 10(10):1598, 2018. URL: https://www.scopus.com/inward/record.uri?eid=2-s2.0-85055437332&doi=10.3390%2frs10101598&partnerID=40&md5=e5d36488ad90f309d138054cf4ebe6b4, doi:10.3390/rs10101598.

[303] Nicola Masini and Rosa Lasaponara. On the reuse of multiscale lidar data to investigate the resilience in the late medieval time: the case study of basilicata in south of italy. *Journal of Archaeological Method and Theory*, 2020. URL: https://www.scopus.com/inward/record.uri?eid=2-s2.0-85096599327&doi=10.1007%2fs10816-020-09495-2&partnerID=40&md5=e9970c3751734fc7e87f419ab9f74c81, doi:10.1007/s10816-020-09495-2.

[304] Nicola Masini and Rosa Lasaponara. Satellite and close range analysis for the surveillance and knowledge improvement of the nasca geoglyphs. *REMOTE SENSING OF ENVIRONMENT*, 236:111447, 2020. URL: https://www.scopus.com/inward/record.uri?eid=2-s2.0-85074655608&doi=10.1016%2fj.rse.2019.111447&partnerID=40&md5=05426aae8f8e2ac8bed272df72f4351f, doi:10.1016/j.rse.2019.111447.

[305] N. Masini and R. Lasaponara. Remote and close range sensing for the automatic identification and characterization of archaeological looting. the case of peru. *Journal of Computer Applications in Archaeology*, 4(1):126–144, 2021. URL: https://www.scopus.com/inward/record.uri?eid=2-s2.0-85108843811&doi=10.5334%2fjcaa.73&partnerID=40&md5=5c2fa14be168d9b6e56a320e1e42bb3e, doi:10.5334/jcaa.73.

[306] N. Masini, N. Abate, F. T. Gizzi, V. Vitale, A. Minervino Amodio, M. Sileo, M. Biscione, R. Lasaponara, M. Bentivenga, and F. Cavalcante. Uav lidar based approach for the detection and interpretation of archaeological micro topography under canopy—the rediscovery of perticara (basilicata, italy). *Remote Sensing*, 2022. URL: https://www.scopus.com/inward/record.uri?eid=2-s2.0-85143801753&doi=10.3390%2frs14236074&partnerID=40&md5=82760ca04ceaecb1bbd4c28ceee731b6, doi:10.3390/rs14236074.

[307] Jesús Mateo Lázaro, José Ángel Sánchez Navarro, Alejandro García Gil, and Vanesa Edo Romero. 3d-geological structures with digital elevation models using gpu programming. *Computers and Geosciences*, 70:138–146, 2014. URL: https://www.scopus.com/inward/record.uri?eid=2-s2.0-84903526373&doi=10.1016%2fj.cageo.2014.05.014&partnerID=40&md5=f1e4ba893533622a0ad97bbe521ec8ff, doi:10.1016/j.cageo.2014.05.014.

[308] Jesús Mateo-Lázaro, Jorge Castillo-Mateo, Alejandro García-Gil, José Ángel Sánchez-Navarro, Víctor Fuertes-Rodríguez, and Vanesa Edo-Romero. Comparative hydrodynamic analysis by using twodimensional models and application to a new bridge. *Water (Switzerland)*, 12(4):997, 2020. URL: https://www.scopus.com/inward/record.uri?eid=2-s2.0-85086769563&doi=10.3390%2fW12040997&partnerID=40&md5=de1902281bcdadae32b67b3e160a8f0e, doi:10.3390/W12040997.

[309] Rémi Matos–Machado, Jean–Pierre Toumazet, Jean–Claude Bergès, Jean–Paul Amat, Gilles Arnaud–Fassetta, François Bétard, Clélia Bilodeau, Joseph P. Hupy, and Stéphanie Jacquemot. War landform mapping and classification on the verdun battlefield (france) using airborne lidar and multivariate analysis. *Earth Surface Processes and Landforms*, 44(7):1430–1448, 2019. URL: https://www.scopus.com/inward/record.uri?eid=

2-s2.0-85061842864&doi=10.1002%2fesp.4586&partnerID=40&md5=c8612d15d4e9f80dfa9a727456e6fb61, doi:10.1002/esp.4586.

[310] A. Mayoral, J.-P. Toumazet, F.-X. Simon, Franck Vautier, and J.-L. Peiry. The highest gradient model: a new method for analytical assessment of the efficiency of lidar-derived visualization techniques for landform detection and mapping. *Remote Sensing*, 2017. URL: https://www.scopus.com/inward/record.uri?eid=2-s2.0-85013684476&doi=10.3390%2frs90201020&partnerID=40&md5=c8ffc0dc5c41e3af6bca51981196ec9a, doi:10.3390/rs90201020.

[311] Mark D. McCoy, Gregory P. Asner, and Michael W. Graves. Airborne lidar survey of irrigated agricultural landscapes: an application of the slope contrast method. *Journal of Archaeological Science*, 38(9):2141–2154, 2011. URL: https://www.scopus.com/inward/record.uri?eid=2-s2.0-79960087476&doi=10.1016%2fj.jas.2011.02.033&partnerID=40&md5=67fda84bc9d73af58bce4cbc4d53822c, doi:10.1016/j.jas.2011.02.033.

[312] Mark D. McCoy, Jesse Casana, Austin Chad Hill, Elise Jakoby Laugier, Mara A. Mulrooney, and Thegn N. Ladefoged. Unpiloted aerial vehicle acquired lidar for mapping monumental architecture. *Advances in Archaeological Practice*, 9(2):160–174, 2021. URL: https://www.scopus.com/inward/record.uri?eid=2-s2.0-85106729519&doi=10.1017%2faap.2021.5&partnerID=40&md5=6cf769b902a9050c9483232a5e18e51d, doi:10.1017/aap.2021.5.

[313] William Megarry, Gabriel Cooney, Douglas Comer, and Carey Priebe. Posterior probability modeling and image classification for archaeological site prospection: building a survey efficacy model for identifying neolithic felsite workshops in the shetland islands. *Remote Sensing*, 8(6):529, 2016. URL: https://www.scopus.com/inward/record.uri?eid=2-s2.0-85019927382&doi=10.3390%2frs8060529&partnerID=40&md5=ffb806f6fa180a8d613ee80a8124db5f, doi:10.3390/rs8060529.

[314] William P. Megarry, Bryce A. Davenport, and Douglas C. Comer. Emerging applications of lidar / airborne laser scanning in the management of world heritage sites. *CONSERVATION AND MANAGEMENT OF ARCHAEOLOGICAL SITES*, 18(4):393–410, 2016. URL: https://www.scopus.com/inward/record.uri?eid=2-s2.0-85018706918&doi=10.1080%2f13505033.2016.1290481&partnerID=40&md5=e56986b152b401665a9c2dd4340264b9, doi:10.1080/13505033.2016.1290481.

[315] M. Meliho, A. Khattabi, D. Zejli, C. A. Orlando, and C. E. Dansou. Artificial intelligence and remote sensing for spatial prediction of daily air temperature: case study of souss watershed of morocco. *Geo-Spatial Information Science*, 2022. URL: https://www.scopus.com/inward/record.uri?eid=2-s2.0-85122460017&doi=10.1080%2f10095020.2021.2014765&partnerID=40&md5=829e2d6a18d022ac9574f3ae626093c7, doi:10.1080/10095020.2021.2014765.

[316] Andrés Menéndez Blanco, Jesús García Sánchez, José Manuel Costa-García, João Fonte, David González-Álvarez, and Víctor Vicente García. Following the roman army between the southern foothills of the cantabrian mountains and the northern plains of castile and león (north of spain): archaeological applications of remote sensing and geospatial tools. *Geosciences (Switzerland)*, 10(12):485, 2020. URL: https://www.scopus.com/inward/record.uri?eid=2-s2.0-85097317354&doi=10.3390%2fgeosciences10120485&partnerID=40&md5=9798bbfe840daf33a9de9a0c4968a10d, doi:10.3390/geosciences10120485.

[317] Q. Meng, W. Liu, L. Zhang, M. Allam, Y. Bi, X. Hu, J. Gao, D. Hu, and T. Jancsó. Relationships between land surface temperatures and neighboring environment in highly urbanized areas: seasonal and scale effects analyses of beijing, china. *Remote Sensing*, 2022. URL: https://www.scopus.com/inward/record.uri?eid=2-s2.0-85137918893&doi=10.3390%2frs14174340&partnerID=40&md5=03e893b56690ce03aa758266c9537513, doi:10.3390/rs14174340.

[318] M. Fabian Meyer-Heß. Identification of archaeologically relevant areas using open geodata. *KN - Journal of Cartography and Geographic Information*, 70(3):107–125, 2020. URL: https://www.scopus.com/inward/record.uri?eid=2-s2.0-85089247166&doi=10.1007%2fs42489-020-00049-w&partnerID=40&md5=aa9809e2ff2ce602641c8e94f4bae49a, doi:10.1007/s42489-020-00049-w.

[319] E. Meylemans, G. Creemers, M. de Bie, and J. Paesen. Revealing extensive protohistoric field systems through high resolution lidar data in the northern part of belgium. *ARCHAOLOGISCHES KORRESPONDENZBLATT*,

45(2):197–213, 2015. URL: https://www.scopus.com/inward/record.uri?eid=2-s2.0-84940646573&partnerID=40&md5=62f878f084781ae946564689ef760936.

[320] Chunping Miao, Shuai Yu, Yuanman Hu, Huiwen Zhang, Xingyuan He, and Wei Chen. Review of methods used to estimate the sky view factor in urban street canyons. *BUILDING AND ENVIRONMENT*, 168:106497, 2020. URL: https://www.scopus.com/inward/record.uri?eid=2-s2.0-85074074376&doi=10.1016%2fj.buildenv.2019.106497&partnerID=40&md5=0ec6ed4f381380469d2ff9ebf5dd4fcc, doi:10.1016/j.buildenv.2019.106497.

[321] Ariane Middel, Jonas Lukasczyk, and Ross Maciejewski. Sky view factors from synthetic fisheye photos for thermal comfort routing—a case study in phoenix, arizona. *URBAN PLANNING*, 2(1):19–30, 2017. URL: https://www.scopus.com/inward/record.uri?eid=2-s2.0-85027725716&doi=10.17645%2fup.v2i1.855&partnerID=40&md5=d9578eabe77e4a355f14a333c0f642a2, doi:10.17645/up.v2i1.855.

[322] Ariane Middel, Jonas Lukasczyk, Ross Maciejewski, Matthias Demuzere, and Matthias Roth. Sky view factor footprints for urban climate modeling. *URBAN CLIMATE*, 25:120–134, 2018. URL: https://www.scopus.com/inward/record.uri?eid=2-s2.0-85046366561&doi=10.1016%2fj.uclim.2018.05.004&partnerID=40&md5=f4954e6099d242cf42072a350287a9a4, doi:10.1016/j.uclim.2018.05.004.

[323] Maarit Middleton, Jukka Heikkonen, Paavo Nevalainen, Eija Hyvönen, and Raimo Sutinen. Machine learning-based mapping of micro-topographic earthquake-induced paleo-pulju moraines and liquefaction spreads from a digital elevation model acquired through laser scanning. *Geomorphology*, 358:107099, 2020. URL: https://www.scopus.com/inward/record.uri?eid=2-s2.0-85080935968&doi=10.1016%2fj.geomorph.2020.107099&partnerID=40&md5=462d6d6ed0d33b7f38fdf926c6c0485a, doi:10.1016/j.geomorph.2020.107099.

[324] R. Miranda-Gómez, H. V. Cabadas-Báez, X. Antonio-Némiga, and N. Dávila-Hernández. Geospatial integration in mapping pre-hispanic settlements within aztec empire limits. *Virtual Archaeology Review*, 13(27):46–65, 2022. URL: https://www.scopus.com/inward/record.uri?eid=2-s2.0-85135253954&doi=10.4995%2fvar.2022.16106&partnerID=40&md5=674c4e69465bc4a7f71f3cc28db02676, doi:10.4995/var.2022.16106.

[325] Fabrice Monna, Yury Esin, Jérome Magail, Ludovic Granjon, Nicolas Navarro, Josef Wilczek, Laure Saligny, Sébastien Couette, Anthony Dumontet, and Carmela Chateau. Documenting carved stones by 3d modelling – example of mongolian deer stones. *JOURNAL OF CULTURAL HERITAGE*, 34:116–128, 2018. URL: https://www.scopus.com/inward/record.uri?eid=2-s2.0-85046679239&doi=10.1016%2fj.culher.2018.04.021&partnerID=40&md5=bf391ad1cd57a53e1213b2cb804fc2da, doi:10.1016/j.culher.2018.04.021.

[326] Kelly Monteleone, Amy E. Thompson, and Keith M. Prufer. Virtual cultural landscapes: geospatial visualizations of past environments. *Archaeological Prospection*, 2021. URL: https://www.scopus.com/inward/record.uri?eid=2-s2.0-85106326163&doi=10.1002%2farp.1830&partnerID=40&md5=73b439da31493ec9ab31f4bb1dac9c82, doi:10.1002/arp.1830.

[327] Reinaldo A. Moralejo, Diego Gobbo, Daniel Del Cogliano, and Leandro Pinto. Aplicación de tecnología lidar en el shincal de quimivil, londres, catamarca. *ARQUEOLOGIA*, 24(3):165, 2018. URL: https://www.scopus.com/inward/record.uri?eid=2-s2.0-85063462723&doi=10.34096%2farqueologia.t24.n3.5386&partnerID=40&md5=a774f6946f164fecdd31ec19adf4d52b, doi:10.34096/arqueologia.t24.n3.5386.

[328] Fernando Morales Hernández and Ángel Morillo Cerdán. Nuevas aportaciones sobre el campamento iii de renieblas (soria): ¿castra de nobilior o castra de escipion? *CUADERNOS DE PREHISTORIA Y ARQUEOLOGIA-UNIVERSIDAD AUTONOMA DE MADRID*, pages 187–214, 2020. doi:10.15366/cupauam2020.46.007.

[329] Katie M. Moriarty and Clinton W. Epps. Retained satellite information influences performance of gps devices in a forested ecosystem. *WILDLIFE SOCIETY BULLETIN*, 39(2):349–357, 2015. URL: https://www.scopus.com/inward/record.uri?eid=2-s2.0-84945447381&doi=10.1002%2fwsb.524&partnerID=40&md5=a354efb66ccabcabb0b848be38a263c9, doi:10.1002/wsb.524.

[330] Á. Morillo, B. X. Currás, A. Orejas, and A. Nobilini. Roman practice camps at trobajo del camino (san andrés de rabanedo) and oteruelo de la valdoncina (león). a preliminary approach. *Gladius*, 41:91–119, 2021. URL: https://www.scopus.com/inward/record.uri?eid=2-s2.0-85111492768&doi=10.3989%2fGLADIUS.2021.05&partnerID=40&md5=f9f650dbf6938c9af27be3b54ca7607b, doi:10.3989/GLADIUS.2021.05.

[331] Holley Moyes and Shane Montgomery. Locating cave entrances using lidar-derived local relief modeling. *Geosciences (Switzerland)*, 9(2):98, 2019. URL: https://www.scopus.com/inward/record.uri?eid=2-s2.0-85065191449&doi=10.3390%2fgeosciences9020098&partnerID=40&md5=f0a0698215541dd45030a39531e8c088, doi:10.3390/geosciences9020098.

[332] David Muñoz, Benoit Beckers, Gonzalo Besuievsky, and Gustavo Patow. A technique for massive sky view factor calculations in large cities. *INTERNATIONAL JOURNAL OF REMOTE SENSING*, 39(12):4040–4058, 2018. URL: https://www.scopus.com/inward/record.uri?eid=2-s2.0-85054885133&doi=10.1080%2f01431161.2018.1452071&partnerID=40&md5=0b5fec2e62bb48e00111e0cd1aa5aa37, doi:10.1080/01431161.2018.1452071.

[333] David Muñoz, Gonzalo Besuievsky, and Gustavo Patow. A procedural technique for thermal simulation and visualization in urban environments. *BUILDING SIMULATION*, 12(6):1013–1031, 2019. URL: https://www.scopus.com/inward/record.uri?eid=2-s2.0-85068870083&doi=10.1007%2fs12273-019-0549-x&partnerID=40&md5=9a920d0b5bc67596809265269415 2f8d, doi:10.1007/s12273-019-0549-x.

[334] Guglielmina Mutani and Valeria Todeschi. Building energy modeling at neighborhood scale. *ENERGY EFFICIENCY*, 13(7):1353–1386, 2020. URL: https://www.scopus.com/inward/record.uri?eid=2-s2.0-85088395375&doi=10.1007%2fs12053-020-09882-4&partnerID=40&md5=cf0751f9e20de4a51af33c2a64bc5a66, doi:10.1007/s12053-020-09882-4.

[335] Bilguunmaa Myagmardulam, Ryu Miura, Fumie Ono, Toshinori Kagawa, Lin Shan, Tadachika Nakayama, Fumihide Kojima, and Baasandash Choijil. Performance evaluation of lora 920 mhz frequency band in a hilly forested area. *Electronics (Switzerland)*, 10(4):502, 2021. URL: https://www.scopus.com/inward/record.uri?eid=2-s2.0-85100941952&doi=10.3390%2felectronics10040502&partnerID=40&md5=c09571754baae22c143536233cf5e825, doi:10.3390/electronics10040502.

[336] Ahmed K. Nassar, G. Alan Blackburn, and J. Duncan Whyatt. Dynamics and controls of urban heat sink and island phenomena in a desert city: development of a local climate zone scheme using remotely-sensed inputs. *INTERNATIONAL JOURNAL OF APPLIED EARTH OBSERVATION AND GEOINFORMATION*, 51:76–90, 2016. URL: https://www.scopus.com/inward/record.uri?eid=2-s2.0-84997113230&doi=10.1016%2fj.jag.2016.05.004&partnerID=40&md5=5c45e0b4125eaee9d578c13a25ba3c7b, doi:10.1016/j.jag.2016.05.004.

[337] Panagiotis T. Nastos, Emmanuel Vassilakis, Marina-Panagiota P. Nastos, Ioannis Charalampopoulos, and Andreas Matzarakis. Assessment of continuous sky view factor based on ultra-high resolution natural colour images acquired by remotely piloted airborne systems for applications in an urban area of athens. *INTERNATIONAL JOURNAL OF REMOTE SENSING*, 38(20):5814–5829, 2017. URL: https://www.scopus.com/inward/record.uri?eid=2-s2.0-85046264738&doi=10.1080%2f01431161.2017.1346845&partnerID=40&md5=35fa12ecb6a67821d89e1ba59b7b58fd, doi:10.1080/01431161.2017.1346845.

[338] Mihai Niculiță. Geomorphometric methods for burial mound recognition and extraction from high-resolution lidar dems. *Sensors (Switzerland)*, 2020. URL: https://www.scopus.com/inward/record.uri?eid=2-s2.0-85079867160&doi=10.3390%2fs20041192&partnerID=40&md5=95931a22991cbd803eec15c1b2b200ef, doi:10.3390/s20041192.

[339] S. Nión-Álvarez. A methodological approach to identify roman roads using lidar sensing technology and aerial orthoimages. the case of viae xix and xx (nw iberia). *Journal of Archaeological Science: Reports*, 2022. URL: https://www.scopus.com/inward/record.uri?eid=2-s2.0-85136527087&doi=10.1016%2fj.jasrep.2022.103612&partnerID=40&md5=ab8dbbde0ab8601712b57ae1518354eb, doi:10.1016/j.jasrep.2022.103612.

[340] D. Noack. Gis-based analysis for the detection of medieval ridge-andfurrow soil cultivation patterns within the prignitz region (north-eastern germany). *AGIT- Journal fur Angewandte Geoinformatik*, 5:60–72, 2019. URL: https://www.scopus.com/inward/record.uri?eid=2-s2.0-85091979369&doi=10.14627%2f537669006&partnerID=40&md5=3c39f3a1f90252f4ae6f76c9c734a229, doi:10.14627/537669006.

[341] A. Novak and K. Oštir. Towards better visualisation of alpine quaternary landform features on high-resolution digital elevation models. *Remote Sensing*, 2021. URL: https://www.scopus.com/inward/record.uri?eid=2-s2.0-85118135708&doi=10.3390%2frs13214211&partnerID=40&md5=bc7faf6973a7fe7efb0560cbcb87a183, doi:10.3390/rs13214211.

[342] E. Oduncu and S. E. Yüksel. An investigation of the effect of neighboring objects to shadow areas on real data based on the physical radiance model. *Journal of the Faculty of Engineering and Architecture of Gazi University*, 33(3):887–894, 2018. URL: https://www.scopus.com/inward/record.uri?eid=2-s2.0-85068919599&partnerID=40&md5=20ae65dc62ec000b35dfd38147b9362f.

[343] E. Oduncu and S. E. Yuksel. An in-depth analysis of hyperspectral target detection with shadow compensation via lidar. *Signal Processing: Image Communication*, 2021. URL: https://www.scopus.com/inward/record.uri?eid=2-s2.0-85115030475&doi=10.1016%2fj.image.2021.116427&partnerID=40&md5=78e79a86193f3311a15570ea3354c49b, doi:10.1016/j.image.2021.116427.

[344] C. Oliveira, S. Aravecchia, C. Pradalier, V. Robin, and S. Devin. The use of remote sensing tools for accurate charcoal kilns' inventory and distribution analysis: comparative assessment and prospective. *INTERNATIONAL JOURNAL OF APPLIED EARTH OBSERVATION AND GEOINFORMATION*, 2021. URL: https://www.scopus.com/inward/record.uri?eid=2-s2.0-85121613049&doi=10.1016%2fj.jag.2021.102641&partnerID=40&md5=275da4134fc23a997f1cdf6145299c81, doi:10.1016/j.jag.2021.102641.

[345] Michael A. O'Neal. An objective approach to defining earthwork geometries using subdecimeter digital elevation models. *Geoarchaeology*, 27(2):157–165, 2012. URL: https://www.scopus.com/inward/record.uri?eid=2-s2.0-84867355439&doi=10.1002%2fgea.21404&partnerID=40&md5=33b8ff18013ae06c71b0c4fdf62f6b4d, doi:10.1002/gea.21404.

[346] Hector A. Orengo and Carl Knappett. Toward a definition of minoan agro-pastoral landscapes: results of the survey at palaikastro (crete). *AMERICAN JOURNAL OF ARCHAEOLOGY*, 122(3):479, 2018. URL: https://www.scopus.com/inward/record.uri?eid=2-s2.0-85051504574&doi=10.3764%2faja.122.3.0479&partnerID=40&md5=38c19fc0af3c09426f6b95dde0e3f86a, doi:10.3764/aja.122.3.0479.

[347] Hector A. Orengo and Cameron A. Petrie. Multi-scale relief model (msrm): a new algorithm for the visualization of subtle topographic change of variable size in digital elevation models. *Earth Surface Processes and Landforms*, 43(6):1361–1369, 2018. URL: https://www.scopus.com/inward/record.uri?eid=2-s2.0-85041330903&doi=10.1002%2fesp.4317&partnerID=40&md5=d740c9054f0d5735b1ffecea1e22eea7, doi:10.1002/esp.4317.

[348] X. Ouyang, Y. Dou, J. Yang, X. Chen, and J. Wen. High spatiotemporal rugged land surface temperature downscaling over saihanba forest park, china. *Remote Sensing*, 2022. URL: https://www.scopus.com/inward/record.uri?eid=2-s2.0-85132285184&doi=10.3390%2frs14112617&partnerID=40&md5=215c99c2c4e012a8aa1ece4a7dd71fb4, doi:10.3390/rs14112617.

[349] G. Paliaga, F. Luino, L. Turconi, M. Profeta, Z. Vojinovic, S. Cucchiaro, and F. Faccini. Terraced landscapes as nbss for geo-hydrological hazard mitigation: towards a methodology for debris and soil volume estimations through a lidar survey. *Remote Sensing*, 2022. URL: https://www.scopus.com/inward/record.uri?eid=2-s2.0-85137023050&doi=10.3390%2frs14153586&partnerID=40&md5=08dba6c5f0f4ba728bb97fe4e20bb800, doi:10.3390/rs14153586.

[350] Jamie L. Peeler and Erica A. H. Smithwick. Seed source pattern and terrain have scale-dependent effects on post-fire tree recovery. *LANDSCAPE ECOLOGY*, 35(9):1945–1959, 2020. URL: https://www.scopus.com/inward/record.uri?eid=2-s2.0-85088302032&doi=10.1007%2fs10980-020-01071-z&partnerID=40&md5=5ef6517943900c6ee830133ab1e543d6, doi:10.1007/s10980-020-01071-z.

[351] J. L. Peeler and E.A.H. Smithwick. Interactions between landscape and local factors inform spatial action planning in post-fire forest environments. *LANDSCAPE ECOLOGY*, 2021. URL: https://www.scopus.com/inward/record.uri?eid=2-s2.0-85113268428&doi=10.1007%2fs10980-021-01325-4&partnerID=40&md5=bcc2490189e453251d01a5363e2f7845, doi:10.1007/s10980-021-01325-4.

[352] R. Perarnau, A. Devos, A. Quiquerez, J. Brenot, P. Taborelli, S. Ortonovi, and B. Furlani. Assessing the role of slope, lithology and land use in the formation and conservation of war-related geomorphic features (case study of ww1 railway artillery in montagne de reims, marne, france). *APPLIED GEOGRAPHY*, 2022. URL: https://www.scopus.com/inward/record.uri?eid=2-s2.0-85127352524&doi=10.1016%2fj.apgeog.2022.102691&partnerID=40&md5=4c5bf5a6c253cfb8b4e69079235e68ce, doi:10.1016/j.apgeog.2022.102691.

[353] Anna Petrasova, Brendan Harmon, Vaclav Petras, and Helena Mitasova. *Tangible Modeling with Open Source GIS*. Tangible Modeling with Open Source GIS. Springer International Publishing, Cham, 2015. URL: https://www.scopus.com/inward/record.uri?eid=2-s2.0-85012134759&doi=10.1007%2f978-3-319-25775-4&partnerID=40&md5=33334f0bbe4ca0b0149c7c98e3d15217, doi:10.1007/978-3-319-25775-4.

[354] I. Pikirayi, F. Sulas, B. Nxumalo, M. E. Sagiya, D. Stott, S. M. Kristiansen, S. Chirikure, and T. Musindo. Climate-smart harvesting and storing of water: the legacy of dhaka pits at great zimbabwe. *ANTHROPOCENE*, 2022. URL: https://www.scopus.com/inward/record.uri?eid=2-s2.0-85143868586&doi=10.1016%2fj.ancene.2022.100357&partnerID=40&md5=d74f56c0382ff3832767fe8cabbc1545, doi:10.1016/j.ancene.2022.100357.

[355] Thomas Pingel and Keith Clarke. Perceptually shaded slope maps for the visualization of digital surface models. *Cartographica: The International Journal for Geographic Information and Geovisualization*, 49(4):225–240, 2014. doi:10.3138/carto.49.4.2141.

[356] Thomas J. Pingel, Keith Clarke, and Anabel Ford. Bonemapping: a lidar processing and visualization technique in support of archaeology under the canopy. *Cartography and Geographic Information Science*, 42(sup1):18–26, 2015. URL: https://www.scopus.com/inward/record.uri?eid=2-s2.0-84939792012&doi=10.1080%2f15230406.2015.1059171&partnerID=40&md5=e8761d72474a3e32e15ff0ae77316233, doi:10.1080/15230406.2015.1059171.

[357] Helena Saraiva Koenow Pinheiro, Waldir de Carvalho Junior, César Silva Da Chagas, Lúcia Helena Cunha dos Anjos, and Phillip Ray Owens. Prediction of topsoil texture through regression trees and multiple linear regressions. *REVISTA BRASILEIRA DE CIENCIA DO SOLO*, 2018. URL: https://www.scopus.com/inward/record.uri?eid=2-s2.0-85045696180&doi=10.1590%2f18069657rbcs20170167&partnerID=40&md5=e16df95362ca3e8bc3992f0fcfc20f40, doi:10.1590/18069657rbcs20170167.

[358] Primož Pipan and Žiga Kokalj. Transformation of the jeruzalem hills cultural landscape with modern vineyard terraces. *Acta Geographica Slovenica*, 57(2):149–162, 2017. URL: https://www.scopus.com/inward/record.uri?eid=2-s2.0-85019745053&doi=10.3986%2fAGS.4629&partnerID=40&md5=95ae46abca4dfbf6d6c0564012a41d4c, doi:10.3986/AGS.4629.

[359] Tomislav Popit, Blaž Supej, Žiga Kokalj, and Timotej Verbovšek. Comparison of methods for geomorphometric analyzes of surface roughness in the vipava valley. *GEODETSKI VESTNIK*, 60(02):227–240, 2016. URL: https://www.scopus.com/inward/record.uri?eid=2-s2.0-84977474276&doi=10.15292%2fgeodetski-vestnik.2016.02.227-240&partnerID=40&md5=c81425c7c42d9d500684843564c2c3c5, doi:10.15292/geodetski-vestnik.2016.02.227-240.

[360] T. Popit, B. Rožič, A. Šmuc, A. Novak, and T. Verbovšek. Using a lidar-based height variability method for recognizing and analyzing fault displacement and related fossil mass movement in the vipava valley, sw slovenia. *Remote Sensing*, 2022. URL: https://www.scopus.com/inward/record.uri?eid=2-s2.0-85129178184&doi=10.3390%2frs14092016&partnerID=40&md5=2c40b3e3a048be8a9312509c7656237b, doi:10.3390/rs14092016.

[361] Sara Popović, Davor Bulić, Robert Matijašić, Katarina Gerometta, and Giovanni Boschian. Roman land division in istria, croatia: historiography, lidar, structural survey and excavations. *Mediterranean Archaeology and Archaeometry*, 21(1):165–178, 2020. URL: https://www.scopus.com/inward/record.uri?eid=2-s2.0-85099256112&doi=10.5281%2fzenodo.4394051&partnerID=40&md5=cf328514f874ad245413608abf304002, doi:10.5281/zenodo.4394051.

[362] S. J. Price, M. J. Adams, and Y. Tepper. An integrated spatial approach to archaeological prospection using gis and pedestrian survey data at tell abu shusha, israel. *Archaeological Prospection*, 2022. URL: https://www.scopus.com/inward/record.uri?eid=2-s2.0-85144045767&doi=10.1002%2farp.1888&partnerID=40&md5=a5eb4d07e11ddb627b060c18b7779ef6, doi:10.1002/arp.1888.

[363] Keith M. Prufer, Amy E. Thompson, and Douglas J. Kennett. Evaluating airborne lidar for detecting settlements and modified landscapes in disturbed tropical environments at uxbenká, belize. *Journal of Archaeological Science*, 57:1–13, 2015. URL: https://www.scopus.com/inward/record.uri?eid=2-s2.0-84924151275&doi=10.1016%2fj.jas.2015.02.013&partnerID=40&md5=be65b22fd99a80b7f6a58c2498f440a2, doi:10.1016/j.jas.2015.02.013.

[364] JinLing Quan. Enhanced geographic information system-based mapping of local climate zones in beijing, china. *Science China Technological Sciences*, 62(12):2243–2260, 2019. URL: https://www.scopus.com/inward/record.uri?eid=2-s2.0-85068458941&doi=10.1007%2fs11431-018-9417-6&partnerID=40&md5=f59a860041ecfcbe02bb3cbe3fa2ac41, doi:10.1007/s11431-018-9417-6.

[365] Włodzimierz Rączkowski. Power and/or penury of visualizations: some thoughts on remote sensing data and products in archaeology. *Remote Sensing*, 12(18):2996, 2020. URL: https://www.scopus.com/inward/record.uri?eid=2-s2.0-85092152307&doi=10.3390%2fRS12182996&partnerID=40&md5=1189868110d9d8f5d0e97c3b097d5fb6, doi:10.3390/RS12182996.

[366] Mario Ramírez Galán. If the archaeological context is missing: the use of lidar prospection to uncover features at the medieval christian position on malvecino hill (alcalá de henares, spain). *Archaeological Prospection*, 28(1):25–33, 2021. URL: https://www.scopus.com/inward/record.uri?eid=2-s2.0-85088292232&doi=10.1002%2farp.1791&partnerID=40&md5=9dba0ae794b2a7fa116a100dff6c780a, doi:10.1002/arp.1791.

[367] L. A. Reeder-Myers, W. A. Goodwin, A. J. Figueroa, A. I. Domic, and J. C. Fernandez-Diaz. Cultural landscapes of resilience and vulnerability: the selin farm site, northeastern honduras. *Journal of Field Archaeology*, 2022. URL: https://www.scopus.com/inward/record.uri?eid=2-s2.0-85142141279&doi=10.1080%2f00934690.2022.2141888&partnerID=40&md5=b59a47472fc0de57830706f1e47b807b, doi:10.1080/00934690.2022.2141888.

[368] Naveed Ur Rehman and Mubashir Ali Siddiqui. A novel method for determining sky view factor for isotropic diffuse radiations for a collector in obstacles-free or urban sites. *JOURNAL OF RENEWABLE AND SUSTAINABLE ENERGY*, 7(3):033110, 2015. URL: https://www.scopus.com/inward/record.uri?eid=2-s2.0-84929992091&doi=10.1063%2f1.4921386&partnerID=40&md5=983133279e66fbd39256c198cee5b148, doi:10.1063/1.4921386.

[369] Jeroen de Reu, Jan Trachet, Pieter Laloo, and Wim de Clercq. From low cost uav survey to high resolution topographic data: developing our understanding of a medieval outport of bruges. *Archaeological Prospection*, 23(4):335–346, 2016. URL: https://www.scopus.com/inward/record.uri?eid=2-s2.0-84990040770&doi=10.1002%2farp.1547&partnerID=40&md5=a598cd85a64f95f31adfa7a2e4684008, doi:10.1002/arp.1547.

[370] Ole Risbøl, Ole Martin Bollandsås, Anneli Nesbakken, Hans Ole Ørka, Erik Næsset, and Terje Gobakken. Interpreting cultural remains in airborne laser scanning generated digital terrain models: effects of size and shape on detection success rates. *Journal of Archaeological Science*, 40(12):4688–4700, 2013. doi:10.1016/j.jas.2013.07.002.

[371] Ole Risbøl, Daniel Langhammer, Esben Schlosser Mauritsen, and Oula Seitsonen. Employment, utilization, and development of airborne laser scanning in fenno-scandinavian archaeology—a review. *Remote Sensing*, 12(9):1411, 2020. URL: https://www.scopus.com/inward/record.uri?eid=2-s2.0-85085972258&doi=10.3390%2fRS12091411&partnerID=40&md5=d593c957be01da7dc1576a197585c88d, doi:10.3390/RS12091411.

[372] Mark J. Rochelo, Christian Davenport, and Donna Selch. Revealing pre-historic native american belle glade earthworks in the northern everglades utilizing airborne lidar. *Journal of Archaeological Science: Reports*, 2:624–643, 2015. URL: https://www.scopus.com/inward/record.uri?eid=2-s2.0-84937889559&doi=10.1016%2fj.jasrep.2014.11.009&partnerID=40&md5=f8eb794fb60280212fd1c5003d3668e0, doi:10.1016/j.jasrep.2014.11.009.

[373] J. Rodzik, B. Niezabitowska-Wiśniewska, J. Nitychoruk, J. Budziszewski, and M. Jakubczak. Geological and geomorphologic conditions and traces of prehistoric and historic human settlements in the vicinity of ulów (roztocze region, southeastern poland). *Studia Quaternaria*, 34(2):83–97, 2017. URL: https://www.scopus.com/inward/record.uri?eid=2-s2.0-85039854112&doi=10.1515%2fsqua-2017-007&partnerID=40&md5=bca86482f967f7c74681b0a72d1c6dc5, doi:10.1515/squa-2017-007.

[374] Johanna Roiha, Einari Heinaro, and Markus Holopainen. The hidden cairns—a case study of drone-based als as an archaeological site survey method. *Remote Sensing*, 13(10):2010, 2021. URL: https://www.scopus.com/inward/record.uri?eid=2-s2.0-85107017199&doi=10.3390%2frs13102010&partnerID=40&md5=4688942898ded5336a74b503382f31de, doi:10.3390/rs13102010.

[375] Tanguy Rolland, Fabrice Monna, Jérôme Magail, Yuri Esin, Nicolas Navarro, Josef Wilczek, Jamiyan-Ombo Gantulga, and Carmela Chateau-Smith. Documenting carved stones from 3d models. part ii — ambient occlusion to reveal carved parts. *JOURNAL OF CULTURAL HERITAGE*, 49:28–37, 2021. URL: https://www.scopus.com/inward/record.uri?eid=2-s2.0-85106294114&doi=10.1016%2fj.culher.2021.03.006&partnerID=40&md5=9de66ef5731ba9463ceb13c83c651d44, doi:10.1016/j.culher.2021.03.006.

[376] T. Rolland, F. Monna, J. F. Buoncristiani, J. Magail, Y. Esin, B. Bohard, and C. Chateau-Smith. Volumetric obscurance as a new tool to better visualize relief from digital elevation models. *Remote Sensing*, 2022. URL: https://www.scopus.com/inward/record.uri?eid=2-s2.0-85126280532&doi=10.3390%2frs14040941&partnerID=40&md5=cb21f269d2c3128f137e57aa40236b6f, doi:10.3390/rs14040941.

[377] Jakob Rom, Florian Haas, Manuel Stark, Fabian Dremel, Michael Becht, Karin Kopetzky, Christoph Schwall, Michael Wimmer, Norbert Pfeifer, Mahmoud Mardini, and Hermann Genz. Between land and sea: an airborne lidar field survey to detect ancient sites in the chekka region/lebanon using spatial analyses. *OPEN ARCHAEOLOGY*, 6(1):248–268, 2020. URL: https://www.scopus.com/inward/record.uri?eid=2-s2.0-85096811647&doi=10.1515%2fopar-2020-0113&partnerID=40&md5=90f154afd8a39e8b6d6e2f64fea4cf18, doi:10.1515/opar-2020-0113.

[378] Anamaria Roman, Tudor-Mihai Ursu, Sorina Fărcaş, Vlad-Andrei Lăzărescu, and Coriolan Horaţiu Opreanu. An integrated airborne laser scanning approach to forest management and cultural heritage issues: a case study at porolissum, romania. *ANNALS OF FOREST RESEARCH*, 0(0):171–187, 2014. URL: https://www.scopus.com/inward/record.uri?eid=2-s2.0-85021700776&doi=10.15287%2fafr.2016.755&partnerID=40&md5=b7e1e6b631c2bfd6f329144114e2fd52, doi:10.15287/afr.2016.755.

[379] Anamaria Roman, Tudor-Mihai Ursu, Vlad-Andrei Lăzărescu, Coriolan Horaţiu Opreanu, and Sorina Fărcaş. Visualization techniques for an airborne laser scanning-derived digital terrain model in forested steep terrain: detecting archaeological remains in the subsurface. *Geoarchaeology*, 32(5):549–562, 2017. URL: https://www.scopus.com/inward/record.uri?eid=2-s2.0-85019145032&doi=10.1002%2fgea.21621&partnerID=40&md5=35f2ee577087909e20f12fa0f2ab5244, doi:10.1002/gea.21621.

[380] Robert M. Rosenswig, Ricardo López-Torrijos, Caroline E. Antonelli, and Rebecca R. Mendelsohn. Lidar mapping and surface survey of the izapa state on the tropical piedmont of chiapas, mexico. *Journal of Archaeological Science*, 40(3):1493–1507, 2013. URL: https://www.scopus.com/inward/record.uri?eid=2-s2.0-84871448867&doi=10.1016%2fj.jas.2012.10.034&partnerID=40&md5=8013deb9f62f343c450309a1b99df493, doi:10.1016/j.jas.2012.10.034.

[381] Robert M. Rosenswig, Ricardo López-Torrijos, and Caroline E. Antonelli. Lidar data and the izapa polity: new results and methodological issues from tropical mesoamerica. *ARCHAEOLOGICAL AND ANTHROPOLOGICAL SCIENCES*, 7(4):487–504, 2015. URL: https://www.scopus.com/inward/record.uri?eid=2-s2.0-84936868111&doi=10.1007%2fs12520-014-0210-7&partnerID=40&md5=6edf3d722c57a099b4b2d1728b1a7f16, doi:10.1007/s12520-014-0210-7.

[382] Laure Roupioz, Francoise Nerry, Li Jia, and Massimo Menenti. Improved surface reflectance from remote sensing data with sub-pixel topographic information. *Remote Sensing*, 6(11):10356–10374, 2014. URL: https://www.scopus.com/inward/record.uri?eid=2-s2.0-84912059184&doi=10.3390%2frs61110356&partnerID=40&md5=a1cd4fb39421a3b07f169fb33a0a283e, doi:10.3390/rs61110356.

[383] Sebastian Różycki, Rafał Zapłata, Jerzy Karczewski, Andrzej Ossowski, and Jacek Tomczyk. Integrated archaeological research: archival resources, surveys, geophysical prospection and excavation approach at an execution and burial site: the german nazi labour camp in treblinka. *Geosciences (Switzerland)*, 10(9):336, 2020. URL: https://www.scopus.com/inward/record.uri?eid=2-s2.0-85090811059&doi=10.3390%2fgeosciences10090336&partnerID=40&md5=b8e05d38c209ef400a112ef87aca7611, doi:10.3390/geosciences10090336.

[384] Paweł Rutkiewicz, Ireneusz Malik, Małgorzata Wistuba, and Aleksandra Osika. High concentration of charcoal hearth remains as legacy of historical ferrous metallurgy in southern poland. *Quaternary International*, 512:133–143, 2019. URL: https://www.scopus.com/inward/record.uri?eid=2-s2.0-85064264371&

doi=10.1016%2fj.quaint.2019.04.015&partnerID=40&md5=419661a9b2334d85965227593da16a08, doi:10.1016/j.quaint.2019.04.015.

[385] F. Sánchez Díaz, L. García Sanjuán, and T. Rivera Jiménez. Potential and limitations of lidar altimetry in archaeological survey. copper age and bronze age settlements in southern iberia. *Archaeological Prospection*, 2022. URL: https://www.scopus.com/inward/record.uri?eid=2-s2.0-85131855188&doi=10.1002%2farp.1869&partnerID=40&md5=b0d865b086f0e56b9cb155db9194eb04, doi:10.1002/arp.1869.

[386] S. Sanlang, S. Cao, M. Du, Y. Mo, Q. Chen, and W. He. Integrating aerial lidar and very-high-resolution images for urban functional zone mapping. *Remote Sensing*, 2021. URL: https://www.scopus.com/inward/record.uri?eid=2-s2.0-85109959703&doi=10.3390%2frs13132573&partnerID=40&md5=f45ac473070889b960a157a516984098, doi:10.3390/rs13132573.

[387] P. Sapirstein. The first doric temple in sicily, its builder, and ig xiv 1. *Hesperia*, 90(3):411–477, 2021. URL: https://www.scopus.com/inward/record.uri?eid=2-s2.0-85120851461&doi=10.2972%2fhesperia.90.3.0411&partnerID=40&md5=7ad4d1555f8951f7c826c7075dce0a2f, doi:10.2972/hesperia.90.3.0411.

[388] Sanna Saunaluoma, Niko Anttiroiko, and Justin Moat. Uav survey at archaeological earthwork sites in the brazilian state of acre, southwestern amazonia. *Archaeological Prospection*, 26(4):325–331, 2019. URL: https://www.scopus.com/inward/record.uri?eid=2-s2.0-85070841005&doi=10.1002%2farp.1747&partnerID=40&md5=50ca19741f8fefa18d846a3b5f4aa492, doi:10.1002/arp.1747.

[389] M. Scarano and F. Mancini. Assessing the relationship between sky view factor and land surface temperature to the spatial resolution. *INTERNATIONAL JOURNAL OF REMOTE SENSING*, 38(23):6910–6929, 2017. URL: https://www.scopus.com/inward/record.uri?eid=2-s2.0-85054263948&doi=10.1080%2f01431161.2017.1368099&partnerID=40&md5=d0d6c3babb731b45f06c2d2a56adc2d1, doi:10.1080/01431161.2017.1368099.

[390] Whittaker Schroder, Timothy Murtha, Charles Golden, Armando Anaya Hernández, Andrew Scherer, Shanti Morell-Hart, Angélica Almeyda Zambrano, Eben Broadbent, and Madeline Brown. The lowland maya settlement landscape: environmental lidar and ecology. *Journal of Archaeological Science: Reports*, 33:102543, 2020. URL: https://www.scopus.com/inward/record.uri?eid=2-s2.0-85091084297&doi=10.1016%2fj.jasrep.2020.102543&partnerID=40&md5=6e649e61421a5d038047ba3a4bd64ab0, doi:10.1016/j.jasrep.2020.102543.

[391] Whittaker Schroder, Timothy Murtha, Eben N. Broadbent, and Angélica M. Almeyda Zambrano. A confluence of communities: households and land use at the junction of the upper usumacinta and lacantún rivers, chiapas, mexico. *World Archaeology*, pages 1–28, 2021. doi:10.1080/00438243.2021.1930135.

[392] Jennifer von Schwerin, Heather Richards-Rissetto, Fabio Remondino, Maria Grazia Spera, Michael Auer, Nicolas Billen, Lukas Loos, Laura Stelson, and Markus Reindel. Airborne lidar acquisition, post-processing and accuracy-checking for a 3d webgis of copan, honduras. *Journal of Archaeological Science: Reports*, 5:85–104, 2016. URL: https://www.scopus.com/inward/record.uri?eid=2-s2.0-84946866858&doi=10.1016%2fj.jasrep.2015.11.005&partnerID=40&md5=605f073d302b57f411cddb5875e2dc5a, doi:10.1016/j.jasrep.2015.11.005.

[393] Oula Seitsonen and Janne Ikäheimo. Detecting archaeological features with airborne laser scanning in the alpine tundra of sápmi, northern finland. *Remote Sensing*, 13(8):1599, 2021. URL: https://www.scopus.com/inward/record.uri?eid=2-s2.0-85105051031&doi=10.3390%2frs13081599&partnerID=40&md5=66766b09b671e73ae57a435ff4e3a78f, doi:10.3390/rs13081599.

[394] Christopher Sevara, Michael Pregesbauer, Michael Doneus, Geert Verhoeven, and Immo Trinks. Pixel versus object — a comparison of strategies for the semi-automated mapping of archaeological features using airborne laser scanning data. *Journal of Archaeological Science: Reports*, 5:485–498, 2016. URL: https://www.scopus.com/inward/record.uri?eid=2-s2.0-84954512314&doi=10.1016%2fj.jasrep.2015.12.023&partnerID=40&md5=eb0980609006defefc826d5cf76359bc, doi:10.1016/j.jasrep.2015.12.023.

[395] M. Slámová, N. B. Pažinová, I. Belčáková, J. Beljak, and P. Maliniak. Identification of historical trackways in forests using contextual geospatial analyses. *Archaeological Prospection*, 2022. URL: https://www.scopus.com/inward/record.uri?eid=2-s2.0-85141392882&doi=10.1002%2farp.1882&partnerID=40&md5=cab807a193b4a5876000fe44d70c132a, doi:10.1002/arp.1882.

[396] Devin F. Smith, Steven T. Goldsmith, Brendan A. Harmon, Jorge A. Espinosa, and Russell S. Harmon. Physical controls and enso event influence on weathering in the panama canal watershed. *SCIENTIFIC REPORTS*, 10(1):10861, 2020. URL: https://www.scopus.com/inward/record.uri?eid=2-s2.0-85087348035&doi=10.1038%2fs41598-020-67797-7&partnerID=40&md5=cd477ba133cb3430c3b0fab9023be7ab, doi:10.1038/s41598-020-67797-7.

[397] Aleš Smrekar, Mateja Breg Valjavec, Katarina Polajnar Horvat, and Jernej Tiran. The geography of urban environmental protection in slovenia: the case of ljubljana. *Acta Geographica Slovenica*, 59(3):5–70, 2020. URL: https://www.scopus.com/inward/record.uri?eid=2-s2.0-85085936664&doi=10.3986%2fAGS.7638&partnerID=40&md5=f89b8c564f3dbd4290c85f95da77bf06, doi:10.3986/AGS.7638.

[398] Zbyněk Sokol, Vojtěch Bližňák, Pavel Sedlák, Petr Zacharov, Petr Pešice, and Miroslav Škuthan. Ensemble forecasts of road surface temperatures. *ATMOSPHERIC RESEARCH*, 187:33–41, 2017. URL: https://www.scopus.com/inward/record.uri?eid=2-s2.0-85007391676&doi=10.1016%2fj.atmosres.2016.12.010&partnerID=40&md5=9d56a3c4e0bfa85a40c9bce13524f4c7, doi:10.1016/j.atmosres.2016.12.010.

[399] Ion Sola, Maria Gonzalez-Audicana, Jesus Alvarez-Mozos, and Jose Luis Torres. Synthetic images for evaluating topographic correction algorithms. *IEEE TRANSACTIONS ON GEOSCIENCE AND REMOTE SENSING*, 52(3):1799–1810, 2014. URL: https://www.scopus.com/inward/record.uri?eid=2-s2.0-84891555451&doi=10.1109%2fTGRS.2013.2255296&partnerID=40&md5=c5cada5eaa52cbf630319421d78441c4, doi:10.1109/TGRS.2013.2255296.

[400] Ion Sola, María González-Audícana, and Jesús Álvarez-Mozos. Validation of a simplified model to generate multispectral synthetic images. *Remote Sensing*, 7(3):2942–2951, 2015. URL: https://www.scopus.com/inward/record.uri?eid=2-s2.0-84926315348&doi=10.3390%2frs70302942&partnerID=40&md5=28364e169a2062ae9ae3c6fc247c9eae, doi:10.3390/rs70302942.

[401] Maja Somrak, Sašo Džeroski, and Žiga Kokalj. Learning to classify structures in als-derived visualizations of ancient maya settlements with cnn. *Remote Sensing*, 12(14):2215, 2020. URL: https://www.scopus.com/inward/record.uri?eid=2-s2.0-85088632320&doi=10.3390%2frs12142215&partnerID=40&md5=a917f9c1d5fd4ffa859277b4a70a6fbf, doi:10.3390/rs12142215.

[402] Till Sonnemann, Jorge Ulloa Hung, and Corinne Hofman. Mapping indigenous settlement topography in the caribbean using drones. *Remote Sensing*, 8(10):791, 2016. URL: https://www.scopus.com/inward/record.uri?eid=2-s2.0-85019720157&doi=10.3390%2frs8100791&partnerID=40&md5=5b0e85426b37c72a5171a4bf39a64e4e, doi:10.3390/rs8100791.

[403] Ivan Šprajc, Nicholas P. Dunning, Jasmina Štajdohar, Quintin Hernández Gómez, Israel Chato López, Aleš Marsetič, Joseph W. Ball, Sara Dzul Góngora, Octavio Q. Esparza Olguín, Atasta Flores Esquivel, and Žiga Kokalj. Ancient maya water management, agriculture, and society in the area of chactún, campeche, mexico. *JOURNAL OF ANTHROPOLOGICAL ARCHAEOLOGY*, 61:101261, 2021. URL: https://www.scopus.com/inward/record.uri?eid=2-s2.0-85098711820&doi=10.1016%2fj.jaa.2020.101261&partnerID=40&md5=f0ce6be5bad962f266baefad77b49d13, doi:10.1016/j.jaa.2020.101261.

[404] I. Šprajc, A. Marsetič, J. Štajdohar, S. D. Góngora, J. W. Ball, O. E. Olguín, and Ž. Kokalj. Archaeological landscape, settlement dynamics, and sociopolitical organization in the chactún area of the central maya lowlands. *PLoS ONE*, 2022. URL: https://www.scopus.com/inward/record.uri?eid=2-s2.0-85123352170&doi=10.1371%2fjournal.pone.0262921&partnerID=40&md5=7e2880fcb466a8637a4e77ca8d10f63d, doi:10.1371/journal.pone.0262921.

[405] Adam P. Spring and Caradoc Peters. Developing a low cost 3d imaging solution for inscribed stone surface analysis. *Journal of Archaeological Science*, 52:97–107, 2014. URL: https://www.scopus.com/inward/record.uri?eid=2-s2.0-84907168864&doi=10.1016%2fj.jas.2014.08.017&partnerID=40&md5=ec043967b92d485f4255df764cf559e6, doi:10.1016/j.jas.2014.08.017.

[406] C. Stal, C. Covataru, J. Müller, V. Parnic, T. Ignat, R. Hofmann, and C. Lazar. Supporting long-term archaeological research in southern romania chalcolithic sites using multi-platform uav mapping. *Drones*, 2022. URL: https://www.scopus.com/inward/record.uri?eid=2-s2.0-85140622841&doi=10.3390%2fdrones6100277&partnerID=40&md5=58132f1b8b1720d1e71c100e7d6e8046, doi:10.3390/drones6100277.

[407] Marialuce Stanganelli and Carlo Gerundo. Understanding the role of urban morphology and green areas configuration during heat waves. *International Journal of Agricultural and Environmental Information Systems*, 8(2):50–64, 2017. URL: https://www.scopus.com/inward/record.uri?eid=2-s2.0-85016060699&doi=10.4018%2fIJAEIS.2017040104&partnerID=40&md5=d8141da064fe48da040710caac596255, doi:10.4018/IJAEIS.2017040104.

[408] Lenka Starková. Toward a high-definition remote sensing approach to the study of deserted medieval cities in the near east. *Geosciences*, 10(9):369, 2020. doi:10.3390/geosciences10090369.

[409] M.-M. Ștefan, D. Ștefan, V. Sîrbu, S.-C. Ailincăi, and A. Țârlea. The emergence of inland settlements in northern dobruja at the end of the archaic period. a newly surveyed settlement on celic dere valley. *Peuce*, 2021(19):79–122, 2021. URL: https://www.scopus.com/inward/record.uri?eid=2-s2.0-85120037634&partnerID=40&md5=8d316e1abcd5ab622a969106ae4d2bbc.

[410] C. R. Steger, B. Steger, and C. Schär. Horayzon v1.2: an efficient and flexible ray-tracing algorithm to compute horizon and sky view factor. *Geoscientific Model Development*, 15(17):6817–6840, 2022. URL: https://www.scopus.com/inward/record.uri?eid=2-s2.0-85140410867&doi=10.5194%2fgmd-15-6817-2022&partnerID=40&md5=8520592dfe9d5970f3e2838d491bc7bb, doi:10.5194/gmd-15-6817-2022.

[411] Ronan Steinmann, Jean-Pierre Garcia, Annie Dumont, and Amélie Quiquerez. Aspects méthodologiques de l'approche intégrée des comblements postglaciaires : apports pour la reconstitution de la dynamique fluviale de la loire au cours de l'holocène. *Geomorphologie: Relief, Processus, Environnement*, 23(1):83–104, 2017. URL: https://www.scopus.com/inward/record.uri?eid=2-s2.0-85030310006&doi=10.4000%2fgeomorphologie.11650&partnerID=40&md5=7ea9c8ac734c6260fd90d2ebf70dce12, doi:10.4000/geomorphologie.11650.

[412] Krzysztof Stereńczak, Rafał Zapłata, Jarosław Wójcik, Bartłomiej Kraszewski, Miłosz Mielcarek, Krzysztof Mitelsztedt, Małgorzata Białczak, Grzegorz Krok, Łukasz Kuberski, Anna Markiewicz, Aneta Modzelewska, Karolina Parkitna, Żaneta Piasecka, Kamil Pilch, Karol Rzeczycki, Rafał Sadkowski, Martyna Wietecha, Piotr Rysiak, Klaus von Gadow, and Chris J. Cieszewski. Als-based detection of past human activities in the białowieża forest—new evidence of unknown remains of past agricultural systems. *Remote Sensing*, 12(16):2657, 2020. URL: https://www.scopus.com/inward/record.uri?eid=2-s2.0-85090357412&doi=10.3390%2fRS12162657&partnerID=40&md5=34d16c2d35f3fafde6f8487ae0c53c6f, doi:10.3390/RS12162657.

[413] Birger Stichelbaut, Wouter Gheyle, Timothy Saey, Veerle van Eetvelde, Marc van Meirvenne, Nicolas Note, Hanne van den Berghe, and Jean Bourgeois. The first world war from above and below. historical aerial photographs and mine craters in the ypres salient. *APPLIED GEOGRAPHY*, 66:64–72, 2016. URL: https://www.scopus.com/inward/record.uri?eid=2-s2.0-84949309354&doi=10.1016%2fj.apgeog.2015.11.020&partnerID=40&md5=4e746984175f3dd6715b6701da174cf0, doi:10.1016/j.apgeog.2015.11.020.

[414] Wesley D. Stoner, Barbara L. Stark, Amber VanDerwarker, and Kyle R. Urquhart. Between land and water: hydraulic engineering in the tlalixcoyan basin, veracruz, mexico. *JOURNAL OF ANTHROPOLOGICAL ARCHAEOLOGY*, 61:101264, 2021. URL: https://www.scopus.com/inward/record.uri?eid=2-s2.0-85100110766&doi=10.1016%2fj.jaa.2020.101264&partnerID=40&md5=c6da8323397616a79d96c5a008c6aabf, doi:10.1016/j.jaa.2020.101264.

[415] M. Storch, T. Jarmer, M. Adam, and N. de Lange. Systematic approach for remote sensing of historical conflict landscapes with uav-based laserscanning. *Sensors*, 2022. URL: https://www.scopus.com/inward/record.uri?eid=2-s2.0-85121768577&doi=10.3390%2fs22010217&partnerID=40&md5=fb2b47fac28ad0a419aa21a9053c745b, doi:10.3390/s22010217.

[416] David Stott, Søren Munch Kristiansen, Achim Lichtenberger, and Rubina Raja. Mapping an ancient city with a century of remotely sensed data. *Proceedings of the National Academy of Sciences of the United States of America*, 115(24):E5450–E5458, 2018. URL: https://www.scopus.com/inward/record.uri?eid=2-s2.0-85048548316&doi=10.1073%2fpnas.1721509115&partnerID=40&md5=cb3e4a5184092110b66619f65ddd127f, doi:10.1073/pnas.1721509115.

[417] B. Štular. The use of lidar-derived relief models in archaeological topography: the kobarid region (slovenia) case study. *Arheoloski Vestnik*, 62:393–432, 2011. URL: https://www.scopus.com/inward/record.uri?eid=2-s2.0-84856556104&partnerID=40&md5=72bd5538d91ab48a0686bfe8be37cedf.

[418] Benjamin Štular, Žiga Kokalj, Krištof Oštir, and Laure Nuninger. Visualization of lidar-derived relief models for detection of archaeological features. *Journal of Archaeological Science*, 39(11):3354–3360, 2012. URL: https://www.scopus.com/inward/record.uri?eid=2-s2.0-84864320409&doi=10.1016%2fj.jas.2012.05.029&partnerID=40&md5=bfa3c4b240a57c557bfe2c792b134c55, doi:10.1016/j.jas.2012.05.029.

[419] Benjamin Štular, Stefan Eichert, and Edisa Lozić. Airborne lidar point cloud processing for archaeology. pipeline and qgis toolbox. *Remote Sensing*, 13(16):3225, 2021. doi:10.3390/rs13163225.

[420] Benjamin Štular, Edisa Lozić, and Stefan Eichert. Airborne lidar-derived digital elevation model for archaeology. *Remote Sensing*, 13(9):1855, 2021. URL: https://www.scopus.com/inward/record.uri?eid=2-s2.0-85106495800&doi=10.3390%2frs13091855&partnerID=40&md5=402b551b153e03cb1d745136915f4450, doi:10.3390/rs13091855.

[421] B. Štular and E. Lozic. Airborne lidar data in landscape archaeology. an introduction for non-archaeologists. *IT - Information Technology*, 2022. URL: https://www.scopus.com/inward/record.uri?eid=2-s2.0-85135498653&doi=10.1515%2fitit-2022-0001&partnerID=40&md5=44faae83985c7be0b0fb211acb854a30, doi:10.1515/itit-2022-0001.

[422] J. W. Suh, E. Anderson, W. Ouimet, K. M. Johnson, and C. Witharana. Mapping relict charcoal hearths in new england using deep convolutional neural networks and lidar data. *Remote Sensing*, 2021. URL: https://www.scopus.com/inward/record.uri?eid=2-s2.0-85119718322&doi=10.3390%2frs13224630&partnerID=40&md5=56292b1825b1fdf919712ef92066a63a, doi:10.3390/rs13224630.

[423] M. Szczęch and M. Cieszkowski. Geology of the magura nappe, south-western gorce mountains (outer carpathians, poland). *Journal of Maps*, 2021. URL: https://www.scopus.com/inward/record.uri?eid=2-s2.0-85110881206&doi=10.1080%2f17445647.2021.1950579&partnerID=40&md5=cccfa84973b97b30da4e9aae93b2219d, doi:10.1080/17445647.2021.1950579.

[424] Atsushi Takizawa and Hina Kinugawa. Deep learning model to reconstruct 3d cityscapes by generating depth maps from omnidirectional images and its application to visual preference prediction. *Design Science*, 2020. URL: https://www.scopus.com/inward/record.uri?eid=2-s2.0-85096133851&doi=10.1017%2fdsj.2020.27&partnerID=40&md5=a6583c544961cc4b04185596fa4794f3, doi:10.1017/dsj.2020.27.

[425] M. Tanu, W. Amponsah, B. Yahaya, E. Bessah, S. O. Ansah, C. S. Wemegah, and W. A. Agyare. Evaluation of global solar radiation, cloudiness index and sky view factor as potential indicators of ghana's solar energy resource. *Scientific African*, 2021. URL: https://www.scopus.com/inward/record.uri?eid=2-s2.0-85120163475&doi=10.1016%2fj.sciaf.2021.e01061&partnerID=40&md5=0e83cd1f37b97118bf408b8d9ebf5b62, doi:10.1016/j.sciaf.2021.e01061.

[426] Paolo Tarolli, Wenfang Cao, Giulia Sofia, Damian Evans, and Erle C. Ellis. From features to fingerprints: a general diagnostic framework for anthropogenic geomorphology. *Progress in Physical Geography: Earth and Environment*, 43(1):95–128, 2019. doi:10.1177/0309133318825284.

[427] Simone Tarquini and Luca Nannipieri. The 10 m-resolution tinitaly dem as a trans-disciplinary basis for the analysis of the italian territory: current trends and new perspectives. *Geomorphology*, 281:108–115, 2017. URL: https://www.scopus.com/inward/record.uri?eid=2-s2.0-85009736240&doi=10.1016%2fj.geomorph.2016.12.022&partnerID=40&md5=54e4951c849b02a2cb63e3c4f844617b, doi:10.1016/j.geomorph.2016.12.022.

[428] Richard Thér. Ceramic technology. how to reconstruct and describe pottery-forming practices. *ARCHAEOLOGICAL AND ANTHROPOLOGICAL SCIENCES*, 2020. URL: https://www.scopus.com/inward/record.uri?eid=2-s2.0-85087856600&doi=10.1007%2fs12520-020-01131-0&partnerID=40&md5=2044c95db2ae53c3e83b2fd0f25f3630, doi:10.1007/s12520-020-01131-0.

[429] Amy E. Thompson. Detecting classic maya settlements with lidar-derived relief visualizations. *Remote Sensing*, 12(17):2838, 2020. URL: https://www.scopus.com/inward/record.uri?eid=2-s2.0-85095110114&doi=10.3390%2frs12172838&partnerID=40&md5=29dc203b3b65750de9edf138153e4d52, doi:10.3390/rs12172838.

[430] Alma Elizabeth Thuestad, Ole Risbøl, Jan Ingolf Kleppe, Stine Barlindhaug, and Elin Rose Myrvoll. Archaeological surveying of subarctic and arctic landscapes: comparing the performance of airborne laser scanning and remote sensing image data. *Sustainability (Switzerland)*, 13(4):1917, 2021. URL:

https://www.scopus.com/inward/record.uri?eid=2-s2.0-85100870449&doi=10.3390%2fsu13041917&partnerID=40&md5=6b3f66afb6b29328050df1d316903e5f, doi:10.3390/su13041917.

[431] Yunyu Tian, Weiqi Zhou, Yuguo Qian, Zhong Zheng, and Jingli Yan. The effect of urban 2d and 3d morphology on air temperature in residential neighborhoods. *LANDSCAPE ECOLOGY*, 34(5):1161–1178, 2019. URL: https://www.scopus.com/inward/record.uri?eid=2-s2.0-85065498028&doi=10.1007%2fs10980-019-00834-7&partnerID=40&md5=142efe36d8d6ddbb0c0ba1336aae6ab2, doi:10.1007/s10980-019-00834-7.

[432] Y. Tian, P. Desouza, S. Mora, X. Yao, F. Duarte, L. K. Norford, H. Lin, and C. Ratti. Evaluating the meteorological effects on the urban form-air quality relationship using mobile monitoring. *Environmental Science and Technology*, 2021. URL: https://www.scopus.com/inward/record.uri?eid=2-s2.0-85124342510&doi=10.1021%2facs.est.1c04854&partnerID=40&md5=5abc07b7b9ffff333024c92679047b6d, doi:10.1021/acs.est.1c04854.

[433] Anna Tirpáková, Jana Vojteková, Matej Vojtek, and Ivona Vlkolinská. Using fuzzy logic to analyze the spatial distribution of pottery in unstratified archaeological sites: the case of the pobedim hillfort (slovakia). *Land*, 10(2):103, 2021. URL: https://www.scopus.com/inward/record.uri?eid=2-s2.0-85099939445&doi=10.3390%2fland10020103&partnerID=40&md5=442c5a61f0a5d0620bbcf4d8a8b48562, doi:10.3390/land10020103.

[434] Ali Torabi Haghighi, Hamid Darabi, Zahra Karimidastenaei, Ali Akbar Davudirad, Sajad Rouzbeh, Omid Rahmati, Farzaneh Sajedi-Hosseini, and Björn Klöve. Land degradation risk mapping using topographic, human-induced, and geo-environmental variables and machine learning algorithms, for the pole-doab watershed, iran. *ENVIRONMENTAL EARTH SCIENCES*, 2021. URL: https://www.scopus.com/inward/record.uri?eid=2-s2.0-85098271591&doi=10.1007%2fs12665-020-09327-2&partnerID=40&md5=31949c0d5755e2288b30f98e03962bba, doi:10.1007/s12665-020-09327-2.

[435] David Torregrosa-Fuentes, Yolanda Spairani Berrio, José Antonio Huesca Tortosa, Jaime Cuevas González, and Adrián José Torregrosa Fuentes. Aplicación de la fotogrametría automatizada y de técnicas de iluminación con herramientas sig para la visualización y el análisis de una piedra con relieves antropomorfos. *Virtual Archaeology Review*, 9(19):114, 2018. URL: https://www.scopus.com/inward/record.uri?eid=2-s2.0-85050307101&doi=10.4995%2fvar.2018.9531&partnerID=40&md5=a00686be82838849187f2053a4c1caac, doi:10.4995/var.2018.9531.

[436] Zsuzsanna Tóth, Stephen McCarron, Andrew J. Wheeler, Stefan Wenau, Stephen Davis, Aaron Lim, and Volkhard Spiess. Geomorphological and seismostratigraphic evidence for multidirectional polyphase glaciation of the northern celtic sea. *JOURNAL OF QUATERNARY SCIENCE*, 35(3):465–478, 2020. URL: https://www.scopus.com/inward/record.uri?eid=2-s2.0-85083540653&doi=10.1002%2fjqs.3189&partnerID=40&md5=e8e3616fac65ffcaed9eb5e094696178, doi:10.1002/jqs.3189.

[437] Jean-Pierre Toumazet, Franck Vautier, Erwan Roussel, and Bertrand Dousteyssier. Automatic detection of complex archaeological grazing structures using airborne laser scanning data. *Journal of Archaeological Science: Reports*, 12:569–579, 2017. URL: https://www.scopus.com/inward/record.uri?eid=2-s2.0-85015241986&doi=10.1016%2fj.jasrep.2017.03.012&partnerID=40&md5=e0db0e3c99625cd93f5bf0fd97fba1b4, doi:10.1016/j.jasrep.2017.03.012.

[438] Øivind Due Trier and Lars Holger Pilø. Automatic detection of pit structures in airborne laser scanning data. *Archaeological Prospection*, 19(2):103–121, 2012. URL: https://www.scopus.com/inward/record.uri?eid=2-s2.0-84861895524&doi=10.1002%2farp.1421&partnerID=40&md5=db8cee98b430ca81327230c67e7d57d0, doi:10.1002/arp.1421.

[439] Øivind Due Trier, Maciel Zortea, and Christer Tonning. Automatic detection of mound structures in airborne laser scanning data. *Journal of Archaeological Science: Reports*, 2:69–79, 2015. URL: https://www.scopus.com/inward/record.uri?eid=2-s2.0-84922698876&doi=10.1016%2fj.jasrep.2015.01.005&partnerID=40&md5=447f4ab82a49609349ba7cc4c8c5ce05, doi:10.1016/j.jasrep.2015.01.005.

[440] Ching-Ying Tsou, Masahiro Chigira, Yuki Matsushi, Narumi Hiraishi, and Noriyuki Arai. Coupling fluvial processes and landslide distribution toward geomorphological hazard assessment: a case study in a transient landscape in japan. *LANDSLIDES*, 14(6):1901–1914, 2017. URL: https:

//www.scopus.com/inward/record.uri?eid=2-s2.0-85019589894&doi=10.1007%2fs10346-017-0838-3&partnerID=40&md5=2e6a41e531e491b30b77f8743154ddaf, doi:10.1007/s10346-017-0838-3.

[441] Richard Tuffin, David Roe, Martin Gibbs, Donald Clark, and Marcus Clark. Landscapes of production and punishment: lidar and the process of feature identification and analysis at a tasmanian convict station. *Australian Archaeology*, 86(1):37–56, 2020. doi:10.1080/03122417.2020.1749406.

[442] Mark Axel Tveskov, Chelsea Rose, Geoffrey Jones, and David Maki. Every rusty nail is sacred, every rusty nail is good: conflict archaeology, remote sensing, and community engagement at a northwest coast settler fort. *American Antiquity*, 84(1):48–67, 2019. URL: https://www.scopus.com/inward/record.uri?eid=2-s2.0-85061008015&doi=10.1017%2faaq.2018.80&partnerID=40&md5=9557864db5bc606b2805b275e0394ba4, doi:10.1017/aaq.2018.80.

[443] E. L. Usery, S. T. Arundel, E. Shavers, L. Stanislawski, P. Thiem, and D. Varanka. Geoai in the us geological survey for topographic mapping. *Transactions in GIS*, 2021. URL: https://www.scopus.com/inward/record.uri?eid=2-s2.0-85113892394&doi=10.1111%2ftgis.12830&partnerID=40&md5=9c29af42827dce19f84c61b87079c714, doi:10.1111/tgis.12830.

[444] L.-M.L. Valdes, M. Katurji, and H. Meyer. A machine learning based downscaling approach to produce high spatio-temporal resolution land surface temperature of the antarctic dry valleys from modis data. *Remote Sensing*, 2021. URL: https://www.scopus.com/inward/record.uri?eid=2-s2.0-85119895178&doi=10.3390%2frs13224673&partnerID=40&md5=a41f55ea0a292028dc88ef3b4aeb55a1, doi:10.3390/rs13224673.

[445] Hanne van den Berghe, W. Gheyle, N. Note, B. Stichelbaut, M. van Meirvenne, J. Bourgeois, and V. van Eetvelde. Revealing the preservation of first world war shell hole landscapes based on a landscape change study and lidar. *Geografisk Tidsskrift - Danish Journal of Geography*, 119(1):38–51, 2019. URL: https://www.scopus.com/inward/record.uri?eid=2-s2.0-85058647072&doi=10.1080%2f00167223.2018.1556105&partnerID=40&md5=44537c8c97c07bc53bca9f99748191fd, doi:10.1080/00167223.2018.1556105.

[446] Miet van den Eeckhaut, Norman Kerle, Jean Poesen, and Javier Hervás. Object-oriented identification of forested landslides with derivatives of single pulse lidar data. *Geomorphology*, 173-174:30–42, 2012. URL: https://www.scopus.com/inward/record.uri?eid=2-s2.0-84865970067&doi=10.1016%2fj.geomorph.2012.05.024&partnerID=40&md5=07efdb27b1dc330604b81379d99d1441, doi:10.1016/j.geomorph.2012.05.024.

[447] Frank van der Hoeven and Alexander Wandl. Amsterwarm: mapping the landuse, health and energy-efficiency implications of the amsterdam urban heat island. *Building Services Engineering Research and Technology*, 36(1):67–88, 2015. URL: https://www.scopus.com/inward/record.uri?eid=2-s2.0-84915745926&doi=10.1177%2f0143624414541451&partnerID=40&md5=38dbf7471d98e64e4e9343ade9f0397d, doi:10.1177/0143624414541451.

[448] Frank van der Hoeven and Alexander Wandl. Hotterdam: mapping the social, morphological, and land-use dimensions of the rotterdam urban heat island. *Urbani Izziv*, 29(1):58–72, 2018. URL: https://www.scopus.com/inward/record.uri?eid=2-s2.0-85049352484&doi=10.5379%2furbani-izziv-en-2018-29-01-001&partnerID=40&md5=af89b0e0869b621b243a54143e5a0c1f, doi:10.5379/urbani-izziv-en-2018-29-01-001.

[449] H. van Gils and T. Kasielke. Historical parcellation and ridge-and-furrow relics of open strip-fields in the north-west european lowlands. *Landscape History*, 43(2):77–102, 2022. URL: https://www.scopus.com/inward/record.uri?eid=2-s2.0-85143356492&doi=10.1080%2f01433768.2022.2143158&partnerID=40&md5=7c19b09b1182e86c09918bb49dee8fd5, doi:10.1080/01433768.2022.2143158.

[450] Aristotelis Vartholomaios. A machine learning approach to modelling solar irradiation of urban and terrain 3d models. *Computers, Environment and Urban Systems*, 78:101387, 2019. URL: https://www.scopus.com/inward/record.uri?eid=2-s2.0-85070681993&doi=10.1016%2fj.compenvurbsys.2019.101387&partnerID=40&md5=d43df2d67d9c25608ddd7f46d42e9237, doi:10.1016/j.compenvurbsys.2019.101387.

[451] Timotej Verbovšek, Tomislav Popit, and Žiga Kokalj. Vat method for visualization of mass movement features: an alternative to hillshaded dem. *Remote Sensing*, 11(24):2946, 2019. URL: https://www.scopus.com/inward/record.uri?eid=2-s2.0-85077893489&doi=10.3390%2frs11242946&partnerID=40&md5=e75ae2b9e0ac88cb64a7b4ced5540233, doi:10.3390/rs11242946.

[452] Geert Verhoeven and Frank Vermeulen. Engaging with the canopy—multi-dimensional vegetation mark visualisation using archived aerial images. *Remote Sensing*, 8(9):752, 2016. URL: https://www.scopus.com/inward/record.uri?eid=2-s2.0-85019352916&doi=10.3390%2frs8090752&partnerID=40&md5=ecceeaabee06785fe99f9b93f39b5e44, doi:10.3390/rs8090752.

[453] Geert J. Verhoeven. Mesh is more—using all geometric dimensions for the archaeological analysis and interpretative mapping of 3d surfaces. *Journal of Archaeological Method and Theory*, 24(4):999–1033, 2017. URL: https://www.scopus.com/inward/record.uri?eid=2-s2.0-84994442693&doi=10.1007%2fs10816-016-9305-z&partnerID=40&md5=d3cd1cbbcfc1aa2c300e92422d7c21fa, doi:10.1007/s10816-016-9305-z.

[454] Julio Manuel Vidal Encinas, José Manuel Costa García, David González Álvarez, and Andrés Menéndez Blanco. La presencia del ejército romano en las montañas de el bierzo (león): novedades arqueológicas. *Anales de Arqueologia Cordobesa*, 29:85–110, 2019. URL: https://www.scopus.com/inward/record.uri?eid=2-s2.0-85061162040&doi=10.21071%2faac.v29i0.11021&partnerID=40&md5=4fb2f8bb4498ae5fb9b50873253a2b66, doi:10.21071/aac.v29i0.11021.

[455] F. H. Wagner, V. Peripato, R. Kipnis, S. L. Werdesheim, R. Dalagnol, L.E.O.C. Aragão, and M.C.M. Hirye. Fast computation of digital terrain model anomalies based on lidar data for geoglyph detection in the amazon. *Remote Sensing Letters*, 13(9):935–945, 2022. URL: https://www.scopus.com/inward/record.uri?eid=2-s2.0-85136183338&doi=10.1080%2f2150704X.2022.2109942&partnerID=40&md5=2862f1a9d80e2fa7d23f79d60df3d1c4, doi:10.1080/2150704X.2022.2109942.

[456] Alina Walch, Roberto Castello, Nahid Mohajeri, and Jean-Louis Scartezzini. Big data mining for the estimation of hourly rooftop photovoltaic potential and its uncertainty. *APPLIED ENERGY*, 262:114404, 2020. URL: https://www.scopus.com/inward/record.uri?eid=2-s2.0-85078898823&doi=10.1016%2fj.apenergy.2019.114404&partnerID=40&md5=e846207e62ab674500553b016d30cbf7, doi:10.1016/j.apenergy.2019.114404.

[457] Wei Wang, Gaofei Yin, Wei Zhao, Fengping Wen, and Daijun Yu. Spatial downscaling of msg downward shortwave radiation product under clear-sky condition. *IEEE TRANSACTIONS ON GEOSCIENCE AND REMOTE SENSING*, 58(5):3264–3272, 2020. URL: https://www.scopus.com/inward/record.uri?eid=2-s2.0-85084129695&doi=10.1109%2fTGRS.2019.2951699&partnerID=40&md5=c18eb943b288e1dc7ba72780ed0a0a44, doi:10.1109/TGRS.2019.2951699.

[458] L. Wang, B. Wu, A. Elnashar, W. Zhu, N. Yan, Z. Ma, S. Liu, and X. Niu. Incorporation of net radiation model considering complex terrain in evapotranspiration determination with sentinel-2 data. *Remote Sensing*, 2022. URL: https://www.scopus.com/inward/record.uri?eid=2-s2.0-85126336910&doi=10.3390%2frs14051191&partnerID=40&md5=6d13a6217a18b427c3c5490b2927a299, doi:10.3390/rs14051191.

[459] Marcus White, Youpei Hu, Nano Langenheim, Wowo Ding, and Mark Burry. Cool city design: integrating real-time urban canyon assessment into the design process for chinese and australian cities. *URBAN PLANNING*, 1(3):25–37, 2016. URL: https://www.scopus.com/inward/record.uri?eid=2-s2.0-85044438667&doi=10.17645%2fup.v1i3.646&partnerID=40&md5=684b3a3dcf1a43134747dae13ee46e1e, doi:10.17645/up.v1i3.646.

[460] Chandi Witharana, William B. Ouimet, and Katharine M. Johnson. Using lidar and geobia for automated extraction of eighteenth–late nineteenth century relict charcoal hearths in southern new england. *GIScience and Remote Sensing*, 55(2):183–204, 2018. URL: https://www.scopus.com/inward/record.uri?eid=2-s2.0-85041568131&doi=10.1080%2f15481603.2018.1431356&partnerID=40&md5=3abca52f5d874c9a696f8d3f60261993, doi:10.1080/15481603.2018.1431356.

[461] Shengbiao Wu, Jianguang Wen, Dongqin You, Hailong Zhang, Qing Xiao, and Qinhuo Liu. Algorithms for calculating topographic parameters and their uncertainties in downward surface solar radiation (dssr) estimation. *IEEE GEOSCIENCE AND REMOTE SENSING LETTERS*, 15(8):1149–1153, 2018. URL: https://www.scopus.com/inward/record.uri?eid=2-s2.0-85047014707&doi=10.1109%2fLGRS.2018.2831916&partnerID=40&md5=6c34cd1ed2a3951331df99e92521dc89, doi:10.1109/LGRS.2018.2831916.

[462] Yuwei Wu, Ninglian Wang, Zhen Li, Anan Chen, Zhongming Guo, and Yufan Qie. The effect of thermal radiation from surrounding terrain on glacier surface temperatures retrieved from remote sensing data: a case study from qiyi glacier, china. *REMOTE SENSING OF ENVIRONMENT*, 231:111267, 2019. URL:

https://www.scopus.com/inward/record.uri?eid=2-s2.0-85067871204&doi=10.1016%2fj.rse.2019.111267&partnerID=40&md5=bb94b97d03b8f7839792dbe94d1f7f8d, doi:10.1016/j.rse.2019.111267.

[463] Xinyao Xie and Ainong Li. An adjusted two–leaf light use efficiency model for improving gpp simulations over mountainous areas. *Journal of Geophysical Research: Atmospheres*, 2020. URL: https://www.scopus.com/inward/record.uri?eid=2-s2.0-85087695104&doi=10.1029%2f2019JD031702&partnerID=40&md5=5edc2103e8a6be2a74ae31987029edf8, doi:10.1029/2019JD031702.

[464] Xinyao Xie, Jing M. Chen, Peng Gong, and Ainong Li. Spatial scaling of gross primary productivity over sixteen mountainous watersheds using vegetation heterogeneity and surface topography. *Journal of Geophysical Research: Biogeosciences*, 2021. URL: https://www.scopus.com/inward/record.uri?eid=2-s2.0-85106908599&doi=10.1029%2f2020JG005848&partnerID=40&md5=f8868f1c3c4b8e4603456f3c82217c5b, doi:10.1029/2020JG005848.

[465] X. Xie, A. Li, H. Jin, J. Bian, Z. Zhang, and X. Nan. Comparing three remotely sensed approaches for simulating gross primary productivity over mountainous watersheds: a case study in the wanglang national nature reserve, china. *Remote Sensing*, 2021. URL: https://www.scopus.com/inward/record.uri?eid=2-s2.0-85114681806&doi=10.3390%2frs13183567&partnerID=40&md5=c78b5cdbbc89d97c5263345cffe59187, doi:10.3390/rs13183567.

[466] X. Xie, A. Li, J. Tian, C. Wu, and H. Jin. A fine spatial resolution estimation scheme for large-scale gross primary productivity (gpp) in mountain ecosystems by integrating an eco-hydrological model with the combination of linear and non-linear downscaling processes. *Journal of Hydrology*, 2023. URL: https://www.scopus.com/inward/record.uri?eid=2-s2.0-85145547978&doi=10.1016%2fj.jhydrol.2022.128833&partnerID=40&md5=843c5eb634b83f187bdacabfe5426626, doi:10.1016/j.jhydrol.2022.128833.

[467] F. Xu, P. Xia, H. You, and J. Du. Robotic cross-platform sensor fusion and augmented visualization for large indoor space reality capture. *Journal of Computing in Civil Engineering*, 2022. URL: https://www.scopus.com/inward/record.uri?eid=2-s2.0-85137739502&doi=10.1061%2f%28ASCE%29CP.1943-5487.0001047&partnerID=40&md5=f717e59c903364f18527465d9e25220e, doi:10.1061/(ASCE)CP.1943-5487.0001047.

[468] X. Xu, W. Qiu, W. Li, D. Huang, X. Li, and S. Yang. Comparing satellite image and gis data classified local climate zones to assess urban heat island: a case study of guangzhou. *Frontiers in Environmental Science*, 2022. URL: https://www.scopus.com/inward/record.uri?eid=2-s2.0-85143373848&doi=10.3389%2ffenvs.2022.1029445&partnerID=40&md5=c9119ef396eda5eb281fa6586313a531, doi:10.3389/fenvs.2022.1029445.

[469] Jinxin Yang, Man Sing Wong, Massimo Menenti, and Janet Nichol. Modeling the effective emissivity of the urban canopy using sky view factor. *ISPRS JOURNAL OF PHOTOGRAMMETRY AND REMOTE SENSING*, 105:211–219, 2015. URL: https://www.scopus.com/inward/record.uri?eid=2-s2.0-84928676341&doi=10.1016%2fj.isprsjprs.2015.04.006&partnerID=40&md5=597e04df6e880e9baa990d1a0173ed7b, doi:10.1016/j.isprsjprs.2015.04.006.

[470] Jinxin Yang, Man Sing Wong, Massimo Menenti, and Janet Nichol. Study of the geometry effect on land surface temperature retrieval in urban environment. *ISPRS JOURNAL OF PHOTOGRAMMETRY AND REMOTE SENSING*, 109:77–87, 2015. URL: https://www.scopus.com/inward/record.uri?eid=2-s2.0-84942515396&doi=10.1016%2fj.isprsjprs.2015.09.001&partnerID=40&md5=7d2feb6493039e00d736f401ef375c76, doi:10.1016/j.isprsjprs.2015.09.001.

[471] Jinxin Yang, Man Sing Wong, Massimo Menenti, Janet Nichol, James Voogt, E. Scott Krayenhoff, and P. W. Chan. Development of an improved urban emissivity model based on sky view factor for retrieving effective emissivity and surface temperature over urban areas. *ISPRS JOURNAL OF PHOTOGRAMMETRY AND REMOTE SENSING*, 122:30–40, 2016. URL: https://www.scopus.com/inward/record.uri?eid=2-s2.0-84994618751&doi=10.1016%2fj.isprsjprs.2016.09.007&partnerID=40&md5=ceb6600f4b5729757085620df19865de, doi:10.1016/j.isprsjprs.2016.09.007.

[472] Jinxin Yang, Man Sing Wong, and Massimo Menenti. Effects of urban geometry on turbulent fluxes: a remote sensing perspective. *IEEE GEOSCIENCE AND REMOTE SENSING LETTERS*, 13(12):1767–1771, 2016. URL: https://www.scopus.com/inward/record.uri?eid=2-s2.0-84991109565&doi=10.1109%2fLGRS.2016.2607759&partnerID=40&md5=dafce7d0f8baf6c2a6b977e8d892ada8, doi:10.1109/LGRS.2016.2607759.

[473] J. Yang, Q. Shi, M. Menenti, Y. Xie, Z. Wu, Y. Xu, and S. Abbas. Characterizing the thermal effects of vegetation on urban surface temperature. *URBAN CLIMATE*, 2022. URL: https://www.scopus.com/inward/record.uri?eid=2-s2.0-85131838518&doi=10.1016%2fj.uclim.2022.101204&partnerID=40&md5=3bbf050509ca20c95c6379206c1e7b29, doi:10.1016/j.uclim.2022.101204.

[474] Gaofei Yin, Ainong Li, Wei Zhao, Huaan Jin, Jinhu Bian, and Shengbiao Wu. Modeling canopy reflectance over sloping terrain based on path length correction. *IEEE TRANSACTIONS ON GEOSCIENCE AND REMOTE SENSING*, 55(8):4597–4609, 2017. URL: https://www.scopus.com/inward/record.uri?eid=2-s2.0-85018874563&doi=10.1109%2fTGRS.2017.2694483&partnerID=40&md5=b8f5f7b3f3c88b4d0f2752d0c3bc10bd, doi:10.1109/TGRS.2017.2694483.

[475] Gaofei Yin, Ainong Li, Shengbiao Wu, Weiliang Fan, Yelu Zeng, Kai Yan, Baodong Xu, Jing Li, and Qinhuo Liu. Plc: a simple and semi-physical topographic correction method for vegetation canopies based on path length correction. *REMOTE SENSING OF ENVIRONMENT*, 215:184–198, 2018. URL: https://www.scopus.com/inward/record.uri?eid=2-s2.0-85048303820&doi=10.1016%2fj.rse.2018.06.009&partnerID=40&md5=d54a9611d84a479965d40e158ba98cfe, doi:10.1016/j.rse.2018.06.009.

[476] Klemen Zakšek, Kristof Oštir, and Žiga Kokalj. Sky-view factor as a relief visualization technique. *Remote Sensing*, 3(2):398–415, 2011. doi:10.3390/rs3020398.

[477] Klemen Zakšek and Krištof Oštir. Downscaling land surface temperature for urban heat island diurnal cycle analysis. *REMOTE SENSING OF ENVIRONMENT*, 117:114–124, 2012. URL: https://www.scopus.com/inward/record.uri?eid=2-s2.0-84855446968&doi=10.1016%2fj.rse.2011.05.027&partnerID=40&md5=238814fdaff43b49b4d00a39ee79f8df, doi:10.1016/j.rse.2011.05.027.

[478] Yanlin Zhang, Xiaoli Chang, and Ji Liang. Comparison of different algorithms for calculating the shading effects of topography on solar irradiance in a mountainous area. *ENVIRONMENTAL EARTH SCIENCES*, 2017. URL: https://www.scopus.com/inward/record.uri?eid=2-s2.0-85017201939&doi=10.1007%2fs12665-017-6618-5&partnerID=40&md5=53497daef90f3df09eb379594a032569, doi:10.1007/s12665-017-6618-5.

[479] Y. L. Zhang, X. Li, G. D. Cheng, H. J. Jin, D. W. Yang, G. N. Flerchinger, X. L. Chang, X. Wang, and J. Liang. Influences of topographic shadows on the thermal and hydrological processes in a cold region mountainous watershed in northwest china. *JOURNAL OF ADVANCES IN MODELING EARTH SYSTEMS*, 10(7):1439–1457, 2018. URL: https://www.scopus.com/inward/record.uri?eid=2-s2.0-85050827341&doi=10.1029%2f2017MS001264&partnerID=40&md5=82435c07fd1efd62147ffe9ac7305669, doi:10.1029/2017MS001264.

[480] Guan-Ting Zhang, Edward Verbree, and Xiao-Jun Wang. An approach to map visibility in the built environment from airborne lidar point clouds. *IEEE Access*, 9:44150–44161, 2021. URL: https://www.scopus.com/inward/record.uri?eid=2-s2.0-85103418078&doi=10.1109%2fACCESS.2021.3066649&partnerID=40&md5=041d9f20d4d80bbdd5decad25dcc959f, doi:10.1109/ACCESS.2021.3066649.

[481] C. Zhang, Y. Guo, Z. He, L. He, and H. Xu. Analysis of influence mechanism of spatial distribution of incoming solar radiation based on dem. *Earth Science Informatics*, 2022. URL: https://www.scopus.com/inward/record.uri?eid=2-s2.0-85122789952&doi=10.1007%2fs12145-021-00740-0&partnerID=40&md5=11ce6394076baa8151c627fc96637aa5, doi:10.1007/s12145-021-00740-0.

[482] S. Zhang, X. Fang, C. Cheng, L. Chen, L. Zhang, Y. Yu, L. Li, and H. Luo. Research on the planning method and strategy of urban wind and heat environment optimization—taking shenzhen, a sub-tropical megacity in southern china, as an example. *ATMOSPHERE*, 2022. URL: https://www.scopus.com/inward/record.uri?eid=2-s2.0-85138684177&doi=10.3390%2fatmos13091395&partnerID=40&md5=e83ba3ad9b09f94c88f45adfff73e329, doi:10.3390/atmos13091395.

[483] Wei Zhou, Fulong Chen, Huadong Guo, Mingyuan Hu, Qi Li, Panpan Tang, Wenwu Zheng, Jian'an Liu, Rupeng Luo, Kaikai Yan, Ru Li, Pilong Shi, and Sheng Nie. Uav laser scanning technology: a potential cost-effective tool for micro-topography detection over wooded areas for archaeological prospection. *International Journal of Digital Earth*, 13(11):1279–1301, 2020. URL: https://www.scopus.com/inward/record.uri?eid=2-s2.0-85078608030&doi=10.1080%2f17538947.2019.1711209&partnerID=40&md5=1c822767ff74f6bef352578947b8c21e, doi:10.1080/17538947.2019.1711209.

[484] Georg Zotti and Wolfgang Neubauer. Beyond the landscape: analysis of neolithic circular ditch systems of lower austria with advanced virtual archaeoastronomy. *Virtual Archaeology Review*, 10(21):90, 2019. URL: https://www.scopus.com/inward/record.uri?eid=2-s2.0-85071320166&doi=10.4995%2fvar.2019.10772&partnerID=40&md5=1f032a7730cafc39f7a129e87b825d8f, doi:10.4995/var.2019.10772.

PYTHON MODULE INDEX

r

INDEX

H

I

L

M

T

V